Vortex-Induced Vibrations of In-Line Cantilevered Cylinders

A Numerical Investigation for Nuclear Industry Benchmark Testing

Mohammed Muaaz M. D. Hussain

T̃U Delft

NRG

Vortex-Induced Vibrations of In-Line Cantilevered Cylinders

A Numerical Investigation for Nuclear Industry Benchmark Testing

by

Mohammed Muaaz M. D. Hussain

An electronic version of this thesis is available at http://repository.tudelft.nl/.

TUDelft

NRG

Abstract

The advent of global warming has brought an increased interest in non-conventional sources of energy, one of which is nuclear energy. Threatening the almost year-round functioning of nuclear power plants are Flow-Induced Vibrations (FIV). One such mechanism, Vortex-Induced Vibration (VIV), holds importance in areas of cross-flow in nuclear power plants. To make fail-safe designs, computational analysis in the domain of Fluid-Structure Interactions (FSI) has been increasing over the past two decades. The thesis work aims to add to the body of knowledge by making predictions for an in-line two-cylinder configuration, set up as part of a benchmark proposed by the Organization for Economic Co-operation and Development (OECD), using the commercial code *Simcenter STAR-CCM+ (v2020.3.1)*.

The main objective of this study is to test the efficacy of the URANS framework in predicting VIV which is strongly correlated with the objective of the OECD to propose recommendations for the *Best Practice Guidelines*[23]. To do so, it is desired to shortlist the most appropriate turbulence model for the final application and point out gaps in the prediction of the same. The thesis work is thus carried out in three phases: code validation, turbulence model selection and final application. Key results from this study reveal the 'Standard K-Epsilon Low Re: Cubic' model to be the most apt for the final application. Furthermore, gaps are also identified in the application of URANS to predict VIV resonance conditions, the primary of which is the overprediction of the vortex shedding frequency.

Acknowledgements

Contents

List of Figures

List of Tables

1

Introduction

With an increasing worldwide human population comes an increasing energy demand. Different conventional and non-conventional sources of energy are available and made use of which has a direct link to global warming. The Intergovernmental Panel on Climate Change (IPCC) warns humanity about the effects of global warming of 1.5°C above pre-industrial levels and related global greenhouse gas emission pathways.[1] Nuclear energy is a way to transition to a world with low carbon footprint as pointed by many international studies especially when affordability of energy production is considered.[1]–[7]

An advantage of nuclear power plants is its capability of producing electrical power almost year-round with the exception of a 3 week period of refuelling and maintenance. For economic benefit, it is desired that the plants run without any unplanned outages. Another reason for this is the possibility of the nuclear reactor to be unable to restart owing to the build-up of Xenon. After a power decrease or shutdown, it may take upto about 3 days before a typical reactor is able to override the effects of Xenon. Translating the time loss into money at a rate of 1 million euro per day,[8],[9] the desire to avoid outages is made obvious.

A leading reason for the downtime is owed to damage as a result of Flow Induced Vibrations (FIV). FIV has been pointed to be a cause of fatigue problems, stress corrosion, cracking, fretting wear and other possible failure modes in nuclear power plants.[9],[10] Increasing energy demand leads to change of coolant, its flow rate or changes in component material and/or dimensions leading to more prominent FIV.[11] With this in mind, an introduction to nuclear power plants and associated FIV mechanisms are provided in section 1.1 and section 1.2 of this chapter. One such mechanism is brought forth into the limelight through the research objective and associated questions as described in section 1.3. The research methodology adopted in tackling the problem is explained in section 1.4 followed by a general outline of the remainder of the thesis in section 1.5.

1.1. Nuclear Power Plant

A schematic sketch of the secondary circuit of a generic steam-based power plant is shown in Figure 1.1. The steam generated in the steam generator (SG) turns the blades of a turbine (T) which is connected to a generator (G) thereby obtaining electrical energy. After performing work, the steam is condensed in a condenser (C) making use of a water body nearby or a cooling tower (CT). The condensed steam is pumped back to the steam generator via a pump (P) for the cycle to be complete.

1
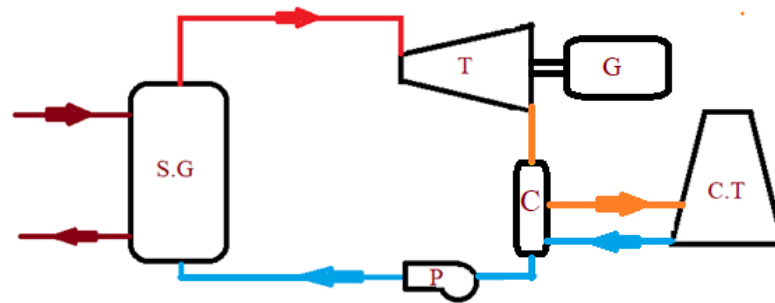
Figure 1.1: Schematic Sketch of a Generic Power Plant

A nuclear power plant makes use of nuclear fission to obtain the energy for converting water to steam in the steam generator. This energy transfer can be done directly as in a *Boiling Water Reactor* (BWR) or indirectly using a primary circuit involving a separate reactor such as the *Pressurized Water Reactor* (PWR). Nuclear reactors can be classified based on the type of nuclear reaction, moderator, coolant, phase of fuel, generation, shape of core and use. Based on the type of nuclear reaction, nuclear reactors can be classified as *thermal neutron reactors* and *fast neutron reactors*. Thermal neutron reactors employ slowed or thermal neutrons by the action of moderator material to increase the probability of fission of an enriched fuel such as uranium-235. Fast neutron reactors employ fast neutrons to cause fission without the use of a moderator, thereby acting on natural or low-enriched fuel to produce another nuclear fuel such as uranium-238 forming plutonium-239 which is better at fissioning than uranium-235.

The Institution of Electrical Engineers has classified the nuclear reactors based on the coolant-moderator combination as follows:[12]

- Gas Cooled & Graphite Moderated - GCR, HTR, AGR
- Hard Water Cooled & Moderated - PHWR, CANDU
- Light Water Cooled & Moderated – PWR, BWR, VVER
- Light Water Cooled & Graphite Moderated – LWGR, RBMK
- Liquid Metal Cooled – FBR, SFR, LFR

Pioneering work on Gas Cooled Reactors (GCR) has been done in the United Kingdom with their fleet of Advanced Gas-cooled Reactors (AGR) that use CO_2 with a graphite moderator. Further development has led to High Temperature Reactors (HTR) which typically uses helium gas as a coolant and a graphite moderator.

Water cooled reactors use either light or heavy water as the coolant. The coolant can also be a moderator or a separate graphite moderator could be used. The most common types are the earlier mentioned PWR and BWR. Besides the difference in the extra circuit, PWR employs light water that is pressured upto about 150 bar which prevents the coolant from boiling in the primary circuit. In both types of such reactors, refuelling has to be done during an outage. This has consequences for the availability (up time) of the reactor. In order to minimise the down-time of a reactor, on-line refuelling, i.e. refuelling during operation, was targeted in other reactor designs. In Russia, this led to the water-cooled graphite-moderated RBMK reactors. In Canada, this led to the so-called CANDU reactors, a Pressurized Heavy Water Reactor (PHWR) type. Besides on-line refuelling, these reactors allow, through the use of heavy water as coolant and moderator, the use of natural uranium, avoiding the need for fuel enrichment required for most other reactors.

For fast neutron reactors, it is desired to split the uranium-239 isotope instead of the uranium-235. To achieve this, moderators are not used in so-called Fast Breeder Reactors (FBR). The most commonly applied coolant is sodium but given its chemically reactive nature, lead and lead-bismuth have also been employed. According to the latest IAEA Power Reactor Information System (PRIS) data[13],[14], the following distribution of reactors in operation and in construction reveals PWR to be the most common type of nuclear reactor.

(a) Operational Reactors

(b) Reactors Under Construction
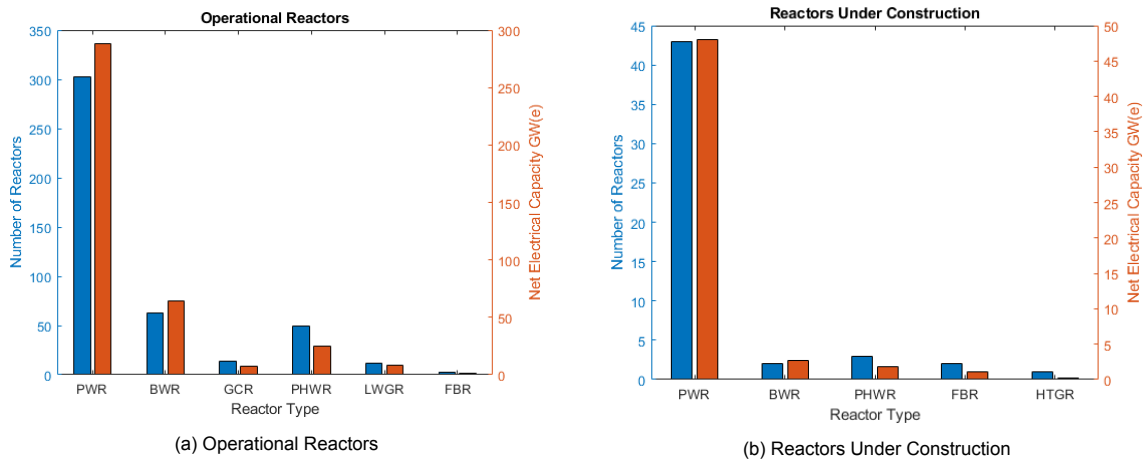
Figure 1.2: Types and Electrical Capacity of Reactors Used and Under Construction Worldwide (as of 12 July 2021)[13],[14]

1.2. Flow Induced Vibration

The term Flow Induced Vibration (FIV) is used to describe all the phenomena that are associated with the response of structures immersed in a flow. In literature for internal flows, the term FIV is used for stationary (statistically steady) flow where interaction is mainly one-way from fluid to solid and Fluid Structure Interaction (FSI) is used for two-way interactions in unsteady flows.[15] However, in this report, both terms are used interchangeably to imply any interaction between solid and fluid for nuclear applications.

Different parts of the nuclear reactor can vibrate due to entirely different excitation mechanisms. Figure 1.3 shows two important areas of concern for a PWR: the pressure vessel (reactor) and the steam generator. Although a vertical steam generator is shown here, horizontal steam generators do exist as have been employed in VVER, a Russian-designed light water cooled and moderated reactor. In fact, they are better than the vertical type on account of easy sludge handling.[16] As far as FIV is concerned, the flow around fuel rods is axial whereas the steam generator tubes have both axial and cross flow. The type of flow along the fuel rods could be single or two-phase. In particular, steam generators have single phase cross flow at the entry, two-phase axial flow in the middle and two-phase cross flow at the U-bend. Such flow conditions decide the nature of interaction between the structure and the fluid.

(a) Pressure Vessel[9]

(b) Steam Generator[17]
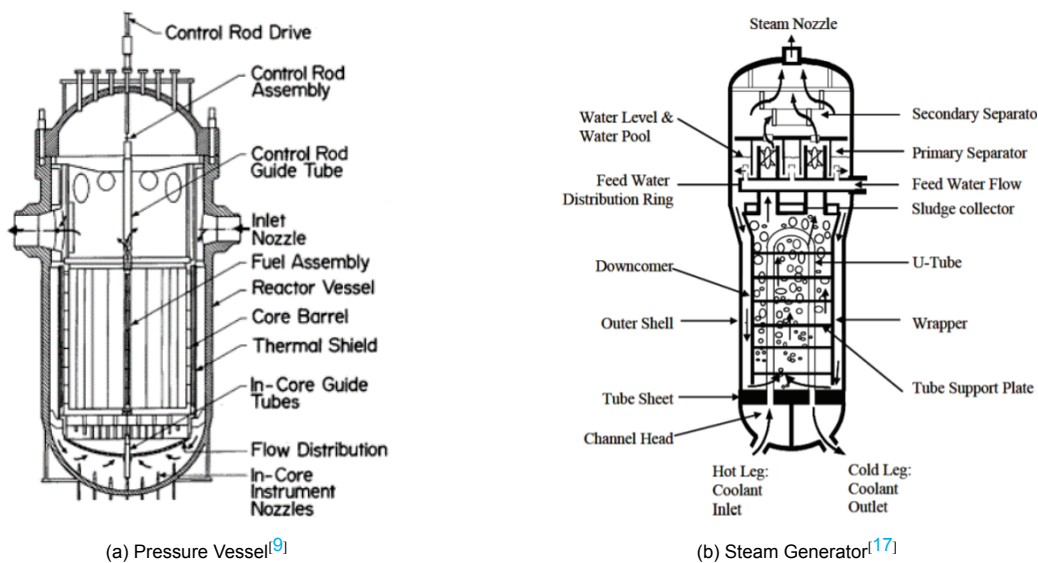
Figure 1.3: Sketches of Areas of Interest for FIV in Nuclear Applications

Pettigrew et. al.[18] provides the following classification of FIV mechanisms in nuclear applications:

1. **Fluid Elastic Instability (FEI)**: This is a result of coupling between fluid-induced dynamic forces and the elastic vibration of structures. When the energy absorbed by structure from the fluid dynamic forces is higher than the energy dissipated by damping, instability occurs. This occurs beyond a certain critical velocity.

2. **Periodic Wake Shedding**: This occurs very readily behind structures in cross flow. With periodic wake or vortex shedding, periodic fluid forces act on the structure which set it to vibrate if the shedding frequency lies in proximity to its natural frequency. The vibration so occurring is termed as Vortex-Induced Vibration (VIV).

3. **Turbulence Excitation**: Turbulence generated locally by the fluid as it flows around a structure (near-field excitation) and that generated by upstream components such as inlet nozzles, elbows, etc. (far-field excitation) can create random pressure fluctuations around the surface of components causing them to vibrate. This vibration is termed as Turbulence Induced Vibration (TIV) and is of prime importance in axial flows.

4. **Acoustic Resonance**: This occurs when the vortex shedding frequency matches with the natural frequency of the acoustic cavity formed by the structures surrounding the primary structure. This is of importance in single phase axial flows as well as tube bundles subjected to gas cross flow.

Figure 1.4 relates the vibration excitation mechanisms to different flow situations in nuclear reactor applications and gives their relative importance. It is observed that for single phase axial flow, acoustic resonance and turbulence excitation are prime suspects for the cause of damage. For steam generators, which generally have cross flow at the entry and the U-bend, fluid elastic instability is the prime suspect for damage. In particular, for liquid flows, periodic shedding and turbulence excitations also have a role to play. For the thesis work, periodic vortex shedding is of prime importance given the operational specifications of the problem fall in the range of the *lock-in regime*, a term that is explained in a subsequent chapter of this report.

Flow situation	Fluidelastic instability	Periodic shedding	Turbulence excitation	Acoustic resonance
Axial flow				
Internal				
Liquid	*	—	**	***
Gas	*	—	*	***
Two-phase	*	—	**	*
External				
Liquid	**	—	**	***
Gas	*	—	*	***
Two-phase	*	—	**	*
Cross flow				
Single cylinders				
Liquid	—	***	**	*
Gas	—	**	*	*
Two-Phase	—	*	**	—
Tube Bundle				
Liquid	***	**	**	*
Gas	***	*	*	***
Two-phase	***	*	**	—

***Most important.   ☐ Steam generator
**Should be considered. ☐ Fuel rods
*Less likely.   ⌐⌐ Steam generator and fuel rods
—, Does not apply.

Figure 1.4: Vibration Excitation Mechanisms (Amended from [18])

Figure 1.5 reveals how these mechanisms may be superimposed to get the vibrational response from a structure. It is observed that FEI is the most destructive mechanism with VIV and acoustic resonance having a specific range in which the destruction is maximum and random vibration or TIV being present in the entire range of flow velocities with its detrimental effect increasing with flow velocity.
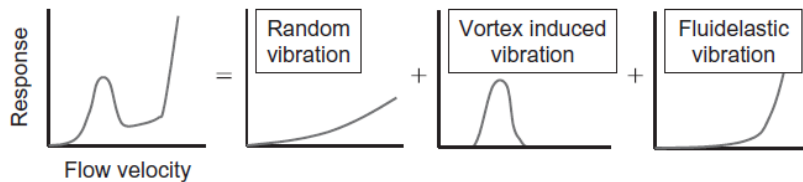
Figure 1.5: Vibrational Response as a Superimposition of Different FIV mechanisms[19]

Another way to classify fluid-structure interaction excitation mechanisms given by Rockwell[20] is based on how they are produced. The categories under this classification are listed below.

1. **Extraneously Induced Excitation**: This is caused by fluctuations in flow velocities or pressure that are independent of any instability due to structural movement except the added mass and fluid damping effects. The exciting force is mostly random but may also be periodic.

2. **Instability Induced Excitation**: The instability is intrinsic to the flow system created by the structure being considered. An example of this would be VIV. There is also a possibility of control mechanisms that can strengthen the excitation such as resonance and fluidelastic feedback.

3. **Movement Induced Excitation**: This occurs due to fluctuating forces that arise due to the movement of a vibrating body. These type of vibrations are thus aptly named self-excited.

Based on the nature of vibrations, Weaver[21] classifies FIV as (a) forced vibrations induced by turbulence, (b) self-controlled vibrations for which some periodicity exists in the flow field that is independent of the movement of the structure, and (c) self-excited vibrations. Blevins[22] uses a phenomenological way of classification, grouping the vibrations as induced by (a) steady flow and (b) unsteady flow. For this report, the classification given by Pettigrew et. al.[18] is deemed more useful in the context of nuclear applications.

1.3. Research Objective

The mechanism of interest in the current study is periodic wake shedding and its associated Vortex-Induced Vibrations (VIV) which is predominant in areas of cross flow around bluff bodies such as that at the inlet and U-bends of steam generators of nuclear power plants. With the advancements in Computational Fluid Dynamics (CFD) and Computational Structural Mechanics (CSM), 'coupled CFD-CSM', or 'FSI' solvers are made use to predict FIV. In particular, FSI calculations must determine forces which act at both the hydrodynamic frequency and the natural frequency of the structure. The complexity of calculations is determined by the problem of separating physical instability in the flow from numerical errors. Therefore, development of recommendations and further update of the *Best Practice Guidelines*[23] on carrying out the coupled calculations appears to be a relevant problem.

In order to deal with this problem, the Organization for Economic Co-operation and Development (OECD) has proposed a benchmark that provides the possibility of joint measurements of the vibration and flow hydrodynamic parameters. The current study, carried out at the Nuclear Research and Consultancy Group (NRG) in The Netherlands, aims to present numerical FSI predictions for this benchmark along with 18 other participants from all around the globe.

For this proposed benchmark, if the challenge is to produce very accurate results, one may very well go for Direct Numerical Simulations (DNS) or Large Eddy Simulations (LES) for the CFD side of the FSI calculations. For the author and NRG, however, an additional constraint is to acquire the calculation results within the timeframe of this Master Thesis which calls for the use of computationally cheaper Unsteady Reynolds-Averaged Navier-Stokes (URANS) models. Thus, the current study aims to judge how well the current state-of-the-art URANS models fair in this challenging FSI benchmark.

Formally, the main goals of the benchmark from the perspective of the OECD organization are:

1. Obtain experimental data on a strongly coupled novel setup relevant for nuclear applications in order to validate the calculations of the participants of the benchmark.

2. Developing recommendations for the Best Practice Guidelines[23] based on the approaches and results of the participants.

The problem so chosen is a novel setup of two in-line cantilevered cylinders (more precisely capped tubes) housed in a rectangular channel subjected to cross flow at subcritical Reynolds number. More details about the same are provided in chapter 5. While the current study inherently conforms to the second goal, the below objective takes the limelight for the thesis work:

"To test the efficacy of URANS models in the prediction of VIV by selecting the best suited URANS model (and associated settings) for the OECD benchmark and establishing the gap between this model and the available experimental data".

The above objective lays the foundation for future improvements in URANS for cross flow FSI predictions, for example via the Pressure Fluctuation Models (PFM) that were proposed earlier in the works of Kottapalli[24] and Sharma[25]. Now although PFM shows best improvements for TIV, it could help in improving predictions of vibrations that are both vortex-induced and turbulence-induced (as in the current study) by providing physical turbulence at the inlet in terms of velocity and pressure fluctuations rather than modelled turbulence in the form of turbulent kinetic energy alone.

The above objective can also be posed as the following question:

"Can URANS accurately capture VIV of in-line cantilevered cylinders?"

To aid in answering the same, the following sub-questions are raised:

1. Which of the two popular URANS models (k-ω SST and k-ϵ) provides the closest prediction to the experimental results?

2. Given the novel nature of the benchmark, what mesh size, time step and total simulation time is to be selected for the simulation? We know that smaller values for the first two and larger values for the third will lead to better predictions.

    (a) What is the expected natural frequency of the structure and the hydrodynamic frequency (vortex shedding frequency) of the flow? A thumb rule of 100 sampling points per cycle can help select a time step, while the CFL criterion can help select a corresponding mesh size.

    (b) How long does the transient phase of the simulation last until the periodic nature of the response sets in? Sufficient simulation time (as a thumb rule 6 flow passes) is required beyond this phase to make sufficiently accurate/detailed frequency-spectra plots.

    (c) Given the timeline of the project, what is the current number of cores available and the physical time taken to compute each time step on these number of cores? This would be a feasibility check on the selection of time step, mesh size and total simulation time as one can predict how long the total simulation will take in real time.

The commercial code *Simcenter STAR-CCM+ (v2020.3.1)* is employed for making the numerical predictions. This particular multi-physics CFD software comes with an in-built FSI solver: in particular, a finite volume flow solver with a wide range of turbulence models, a finite element structural solver and an integrated Gauss-Seidel FSI coupling for the flow and structural solvers.

1.4. Research Methodology

With the objective and research questions in mind, a methodological/sequential process is established with which the aforementioned questions are answered and the end goals set for the current study are achieved. Given that the current study involves the code Simcenter STAR-CCM+, the first logical step is to explore the parameter settings for the associated CFD and CSM solvers as well as the Gauss-Seidel FSI coupling by testing them against an FSI benchmark before using this tool for the OECD Benchmark.

Following the validation test of the tool, the turbulence models with their wide range of settings is to be tested to select/shortlist candidates for the OECD benchmark. Given the large number of options, it is infeasible to work these models on the benchmark directly; instead another experimental benchmark/study is to be adopted that bears some resemblance to the problem but is not as computationally expensive to carry out.

Finally, the shortlisted candidate models are applied to the open phase (where experimental results are *available*) of the OECD benchmark to select the best model and apply it to the blind phase (where experimental results are *not available*) of the OECD Benchmark. Further details of the benchmark are provided in chapter 5 and chapter 6. With these ideas in mind, the current study is structured into the following 3 phases:

1.4.1. Phase 1
The first phase deals with the validation of the commercial code. This will be done by validating the calculations of the setup of the well-known numerical benchmark of Turek & Hron[26]. In particular, the 'CFD3', 'CSM2' and 'FSI3' test cases of this benchmark will be tested. The FSI3 test case is specifically chosen as it is the most strongly coupled test case available (with the fluid and solid densities being equal) and hence also the most challenging to compute numerically. In addition, the thumb rule of 100 sampling points per cycle mentioned in the previous section is tested using the 'CFD3' test case. Details of the setup and obtained solutions are provided in chapter 4.

1.4.2. Phase 2
Once the code is validated, the focus shifts to shortlisting the model candidates for the OECD benchmark. The associated model settings of interest here are '*constitutive relationship*', '*Low Re modification*' and the '*Gamma-Re-Theta transition*'. Theoretical details about these settings are provided in chapter 3. Each of these settings in different combinations are tested. The single elastically mounted rigid cylinder vibration study of Khalak & Williamson[27] is selected for zoning into the candidates for the OECD benchmark given the same mechanism of vibration and a similar range of Reynolds Number. To make it feasible to test the models in the time-frame, a 2D simulation study is carried out. Further details of the setup and obtained solutions are provided in chapter 4.

1.4.3. Phase 3
With the model candidates shortlisted, the OECD benchmark is tackled in two steps:

Open Phase Study
The open phase study of the OECD benchmark contains a setup of two cantilevered in-line cylinders of diameters 7 mm each, placed 45 mm apart in a rectangular channel. The experimental results are available for this setup at two flow rates: one at resonance (16 m^3/h) and other at off-resonance (10 m^3/h). For this phase of the study, the candidate models are applied to simulate the resonance case alone and the one providing the best match with the experimental results is picked for the Blind Phase. Based on the available resources and thumb rules, the mesh size, time step and total run time of the simulations are selected. At this point, we already have some inkling as to the capability of URANS in capturing VIV. Based on the shortcomings of the results, a few hypotheses are formulated about the specific cause of difference.

Blind Phase Study
With the "best" model and settings selected, the same is applied to the blind phase of the OECD benchmark. The setup is exactly the same except for the cylinder size being larger with a diameter of 10 mm. This translates to a different natural frequency thereby requiring different flow rates to test resonance. For this phase, both proposed flow rates for off-resonance (16 m^3/h) and resonance (35 m^3/h) are tested. However, for this phase, the experimental results are not disclosed to the participants. The blind phase study also serves to test the hypotheses drafted in the open phase study of the benchmark. With this final study, the original objective is met.

Further details of the setup and results are provided in chapter 5 and chapter 6 respectively.

1.5. Thesis Outline

In this chapter, an introduction to nuclear power plants and associated FIV mechanisms was provided. This was followed by the research objective and methodology. The remainder of the report is structured as follows:

chapter 2 contains a review on Vortex-Induced Vibrations of single and multi-cylinder configurations as well as the important non-dimensional quantities affecting the same. chapter 3 provides under-the-hood details of the numerical procedures and governing equations solved by the STAR-CCM+ code. chapter 4 provides the details and solutions computed in Phase 1 and 2 of this study. chapter 5 and chapter 6 formally introduce the open and blind phase OECD benchmark problems of Phase 3 and the obtained solutions for the same. The report is concluded with key observations and findings in chapter 7.

2

Vortex-Induced Vibrations

Vortex-Induced Vibration (VIV) is the earliest known mechanism of FIV. In fact, many FEI cases were thought to be due to VIV. It was only in 1980, where the work of Païdoussis[28], which reanalyzed practical experiences, pointed out the true culprit as FEI. However, VIV is just as troublesome when it comes to damaging things in a nuclear reactor.

Since ancient times, the existence of vortex shedding is known. Leonardo da Vinci sketched a row of vortices in the wake of a piling in a stream.[29] This is shown in Figure 2.1. In 1878, Strouhal found that the Aeolian tones generated by a wire in the wind were proportional to the wind speed divided by the wire thickness. He also observed resonance when the natural tones matched with the aeolian tones. In 1879, Lord Rayleigh observed dominant vibrations of a violin string in the transverse direction compared to the longitudinal direction. The vorticity of the wake of a cylinder was associated with vortex formation by Benard in 1908, and with the formation of a stable street of staggered vortices by von Karman in 1912.[22]

Figure 2.1: Sketch by Leonardo da Vinci: Obstacle creating Turbulent Wake[30]

2.1. Mechanism of VIV

To understand VIV, it is best to grasp the concept of vortex shedding. Consider a single cylinder subjected to cross flow. The following text from Blevins[22] sheds light on the matter:

> "*As a fluid particle flows toward the leading edge of a cylinder, the pressure in the fluid particle rises from the free stream pressure to the stagnation pressure. The high fluid pressure near the leading edge impels flow about the cylinder as boundary layers develop about both sides. However, the high pressure is not sufficient to force the flow about the back of the cylinder at high Reynolds numbers. Near the widest section of the cylinder, the boundary layers separate from each side of the cylinder surface and form two shear layers that trail aft in the flow and bound the wake.*

> *Since the innermost portion of the shear layers, which is in contact with the cylinder, moves much more slowly than the outermost portion of the shear layers, which is in contact with the free flow, the shear layers roll into the near wake, where they fold on each other and coalesce into discrete swirling vortices.*[31],[32]"

These vortices interact with the cylinder and are the source of the effects called VIV.

For multi-cylinder arrangements, the cause of vibration is seldom only vortex induced. A typical example is the work of Zdravkovich[33] for two cylinders. He identified 3 regions of positioning a secondary cylinder behind and beside a primary cylinder which influence the response of both cylinders. These are the *proximity interference region* (can be interpreted as strictly FEI), *wake interference region* (can be interpreted as strictly VIV) and a *mixed region* of wake and proximity interference. This is shown in Figure 2.2. The influence of position of the second cylinder and flow velocity is made clear in his work.
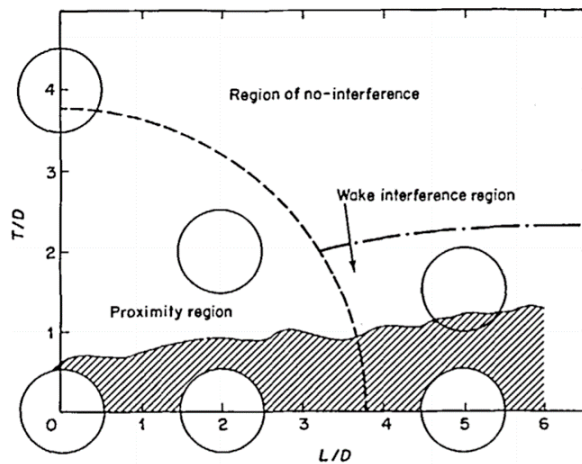
Figure 2.2: Cylinder Interaction Regimes[33]

2.2. Important Parameters influencing VIV

In order to understand VIV, it imperative to look at the non-dimensional parameters that influence the flow behaviour around objects prone to VIV. The most important ones are the Reynolds Number (Re) and the Strouhal Number (St).

2.2.1. Reynolds Number

Vortex shedding is primarily governed by the Reynolds number, Re, which is defined by

$$Re = \frac{UD}{\nu} \tag{2.1}$$

where U is the freestream velocity, D is the characteristic length (diameter of a cylinder for example) and ν is the kinematic viscosity. The major Reynolds Number regimes of vortex shedding from a smooth circular cylinder are shown in Figure 2.3.

For very low Reynolds numbers ($Re < 5$), the flow remains attached to the cylinder. This regime where the viscous forces dominate the inertial forces is also called *Stokes flow*.[34] For $5 < Re < 40$, the flow separates from both sides of the cylinder. The two vortices at both sides can be considered symmetric and stable. In the next flow regime, $40 < Re < 150$, the wake becomes unstable and the vortices are shed alternately from the cylindrical body. In this regime, the vortex street is still laminar. Between $150 < Re < 300$ the flow transitions to turbulent in the vortex wake. From $300 < Re < 1.5 \times 10^5$, the vortex street has become fully turbulent with the boundary layer still being laminar. This range is also called the *subcritical range* where the boundary layer remains fully laminar and the drag coefficient is nearly constant as can be seen from Figure 2.4.
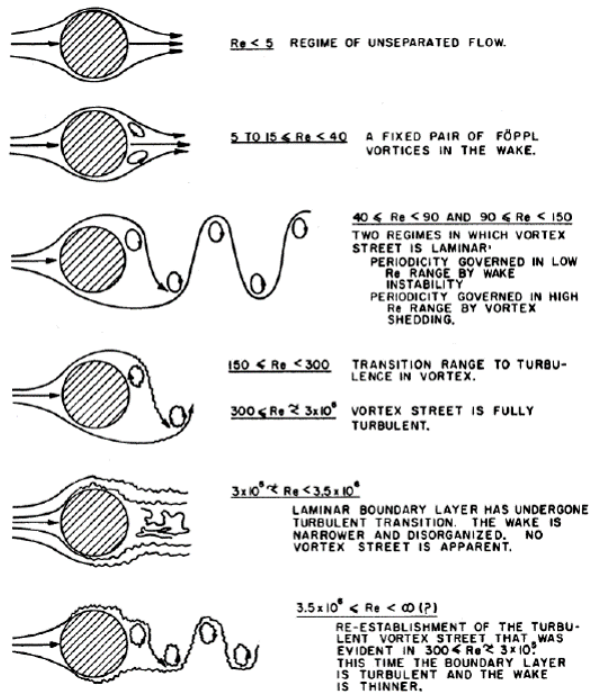
Figure 2.3: Regimes of Fluid Flow across Smooth Circular Cylinders[35]
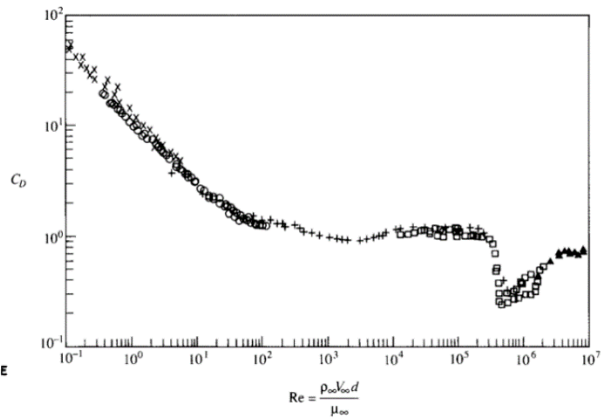
Figure 2.4: Experimental Measurements of Drag Variation with Re[36]

In the *transitional range* from $1.5 \times 10^5 < Re < 3 \times 10^6$, the cylinder boundary layer becomes turbulent and the separation point moves to an aft position. The formation of laminar separation bubbles result in an overall reduction in drag, also called *drag crisis*, as can be seen from Figure 2.4. This flow regime is highly sensitive to inflow turbulence and surface roughness, therefore measurements of C_D are more scattered in this region. Here, the regular shedding process is disrupted and the spectrum of shedding frequencies is broadened for smooth surface cylinders.

The range of $Re > 3 \times 10^6$ is the *supercritical regime*. Laminar separations are no longer formed and the flow transitions to turbulence without separating. The flow remains attached longer and so has higher skin friction. Correspondingly, the drag rises from the dip in the *drag crisis* as can be seen from Figure 2.4. Here, the turbulent vortex shedding is re-established.

2.2.2. Strouhal Number

The Strouhal Number, St, is the dimensionless proportionality constant between the predominant frequency of vortex shedding, f_s, and the free stream velocity, U, divided by the cylinder width, D, and is given by

$$f_s = \frac{StU}{D} \tag{2.2}$$

The Strouhal number of a stationary circular cylinder in a subsonic flow is a function of Reynolds number and, to a lesser extent, surface roughness and free stream turbulence, as shown in Figure 2.5. In particular, the effect of surface roughness is pronounced in the transitional regime, where very smooth surface cylinders have a chaotic, disorganized, high-frequency wake and Strouhal numbers as high as 0.5, while rough surface cylinders have organized, periodic wakes with Strouhal numbers of $St = 0.25$. In general, a Strouhal number of $St = 0.21$ is assumed for single cylinders in cross flow.

However, the same does not hold for multi-cylinder configurations. The array configuration and geometry significantly affect the vortex shedding and thereby the Strouhal Number. In particular, for two cylinder in-line configurations, if the second cylinder is placed further away from the first cylinder, the two cylinders shed their own unique vortices. On the other hand, for small cylinder gaps, the two cylinders behave like a single object and shed a single combined wake.[33]
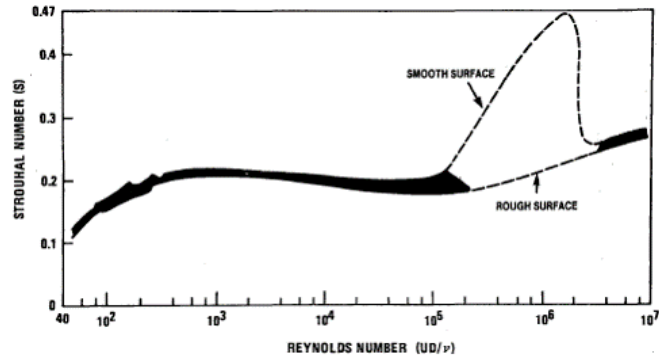
Figure 2.5: Variation of Strouhal Number with Reynolds Number[22]

The discussion so far may give the reader a misconception that vortex shedding is a steady, harmonic, two-dimensional process. This is quite far from the truth. Vortex shedding from a stationary cylinder in the higher Reynolds number range does not occur at a single distinct frequency, but rather it wanders over a narrow band of frequencies with a range of amplitudes and it is not constant along the span. The three-dimensionality of vortex shedding can be characterized by a spanwise correlation length. This correlation length, expressed as multiples of diameter, decreases with increasing Re.[22]

2.2.3. Other Influencing Parameters
Besides the Reynolds number and the Strouhal number, there are other influencing parameters that impact VIV as well. In Figure 2.6 all the influence parameters are illustrated, as summarized by Zdravkovich[37]. These parameters tend to have a smaller effect on VIV than the Reynolds number or Strouhal number, except for the cylinder oscillations. More details about the effect of cylinder oscillations are provided in the following sub-section. Besides the smaller effect of most of the influencing parameters, their effects have also been investigated at high Reynolds numbers. The interested reader is referred to studies of Barnett & Cermack[38] and Achenbach & Heinecke,[39] which addressed the surface roughness and free stream turbulence at supercritical Reynolds numbers, respectively.
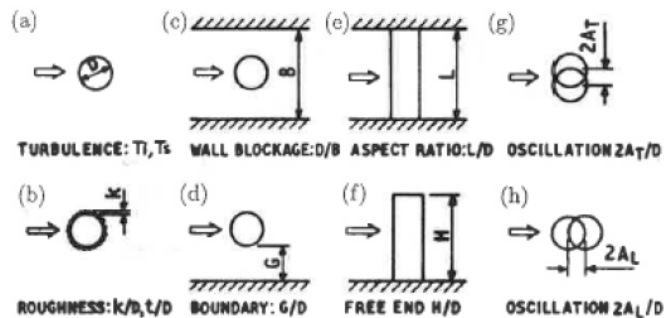
Figure 2.6: Typical Disturbances that have an impact on VIV[37]

2.2.4. Effect of Cylinder Motion on Wake
As mentioned in the previous sub-section, the motion of the cylinder has an influence on the vortex shedding and thereby on VIV. A distinction between in-line oscillations and transverse oscillations has been made (in reality, both occur at the same time as in the current study). The study of Sarpkaya[40] found similar response branches for a 2-DoF experiment as in transverse 1-DoF studies. It was concluded that 2-DoF XY motion studies do not lead to significant variations in maximum resonant amplitudes compared to Y-only studies. Under the conditions when natural frequency is equal in both directions, it was shown by Sarpkaya[40] that the response amplitude is 20% larger and the critical velocity range is also 20% larger. It was reasoned that the transverse oscillations were the main driver of the response amplitude and the critical wind speed range. The focus is thus brought to transverse vibrations.

According to Blevins,[22] there are five main effects of the transverse cylinder motion on the wake. These are

1. The strength of the shed vortices increases.

2. The spanwise correlation of the wake increases.

3. The vortex shedding frequency can shift to the frequency of cylinder vibration leading to *lock-in* or high amplitude vibrations.

4. The mean drag of the cylinder increases.

5. The phase, sequence, and pattern of vortices in the wake can be altered.

The most crucial effects are the alteration of the wake and the lock-in phenomena which relate to the other prescribed effects of cylinder motion. In particular, differences were observed between free vibration and forced vibration. In the critical work by Williamson & Roshko[32], 2S ('S' for single) and 2P ('P' for pair) vortex modes of the wake were discovered for free vibration. On the other hand, for forced vibration, an additional P+S mode was discovered in many experimental studies.[32],[41]−[43] These modes are shown in a vortex wake mode map given in Figure 2.7. In the earliest works, such as those by Bishop & Hassan[44] and Feng[45], a jump in phase of transverse force was observed. This was attributed to a change from 2S to 2P mode by Williamson & Roshko[32] and was experimentally confirmed by Brika & Laneville.[46],[47]
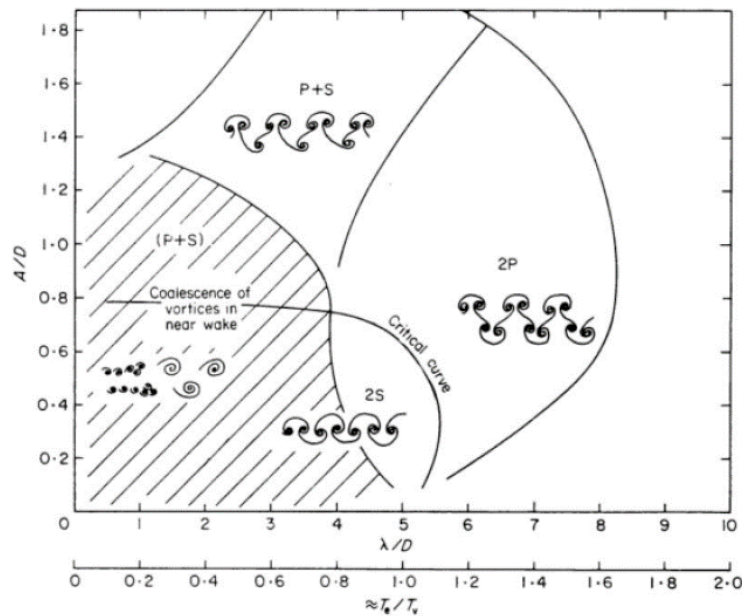
Figure 2.7: Map of Regimes for Vortex Wake Modes[32]

The response of a cylinder in VIV has been found to be greatly influenced by the mass ratio ($m^* = \frac{m}{\frac{\pi}{4}\rho D^2}$) and mass-damping ($m^*\zeta$) parameter. The early works, such as those by Feng[45], were done using air and thus a high mass ratio of $m^* = 248$. In a later work by Khalak & Williamson[48] who used water and thereby a low mass ratio of $m^* = 2.4$, a starkly different response with increasing flow velocity was observed. This is shown in Figure 2.8. Note that the flow velocity has been non-dimensionalized as $U^* = \frac{U}{f_{N,water}D}$, vibrational frequency as $f^* = \frac{f_{obj}}{f_{N,water}}$ and maximum amplitude as $A^*_{max} = \frac{y_{max}}{D}$. In some literature, flow velocity is also represented by the reduced velocity, $U_R = \frac{U}{f_s D}$.

(a) A_{max}^* vs U^* (b) f^* vs U^*
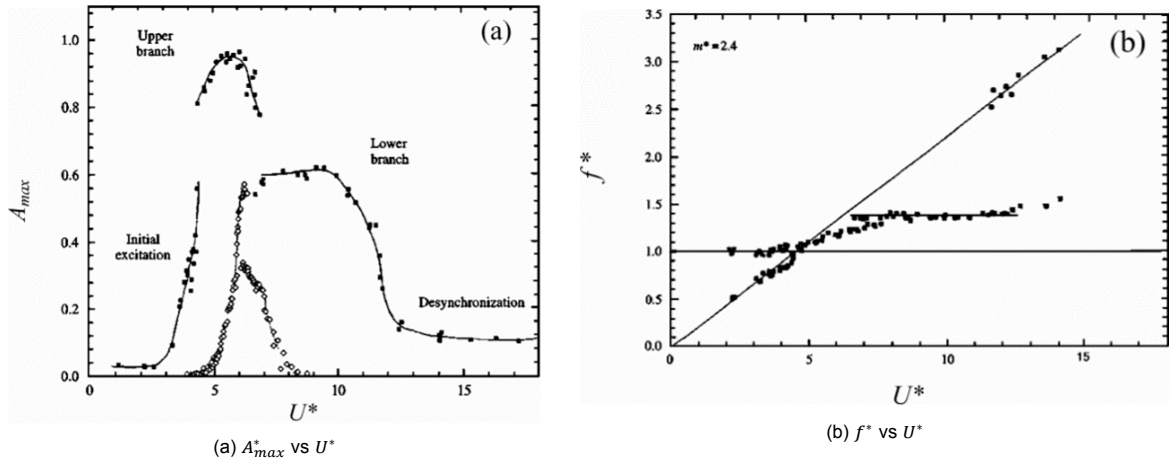
Figure 2.8: Comparison of Response of Low vs High Mass-Damping[49]

Quite some differences are observed from the above figure. In particular, the definition of resonance or lock-in is challenged. The earlier definition of resonance was defined as that range of frequency when the vibrational frequency of the object matches with the natural frequency, i.e $f^* = 1$.[22],[50] This definition was observed to be true for high mass-damping parameter. As we see from Figure 2.8b, for low mass-damping, the value of f^* for the lock-in regime lies at about 1.4. Thus the definition of the condition for resonance was redefined by Sarpkaya[40] to the match of the shedding frequency, f_s with the vibrational frequency of the object, f_{obj}.

Another observation is the existence of different branches in the response curve shown in Figure 2.8a. For the high mass-damping, the curve by Feng[45] shows an 'initial branch' and a 'lower branch'. However, for the low mass-damping, an 'upper branch' is also observed. Furthermore, the range of synchronization or the lock-in regime appears to be larger for the low mass-damping parameter.

Consider the switch in the timing of vortex shedding described by Zdravkovich[51] and Williamson & Roshko[32] when the amplitude jumps from the initial to lower branch in high mass-damping cases such as Feng.[45] In contrast, for low mass and damping, there are two mode jumps, and it is not immediately clear which one corresponds to the switch in vortex shedding timing. To shed light on this question, Govardhan & Williamson[52] considered the "total" fluid force, as well as the "vortex" force. The basis of the theory came from Lighthill[53],[54] who showed that the total fluid force (F_{TOTAL}) can be split into a "potential force" component $F_{POTENTIAL}$, given in this case by the potential added mass force, and a "vortex force" component (F_{VORTEX}) that is due only to the dynamics of all the shed vorticity. Govardhan & Williamson[52] set out to deduce what the vortex force is from direct experimental measurement of the total fluid force. They also defined corresponding phase differences ϕ_{VORTEX} and ϕ_{TOTAL}. Their result is shown in Figure 2.9.
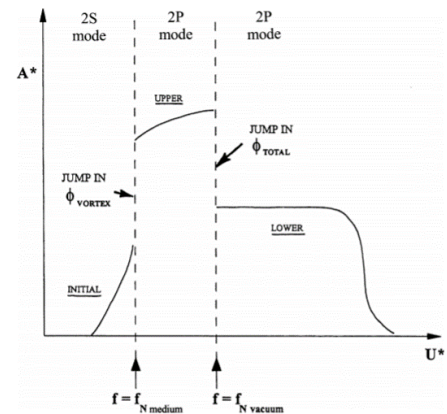
Figure 2.9: Overview of the Low Mass-Damping Response[52]

From their work, it was concluded that while traversing from the initial branch to the upper branch, a jump in vortex phase occurs and thereby a jump from 2S to 2P mode of shedding. On the other hand, while traversing from the upper branch to the lower branch, a jump in the total phase occurs which is not associated with switch in the time of shedding contrasting to Zdravkovich's[51] claim for high mass-damping case.

As mentioned earlier, lowering the mass ratio (m^*) in particular seems to increase the extent of synchronization regime. It could be conjectured that as $m^* \to 0$, the extent of synchronization should tend to infinity. In reality, there exists a finite critical mass ratio, m^*_{CRIT}, below which synchronization regime becomes infinitely wide. In 1999, Khalak & Williamson[55] had provided an expression for the variation of f^* with m^* for high mass-damping. This was given as

$$f^* = \sqrt{\frac{m^* + C_A}{m^* + C_{EA}}} \tag{2.3}$$

where C_A is the potential added mass coefficient (usually taken as 1) and C_{EA} is the effective added mass coefficient. Govardhan & Williamson[52] provided a similar expression for the lower branch for a low mass-damping response given as

$$f^*_{LOWER} = \sqrt{\frac{m^* + 1}{m^* - 0.54}} \tag{2.4}$$

They thus quoted a critical mass ratio of $m^*_{CRIT} = 0.54 \pm 0.02$. This unique critical mass ratio is valid for $(m^* + C_A)\zeta < 0.05$. Figure 2.10 shows the existence of a critical mass ratio. It also shows that for low amplitude vibrations, if the mass ratio is reduced below the critical value, large amplitude oscillations can set in.
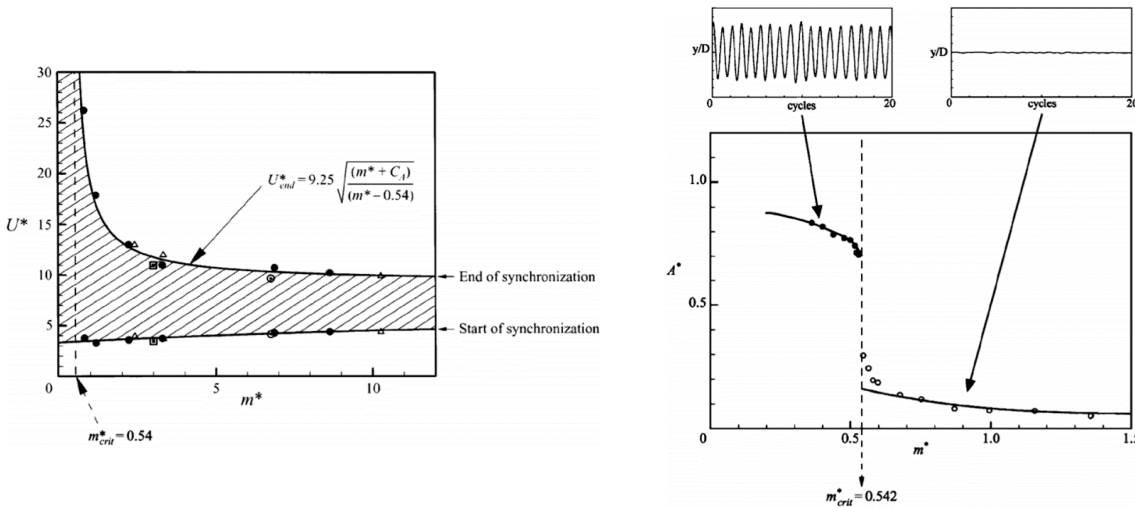
Figure 2.10: Discovery of a Critical Mass[56]

With the realization of the effect of mass-damping on the response, the next step in research was to obtain an expression using the mass-damping parameter that could potentially collapse all A^*_{max} data in a single plot. The use of mass-damping parameter was based on several studies.[56],[57] A parameter was independently derived from a response analysis involving the van der Pol equation by Skop & Griffin,[58] and they compiled data from several different experiments as a means to usefully predict response amplitudes. The combined response parameter was subsequently termed S_G in Skop,[59] and is defined as

$$S_G = 2\pi^3 St^2 (m^* \zeta) \tag{2.5}$$

Griffin[60] made the first extensive compilations of several investigations using S_G and provided the famous Griffin plot as shown in Figure 2.11. Voices against the use of the plot were raised by Sarpkaya on several occasions.[40],[61]–[63] He pointed out that the mass ratio and damping are independent and that the Griffin plot is valid only for $S_G > 1$. On the other hand, Griffin & Ramberg[64] performed two sets of experiments, each for the same value of $S_G = 0.5$–0.6, but with dissimilar mass ratios, $m^* = 4.8$ and 43. The peak amplitude was found to be roughly unchanged with $A^*_{max} = 0.5$ despite $S_G < 1$.
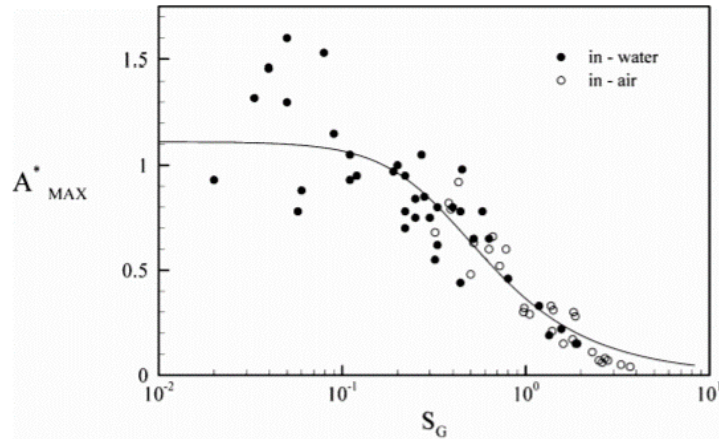
Figure 2.11: The Griffin Plot based on Data collected by Skop & Balasubramanian[65]

To add to this conundrum, using a linear scale as in Figure 2.11 rather than the traditional log-log plot, reveals large scatter in the data. The conclusion made by Khalak & Williamson[55] that it was unreasonable to collapse data for different VIV systems (free cylinder, cantilever, pivoted cylinders, etc.) onto a single plot. In particular, Khalak & Williamson[55] provided a response vs mass ratio plot specifically for elastically mounted cylinders as shown in Figure 2.12. The collapse of data was found to be successful for $m^* > 2$ and $(m^* + C_A)\zeta > 0.006$. This translates to a valid Griffin plot regime down to about $S_G \sim 0.01$, far lower than the value quoted by Sarpkaya[61] of about $S_G \sim 1$.
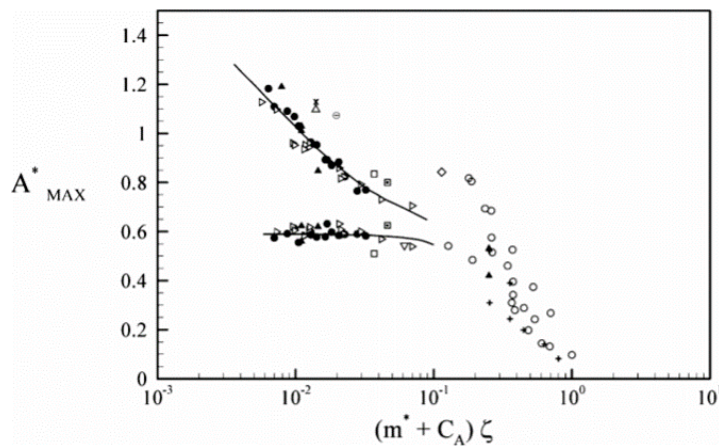
Figure 2.12: Griffin Plot for Elastically Mounted Cylinders based on Data by Khalak & Williamson[55]

2.3. VIV of Multi-Cylinder Configurations

Depending on cylinder spacings, as well as other system parameters, vortex shedding may or may not exist in a cylinder array. Early studies on vibration of cylinder arrays proceeded on the assumption that vortex shedding was the dominant mechanism. Thus, the main objective was to determine the vortex shedding frequency and the Strouhal Number. Key reviews in this area are given by Païdoussis[66] and Weaver & Fitzpatrick[67].

While summarizing the research work on the existence of vortex shedding in tube arrays, Païdoussis[66] stated that periodic vortex shedding or 'Strouhal periodicity' commonly appeared for the first rows provided the upstream turbulence had not suppressed it. The appearance of vortex shedding deep within arrays is found to be dependent on Re, array geometry, mechanical properties of the tubes and the amplitude of tube vibration.

In later research works, Weaver et. al.[68] and Fitzpatrick et. al.[69] observed the presence of vortex shedding, if not a flow periodicity, even deep within the arrays. In an interesting flow visualization study by Abd-Rabbo & Weaver[70], the development of vortex shedding in arrays is observed similar to the classical vortex shedding behind a single cylinder. The Strouhal periodicity is observed in the closely placed staggered array configurations, which is reported to be absent in the in-line array configurations.

Further studies on the in-line tube arrays by Ziada & Oengören[71],[72] has enhanced the understanding of the generation of VIV. The fluid flowing in lanes forms the jet like structures, while the wakes of the cylinders are confined. The vortex shedding excitations are generated in the first row due to the jet instabilities and persist for couple of rows downstream. The tube pitch ratio and the upstream turbulence has a major impact on the vortex shedding in the front rows as well as deep in the arrays.

The vortex shedding in the staggered (normal triangular) arrangement is studied by Polak & Weaver[73] for various pitch ratios and Reynolds numbers. In a comprehensive work by Ziada[74] the vortex shedding is shown to be generated by either jet, wake or shear layer instabilities, depending on the tube spacing, upstream turbulence, Reynolds number and the array configuration. Figure 2.13 shows the vortex shedding patterns in a staggered and in-line tube array. The sub-figures of Figure 2.13a show the influence of increasing Re on the flow vorticity. The closely spaced in-line configuration shown in Figure 2.13b shows the shear layer instabilities as the source of Strouhal periodicities.

(a) Staggered Array

(b) In-Line Array
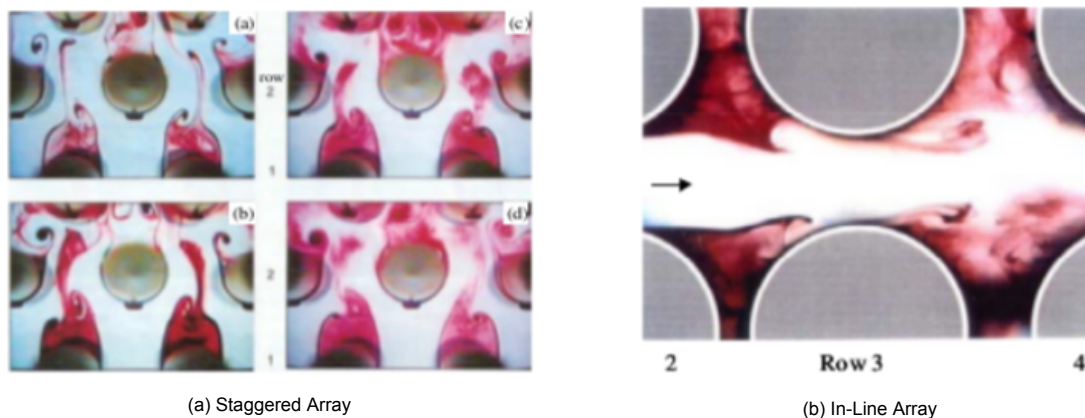
Figure 2.13: Vortex Shedding in Tube Arrays[74]

2.3.1. Two-Cylinder Configurations

Pioneering work for two-cylinder configurations is done by Zdravkovich. He was able to identify a coupled region (proximity interference), a region of wake interference and a region of no interference. Besides classifying the regions, in his work[33], he was able to observe different types of vortex shedding behaviour depending on the cylinder spacing in tandem (as P/D) and side-by-side (as T/D). This is shown in Figure 2.14.

For in-line configurations, the measured Strouhal frequency with varying P/D is provided in Figure 2.15. In general, the vortex shedding frequencies behind the two cylinders are different. No distinct vortex shedding is found behind the upstream cylinders up to $P/D = 3.8$. For $P/D > 3.8$, the vortex shedding frequency reaches the value for an isolated cylinder. The vortex shedding exist in the whole range of spacing behind the downstream cylinder. It decreases with P/D for $1 < P/D < 3.8$, then jumps to higher values at $P/D \sim 3.8$, which is the same spacing at which the vortex shedding appears behind the upstream cylinder.
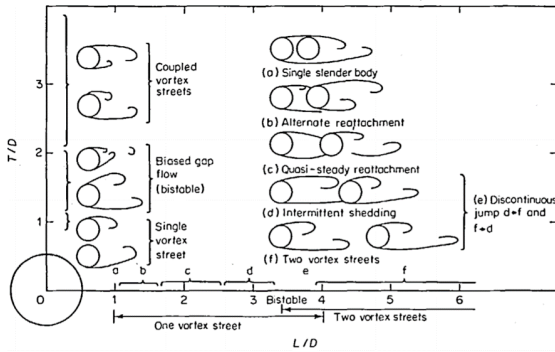
Figure 2.14: Vortex Shedding Dependency on Cylinder Configuration[33]
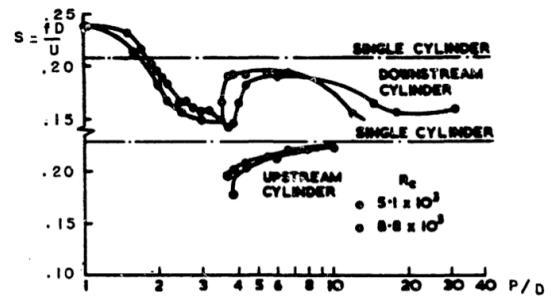
Figure 2.15: Variation of St with P/D[75]

A detailed study of two cylinders in tandem immersed in a water flow and spaced between 0.2 and 4.0 diameters was made by King & Johns[76]. They found that complex mutual interactions can arise between the flow, vortex shedding, and the motion of the cylinders. The dynamic response of the cylinders is a function of pitch ratio, reduced flow velocity, mass ratio, and damping value. Reynolds number was also found to be of key importance: Re must exceed 1200-1500 for in-line oscillation to occur and must exceed 100 for cross flow oscillation to occur. The responses, which depend strongly on P/D, have been summarized by Chen[77] as follows:

- $P/D < 2.75$: Symmetric vortices are shed from both cylinders in the range $1.25 < U_R < 2.5$ and both cylinders oscillate in the in-line direction provided the mass-damping parameter is less than 2.4.

- $P/D > 2.75$: For $1.25 < U_R < 2.5$, the upstream cylinder oscillates inline and sheds symmetric vortices but the downstream cylinders do not oscillate and a wide turbulent wake is formed.

- $1.5 < P/D < 7$: For $2.7 < U_R < 3.8$, the alternate wake from the upstream cylinder generally reinforces that from the downstream cylinder.

- $1.25 < P/D < 7$: The alternate vortex shedding associated with the oscillating upstream cylinder generally reinforces that from the downstream cylinder.

Subsequent experimental work after King & Johns[76] was done by Jendrzejczyk et. al.[78] who carried out tests for $P/D = 1.75$. The results for response and orbital paths are given in Figure 2.16 and Figure 2.17. There are two peaks in the response curves in the drag direction. The peaks correspond to the reduced flow velocities equal to 1.7 m/s and 3.0 m/s, respectively. This is consistent with the experimental results by King & Johns[76].
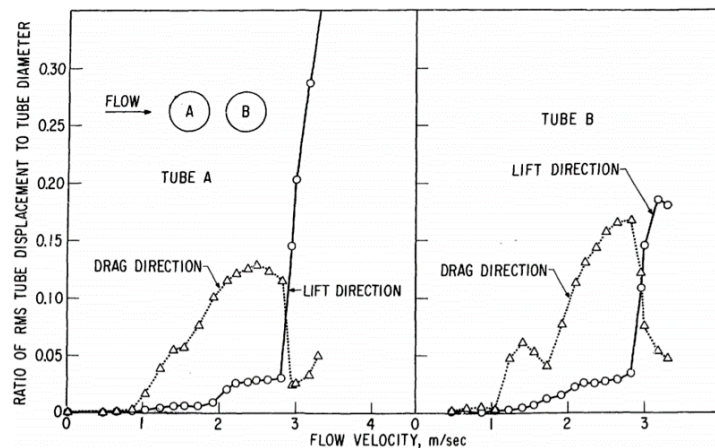
Figure 2.16: Tube Displacement Components for Two Tubes in Tandem[78]
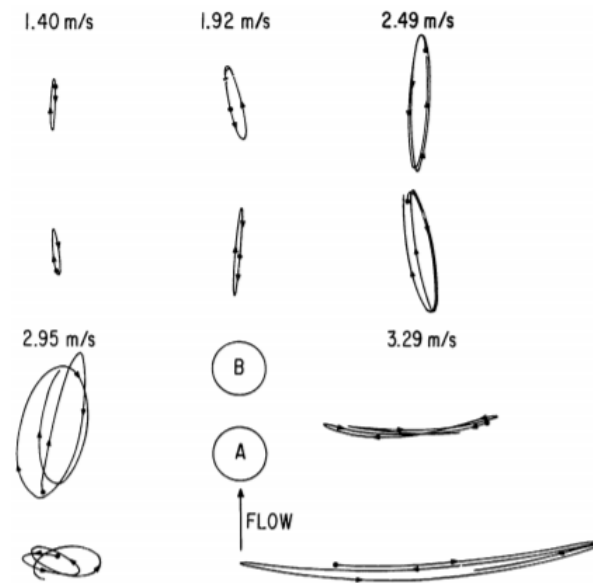
Figure 2.17: Tube Orbital Paths for Two Tubes in Tandem[78]

As the flow velocity increases, predominant cylinder motion changes from the drag direction to the lift direction. At large oscillations, the upstream cylinder vibrates more severely than the downstream one. The two cylinders vibrate out of phase when they execute large oscillations. The orbital paths bend in the downstream direction. This can be attributed to the drag variation—that is, when the cylinders are farthest from the equilibrium position, the drag force acting on the cylinders becomes larger.

2.4. Conclusion

In this chapter, the most relevant mechanism of FIV for the thesis work is reviewed. This mechanism comes in to play in a range of flow velocities where the vortex shedding frequency latches onto the vibrational frequency of the object. The Reynolds number, Strouhal number and the mass-damping of the system greatly influence the response. Furthermore, for tube arrays, the array geometry and configuration has an equally important role to play. For in-line two cylinder arrays, the importance of P/D is highlighted along with the change from a low amplitude in-line vibration to a high amplitude transverse vibration with increasing flow velocity. With this review, a basic qualitative guess on the behaviour of the in-line two cylinder configuration chosen for the thesis are made in chapter 5. The numerical aspects of approaching the problem are discussed in the following chapter of this report.

3

Numerical Methods

Every numerical simulation is based on a mathematical model that tries to describe the physics of the phenomenon being studied. When considering Fluid Structure Interaction, this involves the equations governing the fluid domain, the structural domain and the ways to couple them both. This chapter provides a brief overview of the equations governing fluid dynamics, its associated turbulence modelling, structural dynamics and the Gauss-Seidel technique available in STAR-CCM+ to couple the two separate domains. Before diving into the above topics, a brief note on the frames of reference is provided.

3.1. Frames of Reference

While observing any physical phenomenon, choosing an appropriate frame of reference can simplify the numerical analysis, making it easier to interpret. An example of this would be the choice made by the astronomer Copernicus to analyze the trajectories of the planets keeping the sun as the center instead of earth. This small change in frame of reference simplified the complicated motion of the planets to just ellipses. The two basic frames of reference typically used in continuum mechanics are the *Lagrangian* and the *Eulerian* approach. The point of view particularly suitable for FSI is the *Arbitrary Lagrangian-Eulerian* (ALE) approach. The three approaches are qualitatively illustrated in Figure 3.1.
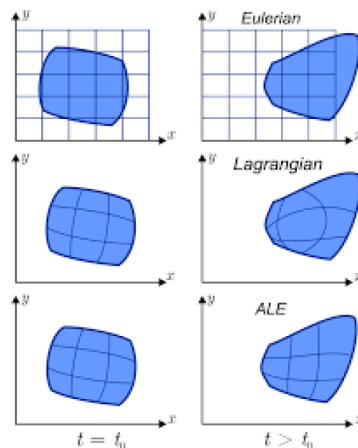
Figure 3.1: Working of Different Frames of Reference on a Fluid Domain (Amended from [79])

3.1.1. Lagrangian Approach

The frame of reference is fixed to the material domain in this approach. The frame of reference moves according to the movement or deformation of the domain as shown in Figure 6.1. As can be seen in Figure 6.1a, the mesh points (dashed circles) move according to the movement of the material points (filled circles). This approach is often used in structural mechanics as it allows implicit treatment of moving boundaries and defines a property history to each material point.

3.1.2. Eulerian Approach

In the Eulerian approach, the frame of reference is fixed to a particular spatial location regardless of the movement of the material being observed as shown in Figure 6.1b. Thus to measure the change in any given property f over time at a given location x, one must add the change of the property at that location with time and the convective transport of neighboring material to that location with a material velocity U. This change is often taken care by the material derivative,

$$\frac{\mathrm{D}f}{\mathrm{D}t} = \frac{\partial f}{\partial t} + (U \cdot \nabla)f \qquad (3.1)$$

Given that it can handle any arbitrary deformation, it is quite popularly used in fluid dynamics.

3.1.3. Arbitrary Lagrangian-Eulerian Approach

The Arbitrary Lagrangian-Eulerian (ALE) approach allows to move the frame of reference independent of the material motion. Figure 6.1c depicts the motion of the frame of reference with this approach. This method brings together the best of both the aforementioned approaches by following the motion of the material at the fluid-structure interface in a Lagrangian way, while the computational mesh in the interior can be moved arbitrarily to optimize the shape of the elements. In this frame of reference, the velocity in the governing equations becomes relative to the deforming mesh.

(a) Lagrangian viewpoint.

(b) Eulerian viewpoint.

(c) Arbitrary Eulerian-Lagrangian viewpoint.
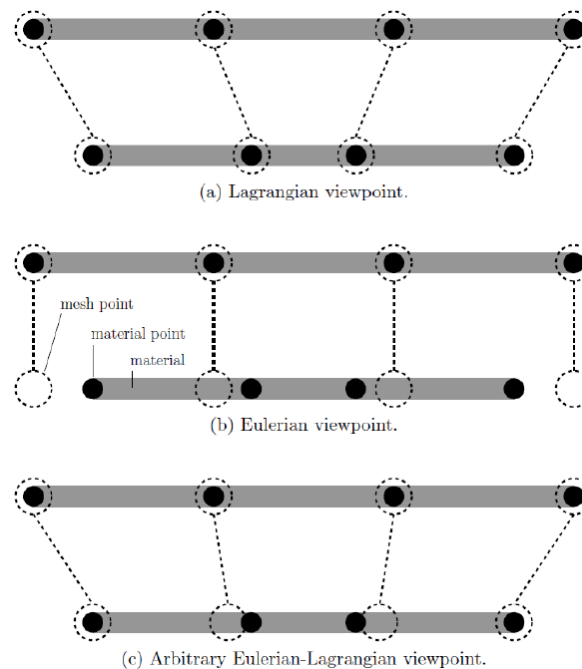
Figure 3.2: Lagrangian, Eulerian and ALE Frames of Reference shown with 1-D Computation Grid (dashed circles), Material Points (filled circles) and Material Domain (grey lines)[80]

3.2. Solid Mechanics

Solid Mechanics describes the behavior of a solid continuum in response to applied loads. Applied loads include body forces, surface loads, point forces, or thermal loads that result from changes in the solid temperature. Applied loads induce a stress field in the structure and can cause displacement of the structure, a quantity we would like to solve. A few key terms are now described before presenting the governing equation.

3.2.1. Displacement

As mentioned above, applied loads can result in a displacement of the solid structure from an initial configuration to a deformed configuration. The total displacement is a combination of rigid body motion and the relative displacements of the points in the body, which determine the deformation of the solid structure.

If the position of a material point in the undeformed configuration is **X**, and the displacement of this point to the deformed configuration is $\mathbf{u}(\mathbf{X}, t)$, the position of the material point in the deformed configuration is:

$$\mathbf{x}(\mathbf{X}, t) = \mathbf{X} + \mathbf{u}(\mathbf{X}, t) \tag{3.2}$$

In component form, the displacement can be expressed as:

$$\mathbf{u} = \begin{bmatrix} u_x & u_y & u_z \end{bmatrix}^T \tag{3.3}$$

The displacement field of a rigid body is completely defined by a single displacement vector while that of a deformable body is defined by the set of displacement vectors of its material points.

3.2.2. Deformation Gradient

The deformation gradient tensor **F** measures how the deformation changes from point to point:

$$\mathbf{F} = \frac{\partial \mathbf{x}}{\partial \mathbf{X}} = \mathbf{I} + \frac{\partial \mathbf{u}}{\partial \mathbf{X}} = \mathbf{I} + \begin{bmatrix} \frac{\partial u_x}{\partial X} & \frac{\partial u_x}{\partial Y} & \frac{\partial u_x}{\partial Z} \\ \frac{\partial u_y}{\partial X} & \frac{\partial u_y}{\partial Y} & \frac{\partial u_y}{\partial Z} \\ \frac{\partial u_z}{\partial X} & \frac{\partial u_z}{\partial Y} & \frac{\partial u_z}{\partial Z} \end{bmatrix} \tag{3.4}$$

where **I** is the identity matrix and X, Y, and Z are the Cartesian components of the material point position vector **X**.

3.2.3. Stress

Stress is a measure of the force per unit area acting on a surface. In a solid structure, external forces or temperature changes induce a stress field, which can lead to motion and deformation of the solid structure. Internal forces that oppose the deformation of the structure also induce an internal elastic stress that tends to restore the structure to the original undeformed state. Some materials also present built-in stress, that exists in absence of applied forces and deformations.

In general, the stress acting on a plane section of a body is defined by a vector $\vec{\tau}$, which is known as stress vector, or traction, as:

$$\vec{\tau} = \begin{bmatrix} \tau_x \\ \tau_y \\ \tau_z \end{bmatrix} = \begin{bmatrix} F_x/A \\ F_y/A \\ F_z/A \end{bmatrix} \tag{3.5}$$

where **F** is the force acting on the plane and A is the area of the plane.

The stress at a point is the force per unit area, as the area over which the force is applied approaches zero. At a point, there is an infinite number of plane sections of the body. However, the state of stress at the point is completely defined by the stress vectors that are associated with three mutually perpendicular planes passing through the point. Therefore, the state of stress at any point, on any plane, is defined by a second-order tensor of the following form:

$$\underline{\sigma} = \begin{bmatrix} \sigma_{xx} & \sigma_{xy} & \sigma_{xz} \\ \sigma_{yx} & \sigma_{yy} & \sigma_{yz} \\ \sigma_{zx} & \sigma_{zy} & \sigma_{zz} \end{bmatrix} \tag{3.6}$$

Since the sum of moments must go to zero as the body volume shrinks to zero, the stress tensor is symmetric. The off-diagonal terms are called *shear stresses*, since they act tangentially to a face. The diagonal terms are referred to as *normal stresses*, since they act normal to a face.

The stress vector on a plane can be written as the matrix product:

$$\vec{\tau} = \underline{\sigma} \cdot \mathbf{n} = \begin{bmatrix} \sigma_{xx} & \sigma_{xy} & \sigma_{xz} \\ \sigma_{yx} & \sigma_{yy} & \sigma_{yz} \\ \sigma_{zx} & \sigma_{zy} & \sigma_{zz} \end{bmatrix} \begin{bmatrix} n_x \\ n_y \\ n_z \end{bmatrix} \tag{3.7}$$

where **n** is the unit vector normal to the plane.

Stress Definitions

Stress can be defined in various ways. For example, you can define it in either the undeformed configuration or in the deformed configuration. For infinitesimal strains (see Equation 3.11), the undeformed and deformed configurations are equivalent. While there are many ways to represent the stress, only two relevant types are discussed below:

- **Cauchy Stress**: The stress tensor in Equation 3.6 is defined in the deformed configuration and is more formally called Cauchy stress, or true stress. Cauchy stress is a direct measure of the traction acting on any surface of the body, in the current configuration. For output, STAR-CCM+ uses the Cauchy stress.

- **Second Piola-Kirchhoff Stress**: The second Piola-Kirchhoff stress tensor **S** is defined as:

$$\mathbf{S} = \det\{\mathbf{F}\}\mathbf{F}^{-1}\underline{\sigma}\mathbf{F}^{-T} \tag{3.8}$$

  where $\underline{\sigma}$ is the Cauchy stress and **F** is the deformation gradient tensor. This definition is also attractive as it relates the forces in the undeformed configuration to areas in the undeformed configuration.

3.2.4. Strain

Strain is a measure of the deformation of a body in terms of the relative displacement of its material points. Consider two material points in a body that deforms from an initial configuration to some deformed configuration. In 1D, the strain $\underline{\epsilon}$ can be defined in terms of the distance between the points in either the initial or the current configuration, as a scalar:

$$\epsilon_G = \frac{\mathrm{d}u}{\mathrm{d}X} \qquad \text{or} \qquad \epsilon_A = \frac{\mathrm{d}u}{\mathrm{d}x} \tag{3.9}$$

where ϵ_G is known as Green strain, ϵ_A is known as Almansi strain, $\mathrm{d}X$ and $\mathrm{d}x$ are the distances between the points in the initial and current configuration, respectively, and $\mathrm{d}u = \mathrm{d}x - \mathrm{d}X$ is the displacement.

In 3D, the state of strain at any point in a body is fully described by a second-order symmetric tensor:

$$\underline{\epsilon} = \begin{bmatrix} \epsilon_{xx} & \epsilon_{xy} & \epsilon_{xz} \\ \epsilon_{yx} & \epsilon_{yy} & \epsilon_{yz} \\ \epsilon_{zx} & \epsilon_{zy} & \epsilon_{zz} \end{bmatrix} \tag{3.10}$$

The diagonal terms are called *normal* or *extensional strains* and the off-diagonal terms are called *shear strains*.

Strain Definitions

STAR-CCM+ allows the user to model linear geometry applications, where both displacements and strains are small, and nonlinear geometry applications with large displacements but small strains. In linear geometry applications, the strain can be described using the infinitesimal strain approximation, whereas nonlinear geometry applications require a finite strain (nonlinear) approximation to describe the state of strain.

The infinitesimal strain assumption is often used in structural engineering to describe the elastic behavior of materials such as steel or concrete, for which the deformations are usually small. The large-displacement, small-strain assumption is useful to describe the deformation of thin structures, that are often subject to large rotations with relatively small strains.

- **Infinitesimal Strain**: The infinitesimal strain is defined as:

$$\underline{\epsilon} = \frac{1}{2}\left(\frac{\partial \mathbf{u}}{\partial \mathbf{X}} + \left[\frac{\partial \mathbf{u}}{\partial \mathbf{X}}\right]^T\right) \tag{3.11}$$

  The infinitesimal strain is also called *linear strain*, since the strain depends linearly on the displacement.

- **Green-Lagrange Finite Strain**: The Green-Lagrange strain tensor defines the strain in the undeformed configuration as:

$$\mathbf{E} = \frac{1}{2}(\mathbf{F}^T\mathbf{F} - \mathbf{I}) \tag{3.12}$$

  where **F** is the deformation gradient and **I** is the 3×3 identity matrix.

- **Euler-Almansi Finite Strain**: The Euler-Almansi strain tensor defines the strain in the deformed configuration as:

$$\mathbf{e} = \frac{1}{2}(\mathbf{I} - \mathbf{F}^{-T}\mathbf{F}^{-1}) \tag{3.13}$$

  where **F** is the deformation gradient and **I** is the 3×3 identity matrix. For infinitesimal strains, the Green-Lagrange strain and Euler-Almansi strain tensors are equivalent.

- **Thermal Strain**: Thermal strain is a measure of the deformation of a body due to changes in the body temperature. If the solid is in an unconstrained state, a change in the temperature does not induce internal stresses and the material is free to expand due to a temperature increase, or to shrink due to a temperature decrease. If a solid body is constrained, a change in the temperature induces thermal stresses in the body. The thermal strain $\underline{\epsilon}_T$ is defined as:

$$\underline{\epsilon}_T = \underline{\alpha}(T - T_{ref}) \tag{3.14}$$

  where the reference temperature T_{ref} is the temperature at which the thermal strain is assumed to be zero and $\underline{\alpha}$ is the vector of thermal expansion coefficients α_i.

3.2.5. Energy-Conjugate Stress-Strain Pairs

The variation of the strain energy per unit volume, due to stress, can be expressed in either the initial or current configuration, by using the correct pairing of stress and strain definitions:

$$\delta W = \delta \mathbf{e} : \underline{\sigma} = \delta \mathbf{E} : \mathbf{S} \tag{3.15}$$

where $\underline{\sigma}$ is the Cauchy stress, $\delta \mathbf{e}$ is the variation of the Euler-Almansi strain, $\delta \mathbf{E}$ is the variation of the Green-Lagrange strain, and **S** is the 2nd Piola-Kirchhoff stress tensor. $\underline{\sigma}$ and $\delta \mathbf{e}$ are called a *conjugate stress-strain pair*, and so are called **S** and $\delta \mathbf{E}$.

$\delta \mathbf{e}$ and $\delta \mathbf{E}$ can be written as:

$$\delta \mathbf{e} = \frac{1}{2}\left[\frac{\partial \delta \mathbf{u}}{\partial \mathbf{x}} + \left(\frac{\partial \delta \mathbf{u}}{\partial \mathbf{x}}\right)^T\right]$$
$$\delta \mathbf{E} = \frac{1}{2}(\delta \mathbf{F}^T\mathbf{F} + \mathbf{F}^T\delta \mathbf{F}) = \frac{1}{2}\left[\left(\frac{\partial \delta \mathbf{u}}{\partial \mathbf{x}}\right)^T \mathbf{F} + \mathbf{F}^T\frac{\partial \delta \mathbf{u}}{\partial \mathbf{x}}\right] \tag{3.16}$$

3.2.6. Governing Equations

Solid Mechanics studies the motion and deformation of a solid continuum under prescribed loads and constraints. The fundamental laws that govern the mechanics of solids are the same laws that describe the mechanics of fluids, namely, the conservation of mass, linear momentum, angular momentum, and energy. Unlike Fluid Mechanics which uses an Eulerian approach, here it is more natural to express the conservation laws using a Lagrangian approach, where the observer follows the solid material as it moves through space and time.

Conservation of Mass
In the Lagrangian approach, mass is always conserved within the control volume. The mass that is contained in any deformed volume is the same mass that was originally contained in the undeformed volume:

$$M = \int_{V(t)} \rho(t) \; \mathrm{d}V = \int_{V_0} \rho_0 \; \mathrm{d}V \qquad (3.17)$$

Since the mass within the volume is conserved, volume changes result in density changes. In fact, this leads to a slightly different interpretation of the material density specified by the user in STAR-CCM+. The specified density is the material density in the undeformed configuration, at a reference temperature.

Conservation of Momentum: Equation of Motion
The motion of a solid body is governed by Cauchy's equilibrium equation, which expresses the conservation of linear momentum for a continuum as given by:

$$\rho \ddot{\mathbf{u}} - \nabla \cdot \underline{\sigma} - \mathbf{b} = 0 \qquad (3.18)$$

where $\mathbf{u}$ is the displacement of the solid body, $\mathbf{b}$ is the total body force per unit volume and $\underline{\sigma}$ is the symmetric Cauchy stress tensor. The above equation is usually accompanied with Dirichlet and Neumann boundary conditions, which in Solid Mechanics jargon are called constraints and loads respectively.

The above equation holds for deformable solids. On the other hand, the governing equation for the motion of the center of mass of an elastically mounted rigid translating body is given by:

$$m\ddot{\mathbf{x}} + k_d \dot{\mathbf{x}} + k_{eff}(\mathbf{x} - \mathbf{x}_l) = \mathbf{f} \qquad (3.19)$$

where m is the mass of the body, k_d is the damping coefficient, k_{eff} is the effective spring stiffness, $\mathbf{f}$ is the resultant force acting on the body, $\mathbf{x}$ is the body displacement and $\mathbf{x}_l$ is the free length of the spring.

3.2.7. Constitutive Relations: Material Models
The strain tensor is directly related to the gradient of the displacement, whereas the stress tensor is related to the displacement through the strain tensor. Constitutive relations complete the formulation by describing the relationship between stress and strain. In STAR-CCM+, models are available for approximating the stress-strain curves of linear elastic solids (isotropic, orthotropic, and anisotropic), elastoplastic solids, hyperelastic solids and nearly incompressible solids. All the problems dealt in the current study make use of isotropic linear elastic structures. Thus only this model is briefly discussed.

Linear Elastic Materials
Linear elastic materials extend proportionally to the applied load and return to the original configuration when the load is removed. The stress-strain relationship for linear elastic materials is linear and is given by Hooke's law. The linear elastic assumption, which is valid for small strains, assumes a stress-strain relationship of the form:

$$\underline{\sigma} = \mathbf{D}(\underline{\epsilon} - \underline{\epsilon}_T) \qquad (3.20)$$

where $\mathbf{D}$ is called the material tangent, $\underline{\epsilon}_T$ is the thermal strain, and $\underline{\sigma}$ and $\underline{\epsilon}$ are an energy conjugate stress-strain pair (either Cauchy stress and Euler-Almansi strain, or 2nd Piola-Kirchhoff stress and Green-Lagrange strain). The formulation is valid for elastic materials with Poisson's ratio $\nu \leq 0.45$. For $\nu > 0.5$, materials are considered incompressible and require a two-field formulation, a topic that lies out of the scope of the current study.

3.2.8. Finite Element Discretization
STAR-CCM+ calculates the displacement of a solid based on the principle of virtual work, which is discretized using the Finite Element Method. The principle of virtual work involves creating the weak form of Equation 3.18 by multiplying it with a test function $\delta\mathbf{u}$ and integrating over the structural domain. Converting the frame of reference of this weak form to that based on the initial configuration gives:

$$\delta\Pi = \int_{V_0} \delta\mathbf{u} \cdot \rho \ddot{\mathbf{u}} \; \mathrm{d}V - \int_{V_0} \delta\mathbf{u} \cdot \mathbf{b} \; \mathrm{d}V + \int_{V_0} \delta\mathbf{E} : \mathbf{S} \; \mathrm{d}V - \int_{\Gamma_\tau} \delta\mathbf{u} \cdot \underline{\tau} \; \mathrm{d}\Gamma = 0 \qquad (3.21)$$

This approach employed by STAR-CCM+ follows the total Lagrangian displacement Finite Element formulation by Zienkiewicz & Taylor[81]. The continuous space domain is discretized into a finite number of elements, which are interconnected at the vertices. In each element, the nodal positions and displacements are interpolated with nodal shape functions $\mathcal{N}_M$:

$$\begin{aligned} \mathbf{x} &= \mathbf{X} + \mathbf{u} \\ \mathbf{X} &= \mathcal{N}_M \mathbf{X}_M \\ \mathbf{u} &= \mathcal{N}_M \mathbf{u}_M \end{aligned} \tag{3.22}$$

where $\mathbf{x}$ and $\mathbf{X}$ denotes the position vectors in the current and initial configuration, respectively. $\mathbf{X}_M$ and $\mathbf{u}_M$ are the position and displacement at the node M, and $\mathcal{N}_M$ is a node-oriented Lagrange shape function.

The discretized form of the variation of the Green-Lagrange strain is:

$$\delta \mathbf{E} = \hat{\mathbf{B}}_M \delta \mathbf{u}_M \tag{3.23}$$

where $\hat{\mathbf{B}}_M$ is the strain-displacement matrix that involves the dicretized deformation gradient given by:

$$F_{iJ} = \delta_{iJ} + u_{Mi} \frac{\partial \mathcal{N}_M(\mathbf{X})}{\partial X_J} \tag{3.24}$$

Substituting the discretized displacements and the discretized form of $\delta \mathbf{E}$ in the weak form gives the following compact discrete equilibrium equations:

$$\mathbf{f}_M^{int} + \mathbf{M}_{MN} \ddot{\mathbf{u}}_N = \mathbf{f}_M^{ext} \tag{3.25}$$

where $\mathbf{f}_M^{int}$ is the internal force at node M, $\mathbf{M}_{MN} \ddot{\mathbf{u}}_N$ is the inertial term, and $\mathbf{f}_M^{ext}$ is the external force applied at node M which includes nodal forces resulting from prescribed body forces, surface tractions, line loads, and point forces. The internal force can also be represented as a stiffness matrix times the displacement at node M. This stiffness matrix is actually the sum of two terms, the material stiffness and the geometric stiffness. For linear geometry (infinitesimal strain assumption), the geometric stiffness is neglected. If the stress-strain relationship is also linear, the internal nodal forces become linear functions of the nodal displacements:

$$\mathbf{f}_M^{int} = \mathbf{K}_{MN}^{mat} \mathbf{u}_N \tag{3.26}$$

3.2.9. Modelling Structural Damping: Rayleigh Damping Model

The formulation presented in Equation 3.18 does not take into account the damping mechanisms that arise in time-dependent systems. Damping is the dissipation of energy in the solid structure due to a combination of different phenomena, including molecular interaction within the material.

In dynamic problems, the contribution of damping forces can be taken into account by including a velocity dependent damping term, $c\dot{\mathbf{u}}$, in the equation of motion:

$$\rho \ddot{\mathbf{u}} + c\dot{\mathbf{u}} - \nabla \cdot \underline{\sigma} - \mathbf{b} = 0 \tag{3.27}$$

which assumes a linear relationship between the damping force and velocity. The weak form of Equation 3.27 can be constructed and discretized as described in the previous sub-section, leading to the general discretized equation for a linear elastic damped system:

$$\mathbf{M}\ddot{\mathbf{u}}(t) + \mathbf{C}\dot{\mathbf{u}}(t) + \mathbf{K}\mathbf{u}(t) = \mathbf{f}^{ext} \tag{3.28}$$

As damping is a complex combination of different phenomena, the damping matrix is often approximated using Rayleigh damping, which models the damping matrix as a linear combination of the stiffness and mass matrices:

$$\mathbf{C} = \tau_K \mathbf{K} + f_M \mathbf{M} \tag{3.29}$$

The scalar coefficients τ_K and f_M can be determined from a desired modal damping factor and the knowledge of the first two eigenfrequencies of the undamped system. With an additional assumption of uniform modal damping factor ζ for both frequencies, τ_K and f_M become:

$$\tau_K = \frac{2\zeta}{\omega_1 + \omega_2}, \qquad\qquad f_M = \frac{2\zeta\omega_1\omega_2}{\omega_1 + \omega_2} \qquad\qquad (3.30)$$

An even simpler choice, as used in the current study, is to restrict the Rayleigh damping to stiffness proportional damping, by assuming $f_M = 0$ and $\tau_K > 0$, and tune the parameter with the fundamental eigenfrequency:

$$\tau_K = \frac{2\zeta}{\omega} \qquad\qquad (3.31)$$

3.2.10. Displacement Field Solution

For infinitesimal strain (linear geometry), the internal forces are linear functions of the nodal displacements (see Equation 3.26). For large deformations, the internal forces are nonlinear in the displacements and STAR-CCM+ solves the governing equations with Newton iterations:

$$\mathbf{K}_{MN}^i \Delta \mathbf{u}_N^i = \mathbf{r}_M^i \qquad\qquad (3.32)$$

where $\mathbf{r}_M^i$ are the residual forces at node M.

Statics

The static solution seeks the displacement field $\mathbf{u}_M$ such that the internal forces are in equilibrium with the external forces. In static problems, the inertial terms are neglected and Equation 3.25 reads:

$$\mathbf{f}_M^{int} = \mathbf{f}_M^{ext} \quad \forall M \in \mathcal{N} \qquad\qquad (3.33)$$

where $\mathcal{N}$ is the set of nodes of an element. The residual forces are then:

$$\mathbf{r}_M^i = \mathbf{f}_M^{ext} - \mathbf{f}_M^{int} \qquad\qquad (3.34)$$

STAR-CCM+ solves Equation 3.32 for the displacement increments $\delta\mathbf{u}_N^i$ and updates the displacements as:

$$\mathbf{u}_N^{i+1} = \mathbf{u}_N^i + \delta\mathbf{u}_N^i \qquad\qquad (3.35)$$

The iteration starts with a given initial condition $\mathbf{u}_N^0$. For a linear problem, the solution is independent of the initial conditions. In addition, a direct solver can compute the solution in one iteration.

Dynamics

The dynamic solution seeks the displacement field $\mathbf{u}_M$ that satisfies the equation:

$$\mathbf{M}_{MN}\ddot{\mathbf{u}}_N + \mathbf{C}_{MN}\dot{\mathbf{u}}_N = \mathbf{f}_M^{ext} - \mathbf{f}_M^{int} \qquad\qquad (3.36)$$

where $\mathbf{M}_{MN}$ and $\mathbf{C}_{MN}$ are the mass and damping matrices. The residual forces are then:

$$\mathbf{r}_M = -\mathbf{M}_{MN}\ddot{\mathbf{u}}_N - \mathbf{C}_{MN}\dot{\mathbf{u}}_N - \mathbf{f}_M^{int} + \mathbf{f}_M^{ext} \qquad\qquad (3.37)$$

STAR-CCM+ provides two different approximations of the accelerations and velocities:

- 1st **Order Backward Euler Method**: This method approximates the acceleration and velocity at time step n as:

$$\ddot{\mathbf{u}}_N^n = \frac{\dot{\mathbf{u}}_N^n - \dot{\mathbf{u}}_N^{n-1}}{\Delta t}$$
$$\dot{\mathbf{u}}_N^n = \frac{\mathbf{u}_N^n - \mathbf{u}_N^{n-1}}{\Delta t} \qquad\qquad (3.38)$$

This first order approximation is not recommended for high-resolution structural dynamics, as it can introduce a large amount of numerical damping. However, the numerical damping can be used to remove unwanted initial transients, or when the goal is to reach a quasi-static solution.

- 2nd **Order Newmark Method**: This method approximates the velocity and position at the time step n as:

$$\dot{\mathbf{u}}_N^n = \dot{\mathbf{u}}_N^{n-1} + (\gamma\ddot{\mathbf{u}}_N^n + (1-\gamma)\ddot{\mathbf{u}}_N^{n-1})\Delta t$$
$$\mathbf{u}_N^n = \mathbf{u}_N^{n-1} + \dot{\mathbf{u}}_N^{n-1}\Delta t + (\beta\ddot{\mathbf{u}}_N^n + (0.5-\beta)\ddot{\mathbf{u}}_N^{n-1})\Delta t^2$$

(3.39)

In general, on the initial time step the acceleration $\ddot{\mathbf{u}}_N^0$ is assumed to be zero. The method is 2nd order accurate when $\gamma = 0.5$ and $\beta = 0.25$. The method is absolutely stable when $\gamma \geq 0.5$ and $\beta = 0.25(0.5 + \gamma)^2$. However, values of $\gamma > 0.5$ introduce numerical damping. The effective stiffness matrix for the Newmark method is:

$$\tilde{\mathbf{K}}_{MN} = -\frac{\partial \mathbf{r}_M}{\partial \mathbf{u}_N} = \mathbf{K}_{MN} + \frac{\mathbf{M}_{MN}}{\beta\Delta t^2} + \frac{\gamma\mathbf{C}_{MN}}{\beta\Delta t}$$

(3.40)

3.3. Fluid Mechanics

In this section, the key equations governing fluid flow are introduced along with the associated turbulence and transition modelling.

3.3.1. Governing Equations

The governing equations of fluid flow, also called the *Navier-Stokes Equations*, over a finite control volume can be written in an integral sense (conservation form) as:

Conservation of Mass: Continuity Equation

$$\frac{\partial}{\partial t}\int_V \rho \,\mathrm{d}V + \oint_A \rho\mathbf{v}\cdot \,\mathrm{d}\mathbf{a} = \int_V S_u \,\mathrm{d}V$$

(3.41)

where t is time, V is the control volume, $\mathrm{d}\mathbf{a}$ is the area vector, ρ is the fluid density, $\mathbf{v}$ is the flow velocity vector and S_u is a source term. In the current study, the right hand side term is zero.

Conservation of Momentum: Momentum Equation

$$\frac{\partial}{\partial t}\int_V \rho\mathbf{v} \,\mathrm{d}V + \oint_A \rho\mathbf{v}\times\mathbf{v}\cdot \,\mathrm{d}\mathbf{a} = -\oint_A p\mathbf{I}\cdot \,\mathrm{d}\mathbf{a} + \oint_A \mathbf{T}\cdot \,\mathrm{d}\mathbf{a} + \int_V \mathbf{f}_b \,\mathrm{d}V + \int_V \mathbf{s}_u \,\mathrm{d}V$$

(3.42)

where p is the pressure, $\mathbf{T}$ is the viscous stress tensor, $\mathbf{f}_b$ is the resultant of body forces and $\mathbf{s}_u$ is the source term.

Conservation of Energy: Energy Equation

$$\frac{\partial}{\partial t}\int_V \rho E \,\mathrm{d}V + \oint_A \rho H\mathbf{v}\cdot \,\mathrm{d}\mathbf{a} = -\oint_A \mathbf{q}\cdot \,\mathrm{d}\mathbf{a} + \oint_A \mathbf{T}\cdot\mathbf{v} \,\mathrm{d}\mathbf{a} + \int_V \mathbf{f}_b\cdot\mathbf{v} \,\mathrm{d}V + \int_V S_e \,\mathrm{d}V$$

(3.43)

where E is the total energy, H is the total enthalpy, $\mathbf{q}$ is the heat flux and S_e is the source term. For incompressible flows, this equation is automatically satisfied.

3.3.2. Constitutive Relations

In order to solve the momentum equations for the velocity field, closure must be provided between the stress tensor and the velocity field of the fluid. A large number of constitutive equations exist that incorporate different material properties of the fluid such as viscosity, first and second normal stress coefficient. In addition, the equations of state, which are also constitutive relations, are required for the closure of the system of equations that is described above.

Equation of State

The equations of state are constitutive relations that describe the relation between the density and the internal energy to the two basic thermodynamic variables pressure and temperature.

STAR-CCM+ allows for selecting among the following relations:

- Constant Density: $\rho = \rho_0$

- Polynomial Density: $\rho = \sum_{i=0}^{n} a_i \cdot T^{i-1}$
- Ideal Gas: $p = \rho RT$
- Real Gas: Van der Waals, Peng Robinson, Redlich-Kwong, Soave-Redlich-Kwong

In the current study, since the working fluid is water at near room temperature flowing at a low flow rate (ensuring Mach Number $M << 0.33$), only the Constant Density option is made use of.

Newtonian Fluids
A Newtonian fluid is described by an explicit constitutive equation that relates the viscous stress tensor **T** to the velocity field through a constant viscosity. The relation between the shear stress and the shear rate is linear.

The viscous stress tensor in Equation 3.42 is not constant, but a variable function of the velocity field for a particular fluid. Typically, in a constitutive relation, the velocity field is expressed in the form of the rate of deformation tensor:

$$\mathbf{D} = \frac{1}{2}(\nabla \mathbf{v} + (\nabla \mathbf{v})^T) \tag{3.44}$$

Newtonian fluid uses the simplest mathematical model to describe the viscous behavior of many liquids and gases such as water and air. The stress tensor is given by:

$$\mathbf{T} = 2\mu \mathbf{D} - \frac{2}{3}\mu(\nabla \cdot \mathbf{v})\mathbf{I} \tag{3.45}$$

where μ is the constant dynamic viscosity of the fluid and **D** is the rate of deformation (strain) tensor given by Equation 3.44. For incompressible flows, the second term in Equation 3.45 is zero due to the continuity equation.

3.3.3. Finite Volume Discretization
Generally, numerical methods, and this includes the finite-volume method, transform the mathematical model into a system of algebraic equations. This transformation involves discretizing the governing equations in space and time. The resulting linear equations are then solved with an algebraic multigrid solver.

General Transport Equation
When the appropriate constitutive relations are introduced into the conservation equations a closed set of equations is obtained. All conservation equations can be written in terms of a generic transport equation. By integrating the generic transport equation over a control volume V and applying Gauss's divergence theorem, the following integral form of the transport equation is obtained:

$$\frac{\mathrm{d}}{\mathrm{d}t}\int_V \rho\phi \ \mathrm{d}V + \oint_A \rho\mathbf{v}\phi \cdot \ \mathrm{d}\mathbf{a} = \oint_A \Gamma\nabla\phi \ \mathrm{d}\mathbf{a} + \int_V S_\phi \ \mathrm{d}V \tag{3.46}$$

where ϕ represents the transport of a scalar property, A is the surface area of the control volume and d**a** denotes the surface vector. By setting ϕ, for example, equal to 1, u, v, w, or E and selecting appropriate values for the diffusion coefficient Γ and source terms, special forms of the partial differential equations for mass, momentum and energy conservation can be obtained.

Equation 3.46 has four distinct terms:

- The *transient term*, which signifies the time rate of change of fluid property ϕ inside the control volume.
- The *convective flux*, which expresses the net rate of decrease of fluid property ϕ across the control volume boundaries due to convection.
- The *diffusive flux*, which corresponds to the net rate of increase of fluid property ϕ across the control volume boundaries due to diffusion.
- The *source term*, which expresses the generation/destruction of fluid property ϕ inside the control volume.

The integrals are approximated using second order quadrature rules that use cell face center for surface integrals and cell center for volume integrals. The values at the cell face center are not known and are approximated through interpolation in terms of the values at the cell centers. Applying the integration approximations to Equation 3.46 yields the following semi-discrete transport equation:

$$\frac{\mathrm{d}}{\mathrm{d}t}(\rho\phi V)_0 + \sum_f [\rho\phi(\mathbf{v}\cdot\mathbf{a})]_f = \sum_f (\Gamma\nabla\phi\cdot\mathbf{a})_f + (S_\phi V)_0 \tag{3.47}$$

Convective Term

The discretized convective term at a face can be rearranged as follows:

$$(\rho\phi\mathbf{v}\cdot\mathbf{a})_f = (\dot{m}\phi)_f = \dot{m}_f\phi_f \tag{3.48}$$

where $\dot{m}_f$ is the mass flow rate at the face. The above equation requires the values of fluid property ϕ_f at the face. The manner in which the fluid property face value ϕ_f is computed from the cell values has a profound effect on the stability and accuracy of the numerical scheme. For a second-order upwind (SOU) scheme, the convective flux is computed as:

$$(\dot{m}\phi)_f = \begin{cases} \dot{m}_f\phi_{f,0} & \dot{m}_f \geq 0 \\ \dot{m}_f\phi_{f,1} & \dot{m}_f < 0 \end{cases} \tag{3.49}$$

where the face values $\phi_{f,0}$ and $\phi_{f,1}$, are linearly interpolated from the cell center values on either side of the face:

$$\begin{aligned} \phi_{f,0} &= \phi_0 + (\mathbf{x}_f - \mathbf{x}_0)\cdot(\nabla\phi)_{r,0} \\ \phi_{f,1} &= \phi_1 + (\mathbf{x}_f - \mathbf{x}_1)\cdot(\nabla\phi)_{r,1} \end{aligned} \tag{3.50}$$

The gradients in the above equation require special limiting treatments. These, however, are left at their default choices in STAR-CCM+ and are not discussed here. Interested readers are directed to the User Manual[82] for further reading.

Diffusive Term

The diffusive flux in Equation 3.46 through internal cell faces of a cell is discretized as:

$$D_f = (\Gamma\nabla\phi\cdot\mathbf{a})_f \tag{3.51}$$

where Γ is the face diffusivity, $\nabla\phi$ is the gradient of fluid property ϕ, and $\mathbf{a}$ is the surface area vector. To obtain an accurate second-order expression for an interior face gradient that implicitly involves the cell values ϕ_0 and ϕ_1, the following decomposition is used:

$$\nabla\phi_f = (\phi_1 - \phi_0)\frac{\mathbf{a}}{\mathbf{a}\cdot(\mathbf{x}_1 - \mathbf{x}_0)} + \frac{\nabla\phi_0 + \nabla\phi_1}{2} - \left(\frac{\nabla\phi_0 + \nabla\phi_1}{2}\cdot(\mathbf{x}_1 - \mathbf{x}_0)\right)\frac{\mathbf{a}}{\mathbf{a}\cdot(\mathbf{x}_1 - \mathbf{x}_0)} \tag{3.52}$$

The formulation that is presented above assumes that the centroids of cells 0 and 1 lie on opposing sides of the face. It is further assumed that their location is consistent with the convention that the face area vector points out of cell 0.

Transient Term

A basic second-order temporal discretization of the unsteady/transient term uses the solution at the current time level, $n+1$, as well as the solutions from the previous two time levels, n and $n-1$, in a Backward Differentiation Formula, BDF2 as given by:

$$\frac{\mathrm{d}}{\mathrm{d}t}(\rho\phi V) = \left(\frac{3}{2}(\rho\phi V)_{n+1} - 2(\rho\phi V)_n + \frac{1}{2}(\rho\phi V)_{n-1}\right)\frac{1}{\Delta t} \tag{3.53}$$

On the first time step of a second-order temporal simulation, a first-order discretization is used since only two time levels are available.

3.3.4. Segregated Flow Solver

The segregated flow solver of STAR-CCM+ solves the integral conservation equations of mass and momentum in a sequential manner. The nonlinear governing equations are solved iteratively one after the other for the solution variables such as u, v, w, p.

The solver employs a pressure-velocity coupling algorithm where the mass conservation constraint on the velocity field is fulfilled by solving a pressure-correction equation. The pressure-correction equation is constructed from the continuity equation and the momentum equations such that a predicted velocity field is sought that fulfills the continuity equation, which is achieved by correcting the pressure. This method is also called a *predictor-corrector* approach. Pressure as a variable is obtained from the pressure-correction equation.

STAR-CCM+ implements two pressure-velocity coupling algorithms, namely the SIMPLE scheme and the PISO scheme. Comparing PISO with SIMPLE:

- PISO is faster than SIMPLE at short time steps, though both algorithms have the same level of temporal accuracy.[83]

- PISO becomes unstable at long time steps, when the combined CFL rises much above 10, while SIMPLE remains stable.

- As time step size increases, SIMPLE loses temporal accuracy of transient solutions. However SIMPLE can still obtain accurate steady state solutions, if they exist, by using large time step size.

Given that it is not guaranteed to have a very low CFL in the current study, only the SIMPLE scheme is employed. The exact details of the algorithms can be found in User Manual[82].

3.3.5. Turbulence Modelling

Most fluid flows of engineering interest are characterized by irregularly fluctuating flow quantities. Often these fluctuations are at such small scales and high frequencies that resolving them in time and space comes at excessive computational costs. Instead of solving for the exact governing equations of turbulent flows (Direct Numerical Simulation), it is less expensive to solve for averaged (URANS) or filtered (Large Eddy Simulation) quantities and approximate the impact of the small fluctuating structures. In the current study, the Unsteady Reynolds-Averaged Navier-Stokes (URANS) turbulence models are employed.

Unsteady Reynolds-Averaged Navier-Stokes Turbulence Models

URANS turbulence models provide closure relations for the Reynolds-Averaged Navier-Stokes equations, that govern the transport of the mean flow quantities. To obtain the Reynolds-Averaged Navier-Stokes equations, each solution variable ϕ in the instantaneous Navier-Stokes equations is decomposed into its mean, or averaged, value $\overline{\phi}$ and its fluctuating component ϕ':

$$\phi = \overline{\phi} + \phi' \tag{3.54}$$

where ϕ represents velocity components, pressure or energy. The averaging process may be thought of as time-averaging for steady-state situations and ensemble averaging for repeatable transient situations. Inserting the decomposed solution variables into the Navier-Stokes equations results in equations for the mean quantities as given by:

$$\frac{\partial \rho}{\partial t} + \nabla \cdot (\rho \overline{\mathbf{v}}) = 0$$

$$\frac{\partial}{\partial t}(\rho \overline{\mathbf{v}}) + \nabla \cdot (\rho \overline{\mathbf{v}} \times \overline{\mathbf{v}}) = -\nabla \cdot \overline{p}\mathbf{I} + \nabla \cdot (\overline{\mathbf{T}} + \mathbf{T}_{RANS}) + \mathbf{f}_b \tag{3.55}$$

$$\frac{\partial}{\partial t}(\rho \overline{E}) + \nabla \cdot (\rho \overline{E}\overline{\mathbf{v}}) = -\nabla \cdot \overline{p}\,\overline{\mathbf{v}} + \nabla \cdot (\overline{\mathbf{T}} + \mathbf{T}_{RANS})\overline{\mathbf{v}} - \nabla \cdot \overline{\mathbf{q}} + \mathbf{f}_b \cdot \overline{\mathbf{v}}$$

where the terms are as described in earlier sub-sections with the exception of a new term: the stress tensor $\mathbf{T}_{RANS}$ which is given by

$$\mathbf{T}_{RANS} = \rho \begin{bmatrix} \overline{u'u'} & \overline{u'v'} & \overline{u'w'} \\ \overline{v'u'} & \overline{v'v'} & \overline{v'w'} \\ \overline{w'u'} & \overline{w'v'} & \overline{w'w'} \end{bmatrix} + \frac{2}{3}\rho k \mathbf{I} \tag{3.56}$$

where k is the turbulent kinetic energy.

The challenge is thus to model $\mathbf{T}_{RANS}$ in terms of the mean flow quantities, and hence provide closure of the governing equations. In the URANS or RANS framework, this can be done via Eddy viscosity models and the Reynolds stress transport models. In the current study, the less expensive Eddy viscosity models are employed.

Eddy viscosity models are based on the analogy between the molecular gradient-diffusion process and turbulent motion. The concept of a turbulent eddy viscosity μ_t makes it possible to model the stress tensor as a function of mean flow quantities. The most common model is known as the Boussinesq approximation:

$$\mathbf{T}_{RANS,L} = 2\mu_t \mathbf{S} - \frac{2}{3}(\mu_t \nabla \cdot \overline{\mathbf{v}}) \mathbf{I} \tag{3.57}$$

where $\mathbf{S}$ is the mean strain rate tensor which has the same expression as Equation 3.44 but using the mean velocity, $\overline{\mathbf{v}}$. Another important term that is later used is the mean vorticity tensor $\mathbf{W} = \frac{1}{2}(\nabla\overline{\mathbf{v}} - \nabla\overline{\mathbf{v}}^T)$. The popular k-ϵ and k-ω SST models are employed in the current study that solve additional transport equations for scalar quantities that enable the derivation of μ_t. Note that the stress tensor T_{RANS} finally used in the momentum equation will be the sum of $T_{RANS,L}$, defined above and $T_{RANS,NL}$ defined based on the constitutive relationship chosen for a given model.

K-Epsilon Model
The K-Epsilon turbulence model is a two-equation model that solves transport equations for the turbulent kinetic energy k and the turbulent dissipation rate ϵ in order to determine the turbulent eddy viscosity. In particular, the Low-Reynolds Number variation of the model by Lien et. al.[84] is made use of. This is done in STAR-CCM+ by applying damping functions to some of the coefficients (C_μ, $C_{\epsilon 2}$) in the model. These damping functions modulate the coefficients as functions of a turbulence Reynolds number, often also incorporating the wall distance.

The turbulent eddy viscosity μ_t is calculated as:

$$\mu_t = \rho C_\mu f_\mu k T \tag{3.58}$$

where T is the turbulent time scale which, for the 'Realizable' option, is given by:

$$T = \max\left(\min\left(\frac{k}{\epsilon}, \frac{C_T}{C_\mu f_\mu S}\right), C_t \sqrt{\frac{\nu}{\epsilon}}\right) \tag{3.59}$$

where ν is the kinematic viscosity, S is the modulus of the mean strain rate tensor ($S = |\mathbf{S}| = \sqrt{2\mathbf{S} : \mathbf{S}}$). The transport equations for the kinetic energy k and the turbulent dissipation rate ϵ are:

$$\frac{\partial}{\partial t}(\rho k) + \nabla \cdot (\rho k \overline{\mathbf{v}}) = \nabla \cdot \left[\left(\mu + \frac{\mu_t}{\sigma_k}\right)\nabla k\right] + P_k - \rho\epsilon + S_k$$
$$\frac{\partial}{\partial t}(\rho\epsilon) + \nabla \cdot (\rho\epsilon\overline{\mathbf{v}}) = \nabla\cdot\left[\left(\mu + \frac{\mu_t}{\sigma_\epsilon}\right)\nabla\epsilon\right] + \frac{\epsilon}{k}C_{\epsilon 1}P_\epsilon - C_{\epsilon 2}f_2\rho\frac{\epsilon^2}{k} + S_\epsilon \tag{3.60}$$

For the chosen 'Standard K-Epsilon Low Re' model of STAR-CCM+ with the Yap correction[85] but without buoyancy and compressibility effects, the production terms are given by

$$P_k = G_k$$
$$P_\epsilon = G_k + G_{nl} + G' + \frac{\rho}{C_{\epsilon 1}}Y'_y \tag{3.61}$$

The new terms introduced are defined in Table 3.1. The damping functions f_μ and f_2 are given by:

$$f_2 = 1 - C \exp\left(-Re_t^2\right)$$
$$f_\mu = 1 - \exp[-(C_{d0}\sqrt{Re_d} + C_{d1}Re_d + C_{d2}Re_d^2)]$$

(3.62)

where $Re_d = \frac{\sqrt{k}d}{\mu}$ is the wall distance Reynolds number and $Re_t = \frac{k^2}{\nu\epsilon}$ is the turbulent Reynolds number. All model coefficients are tabulated in Table 3.2.

Table 3.1: Description of Terms

Symbol	Description	Formulation	Where:
G_k	Turbulent production	$\mu_t S^2 - \frac{2}{3}\rho k \nabla \cdot \overline{\mathbf{v}} - \frac{2}{3}\mu_t(\nabla \cdot \overline{\mathbf{v}})^2$	-
G_{nl}	"Nonlinear" production	$(\mathbf{T}_{RANS,NL}) : \nabla\overline{\mathbf{v}}$	$\mathbf{T}_{RANS,NL}$ is the nonlinear contribution to the Constitutive Relationship.
G'	Additional production	$Df_2\left(G_k + 2\mu\frac{k}{d^2}\right)\exp\left(-ERe_d^2\right)$	d is the distance to the wall
Y_y'	Yap correction[85]	$C_W \frac{\epsilon^2}{k}\max\left[\left(\left(\frac{l}{l_\epsilon}-1\right)\left(\frac{l}{l_\epsilon}\right)^2, 0\right)\right]$	l and l_ϵ are length scales defined as $l = \frac{k^{\frac{3}{2}}}{\epsilon}$ and $l_\epsilon = C_l d$

Table 3.2: Model Coefficients

Coefficient	C	C_{d0}	C_{d1}	C_{d2}	C_l	C_t	C_T	C_W
Value	0.3	0.091	0.0042	0.00011	2.55	1	0.6	0.83

Coefficient	$C_{\epsilon 1}$	$C_{\epsilon 2}$	C_μ	D	E	σ_ϵ	σ_k	-
Value	1.44	1.92	0.09	1	0.00375	1.3	1	-

Constitutive Relations

Constitutive relations describe the relation between the stress tensor and the mean strain rate used in the Boussinesq approximation. By default, the Boussinesq approximation implies a linear constitutive relation. Nonlinear constitutive relations[84] account for anisotropy of turbulence by adding nonlinear functions of the strain and rotation tensors. The available relations are tabulated in Table 3.3.

Table 3.3: Constitutive Relations

Constitutive Relation	Formulation	Where:
Quadratic (QCR)	$\mathbf{T}_{RANS,NL} = -4\mu_t\frac{k}{\epsilon}\left\{C_1\left[\mathbf{S}\cdot\mathbf{S} - \frac{1}{3}\mathbf{I}(\mathbf{S}:\mathbf{S})\right]\right.$ $+C_2(\mathbf{W}\cdot\mathbf{S} + \mathbf{S}\cdot\mathbf{W}^T)$ $\left.+C_3\left[\mathbf{W}\cdot\mathbf{W}^T - \frac{1}{3}\mathbf{I}(\mathbf{W}:\mathbf{W}^T)\right]\right\}$	$C_1 = \frac{C_{NL1}}{(C_{NL6}+C_{NL7}\overline{S}^3)C_\mu}$ $C_2 = \frac{C_{NL2}}{(C_{NL6}+C_{NL7}\overline{S}^3)C_\mu}$ $C_3 = \frac{C_{NL3}}{(C_{NL6}+C_{NL7}\overline{S}^3)C_\mu}$
Cubic	$\mathbf{T}_{RANS,NL} = \mathbf{T}_{RANS,quad} - 8\mu_t\frac{k^2}{\epsilon^2}$ $\left\{C_4[(\mathbf{S}\cdot\mathbf{S})\cdot\mathbf{W} + \mathbf{W}^T\cdot(\mathbf{S}\cdot\mathbf{S})]\right.$ $\left.+C_5(\mathbf{S}:\mathbf{S} - \mathbf{W}:\mathbf{W}^T)\left[\mathbf{S} - \frac{1}{3}\mathrm{Tr}(\mathbf{S})\mathbf{I}\right]\right\}$	$\mathbf{T}_{RANS,quad}$ is the QCR formulation of $\mathbf{T}_{RANS,NL}$, $C_4 = C_{NL4}C_\mu^2$ $C_5 = C_{NL5}C_\mu^2$

The coefficient Cµ is given by:

$$C_\mu = \frac{C_{a0}}{C_{a1} + C_{a2}\overline{S} + C_{a3}\overline{W}}$$

(3.63)

where $\overline{S} = \frac{k}{\epsilon}\sqrt{2\mathbf{S}:\mathbf{S}}$ and $\overline{W} = \frac{k}{\epsilon}\sqrt{2\mathbf{W}:\mathbf{W}}$. When nonlinear constitutive relations are used, the variable coefficient C_μ given by Equation 3.63 replaces the constant value of C_μ in the relation for the turbulent viscosity μ_t given in Equation 3.58. The model coefficients are tabulated in Table 3.4.

Table 3.4: Model Coefficients

Coefficient	C_{NL1}	C_{NL2}	C_{NL3}	C_{NL4}	C_{NL5}	C_{NL6}
Value	0.75	3.75	4.75	-10	-2	1000

Coefficient	C_{NL7}	C_{a0}	C_{a1}	C_{a2}	C_{a3}	-
Value	1	0.667	1.25	1	0.9	-

K-Omega SST Model

The K-Omega turbulence model is a two-equation model that solves transport equations for the turbulent kinetic energy k and the specific dissipation rate ω, the dissipation rate per unit turbulent kinetic energy ($\omega \propto \frac{\epsilon}{k}$), in order to determine the turbulent eddy viscosity.

One reported advantage of the K-Omega model over the K-Epsilon model is its improved performance for boundary layers under adverse pressure gradients. Perhaps the most significant advantage, however, is that it may be applied throughout the boundary layer, including the viscous-dominated region, without further modification. On the other hand, the biggest disadvantage of the K-Omega model, in its original form, is that boundary layer computations are sensitive to the values of ω in the free-stream. This translates into extreme sensitivity to inlet boundary conditions for internal flows, a problem that does not exist for the K-Epsilon models.

The problem of sensitivity to free-stream/inlet conditions was addressed by Menter[86], who recognized that the ϵ transport equation from the standard K-Epsilon model could be transformed into an ω transport equation by variable substitution. The transformed equation looks similar to the one in the standard K-Omega model, but adds an additional non-conservative cross-diffusion term containing the dot product $\nabla k \cdot \nabla \omega$. Inclusion of this term in the ω transport equation potentially makes the K-Omega model give identical results to the K-Epsilon model.

Menter suggested using a blending function (which includes functions of wall distance) that would include the cross-diffusion term far from walls, but not near the wall. This approach effectively blends a K-Epsilon model in the far-field with a K-Omega model near the wall. Menter also introduced a modification to the linear constitutive equation and named the model containing this modification the SST (shear-stress transport) K-Omega model.

In this model, the turbulent eddy viscosity μ_t is calculated as:

$$\mu_t = \rho k T \tag{3.64}$$

where T is the turbulent time scale which when calculated using the Durbin's realizability constraint[87] is given by:

$$T = \min\left(\frac{1}{\max(\omega/\alpha^*, (SF_2)/a_1)}, \frac{C_T}{\sqrt{3}S}\right) \tag{3.65}$$

where F_2 is a blending function given by:

$$F_2 = \tanh\left(\left(\max\left(\frac{2\sqrt{k}}{\beta^*\omega d}, \frac{500\nu}{d^2\omega}\right)\right)^2\right) \tag{3.66}$$

The transport equations for the kinetic energy k and the specific dissipation rate ω are:

$$\frac{\partial}{\partial t}(\rho k) + \nabla \cdot (\rho k \bar{\mathbf{v}}) = \nabla \cdot [(\mu + \mu_t \sigma_k)\nabla k] + P_k - \rho\beta^*\omega k + S_k$$
$$\frac{\partial}{\partial t}(\rho\omega) + \nabla \cdot (\rho\omega\bar{\mathbf{v}}) = \nabla \cdot [(\mu + \mu_t \sigma_\omega)\nabla\omega] + P_\omega - \rho\beta\omega^2 + S_\omega \tag{3.67}$$

For the chosen K-Omega SST Model without buoyancy effects, the production terms are given by:

$$P_k = G_k + G_{nl}$$
$$P_\omega = G_\omega + D_\omega \tag{3.68}$$

The contributing terms to the production terms are given in Table 3.5 with model constants tabulated in Table 3.6. The blending function F_1 used in the cross-diffusion term combines the near-wall contribution of a coefficient with its value far away from the wall and is defined as:

$$F_1 = \tanh\left(\left[\min\left(\max\left(\frac{\sqrt{k}}{0.09\omega d}, \frac{500\nu}{d^2\omega}\right), \frac{2k}{d^2 CD_{k\omega}}\right)\right]^4\right) \tag{3.69}$$

where $CD_{k\omega} = \max\left(\frac{1}{\omega}\nabla k \cdot \nabla \omega, 10^{-20}\right)$ is the cross-diffusion coefficient.

Table 3.5: Description of Terms

Symbol	Description	Formulation	Where:
G_k	Turbulent production	$\mu_t f_c S^2 - \frac{2}{3}\rho k \nabla \cdot \overline{\mathbf{v}} - \frac{2}{3}\mu_t(\nabla \cdot \overline{\mathbf{v}})^2$	f_c is the curvature correction factor
G_{nl}	"Nonlinear" production	$(\mathbf{T}_{RANS,NL}) : \nabla\overline{\mathbf{v}}$	$\mathbf{T}_{RANS,NL}$ is a nonlinear Constitutive Relationship
G_ω	Specific dissipation production	$\rho\gamma\left[\left(S^2 - \frac{2}{3}(\nabla \cdot \overline{\mathbf{v}})^2\right) - \frac{2}{3}\omega\nabla \cdot \overline{\mathbf{v}}\right]$	-
D_ω	Cross-diffusion term	$2\rho(1-F_1)\sigma_{\omega 2}\frac{1}{\omega}\nabla k \cdot \nabla \omega$	F_1 is a blending function

Table 3.6: Model Coefficients

Coefficient	β	β_1	β_2	α^*
Value	$F_1\beta_1 + (1-F_1)\beta_2$	0.075	0.0828	1
Coefficient	σ_k	σ_{k1}	σ_{k2}	β^*
Value	$F_1\sigma_{k1} + (1-F_1)\sigma_{k2}$	0.85	1	0.09
Coefficient	σ_ω	$\sigma_{\omega 1}$	$\sigma_{\omega 2}$	C_T
Value	$F_1\sigma_{\omega 1} + (1-F_1)\sigma_{\omega 2}$	0.5	0.856	0.6
Coefficient	γ	γ_1	γ_2	a_1
Value	$F_1\gamma_1 + (1-F_1)\gamma_2$	0.5532	0.4404	0.31

The transport equation for the turbulent kinetic energy is insensitive, by construction, to stabilizing and destabilizing effects usually associated with strong (streamline) curvature and frame-rotation. These effects are incorporated by using a curvature correction factor, f_c, which alters the turbulent kinetic energy production term according to the local rotation and vorticity rates as given by[88]:

$$f_c = \min\left(C_{max}, \frac{1}{C_{r1}(|\eta| - \eta) + \sqrt{1 - \min(C_{r2}, 0.99)}}\right) \tag{3.70}$$

where $C_{max} = 1.25$, $C_{r1} = 0.04645$ and $C_{r2} = 0.25$ are model coefficients and the term η is given by

$$\eta = T^2(\mathbf{S} : \mathbf{S} - \mathbf{W} : \mathbf{W}) \tag{3.71}$$

where the time-scale T is limited in order to have the correct near-wall asymptotic behavior:

$$T = \max\left(\frac{1}{\beta^*\omega}, \left(6\left[\frac{1}{\beta^*\omega}\right]^{2.125}\sqrt{\frac{\nu}{k}}\right)^{\frac{1}{2.625}}\right) \tag{3.72}$$

If the curvature correction is not activated, the correction factor takes the value $f_c = 1$.

Low Reynolds Number Modification
The low Reynolds number modification can be used to account for low Reynolds number and transitional effects. When chosen, the following model coefficients are replaced:

Table 3.7: Modified Model Coefficients

Model Coefficients	Replaced By:	Where:
α	$F_1 \cdot \frac{\beta/3 + Re_t/Re_k}{1 + Re_t/Re_k} + (1 - F_1)$	$Re_k = 6$ is a model constant
β	$F_1 \cdot 0.09 \cdot \frac{4/15 + (Re_t/Re_\beta)^4}{1 + (Re_t/Re_\beta)^4} + (1 - F_1)0.09$	$Re_\beta = 8$ is a model constant
γ_1	$\frac{\gamma_1}{\alpha^*} \cdot \frac{1/9 + Re_t/Re_\omega}{1 + Re_t/Re_\omega}$	$Re_\omega = 2.95$ is a model constant

Constitutive Relations
Constitutive relations describe the relation between the stress tensor and the mean strain rate that is used in the Boussinesq approximation. By default, the Boussinesq approximation implies a linear constitutive relation. Nonlinear constitutive relations account for anisotropy of turbulence by adding nonlinear functions of the strain and vorticity tensors.

Like the K-Epsilon Model, STAR-CCM+ offers implementations of the quadratic (QCR) and cubic relations. However, through past experience at NRG and testing by the author, the cubic relation implementation has failed to pass applicability tests. In particular, using the implementation of the cubic constitutive relation lead to an eventual blow-up of the turbulent kinetic energy during the transient simulation. Thus, only the QCR relation[89] is given below and used in the current study.

$$T_{RANS,NL} = -2\mu_t 0.04645(\mathbf{O} \cdot \mathbf{S} - \mathbf{S} \cdot \mathbf{O})$$
$$\mathbf{O} = \frac{\mathbf{W}}{\sqrt{(\mathbf{S} - \mathbf{W})(\mathbf{S} - \mathbf{W})}} \tag{3.73}$$

3.3.6. Transition Modelling
The term transition refers to the phenomenon of laminar to turbulence transition in boundary layers. A transition model in combination with a turbulence model could help predict the onset of transition in a turbulent boundary layer. Three primary modes of transition are typically involved:[90]

1. *Natural transition*, in which a laminar boundary layer subjected to weak disturbances becomes linearly unstable beyond a critical Reynolds number at which point so-called Tollmien-Schlichting waves start to grow.

2. *Bypass transition*, the process of transition in response to large disturbances outside the boundary layer, typically free-stream turbulence levels in excess of 1%.

3. *Separation-induced transition*, in which separation of the laminar boundary layer gives rise to transition. The laminar boundary layer often reattaches in response to the enhanced mixing caused by the turbulent flow, forming a laminar separation bubble upstream of the transition location.

Examples of other important transition mechanism are: *roughness-induced transition*, which is often used in experiments to "trip" boundary layers towards a fully turbulent state, or *cross flow induced transition*.

There are two approaches available in STAR-CCM+ to account for transition:

1. *Turbulence Suppression model*-this model mimics the effect of transition simply by suppressing the turbulence in a certain pre-defined region and can be combined with any turbulence model.

2. *Gamma ReTheta Transition model* and *Gamma Transition model*-these models are based on correlations and solve additional transport equations that are coupled with the K-Omega SST turbulence model.

The Turbulence Suppression model is a zero-equation model and is thus the fastest and least expensive one, but it requires that you already know the location of transition. The Gamma ReTheta Transition model and the Gamma Transition model are more expensive, but provide a true predictive capability. The Gamma Transition model only solves for one equation-it is therefore faster and less computationally expensive than the Gamma ReTheta Transition model which solves for two additional transport equations in addition to the two-equation K-Omega SST model. The Gamma ReTheta Transition model is chosen for the current study and is described below.

Gamma ReTheta Transition Model
The Gamma ReTheta Transition model is based on the concept of *intermittency*-a measure of the amount of time during which the flow is turbulent. An intermittency value of 1 corresponds to a fully turbulent flow (100% percent of the time) and an intermittency value of 0 corresponds to a fully laminar flow.

The Gamma ReTheta transition model[91],[92] is a correlation-based transition model that has been specifically formulated for unstructured CFD codes. An intermittency transport equation is used in such a way that the source terms attempt to mimic the behavior of the algebraic engineering correlations. The evaluation of momentum thickness Reynolds number is avoided by relating this quantity to a vorticity-based Reynolds number. In addition, a correlation for transition onset momentum thickness Reynolds number defined in the free-stream is transported (by solving a separate transport equation) into the boundary layer.

The Gamma ReTheta transition model was incomplete, as published, since two critical correlations were proprietary and hence omitted. A justification for such an omission is that the model provides a framework for users to implement their own correlations. In the current study, the default correlations implemented by STAR-CCM+ are used. These correlations can be found in the User Manual[82].

Without providing intricate details of the involved terms, the intermittency, γ, and transition momentum thickness Reynolds number, $\overline{Re_{\theta t}}$, transport equations are given below:

$$\frac{\mathrm{d}}{\mathrm{d}t}(\rho\gamma) + \nabla \cdot \rho\gamma\overline{\mathbf{v}} = \nabla \cdot \left[\left(\mu + \frac{\mu_t}{\sigma_f}\right)\nabla\gamma\right] + P_\gamma - E_\gamma$$

$$\frac{\mathrm{d}}{\mathrm{d}t}(\rho\overline{Re_{\theta t}}) + \nabla \cdot (\rho\overline{Re_{\theta t}}\overline{\mathbf{v}}) = \nabla \cdot [\sigma_{\theta t}(\mu + \mu_t)\nabla\overline{Re_{\theta t}}] + P_{\theta t} + D_{SCF}$$

(3.74)

where $\sigma_f = 1$ and $\sigma_{\theta t} = 2$ are model constants, P_γ and $P_{\theta t}$ are production terms, E_γ is the destruction term and D_{SCF} is the cross flow term.

3.4. Coupling of Fluid and Structure Governing Equations

In nuclear reactors, the coupling between the structures and the fluid is usually strong. One of the parameters to quantify the strength of coupling is the density ratio of the solid to the fluid (ρ_s/ρ_f). The value of density ratio can vary from 8.24 (steel-water) to 0.82 (Steel-Lead Bismuth Eutectic). These values of density ratios correspond to strongly coupled systems and hence need a robust and efficient coupling algorithm to be able to handle higher amount of coupling instabilities.

There are broadly two approaches to couple the fluid and structure governing equations: the *monolithic approach* and the *partitioned approach*. In the monolithic approach, the full set of equations (for the fluid, the structure and the interface) is built and solved for simultaneously. In the partitioned approach, the system is set up individually for the fluid and the structure domain, while the coupling is established externally which involves mapping and exchange of data from domain to the other.

In the partitioned approach, different ways of discretization both for space and time can be used for the fluid and structure domains, thus making it more suitable for coupling pre-existing CFD and CSM codes. Usually, the monolithic approach is able to handle greater coupling instabilities.[94] However, new partitioned coupling approaches have been developed recently which extend the range of applicability of the partitioned coupling approach to cases with stronger coupling.[94],[95]

The current study uses the partitioned approach of coupling in STAR-CCM+. In this approach, the domains are coupled at the interface by the *kinematic boundary conditions* (displacement and velocity of both materials are equal at the interface) and *dynamic boundary conditions* (traction at the interface of the structure is in equilibrium with that on the fluid side).

In this section, the fluid and the structural solvers are represented as operators **F** and **S** respectively. The input-output variables for these operators are the kinematic values '**s**' which comprise of displacement and velocities, and the dynamic values '**f**' comprising of forces and stresses. Using a Dirichlet-Neumann decomposition, the flow equations are solved for a given displacement of the fluid-structure interface (Dirichlet boundary condition) and the structural equations are solved for a given traction distribution on the interface (Neumann boundary condition).

The solvers can be written as

$$\mathbf{s} = \mathbf{S}(\mathbf{f})$$
$$\mathbf{f} = \mathbf{F}(\mathbf{s})$$

(3.75)

There exist different schemes to couple these solvers. In STAR-CCM+, a serial scheme called *Block Gauss-Seidel* is implemented. This scheme is further discussed below.

3.4.1. Block Gauss-Seidel

This is one of the most commonly used explicit coupling schemes. Explicit schemes are the ones where Equation 3.75 is solved a fixed number of times per time step. Hence the kinematic and dynamic boundary conditions are not strictly enforced. The steps involved in Block Gauss-Seidel coupling are shown in algorithm 1 and also graphically in Figure 3.3. In this algorithm, the domain which is executed first works in an explicit manner. For example, in the shown algorithm, the fluid solver is executed first taking the structural input from the last time step, whereas the structural solver uses the updated value of the fluid solver in an implicit way.

Algorithm 1: Block Gauss-Seidel Algorithm

---
1 **for** $n = 0$ *to* n_{end} **do**
2   solve $\mathbf{F}^n(\mathbf{s}^n) = \mathbf{f}^{n+1}$;
3   map $\mathbf{f}^{n+1}$ to structure domain;
4   Solve $\mathbf{S}^n(\mathbf{f}^{n+1}) = \mathbf{s}^{n+1}$;
5   map $\mathbf{s}^{n+1}$ to fluid domain;
6 **end**
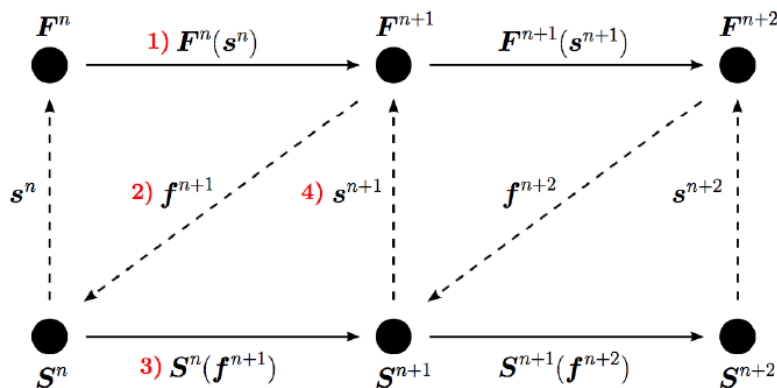
Figure 3.3: Block Gauss-Seidel Coupling Algorithm[80]

This coupling algorithm is first order accurate in time regardless of the order of time integration in the individual fluid and structural solvers. In this type of coupling, both the fluid and structural solver cannot run in parallel (inter-field parallelism) as one is called after the other and depends on the input of the other. Although intra-field parallelism, which means solving the equations of the solver in a parallel way, can be applied to this case. For a total amount of k computational resources distributed among the fluid (k_F) and the structural solver (k_S) such that $k = k_F + k_S$, the computational time for each FSI time step (c) is given by[80]

$$c = \frac{m_f c_f}{k_f} + \frac{m_s c_s}{k_s} \tag{3.76}$$

where m_f and m_s are the number of sub-cycling steps for both the fluid and the structural solver, whereas c_f and c_s refer to computational time taken for each time step of the fluid and the structural solver individually. Sub-cycling allows to decouple the time step sizes required in the fluid and structural solver. However, this feature is not available in the current implementation of STAR-CCM+ and is thus not discussed further.

3.5. Mapping of Data

In FSI problems, it is often the case that the fluid mesh is considerably more refined than the structural mesh. The cells at the interface of the two domains are thus non-conformal and there is a need to map the data from one mesh to the other, such as the displacement from the structural domain to the fluid domain and the forces from the fluid domain onto the structural domain. This mapping could be *consistent* or *conservative*. In the consistent approach, a constant displacement or force is interpolated in such a way that it remains constant over the other domain too, whereas the conservative approach is based on the principle of conservation of energy at the interface.

STAR-CCM+ offers the following methods of mapping: *Nearest Neighbor*, *Least Squares*, *Exact Imprinting* and *Approximate Imprinting*. The last two methods are preferred when a flux-preserving mapping is desired, the source mesh is finer than the target mesh and the surface curvature is adequately resolved. These methods are thus more suitable when remeshing is required which is not the case for the current study. The mesh element count for both domains at the interface is kept similar in the current study. For such a scenario, the first two methods have similar accuracy. However, owing to its low computational cost, only the first method is used in the current study and is briefly described below.

3.5.1. Nearest Neighbor Mapping

This is the simplest way of mapping data from one mesh to the other. Assuming data is to be transferred from mesh A to mesh B, this approach finds the closest point in mesh A (x_A) for every point of mesh B (x_B) and assigns the value at x_A to x_B. A graphical depiction of this method is shown in Figure 3.4.
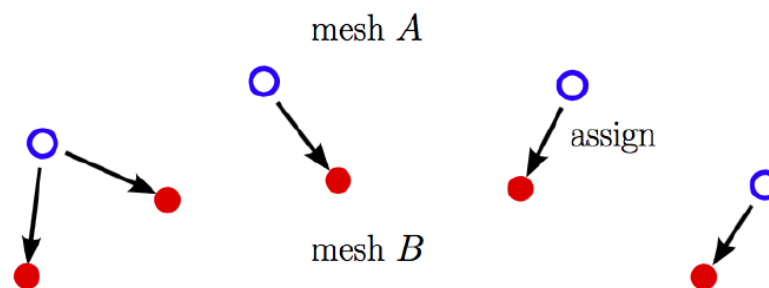
Figure 3.4: Nearest Neighbor Data Mapping Algorithm[80]

3.6. Overset Mesh Technique

Overset meshes are used to discretize a computational domain with several different meshes that overlap each other in an arbitrary manner. They are most useful in problems dealing with large motions, as in the current study for the Khalak & Williamson[27] test case, as well as optimization studies where a geometry can be enclosed in an overset region and set to different positions.

The overset mesh approach couples regions through data exchange between *acceptor cells* of one region and *donor cells* (specially marked active cells) in another region. A typical overset simulation has a background region enclosing the entire solution domain and one overset region that surrounds a body such as a cylinder or an airfoil.

To couple these two regions, STAR-CCM+ applies a hole-cutting process in which cells whose solution is obtained wholly from the overset region are marked as inactive in the background region. Within both the overset and background regions there are several layers of overlapping cells that participate in the data exchange procedure. Further details about the hole-cutting process and the data exchange procedure can be found in the User Manual[82].

The solution is computed for all active cells in all regions simultaneously, that is, the meshes are implicitly coupled. Within the discretized system of equations, when a reference is made to the variable value in an acceptor cell of one region, a blend of variable values at donor cells from another region is used to supply the value. This value is reflected directly in the coefficient matrix of the algebraic equation system. This tight coupling of the overset and background regions allows for a solution that is within an arbitrary low level of iteration errors. The rate of convergence of the iterative solution method is therefore expected to be similar to that of a single mesh of the same resolution.

3.7. Mesh Morphing

When conducting an FSI simulation of a deformable structure, as is done in the current study, the fluid mesh is morphed based on the structural response for each time step. This formally involves redistributing mesh vertices in response to the movement of a set of control points, which one can consider as being a cloud of points overlaid onto the mesh domain. Control points, and their associated displacements, form the underlying framework that the morpher requires to generate an interpolation field. STAR-CCM+ has two morphing methods available to interpolate the displaced surfaces:

1. **Radial Basis Functions (RBF)**: This is undertaken using multiquadratic radial basis splines. The RBF morpher utilizes a thin-out procedure to optimise the number of control points used.

2. **B-Spline**: This is undertaken using a fast, adaptive interpolation algorithm incorporating multilevel, cubic B-Splines. On multiple processors, this method scales better than RBF in many circumstances. It can also better preserve meshes that contain prism layers.

Based on the above reason, the *B-Spline* morphing method is made use of in the current study. The B-Spline algorithm starts from a coarse grid and propagates down to progressively finer levels until no further correction is necessary. The B-Spline algorithm is largely automated in STAR-CCM+ and requires less user intervention (requiring only a morpher tolerance input) than the RBF morpher. Readers interested in the exact algorithm are referred to the work of Lee et. al.[93] which has inspired the current implementation in STAR-CCM+ as given in the User Manual[82].

3.8. Conclusion

In this chapter, the most important numerical concepts concerning FSI problems, in particular the current study, have been reviewed and summarized. This includes the frame of reference that is most beneficial for FSI problems, the differential equations governing the phenomena being studied, turbulence and transition modelling, the discretization methods for both domains, the mapping technique at the interface of two domains and a short note on the overset mesh technique and the mesh morphing method employed.

This chapter thus brings a reader abreast in terms of the technical aspects that go on under-the-hood when specific STAR-CCM+ options are selected at the click of a few buttons. This also lays the foundation for further insightful discussions for the results of the current study. The following chapters concerns itself with the validation of the simulation code, turbulence modelling testing and its eventual application to the OECD Benchmark.

4

Validation Study

In this chapter, the CFD ('Segregated Flow') and CSM ('Solid Stress') solver implementations of STAR-CCM+ are first validated against the flexible beam FSI benchmark of Turek & Hron[26] for stand-alone and coupled calculations. Post validation, the turbulence models available are tested against the VIV study of Khalak & Williamson[27] for selecting/shortlisting models for the OECD Benchmark.

4.1. Flexible Beam FSI Benchmark

The problem at hand is that of an incompressible Newtonian fluid interacting with a flexible beam trailing a fixed cylinder subjected to laminar channel flow as shown in Figure 4.1. This problem was proposed by Turek & Hron[26] in 2006 to assess different FSI coupling schemes for partitioned solvers like the one used in the current study. This numerical benchmark makes its appearance often within the FSI research community[96]−[100] on account of the problem simultaneously including vortex shedding, self-excited oscillations and added mass effects.
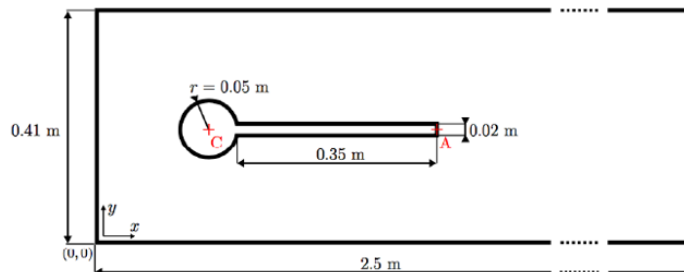
Figure 4.1: Geometry of the Cylinder with Attached Beam of the Turek & Hron Benchmark Case. A is the Reference Point for the Measured Displacement. Amended from [26]

While the benchmark comes with 9 test cases, the following cases are selected for the current study: CFD3, CSM2 and FSI3. CFD3 validates the flow solver by fixing the beam and computing only the flow oscillations. CSM2 considers only the bending of the structure under gravity and is used to validate the structural solver. FSI3 allows for validation of the Gauss-Seidel coupling employed to couple the two solvers. The key parameters for the 3 cases are provided in Table 4.1.

The problem is set up in STAR-CCM+ as follows: For the incompressible fluid, the 'Implicit Unsteady' SIMPLE scheme 'Segregated Flow' solver is selected with a 2nd order upwind convection scheme. The pressure and velocity equations are given Under-Relaxation (UR) factors of 0.2 and 0.6 respectively. Although the benchmark is a 2D problem, the results presented here are for a quasi-2D setup with the geometry extruded 1 m in the z-normal direction. This is done because STAR-CCM+ requires a 3D domain for FSI calculations. A slip wall is prescribed for the z-normal faces of the channel while the other walls are given a no-slip boundary condition. A constant static pressure of 0 Pa is prescribed for the outlet while a time-varying parabolic velocity is prescribed at the inlet given by the equation:

$$u(0,y,t) = \begin{cases} u(0,y)\dfrac{1-\cos\left(\frac{\pi}{2}t\right)}{2}, & \text{if } t < 2.0\,s \\ u(0,y), & \text{otherwise} \end{cases}$$

$$u(0,y) = 1.5\overline{U}\frac{4}{0.1681}y(0.41-y)$$

(4.1)

For the solid (also quasi-2D), the 'Solid Stress' solver is selected along with a 2nd order Newmark implicit integration scheme (Newmark parameter, γ=0.5). At this point, a choice is to be made between the infinitesimal strain and finite strain approximation. This is done after testing the associated 'Linear Geometry' and 'Nonlinear Geometry' models with the CSM2 test case. For the boundary condition, the curved edge connected to the cylinder is grounded while the other faces are declared as an FSI interface. For the FSI coupling, UR factors are prescribed based on the given mesh level.

Table 4.1: Parameter Settings for the Benchmark

Geometry	Position C	(0.2, 0.2)	$(x,y)\,m$
	Position A	(0.6, 0.2)	$(x,y)\,m$
Fluid Properties (CFD3, FSI3)	Density, ρ_f	1000	kg/m^3
	Dynamic Viscosity, μ_f	1	$Pa \cdot s$
	Characteristic Velocity, $\overline{U}$	2	m/s
	Reynolds Number, Re	200	-
Solid Properties (CSM2, FSI3)	Density, ρ_s	1000	kg/m^3
	Poisson Ratio, ν	0.4	-
	Young's Modulus, E	5.6	MPa

The fluid mesh is created using the 'Automatic Mesh' functionality of STAR-CCM+. For the fluid, an unstructured triangle mesh is created with two volume refinements. Approaching the cylinder+beam from the outlet by crossing each refinement region reduces the target base size (bs) by half sequentially. To ensure good transition between the refinement regions, a growth rate of 1.1 is selected. Simulations are conducted for three mesh levels of $bs = 20$, 10 and 5 mm in order to observe mesh convergence. The solid mesh on the other hand is structured with mesh levels: 20×1, 40×2, 80×4, 160×8, 320×16 and 640×32 where entries of a given pair are the number of elements along the length and thickness, respectively. Special cases with a single element along the thickness are also considered for the CSM2 and FSI3 test cases. For increased accuracy, quadratic finite elements are employed by enabling the 'Mid-side Vertex' option. The meshes for the fluid and solid are shown in Figure 4.2. Both the solid and fluid mesh are quasi-2D with only 1 element along the z-normal direction.

(a) Fluid Mesh Level 3 ($bs = 20\ mm$)

(b) Solid Mesh Level 4 (80×4)
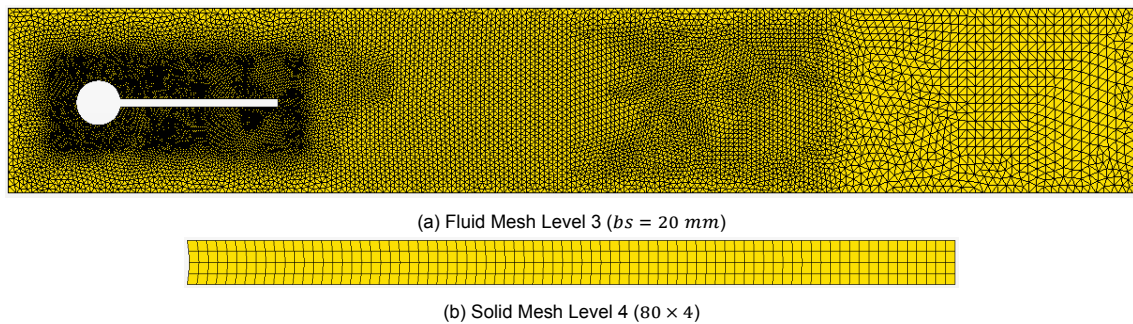
Figure 4.2: Unstructured Fluid Mesh with Refinement Regions and Structured Solid Mesh

4.1.1. CFD3 Benchmark

This case tests the fluid solution alone based on the lift and drag computed for the cylinder+beam. A 2nd order temporal discretization scheme is selected and a time step of $\Delta t = 5\ ms$ is applied with 50 inner iterations per time step. Given the transient nature of the problem, a total of $10\ s$ of simulation time is required to establish a fully developed flow solution with periodic vortex shedding.

Figure 4.3 shows velocity magnitude at the end of the simulation, revealing fluid oscillation or vortex shedding aft of the structure.
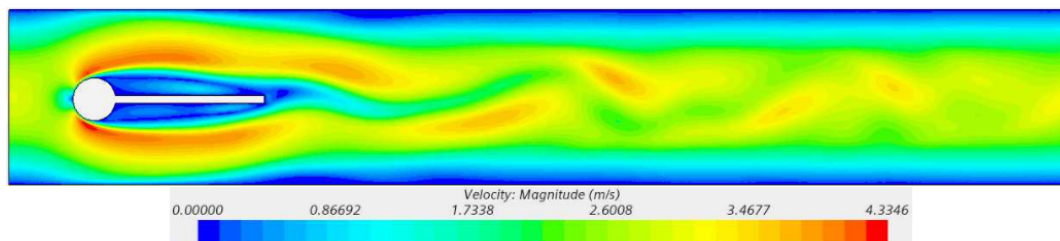
Figure 4.3: Velocity Magnitude at $t = 10\ s$

The results are presented in the same fashion as the benchmark as *mean ± amplitude [frequency]*. To obtain this, the maxima and minima have to be selected. This is done by averaging the extrema for the final 3 oscillations. The average time between the maxima of the 3 oscillations is considered to compute the frequency. In the actual benchmark, these quantities were obtained for a single final interval of the simulation. Since the actual time period used was not clearly indicated, this averaging technique is employed to quote the values.

The results so obtained are tabulated in Table 4.2. For a time step of $\Delta t = 5\ ms$, the drag result for the finest mesh matches well with the reference solution. The mean, amplitude and frequency differ in relative percentages of 0.52%, 24.89% and 1.11% respectively. Mesh convergence is observed for the mean value but not for the amplitude. The lift result at the finest mesh is even further away from the reference solution. The mean value seems to be converging to a neutral value while the amplitude is at an error of 6.74% at the finest mesh level. These results are not alarming, given that other researchers have shown similar relative errors for this time step. Giannelis & Vio[98], for example, quoted errors in amplitude for lift and drag as 3.3% and 13.3% respectively using ANSYS Fluent. Cole & Neu[100], using an older version of STAR-CCM+ (v2017.04), quoted corresponding errors of 5.7% and 16.7% respectively. However, it is suspected that these errors are due the current time step being large.

Table 4.2: CFD3 Results

$\Delta t = 5\ ms$				
Mesh Level	**Base Size** (mm)	**Fluid Elements**	**Drag** ($N\ [Hz]$)	**Lift** ($N\ [Hz]$)
3	20	24695	466.450 ± 6.950 [4.440]	-22.483 ± 455.112 [4.440]
2	10	90274	445.450 ± 5.150 [4.440]	-06.850 ± 420.383 [4.440]
1	5	358601	441.717 ± 7.017 [4.347]	-01.633 ± 467.333 [4.347]
		Reference Solution	439.450 ± 5.618 [4.396]	-11.893 ± 437.810 [4.396]
$\Delta t = 2.275\ ms$				
Mesh Level	**Base Size** (mm)	**Fluid Elements**	**Drag** ($N\ [Hz]$)	**Lift** ($N\ [Hz]$)
3	20	24695	466.900 ± 7.100 [4.440]	-24.350 ± 456.350 [4.440]
2	10	90274	445.450 ± 5.250 [4.440]	-08.250 ± 421.850 [4.440]
1	5	358601	441.500 ± 5.600 [4.440]	-12.100 ± 436.300 [4.440]
		Reference Solution	439.450 ± 5.618 [4.396]	-11.893 ± 437.810 [4.396]

To gauge the temporal convergence, the simulations are re-run with a reduced time step. A thumb rule for selecting a time step is to select one that ensures at least 100 sampling points per fundamental period. In this context, a time step of $\Delta t = 2.275\ ms$ is selected. The results for this time step show improvements on all fronts revealing the importance of this parameter for highly transient problems.

For the finest mesh, the drag mean and amplitude vary only by 0.47% and 0.32% respectively. Drastic improvements are seen for the lift results where the corresponding mean and amplitudes differ only by 1.7% and 0.34% respectively. The lift and drag profiles for this time step are shown in Figure 4.4 after removing the phase difference between results at different mesh levels. The flow solver is thus deemed to be validated based on spatial and temporal convergence.

(a) Lift History   (b) Drag History
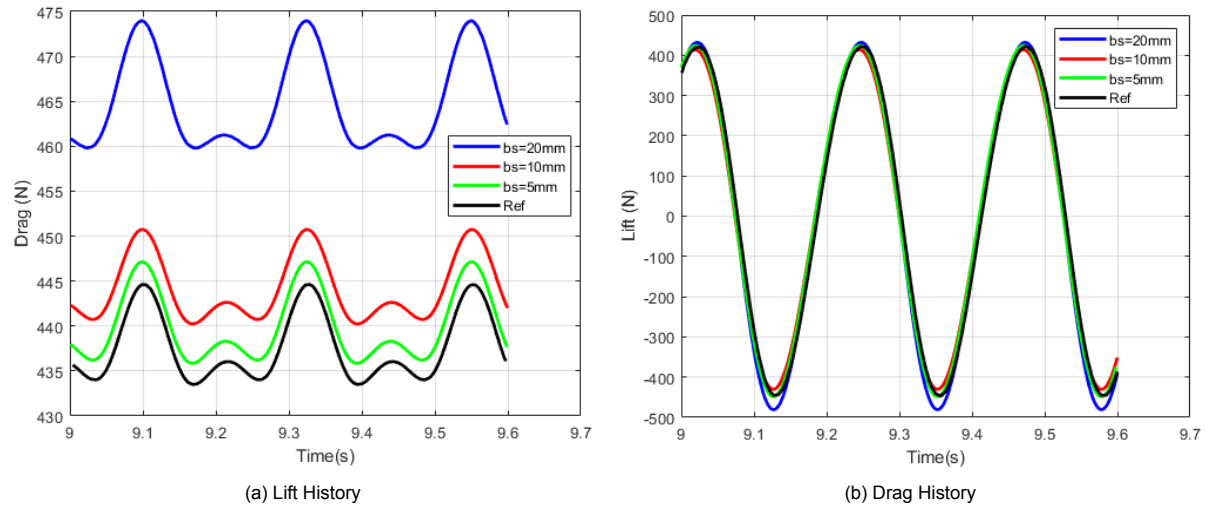
Figure 4.4: Lift and Drag Profiles Compared to the Benchmark for $\Delta t = 2.275 \; ms$

4.1.2. CSM2 Benchmark

This benchmark tests only the structural response using the parameters listed in Table 4.1. These parameters are set using the 'Linear Elastic Material - Isotropic' model of STAR-CCM+. The flexible beam remains cantilevered to the cylinder and is subjected to a gravitational force ($g = -2 \; m/s^2$). For this simulation, the fluid is removed and no numerical damping is applied. In particular, this is a static analysis with the steady state tip displacement computed and compared with the reference result. For each mesh level, 10 iterations are provided to achieve convergence of the Newton iterations. Besides validating the CSM solver, this test case is also used to choose between the infinitesimal strain approximation given by the 'Linear Geometry' model and the finite strain approximation given by the 'Nonlinear Geometry' model. Furthermore, besides the 6 mesh levels listed in section 4.1, a mesh level with just 1 element in the thickness discretization is also considered for the finest mesh level $1b = 640 \times 1$.

The results so obtained with the current STAR-CCM+ implementation are presented in Table 4.3. There is a distinct difference in the solution of the two models. For the 'Linear Geometry' model, the x-displacement predicted is a numerical zero (machine precision) at all mesh levels while the y-displacement appears to converge with mesh refinement albeit to a value slightly over the reference solution. The predicted y-displacement value at mesh level 1 has a relative error of 0.181% which is quite a good prediction.

The infinitesimal strain approximation is expected to work well for predicting dominant displacements that are within 10% of the length of the structure perpendicular to the displacement. This is satisfied for the y-displacement as the reference solution is 4.845% of the beam length. Since the infinitesimal strain approximation does not include the deformation gradient in its formulation, no significant change in the x-displacement was predicted.

The 'Nonlinear Geometry' model, on the other hand, shows promising results for both the x- and y-displacements with predictions converging to the reference solution with mesh refinement. At mesh level 1, the relative errors for the x- and y-displacements are 6.397E-3% and 3.947E-3% respectively. Given that the current test case and the following FSI3 test case require good predictions for both directions of displacement, the 'Nonlinear Geometry' model is selected for the successive validation study.

Table 4.3: CSM2 Results

Mesh Level	N_{Length}	$N_{Thickness}$	Solid Elements	X-disp. of A (mm)		Y-disp. of A (mm)	
				Linear	Nonlinear	Linear	Nonlinear
6	20	1	20	6.80702E-15	-0.45368	-16.68158	-16.65154
5	40	2	80	1.42124E-14	-0.46608	-16.94415	-16.91298
4	80	4	320	6.56936E-15	-0.46830	-16.99073	-16.95935
3	160	8	1280	4.37086E-15	-0.46875	-17.00012	-16.96869
2	320	16	5120	7.79833E-15	-0.46891	-17.00334	-16.97190
1	640	32	20480	2.99491E-15	-0.46897	-17.00467	-16.97323
1b	640	1	640	1.79593E-13	-0.46974	-17.01728	-16.98577
			Reference Solution	-0.46900		-16.97390	

It is also observed from the 'Nonlinear Geometry' model results of Table 4.3 that the thickness discretization is not as important as the length discretization by comparing the relative errors of mesh level 6 vs 1b and that of mesh level 1b vs 1 with both of the scenarios having a constant multiplication factor of 32. It is thus shown that the increased accuracy in bending brought about by quadratic elements suppresses the improvements due to increased thickness discretization. The efficacy of the 'b' mesh levels is further investigated in the FSI3 test case.

4.1.3. FSI3 Benchmark

With the CFD and CSM solvers validated, this benchmark is used to validate the Gauss-Seidel coupling implementation of STAR-CCM+. The prescribed parameters in Table 4.1 for FSI3 result in large beam deflections and strong artificial added mass effects given $\rho_f/\rho_s = 1$ and $Re = 200$. During the FSI simulations, the fluid mesh is moved using the B-Spline mesh morphing method. The simulation is attempted for 12 cases: 6 cases each for time steps of $\Delta t = 1\ ms$ which falls short of the 100 sampling point rule (requiring $\Delta t = 0.92\ ms$) and $\Delta t = 0.5\ ms$.

The results obtained for the cases are tabulated in Table 4.4. The mesh levels are provided as $F + S$ where F is the fluid mesh level and S is the solid mesh level as per Table 4.2 and Table 4.3. Associated Sb levels correspond to 1 thickness element cases. The combinations of $F + S$ mesh levels ensure similar number of solid and fluid elements over the FSI interface. Each case required a certain FSI UR to keep the coupling iterations stable. Mesh levels 3+4(b), 2+3(b) and 1+2(b) were given FSI UR's of 0.50, 0.30 and 0.15 respectively, where the notation $F + S$(b) denotes the pair of mesh levels $F + S$ and $F + S$b. In order to have all the cases sufficiently converged, especially the low FSI UR cases, a rather conservative number of 100 inner iterations per time step is provided for the coupled solvers. A total simulation time of 20 s allows for the fully developed flow solution with periodic flapping to establish.

The results from Table 4.4 reveal a mixed performance for spatial refinement on different parameters. Two key observations are common over the results with the exception of the mean lift for mesh levels 3+4(b): 1) There is little to no difference in a given result for a mesh level when comparing the effect of the time step and 2) Comparing the result of any pair of mesh levels $F + S$(b) also reveals very minimal difference for a given time step. This implies temporal convergence for all mesh levels and confirms the minimal effect of thickness discretization on the solution when using quadratic elements.

Coming to the individual results, consider those for the time step of 0.5 ms. For the drag, the mean values monotonically converge towards the reference with the solution at the finest mesh level 1+2 differing only by 1.10% while the frequency remains unchanged at an error of 0.28%. The mean lift also appears to converge, although not monotonically, to the reference value with a higher final error of 53% owing to the low reference value. The corresponding frequency converges to an error of 3.02%. The x-displacement mean and amplitude results at the finest mesh level 1+2 differ from the reference solution by 10.03% and 10.67% respectively. Spatial convergence for this parameter could not be confirmed with the current set of mesh levels. This is also the case for the y-displacement amplitude with the error at the finest mesh level 1+2 at 3.17%. The y-displacement mean, however, appears to converge with the error at the finest mesh level 1+2 at 4.73%.

Table 4.4: FSI3 Results

$\Delta t = 1\ ms$				
Mesh Level	**Drag (N [Hz])**	**Lift (N [Hz])**	**X-disp. (mm [Hz])**	**Y-disp. (mm [Hz])**
3+4b	485.90 $\pm$ 27.90 [10.93]	0.85 $\pm$ 155.85 [5.48]	-3.09 $\pm$ 2.93 [10.93]	2.09 $\pm$ 35.93 [5.48]
2+3b	465.18 $\pm$ 27.58 [10.93]	5.45 $\pm$ 159.30 [5.46]	-2.86 $\pm$ 2.70 [10.93]	1.37 $\pm$ 34.96 [5.46]
1+2b	462.10 $\pm$ 28.50 [10.93]	3.50 $\pm$ 160.80 [5.46]	-2.94 $\pm$ 2.77 [10.93]	1.53 $\pm$ 35.29 [5.46]
3+4	485.90 $\pm$ 27.70 [10.99]	3.00 $\pm$ 157.00 [5.46]	-3.11 $\pm$ 2.95 [10.99]	2.10 $\pm$ 36.06 [5.46]
2+3	465.25 $\pm$ 27.15 [10.93]	5.75 $\pm$ 158.05 [5.43]	-2.87 $\pm$ 2.71 [10.93]	1.37 $\pm$ 35.05 [5.43]
1+2	462.30 $\pm$ 28.10 [10.93]	3.40 $\pm$ 159.10 [5.43]	-2.95 $\pm$ 2.79 [10.93]	1.54 $\pm$ 35.37 [5.43]
Ref. Soln.	457.30 $\pm$ 22.66 [10.90]	2.22 $\pm$ 149.78 [5.30]	-2.69 $\pm$ 2.53 [10.90]	1.48 $\pm$ 34.38 [5.30]
$\Delta t = 0.5\ ms$				
Mesh Level	**Drag (N [Hz])**	**Lift (N [Hz])**	**X-disp. (mm [Hz])**	**Y-disp. (mm [Hz])**
3+4b	486.35 $\pm$ 28.15 [10.93]	1.25 $\pm$ 156.75 [5.49]	-3.11 $\pm$ 2.95 [10.93]	2.19 $\pm$ 35.99 [5.49]
2+3b	465.20 $\pm$ 27.80 [10.93]	5.25 $\pm$ 159.25 [5.49]	-2.87 $\pm$ 2.71 [10.93]	1.36 $\pm$ 35.00 [5.49]
1+2b	462.25 $\pm$ 28.70 [10.93]	3.55 $\pm$ 160.95 [5.49]	-2.95 $\pm$ 2.78 [10.93]	1.54 $\pm$ 35.36 [5.49]
3+4	486.80 $\pm$ 28.10 [10.93]	0.30 $\pm$ 156.70 [5.56]	-3.13 $\pm$ 2.97 [10.93]	2.20 $\pm$ 36.12 [5.46]
2+3	465.35 $\pm$ 27.45 [10.93]	5.70 $\pm$ 158.00 [5.46]	-2.88 $\pm$ 2.72 [10.93]	1.37 $\pm$ 35.10 [5.46]
1+2	462.35 $\pm$ 28.35 [10.93]	3.40 $\pm$ 159.60 [5.46]	-2.96 $\pm$ 2.80 [10.93]	1.55 $\pm$ 35.47 [5.46]
Ref. Soln.	457.30 $\pm$ 22.66 [10.90]	2.22 $\pm$ 149.78 [5.30]	-2.69 $\pm$ 2.53 [10.90]	1.48 $\pm$ 34.38 [5.30]

The profiles for drag, lift, x- and y-displacement are shown in Figure 4.5. It is clearly seen for all plots that the difference between the solution profiles $F + S$(b) is hardly visible. The relative errors in the amplitude of drag and lift profiles are large (25.11% and 9.82% respectively) owing to the noisy nature of the obtained results. These "beatings" in drag and lift are most pronounced at time instants of maximum beam acceleration which are the extremums of the plots, thereby corrupting the estimate for the amplitudes. The effect of these beatings on the mean value is suspected to be minimal.

The maximum acceleration instants are also where the greatest effect of added mass instability is felt. This is an 'artificial' effect given the beatings are a numerical pressure result only. The corresponding displacements are stable throughout the simulation. This behavior was also observed in the results of Cole & Neu[100]. It is also observed that refining the mesh results in smaller beatings in the force plots. This appears to be a combined effect of spatial refinement and reducing the FSI UR.

Although the effect of inner iterations on the beatings in the force plots is not investigated in the current study, it is known that increasing this parameter leads to better predictions of displacement but with greater beatings in the lift.[100] As for the differences between the current solutions and the reference, the averaging technique employed to report the solution as in subsection 4.1.1 could account for a fraction of the relative percentage errors. Further improvements in results require subsequent mesh refinement.

The current study shows that time-accurate results for unsteady FSI problems call for careful selection of time step, FSI UR, and sufficient convergence even for a finely resolved mesh. In summary, the current study using the STAR-CCM+ (v2020.3.1) implementation for this benchmark verifies and validates the associated solvers and the coupling for its use to compute strongly coupled, two-way FSI problems. Additional FSI benchmarks are not tested here, as further verifications can be found in the extensive STAR-CCM+ Verification Suite[101]. The code is thus applied to the following cross flow cylinder vibration problem.

(a) Drag History

(b) Lift History

(c) X-displacement History

(d) Y-displacement History
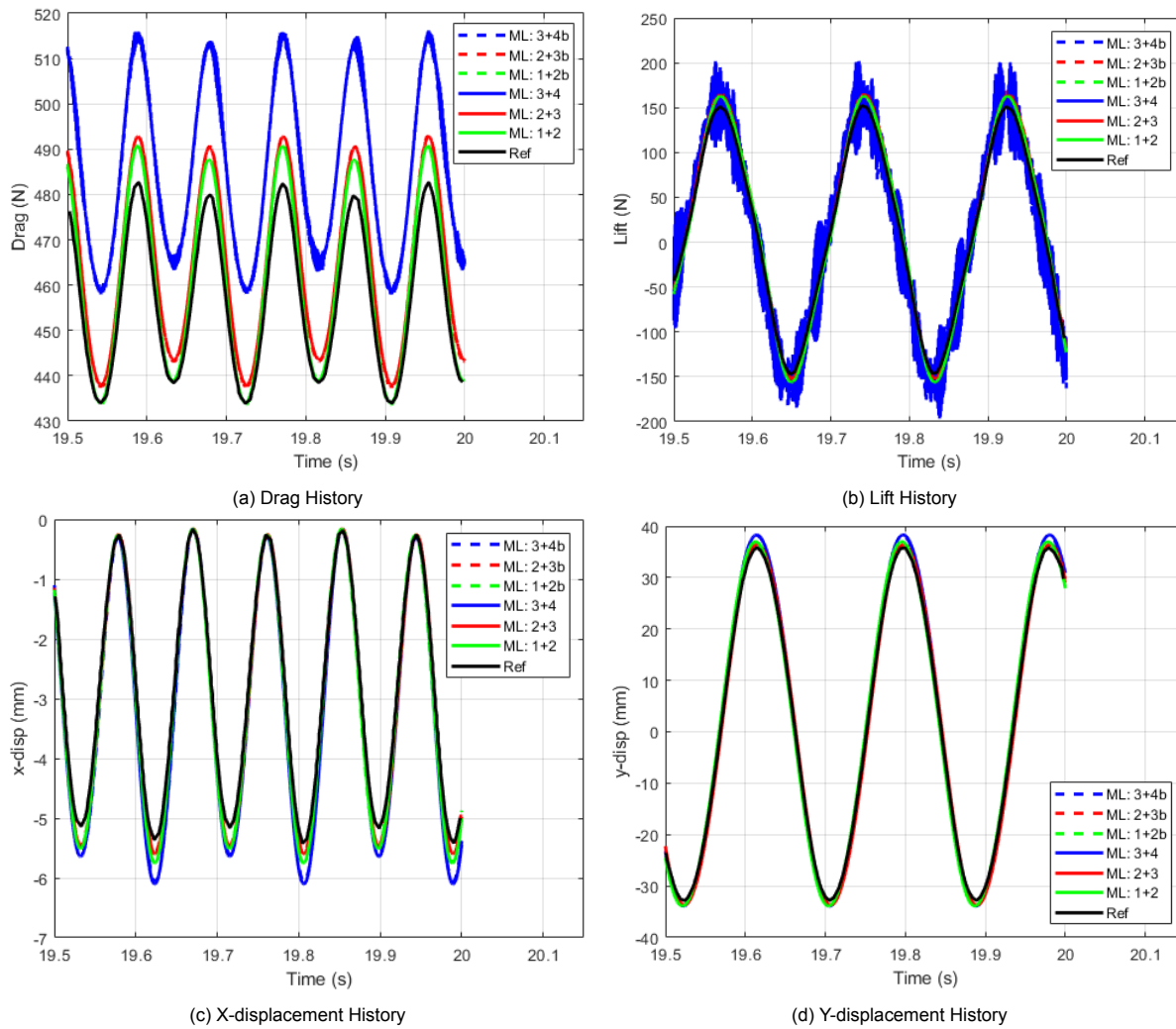
Figure 4.5: Drag, Lift, x-displacement and y-displacement Profiles Compared to the Benchmark for $\Delta t = 0.5\ ms$

4.2. Cross Flow VIV Benchmark

The study of Khalak & Williamson[27] is a pioneering work from 1996 that established the influence of the mass ratio (m^*) at a given mass-damping parameter $(m^*\zeta)$ for VIV of a 1-Dof elastically mounted rigid cylinder. It was shown that a low m^* leads to a larger and wider 3-branch vibrational amplitude response of a structure and the departure of the frequency ratio $(f^* = f_{osc}/f_{n,air})$ from 1. In this section, the efficacy of the URANS turbulence models of the current STAR-CCM+ implementation is tested against this study.

Quite some work has been done on this test case using the popular K-Omega SST model. Guilmineau & Queutey[102] and Dobrucali & Kinaci[103] have used the implementation of this model in ANSYS to make their calculations. However, a recent study by Liparoti[104] shows the possibility of using the 'Standard K-Epsilon Low Re' model in STAR-CCM+ for FSI calculations of rigid cylinders. Given the tested range of $Re \in [1700, 10800]$ being in the subcritical range[35], or to be more precise in the TrSL2 regime[37], the wake of the cylinder is fully turbulent with most of the boundary layer still laminar. For such a situation, it is also interesting to see if using the 'Gamma ReTheta' (GRT) transition model available for the 'K-Omega SST' model in STAR-CCM+ helps make a better prediction than using the base model as a standalone. Furthermore, to better account for the anisotropy of turbulence, constitutive relationship settings of linear, quadratic (QCR) and cubic are available for both 'K-Omega SST' and 'Standard K-Epsilon Low Re' models. Thus, the following 7 models with associated settings are tested:

- K-Omega SST: Linear
- K-Omega SST: Linear + Low Re modification
- K-Omega SST: Linear + GRT transition

- K-Omega SST: QCR
- K-Omega SST: QCR + Low Re modification
- K-Omega SST: QCR + GRT transition

- Standard K-Epsilon Low Re: Cubic (selected based on the work of Liparoti[104])

In particular, for the K-Omega SST model, the curvature correction and the realizability options are enabled. The curvature correction helps in accounting for strong streamline curvature, as is the case in the flow aft of the cylinder, by altering the turbulent kinetic energy production term. Using the realizability constraint, on the other hand, helps to overcome an unexpectedly large growth of turbulent kinetic energy in stagnation point flows which is a common problem for two-equation models.[87] For the Standard K-Epsilon Low Re model, the Yap correction and the realizability options are enabled based on the recommendation by Liparoti[104]. The under-the-hood workings of these options have been explained in chapter 3.

4.2.1. Simulation Setup
Based on the values of mass ratio and mass-damping parameter, an infinite set of cylinder mass, spring stiffness and damping can be chosen. To make a unique selection, information about the Reynolds number is also required. However, the original work[27] does not give a clear indication of this parameter but hints to the tested range of $Re \in [1500, 13000]$. To make a unique selection, the work of Guilmineau & Queutey[102] is referred where pairs of non-dimensional velocity $U^* = U/f_{n,air}D$ and Reynolds number Re are explicitly mentioned. This helps in pinning down the natural frequency of the cylinder in air which allows for the selection of a unique set of cylinder mass, spring stiffness and damping. The key simulation parameters are tabulated in Table 4.5. Note that additional tests for $U^* = 4.50$, 7.00, 9.00 and 10.75 were also carried out by the author as part of an internship, the results of which are also shown and discussed here for completeness.

Table 4.5: Parameter Settings for the Study

Structure Parameters			Flow Parameters		
Cylinder Diameter, D	3.810	cm	Fluid Density, ρ_f	997.561	kg/m^3
Mass Ratio, m^*	2.400	-	Dynamic Viscosity, μ_f	8.8871E-4	$Pa \cdot s$
Mass-Damping, $m^*\zeta$	0.013	-	Tested U^* values	2.00, 3.30, 5.73, 12.50	-
Cylinder Natural Frequency, $f_{n,air}$	0.532	Hz			

For the simulation domain, a 2D channel setup of $35D \times 14D$ is created in STAR-CCM+. The cylinder is placed $10D$ from the inlet. The channel walls and cylinder surface are given a no-slip boundary condition. The inlet is prescribed with a constant velocity inflow while the outlet is prescribed a static pressure of 0 Pa. Due to relatively large expected cylinder displacements (maximum $A^* = y/D$ of 0.95[27]), the overset mesh technique is used instead of the standard mesh morphing used in section 4.1. This technique involves a background mesh with 44184 fluid elements for the channel and a movable overset mesh with 12400 fluid elements for a patch of size $6D \times 6D$ containing the cylinder. A Y^+ value of 1 is targeted at the cylinder wall and channel walls based on a U^* value of 16. For the tested U^* values, this ensures a $Y^+ < 1$ at all times for all of the test cases. The overset and background meshes are shown in Figure 4.6.

The 6-Dof 'Dynamic Fluid Body Interaction' (DFBI) rigid body motion solver is used to solve for the cylinder displacement which is implicitly coupled with the 'Segregated Flow' solver of STAR-CCM+. For the flow solver, a 2nd order upwind convection scheme is selected. Furthermore, a 2nd order temporal discretization scheme is selected. For the cases of $U^* = 2, 3.3, 4.5$ and 5.73, a time step of $\Delta t = 15\ ms$ is selected while for $U^* = 7, 9, 10.75$ and 12.5, a time step of $\Delta t = 7.5\ ms$ is selected to satisfy the 100 sampling point thumb rule and $CFL \leq 1$ criteria. A total of 80 inner iterations per time step are provided with the first 30 inner iterations for the coupled solvers and the remaining with only the flow solver.

(a) Overset Mesh   (b) Background Mesh
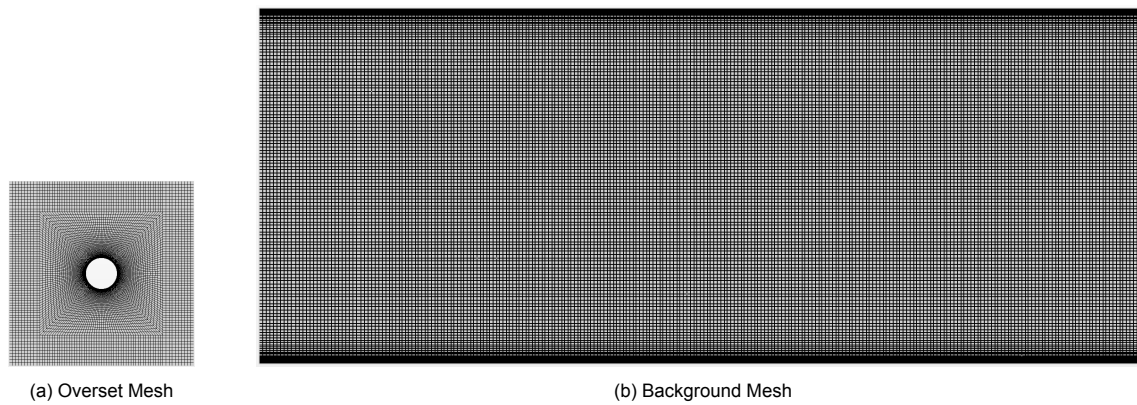
Figure 4.6: Structured Fluid Overset and Background Mesh

From the work of Guilmineau & Queutey[102], it is known that the initial condition greatly influences the

obtained result. For the current study, the "*rest*" initial condition is used. This means that for a given U^*, the flow velocity is prescribed for a fixed cylinder until vortex shedding is fully established. When the lift becomes fully periodic, the elastically mounted cylinder is allowed to oscillate. The total simulation time given is at least 100 s beyond the time instant when the lift becomes periodic. The release time of the cylinder appears to decrease in an asymptotic fashion with increasing U^*, as can be seen in Figure 4.7. This conforms to the idea that the transient phase of the simulation lasts for a specific number of 'flow passes' ($FP = U^* \cdot f_{n,air} \cdot \frac{D}{35D} \cdot t_{release} \approx 4.5 \ \forall \ U^*$). The 'flow pass' is a non-dimensional way of looking at simulation time and is more formally introduced and used in chapter 5.
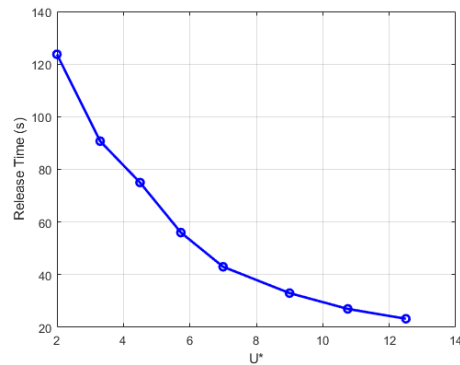
Figure 4.7: Cylinder Release Time vs U^*

4.2.2. Simulation Results

The primary results of this study are amplitude response and the frequency response which are shown in Figure 4.8. The plots also show the 2D numerical results of Dobrucali & Kinaci[103] (D&K), and Guilmineau & Queutey[102] (G&Q) along with the experimental results of Khalak & Williamson[27] (K&W). A mixed performance of models is observed in different branches of the amplitude response curve. There is close agreement between the numerical predictions and the experimental results in the initial branch ($U^* = 2$), the start of the upper branch ($U^* = 4.5$) and the end of the lower branch ($U^* = 12.5$) while the prediction is off in the transition from initial to upper branch ($U^* = 3.3$), the upper branch itself ($U^* = 5.73$ and 7), and in the transition from the upper to lower branch or the start of the desynchronization regime ($U^* = 9$ and 10.75). The underprediction of peak resonance amplitude is expected for URANS models as can be seen from the other reference curves.

In terms of the amplitude response curve, the "best" performing models for each case along with the relative error are tabulated in Table 4.6. For the initial branch and its transition to the upper branch, using the GRT transition model appears to be beneficial. However, using the transition model beyond this branch leads to underpredicted amplitude predictions. The low Re modification also seems to work well for the initial branch and its transition to the upper branch. The constitutive relationship setting also significantly influences the result as is noticed by the gap in the results of same symbol data points.

(a) Amplitude Response   (b) Frequency Response
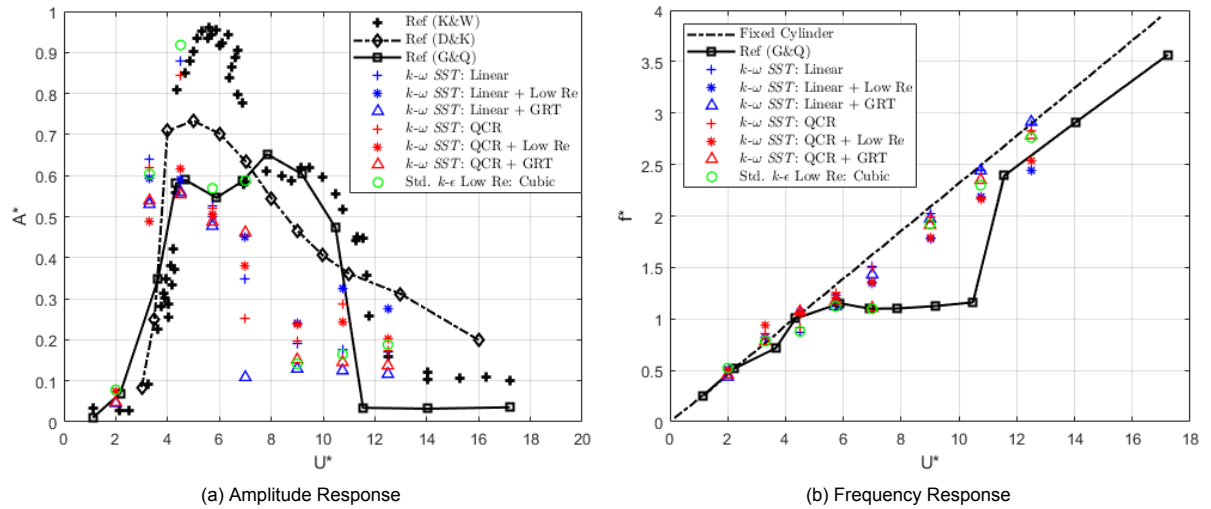
Figure 4.8: Obtained Results using the URANS Framework

Table 4.6: Closest Predicting URANS Turbulence Models to the Experimental Results for Different Test Cases

U^* Value	"Best" Model	Relative Error
2.00	K-Omega SST: Linear + GRT	59.30%
3.30	K-Omega SST: QCR + Low Re	387.40%
4.50	K-Omega SST: QCR	2.07%
5.73	Std. K-Epsilon Low Re: Cubic	40.28%
7.00	Std. K-Epsilon Low Re: Cubic	1.03%
9.00	K-Omega SST: Linear + Low Re	60.51%
10.75	K-Omega SST: Linear + Low Re	37.01%
12.50	K-Omega SST: Linear	6.20%

For the upper branch, the basic K-Omega SST models (Linear and QCR) and the Standard K-Epsilon Low Re model provide good amplitude predictions. For the test case $U^* = 4.5$, both model implementations in STAR-CCM+ predict a response in the upper branch which does not seem to be observed from the other reference URANS curves. However, it is to be noted that Guilmineau & Queutey[102] were also able to predict a similar large amplitude response for this test case, although for an "*increasing velocity*" initial condition. The test case $U^* = 7$, on the other hand, reveals the largest range of predictions for the tested models. This is quite understandable given the tricky location in the amplitude response where the experiment itself reveals multi-valued results in the vicinity of this location. For the desynchronization regime, all models predict low amplitude responses, even for the transition from the upper to lower branch. The K-Omega SST model with and without the low Re modification appears to suffice in the lower branch.

The relative accuracy for the prediction of the frequency response, however, does not follow the same ranking order for the models as the amplitude response. Due to the absence of experimental frequency data in the original work of Khalak & Williamson[27] and the fact that the available experimental frequency data published later by Khalak & Williamson[48] (see Figure 2.8b) is non-dimensionalized with the natural frequency in water (which adds the uncertainty in predicting the required added mass), the frequency response results are viewed in a qualitative manner. For $U^* = 2$, 3.3 and 12.5, the expectation is for the response to be close to that of a fixed cylinder (based on a Strouhal number of 0.21). For $U^* = 2$ and 3.3, the transition model still remains important and has the closest prediction to the fixed cylinder albeit now with the QCR constitutive relationship. For $U^* = 3.3$, the "best" model deviates from the Strouhal relation the most with the closest prediction now given by the Standard K-Epsilon Low Re: Cubic model and K-Omega SST: QCR + GRT model.

At $U^* = 4.5$, the same models that predicted an amplitude response in the upper branch deviate from the fixed cylinder curve. At $U^* = 5.73$, all models correctly deviate from the fixed cylinder curve and predict a value slightly above 1 in the lock-in regime. At $U^* = 7$, only the Standard K-Epsilon Low Re: Cubic model and K-Omega SST: QCR + GRT model predict the lock-in effect while the other models already show signs of desynchronization. For the following two test cases of $U^* = 9$ and 10.75, all models predict a desynchronized frequency back near a fixed cylinder response against expectations. The predictions for the last test case of $U^* = 12.5$ comes with no surprise as this value is already towards the end of the lower branch where the desynchronization is complete.

Another way of interpreting the amplitude and frequency response curves is by looking at the curves as a whole rather than making one-to-one test case comparisons. With such a viewpoint, it can be said that overall with the URANS turbulence models, the three basic branches of a VIV response can be observed. However, the current approach predicts a smaller lock-in range and an earlier and slightly smaller peak amplitude response than expected from the experiments. In particular, this comment about the peak amplitude response can also be made for the reference curve of Dobrucali & Kinaci[103].

With the discussion of the primary results now complete, the focus is brought to the time series of the lift coefficient ($C_l = F_L/(\frac{1}{2}\rho U^2 D)$) and the amplitude response for the set of tested models at $U^* = 5.73$. These are shown along with the experimental amplitude response in Figure 4.9. From the time series, the amplitude for a given model is given by $y = 0.5(y_{max} - y_{min})$ which is then divided by the diameter to give the non-dimensional A^*. In the experiment, this is reported by simply taking the maximum amplitude. Observing Figure 4.9a, we expect a quasi-periodic response from our models. This is observed in the results for all the models except the K-Omega SST models that also employ the GRT transition model. In fact, the results of Guilmineau & Queutey[102] were also perfectly periodic with a single frequency so it is encouraging to see this quasi-periodicity being captured in the current study.

An interesting observation is the apparent shift in the mean position of the cylinder from its neutral value during motion as predicted by the K-Omega SST: Linear model in Figure 4.9c. This was not observed in the original work[27] and is thus purely a numerical artifact and should be preferably removed before quoting an A^* value. It is for this specific reason of removing the influence of the mean position on the quoted amplitude response that the aforementioned formulation of y is adopted in the current study.

The different amplitude response time series for different models are a direct consequence of the computed lift force acting on the cylinder. This lift force pattern is further a consequence of the associated vortex shedding pattern predicted by the model. Such a difference is already seen in the first 56 s of the time series where the response for a fixed cylinder is computed. The $C_{l,max}$ predicted by the models, in the order as they are presented in Figure 4.9, are 1.785, 1.987, 1.998, 1.501, 1.516, 1.774 and 1.818 respectively. For the K-Omega SST models, the effect of the constitutive relationship appears to be minimal for the fixed cylinder response. However, this clearly changes when the cylinder starts oscillating as is seen in Figure 4.9 with a different pattern in lift. Once the cylinder starts oscillating, there exists a transient phase at the end of which the lift and amplitude settle on a single frequency (equal to the vortex shedding frequency in the lock-in regime) and have a fixed phase difference of about 180° between them. To avoid this transient phase in quoting the results, only the last 4 flow passes (corresponding to 46 s) of the simulation are made use of.

With the discussion on the effect of the selected model now complete, the focus is brought to the effect of U^* on the time series for a single model, in particular, the K-Omega: QCR model. These are shown in Figure 4.10. It is observed that the fixed cylinder solution shows an increase in $C_{l,max}$ at first with increasing U^* value with no visible increase after it settles at a value of approximately 2. However, the change in the lift coefficient post the release of the cylinder follows an interesting trend. For the initial branch, releasing the cylinder leads to a slight increase in the lift coefficient. The amplification of the lift is further pronounced in the predicted upper branch ($U^* = 3.3$ and 4.5 for this model). From the beginning of the desynchronization to the end of the lower branch, the lift coefficient falls below the value for a fixed cylinder and is observed to settle roughly at half the value of the fixed cylinder. This observation also conforms with the one made by Guilmineau & Queutey[102].

(a) Experimental Result

(b) Standard K-Epsilon Low Re: Cubic

(c) K-Omega SST: Linear

(d) K-Omega SST: QCR

(e) K-Omega SST: Linear + GRT

(f) K-Omega SST: QCR + GRT

(g) K-Omega SST: Linear + Low Re

(h) K-Omega SST: QCR + Low Re
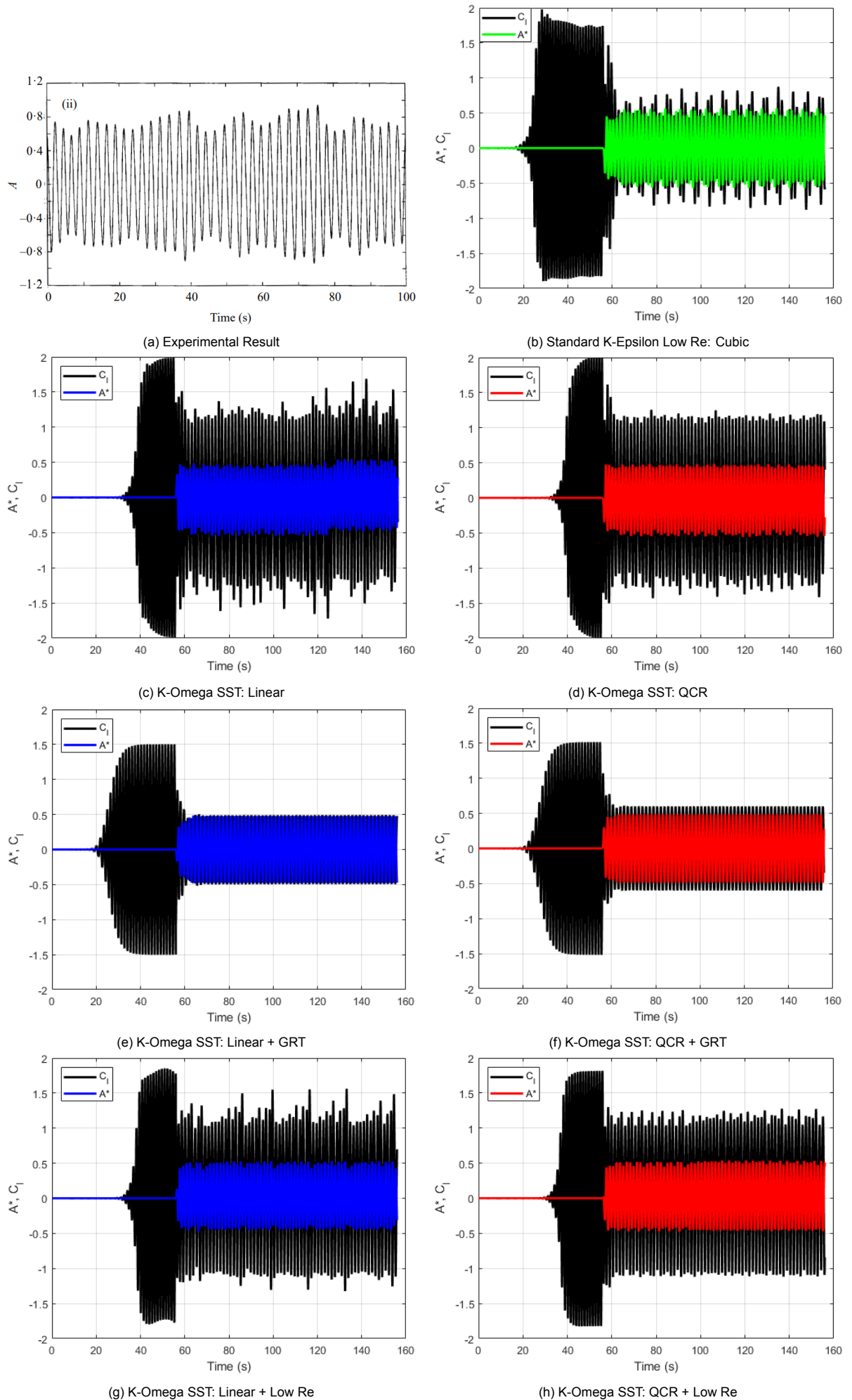
Figure 4.9: Obtained Amplitude and Associated Lift Coefficient Time Series for $U^* = 5.73$ ($Re = 4968.43$)

(a) $U^* = 2.00$ $(Re = 1734.18)$

(b) $U^* = 3.30$ $(Re = 2861.40)$

(c) $U^* = 4.50$ $(Re = 3901.91)$

(d) $U^* = 5.73$ $(Re = 4968.43)$

(e) $U^* = 7.00$ $(Re = 6069.64)$

(f) $U^* = 9.00$ $(Re = 7803.82)$

(g) $U^* = 10.75$ $(Re = 9321.23)$

(h) $U^* = 12.50$ $(Re = 10838.64)$
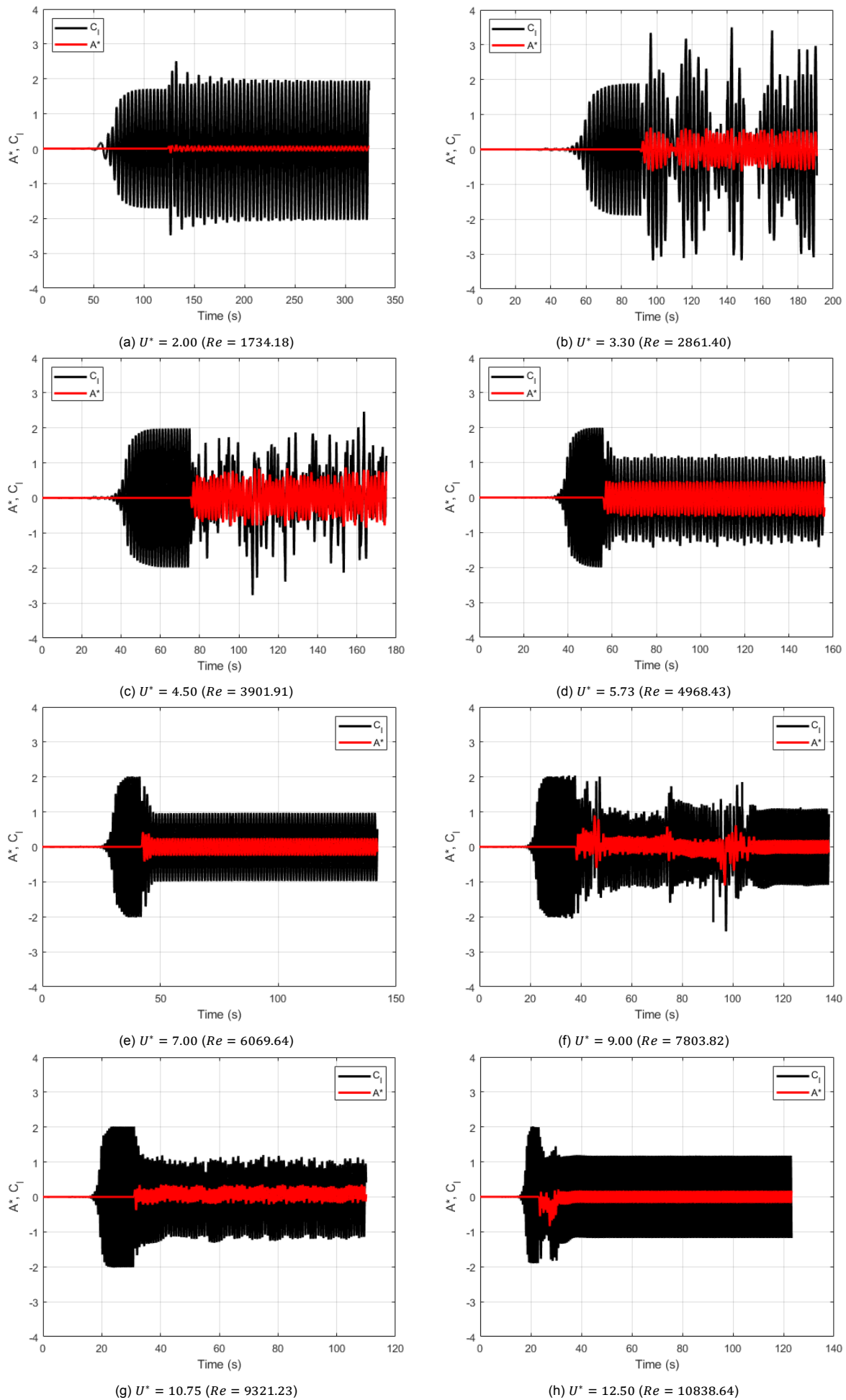
Figure 4.10: Obtained Amplitude and Associated Lift Coefficient Time Series for K-Omega SST: QCR model

The last item for discussion is the vortex shedding phenomena itself that causes a certain lift pattern which in turn results in a peculiar amplitude response of the cylinder. The expectation here is to observe a switch in vortex shedding mode from '2S' to '2P' as discussed in chapter 2. For this, the vorticity magnitude scaled by the cylinder vibration frequency was tracked for all the test models at $U^* = 2.00$ and $U^* = 5.73$. At $U^* = 2.00$, all models correctly predicted the '2S' vortex shedding mode. However, at $U^* = 5.73$, the behaviour of the models were starkly different. The K-Omega SST models that employed the GRT transition still predicted a '2S' vortex shedding mode. All the other K-Omega SST model variants did show a departure from the '2S' vortex shedding mode but the resulting pattern was quite chaotic with no direct sign of the '2P' vortex shedding mode owing to the vortex-vortex interaction in the wake. Only the Standard K-Epsilon Low Re: Cubic model was able to show a clear '2P' vortex shedding mode before the vortices departed from the pattern under the influence of other vortices. The vorticity plots are shown in Figure 4.11.
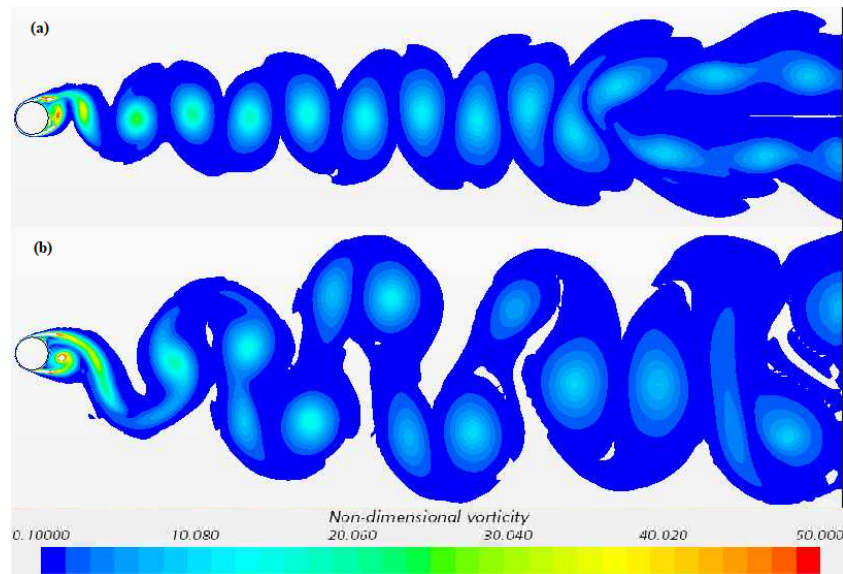
Figure 4.11: Non-dimensional Vorticity Contour Plots as Predicted by the Standard K-Epsilon Low Re: Cubic Model at (a) $U^* = 2.00$ and (b) $U^* = 5.73$

The results discussed so far show qualitative and quantitative differences between the URANS turbulence models and the efficacy of such a scheme in tackling a cross flow VIV problem. A part of the reason for the shortcoming of the results of the current study and the other numerical references[102],[103] is owed to the fact that these are 2D results. In reality, vortex shedding is a 3D phenomenon with the possibility of coalescence and breakdown of vortices, the existence of correlated vortex-cells over the length of the cylinder and the so-called "end effects" which are a consequence of the fact that the cylinder has a finite length. Looking at the drawback of the 2D approach from a theoretical perspective, the 2D vorticity equation, which is obtained by taking the curl of the Navier-Stokes momentum equation, is missing the 'vortex-stretching' term ($\nabla \times \vec{\omega}$) which accounts for why there is no breakdown of vorticity observed here. Subsequent improvements are expected for a 3D simulation but not enough to compete with higher fidelity methods such as LES or DES.

The current test case thus gives an expectation for the URANS scheme to work well in the initial branch and a possible underprediction in the upper branch. Only these two branches are of interest for the OECD benchmark cases. While the current study does not already give a perfect indication of the "best" model that is to be used for the benchmark, the following model implementations of STAR-CCM+ are shortlisted for the open phase of the benchmark:

- K-Omega SST: QCR
- K-Omega SST: QCR + GRT
- Standard K-Epsilon Low Re: Cubic

The above shortlist is made based on the results of the initial and upper branches. While the 2D results indicate minimal difference between the Linear and QCR constitutive relationships, it is expected that QCR would provide superior results in a 3D setting, especially because it is formulated to capture the anisotropy of turbulence better. With the URANS turbulence models now tested and shortlisted, the open phase study of the OECD benchmark will help single out a choice as is discussed in the following chapter.

4.3. Conclusion

In this chapter, the STAR-CCM+ implementation of the flow and structural solvers and their coupling were tested against the numerical benchmark of Turek & Hron[26] for standalone CFD, standalone CSM and coupled CFD-CSM calculations. Along with a successful validation, the 100 sampling points thumb rule for selecting a time step was tested with the CFD3 test case which supports its use for the OECD benchmark. For the structure, the importance of selecting an appropriate approximation for the strain was realized when dealing with displacements comparable to the characteristic length of the structure.

To test the URANS eddy viscosity turbulence model implementations available in STAR-CCM+, the experimental results of the cross flow VIV problem of Khalak & Williamson[27] are made use of. The primary results of the amplitude and frequency response reveal the possibility of capturing the 3-branch VIV response with the URANS framework. However, the current results predict a shorter lock-in regime with an earlier and shorter peak response. Based on the current results and branches of interest for the OECD benchmark, the K-Omega SST: QCR, K-Omega SST: QCR + GRT and Standard K-Epsilon Low Re: Cubic models are shortlisted for testing in the open phase. This is further discussed in the following chapter.

OECD Benchmark: Open Phase

With the STAR-CCM+ code validated and the turbulence models shortlisted, the open phase of the OECD benchmark is formally introduced and tackled. This phase of the benchmark comes with the experimental results available and, in the current study, is mainly used to select one of the shortlisted turbulence models to be employed in the blind phase of this benchmark. This is also a platform to test the URANS framework and based on any shortcomings in the current study, hypothesise possible reasons for the same.

The experimental setup and parameters of interest are given in section 5.1. Based on the available resources and time, different fluid meshes are proposed and tested in a standalone CFD study to make a suitable selection for the FSI study and is provided in subsection 5.2.1. The experimentalists also provide CAD drawings to the participants for the numerical study. In particular, the two cylinders house brass accelerometer mountings of different density which affect the natural frequency of the structure. This is investigated for fine tuning in a pure structural analysis and is discussed in subsection 5.2.2. Once the models and the meshes are selected, the shortlisted turbulence models are put the test against the FSI problem in section 5.3.

5.1. Experimental Setup

The experimental setup consists of two in-line cantilevered cylinders subjected to cross flow in a rectangular channel test section as can be seen in Figure 5.1a. The test facility is located at the JSC "Afrikantov OKBM" in Russia. For the simplicity of the numerical setup, only the channel and its contents are set up for the simulation based on the dimensions prescribed in the CAD drawings made available to the participants of the benchmark. The CAD model so created using STAR-CCM+ is shown in Figure 5.1b.

(a) Experimental Setup

(b) CAD Model for the Simulations
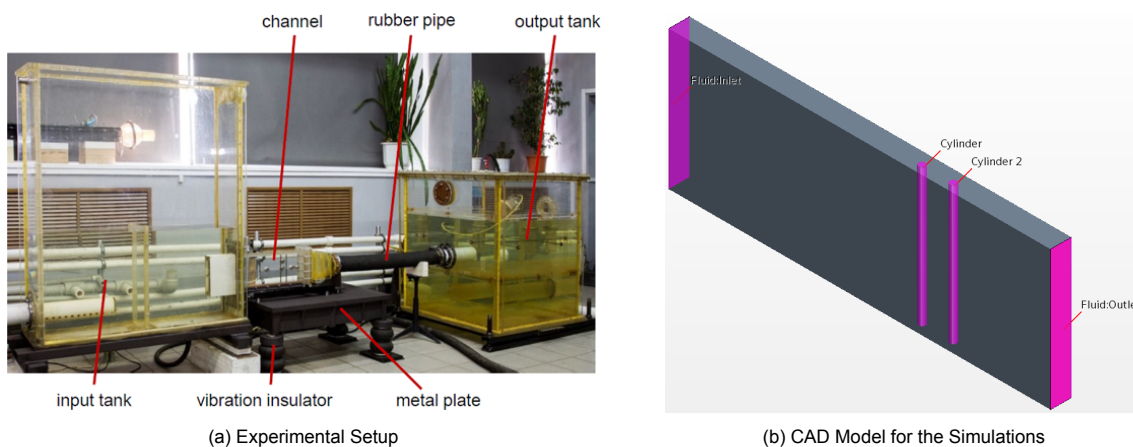
Figure 5.1: Experimental Setup and the Corresponding Domain Setup for Phase 3 Simulations

The experimental study made use of hollow stainless steel cylinders of diameter D=7 mm, wall thickness $0.3\ mm$ and length $198\ mm$ placed $45\ mm$ apart with the first cylinder placed at a distance of $350\ mm$ from the inlet. For the experiment, each cylinder had two brass accelerometer mountings of diameter $6.4\ mm$ and length $12\ mm$ soldered (the length includes the solder deposit) internally at the tip of the cylinder and at near halfway length of the cylinder. These brass bobs for the two cylinders were slightly different in density leading to different natural frequencies of the structures in air and water. The material properties of the structure are provided in Table 5.1. The working fluid was water at $10°\ C$ and was tested for flow rates of 10 m^3/h (off-resonance) and 16 m^3/h (peak resonance) through the aforementioned channel of dimensions $550 \times 200 \times 30\ mm^3$ that houses the cylinders. The reference static pressure was 1 kgf/cm^2 (98.07 kPa). In the current study, only the peak resonance case, which translates to Re=3964.23, is simulated and compared against the experimental results.

Table 5.1: Structural Properties

Structure	Material	Density, ρ_s (kg/m^3)	Young's Modulus, E (GPa)	Poisson's Ratio, ν
Hollow Cylinders 1 & 2	Stainless Steel	7850	180	0.30
Bobs for Cylinder1	Brass	9450	200	0.33
Bobs for Cylinder2	Brass	12450	200	0.33

In the experiment, the natural frequency and structural damping of the cylinders in the channel were analyzed by measuring the vibrations under the impact excitations of the channel and producing a Frequency Response Function (FRF) plot. Based on the test of the channel without water, the natural frequencies of the cylinders were found to be $f_{n1,air} = 107\ Hz$ and $f_{n2,air} = 98\ Hz$ respectively. Based on a similar test of the channel with water, the natural frequencies of the cylinders were found to be $f_{n1,water} = 98\ Hz$ and $f_{n2,water} = 90\ Hz$ respectively. The FRF plot created based on the experimental results provided for the test of the channel with water is provided in Figure 5.2.
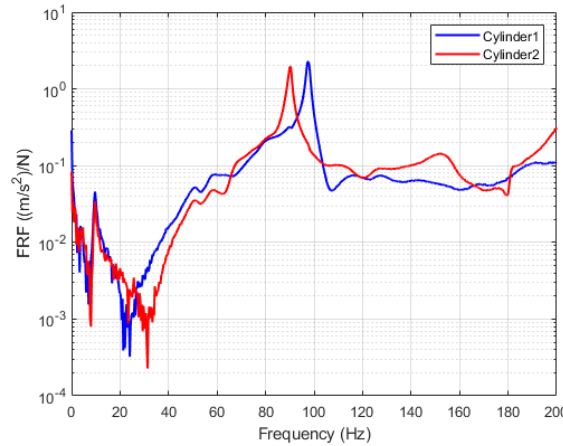
Figure 5.2: FRF Curves for the Two Cylinders under Impact Excitation of the Channel with Water

Using the above plot, the damping ratio (ζ) or its related parameters like the loss factor (η) and quality factor (Q) is found using the 'half-power' or '3 dB' rule. These damping parameters are calculated using

$$\frac{\Delta f}{f} = \eta = \frac{1}{Q} = 2\zeta\sqrt{1 - \zeta^2} \approx 2\zeta \tag{5.1}$$

where Δf is the width of the FRF curve 3 dB below the peak at frequency f. The loss factor for both cylinders vibrating in water comes out to $\eta = 0.016$. The approximation $\zeta = 0.5\eta$ is accurate within 5E-3% for $\eta \in [0, 0.02]$ and is thus made use of giving $\zeta = 0.008$. This value is later used in conjunction with the value from the numerical structural tests to provide structural damping for the FSI tests using the 'Rayleigh Damping' model available in STAR-CCM+. For the cylinders, the Rayleigh damping is restricted to stiffness proportional damping with the corresponding constant calculated as per Equation 3.31 with $\omega = 2\pi f_{n,water}$.

5.1.1. Measurement Systems

To make measurements, various technical instruments were made use of which may have added to the cumulative errors made in the experiment. The test facility allowed static measurement of pressure and temperature with errors of $\pm0.006 \; kgf/cm^2$ and $\pm1°$ respectively. The flow rate was measured by an electromagnetic flow meter with an accuracy of $\pm0.5\%$. Systems based on Particle Image Velocimetry (pulsed and continuous wave lasers) and Laser Doppler Velocimetry (one component) were used to study the hydrodynamics of the flow. As the tracer particles, 10 μm polyamide particles were used. The relative error of the LDV measurement system was estimated to be 1%. The relative error of the velocity measurements by PIV system with pulsed wave laser was accurate to within 3% while those by PIV system with continuous wave laser was accurate to within 4%. General views of the model with PIV and LDV systems installed on the test facility are shown in Figure 5.3.

The pressure pulsations were measured by sensitive dynamic sensors located on the channel wall. The measurement error of pressure pulsations did not exceed 26% with a confidence probability of 0.95. Accelerometers were installed at the top of the cylinders in two mutually perpendicular directions. The measurement error of vibration acceleration did not exceed 28% with a confidence probability of 0.95. Measurements of vibrations, pressure pulsations, as well as velocity pulsations were carried out synchronously. The operability of the accelerometers and pressure pulsation sensors was provided by duplication of measurements using a laser vibrometer and hydrophones, respectively. The synchronization of vibration measurements using accelerometers and a laser vibrometer were carried out by an external trigger.
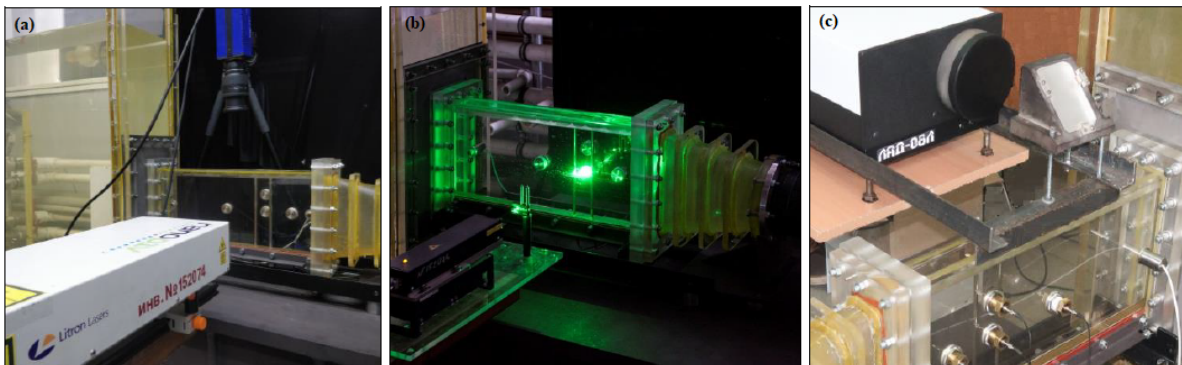
Figure 5.3: General Views of the Measurement Systems: (a) PIV with Pulsed Wave Laser, (b) PIV with Continuous Wave Laser, (c) LDV System

5.1.2. Open Phase Test Parameters

Calculation of FSI can be performed using one-way and two-way methods. The one-way method implies the absence of the influence of structural vibrations on the flow and can be used for relatively small displacements of the structure. The two-way calculation takes into account the feedback of the oscillations of the structure to the flow and can be used for substantial displacements of the structure. In particular, the two-way method is used to describe the lock-in mode with resonance of the structure natural frequency and the vortex shedding frequency (or in this case, its 4th harmonic).

Taking into account the complexity of FSI calculations, NRG and the other participants of the benchmark were provided with experimental data from an open test for the possibility to validate both one-way and two-way methods of vibration calculation. In addition, experimental data allow participants to take part only in the validation of a CFD solution, which affects the accuracy of the hydrodynamic force estimation. Participants were invited to independently determine the scope of validation: one-way calculation of vibration / two-way calculation of vibration / CFD calculation in the mode before the lock-in / CFD calculation in the lock-in mode. In the current study, the CFD calculation in the lock-in mode and two-way calculation of vibration are carried out.

During testing, dynamic parameters were measured correspondingly by different systems. The experimental data were registered as a function of time. The following measurements were performed:

- $v(t)$ – time oscillation of velocity pulsations
- $p(t)$ – time oscillation of pressure pulsations on the channel wall
- $a(t)$ – time oscillation of cylinders' vibration acceleration

Figure 5.4 shows the locations of the measurement points. A coordinate system is used where X-axis is directed along the channel, Y-axis is directed across the channel in the horizontal plane, and Z-axis is directed along the cylinders in the vertical plane. Given that the numerical model constraints the ends of the cylinders to the channel wall perfectly, the accelerometer readings of a_3^{xyz} and a_4^{xyz} (see Figure 5.4b) are not made use of. The Power Spectral Density (hereinafter - spectrum) of velocity and pressure pulsations, as well as vibration accelerations are later calculated based on the time series.
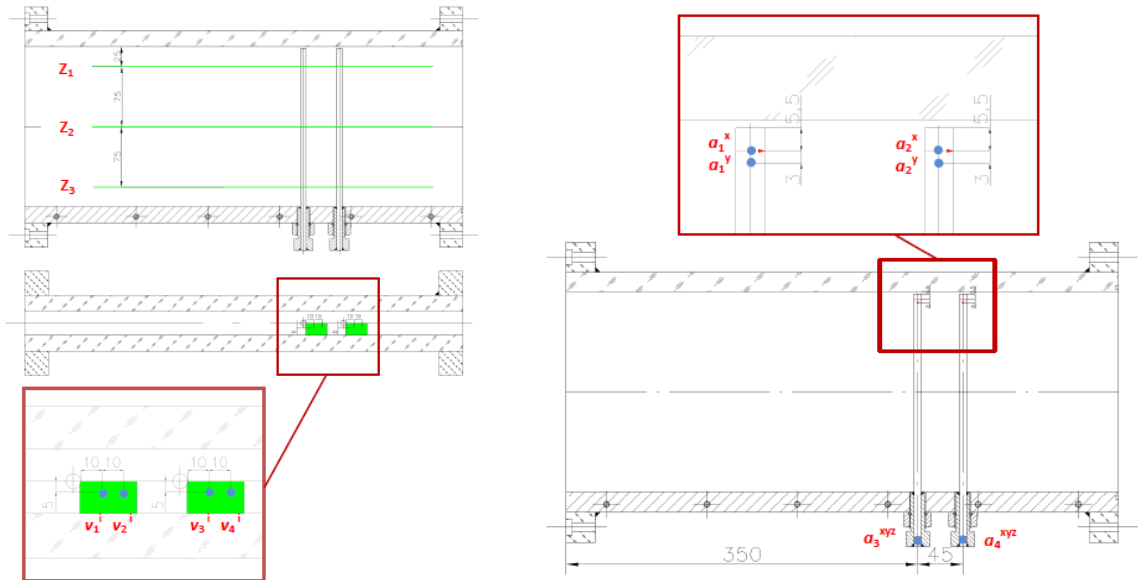
(a) Locations of Velocity Pulsations Measurements in the ith Plane

(b) Locations of Cylinders' Vibration Acceleration Measurement

(c) Locations of Pressure Pulsations Measurements

Figure 5.4: Location of Measurement Points for Different Parameters

Besides measurements at the above locations, horizontal velocity profile measurements were made 10 mm and 20 mm behind the cylinders as shown in Figure 5.5b. Furthermore, to aid in selecting inlet flow conditions, additional velocity profile measurements are made. These measurements are performed in the following sections and are shown in Figure 5.5:

- Average and Root Mean Squared (RMS) profile in the vertical plane of longitudinal velocity $V_x(z)$ in front of the 1st cylinder at a distance of 140 mm
- Average and RMS profile in four horizontal planes (40, 80, 120 and 160 mm) of longitudinal velocity $V_x(y)$ in front of the 1st cylinder at a distance of 200 mm
- Average and RMS profile in three horizontal planes (25, 100 and 175 mm) of longitudinal velocity $V_x(y)$ in front of the 1st cylinder at a distance of 50 mm

(a) Vertical Plane

(b) Horizontal Planes
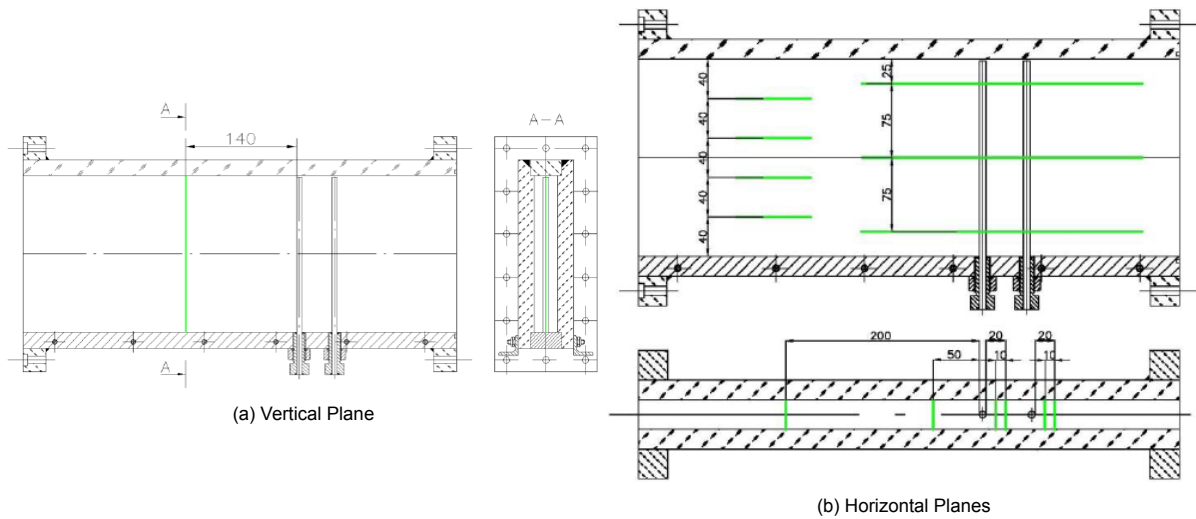
Figure 5.5: Locations of Velocity Profiles Measurement in the Vertical and Horizontal Planes

5.2. Numerical Setup

As mentioned earlier, based on the CAD drawings for the test section (and its contents) of the experimental setup, the simulation domain is set up in STAR-CCM+ and is shown in Figure 5.1b. The problem is set up in STAR-CCM+ as follows: For the incompressible fluid, the 'Implicit Unsteady' SIMPLE scheme 'Segregated Flow' solver is selected with a 2nd order upwind convection scheme. The pressure and velocity equations are given UR factors of 0.2 and 0.6 respectively. The four channel walls and the exposed cylinder surfaces are prescribed a no-slip boundary condition. A constant static pressure of 0 Pa is prescribed for the outlet. For the inlet, a constant uniform velocity of 0.74 m/s (as per a flow rate of 16 m^3/h) is used for the CFD study while a time-varying uniform velocity is prescribed for (numerical stability of) the FSI study as given by the equation:

$$u(0, y, z, t) = \begin{cases} u(0, y, z) \frac{1 - \cos\left(\frac{\pi}{T} t\right)}{2}, & \text{if } t < T \\ u(0, y, z), & \text{otherwise} \end{cases} \tag{5.2}$$

$$u(0, y, z) = 0.74 \, m/s, \quad T = 1.0 \, s$$

For the solid, the 'Solid Stress' solver is selected along with a 2nd order Newmark implicit integration scheme (Newmark parameter, γ=0.5). At this point, a choice is to be made between the infinitesimal strain and finite strain approximation. The expected displacements in both streamwise (x) and cross flow (y) directions are less than 1 mm which, relative to the 198 mm length of the cylinders, is less than 0.51% of the cylinder length. From the validation work of the current study, it seems suitable to go for the infinitesimal strain approximation given by the 'Linear Geometry' model. This is tested in subsection 5.2.2. For the boundary condition, the annular surfaces at the bottom of the cylinders are grounded while the outer wetted surfaces are declared as an FSI interface. Internally, the brass bobs are fixed in their relative positions using the 'bonded' boundary condition between the bob curved surface and the cylinder inner curved surface. For the FSI coupling, a UR factor of 0.5 is prescribed.

The fluid mesh is created using the 'Automatic Mesh' functionality of STAR-CCM+. For the fluid, a structured hexahedral mesh is created with three volume refinements. Approaching the cylinder from the inlet by crossing each refinement region reduces the target base size (bs) of 2.5 mm by half sequentially. To ensure good transition between the refinement regions, a growth rate of 1.1 is selected. Given a budget of 128 allocated cores, 2 months of physical time for this phase of the current study and past experience in CFD simulations, a maximum allowable number of fluid elements is capped at 8 million (M). To select a suitable mesh in this budget, a CFD study is carried out. Further details are provided in subsection 5.2.1.

For the experimental study, it was mentioned that the brass bobs were 12 mm in length including the solder. Furthermore, the cylinders had additional length that ran into the wall of the channel which was then fixed by a tightening nut arrangement. This and the fact that there was additional mass due to the soldering process and the accelerometer itself, there is a need to fine tune the structural model to have the same natural frequency as the experiment. This is done by altering the length of the bobs and is discussed further in subsection 5.2.2.

For the solid, unstructured meshes are set up for the cylinders and their internal bobs. The solid mesh for the cylinders is also created using the 'Automatic Mesh' functionality of STAR-CCM+. The 'Thin Mesher' and 'Tetrahedral Mesher' are selected with one thin layer, the 'Quad Dominant' meshing method and a target bs of 0.7 mm which, in this case, leads to a mesh with 68842 elements for each cylinder. For the bobs, the 'Directed Mesh' functionality is used which creates a given number of layers of the same planar or 'Patch Mesh'. For the 'Patch Mesh', the 'Automatic Mesh' functionality is selected along with the 'Quadrilateral Mesher'. The mesh is given 30 layers and a target bs of 0.35 mm which leads to 12030 elements for each one of the four bobs. Sectional views of the solid mesh are shown in Figure 5.6. For low computational effort, linear finite elements are employed by disabling the 'Mid-side Vertex' option.
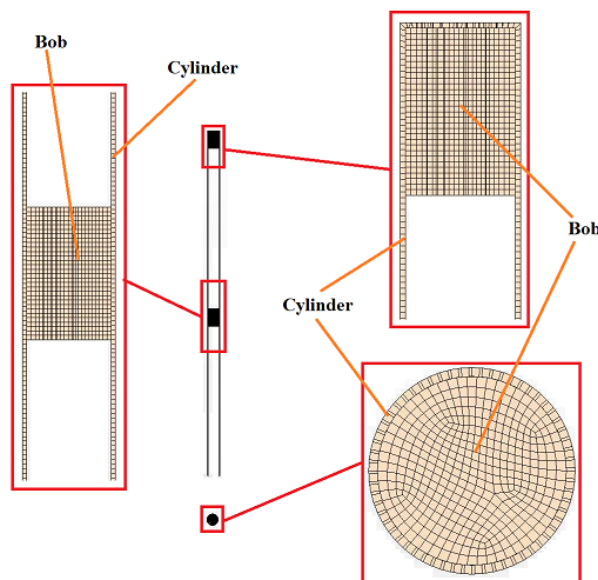
Figure 5.6: Sectional Views of the Structural Mesh

5.2.1. CFD Study

As mentioned earlier, given a budget of 8M fluid elements, a choice has to be made with regard to the 3 refinement regions labelled 'Refine1', 'Refine2' and 'Refine3' respectively. By making different choices, three different meshes labelled CFD1, CFD2 and CFD3 are set up with element counts of 4.89M, 5.44M and 7.05M respectively. Sectional views of these meshes are shown in Figure 5.7. For all the meshes, care is also taken to ensure a Y^+ value of 1 over all surfaces of the domain.

The basic setup of the simulation is as described earlier. Following those settings, the K-Omega SST: QCR turbulence model is selected for all test cases in this CFD study. Additionally, the curvature correction and the realizability options are enabled to reap the aforementioned benefits. As per the experimental results, the average vortex shedding frequency over the length of the cylinder is 25 Hz. Using this knowledge for the 100 sampling point thumb rule estimate of the time step gives a time step size of 0.4 ms. For the flow solver, 50 inner iterations per time step are provided. The simulation uses an initial condition of 0.74 m/s uniform velocity throughout the domain. To accommodate the transient phase and have sufficient usable data, a total simulation time of 4 s is given.
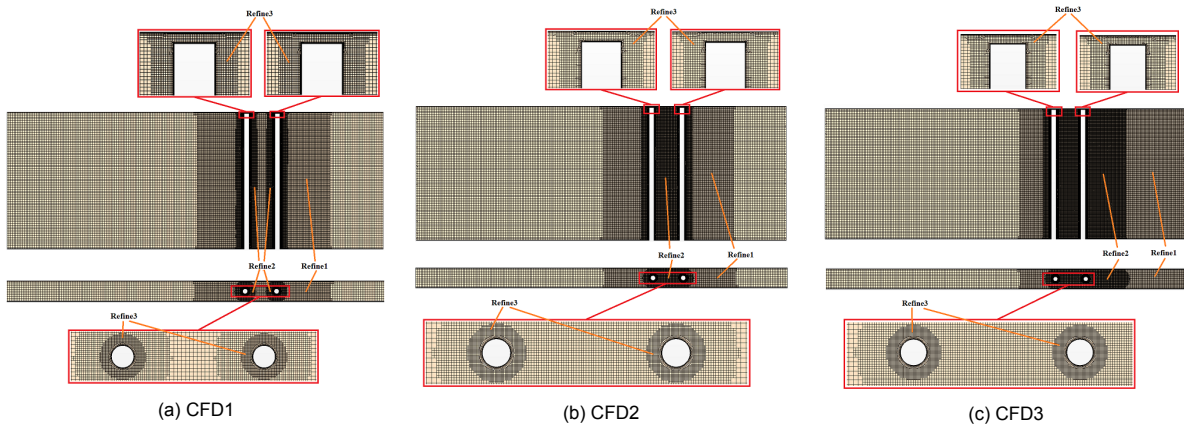
Figure 5.7: Proposed Fluid Meshes for Testing

An inlet turbulence is provided by prescribing a turbulence intensity of 2% and a turbulent length scale of $0.07D$ which floods in "turbulence" in the form of turbulent kinetic energy. However, given the relatively large length of channel before the cylinder, it was observed in the simulation that the turbulent kinetic energy was already dissipated before it reached the cylinder. Based on this observation, a higher value is motivated and prescribed for the FSI study as will be discussed in section 5.3.

Coming back to the aforementioned simulation time, the term 'flow passes', FP is mathematically defined here as

$$FP = \frac{U_\infty T}{L} \tag{5.3}$$

where $U_\infty = u(0, y, z)$ is the uniform inlet velocity, T is the simulation time and L=0.55 m is the length of the channel. One FP can thus be defined as the time needed for the fluid to travel from the inlet to the outlet assuming a constant velocity from the inlet. Here, this translates the total simulation time of 4 s to 5.387 FP. As mentioned earlier, all results in the experiment and the current numerical study are first obtained as a time series and then presented as a spectra plots by computing the Power Spectral Density (PSD). From the time series plots, using a back-windowing approach, it was found that the first flow pass showed transient results and is thus removed before calculating the spectra. To remedy the fact that the time series used for creating the spectra doesn't start and end with the mean of the signal, the Hann window is applied. The results so obtained are discussed below.

Obtained Results
The results of interest for the CFD study are the velocity and pressure spectra for the points as per Figure 5.4a and Figure 5.4c respectively. The pressure spectra plots for the different meshes are shown along with the FSI experimental results in Figure 5.8. To obtain clean spectra plots, linear averaging is applied with a window size of 30 and 4 for the experimental results and numerical results respectively. The experimental results show several peaks in the plots. These correspond to the vortex shedding frequency (f_s=24.4 Hz) and its multiples as well as the natural frequencies of the cylinders (f_{n1}=98 Hz and f_{n2}=90 Hz) and its multiples. Additional peaks labelled by f^* and its multiples are linked with the frequency of the pump. It is observed that the largest peak corresponds to the natural frequency of Cylinder1 which coincides with the 4th harmonic of the vortex shedding frequency. Furthermore, this also coincides with the 3rd harmonic of pump frequency. This is not good as the synergy with the pump would lead to an overestimated PSD for f_{n1}, something that would not be expected from an ideal inlet used in the simulation.

In this CFD study, however, the concern here is to correctly capture the vortex shedding frequency and its multiples as the natural frequency only comes to play for the FSI study. In that regard, the pressure spectra plots do not reveal a clear superior mesh given the near identical predictions. From Figure 5.8, it is observed that the CFD results predict an overestimated vortex shedding frequency of 27 Hz as compared to the ~24.4 Hz captured by the experiment. In particular, the predicted 4th harmonic of the predicted frequency is 10 Hz higher than the natural frequency of Cylinder1. This means that already for the FSI results with this turbulence model, capturing resonance seems unlikely.
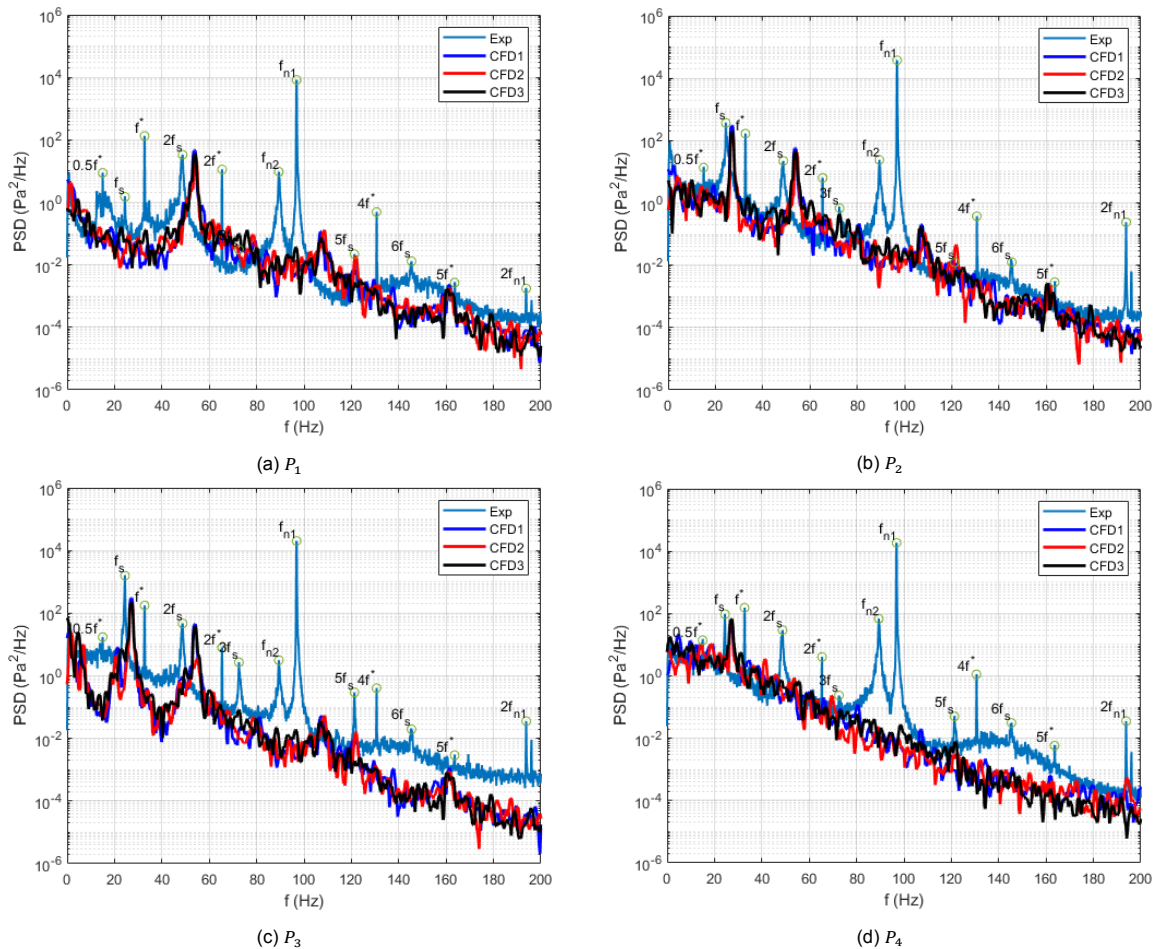
Figure 5.8: Pressure Spectra Plots

The overall trend of decreasing spectral density with increasing frequency is captured well by the CFD results. However, not all peaks are clearly identified. For P_1, which lies upstream of Cylinder1, only the even harmonics of f_s are distinct. For P_2 and P_3, which lie in between the cylinders, only the first harmonic and even harmonics of f_s are distinct. For P_4, which lies downstream of Cylinder2, only the first harmonic of f_s is distinct. These observations imply easier propagation of the frequency pertinent to the streamwise direction (even harmonics) than it is for the cross flow (odd harmonics) and that the first harmonic is more easily captured downstream of the source (the cylinders) rather than upstream.

The velocity spectra plots for the different meshes are shown along with the FSI experimental results in Figure 5.9 through Figure 5.11. The spectra, in principle, captures the turbulence present in the flow from the inlet (relevant for all planes) as well as that generated at the channel walls (relevant for planes Z_1 and Z_3), the cylinder curved surface (relevant for all planes) and the 2 mm gap at the free end of the cylinder (relevant for plane Z_1). To obtain clean spectra plots, linear averaging is applied with a window size of 30, 5 and 3 for the LDV and PIV experimental results and numerical results respectively. The experimental results show peaks for vortex shedding frequency and different harmonics. Not all peaks are distinct with some expected peaks being at the same level as the background spectra.

Similar trends are also seen for the CFD results with the spectra towards higher frequencies ($> 100\,Hz$) showing underpredicted results especially for plane Z_1 as can be seen in Figure 5.9. This is expected since higher frequencies imply smaller time scales and thereby smaller turbulent structures which cannot be accurately resolved with the current choice of time step, meshes and the URANS scheme. However, even with such a choice of time step, it is seen from Figure 5.9 that the CFD3 mesh has the least underprediction at higher frequencies at plane Z_1. This is also a critical zone given the influence of the turbulence generated at the free end of the cylinder in the 2 mm gap between the channel wall.

(a) V_1^1: x-direction

(b) V_1^1: y-direction

(c) V_2^1: x-direction

(d) V_2^1: y-direction

(e) V_3^1: x-direction

(f) V_3^1: y-direction

(g) V_4^1: x-direction

(h) V_4^1: y-direction
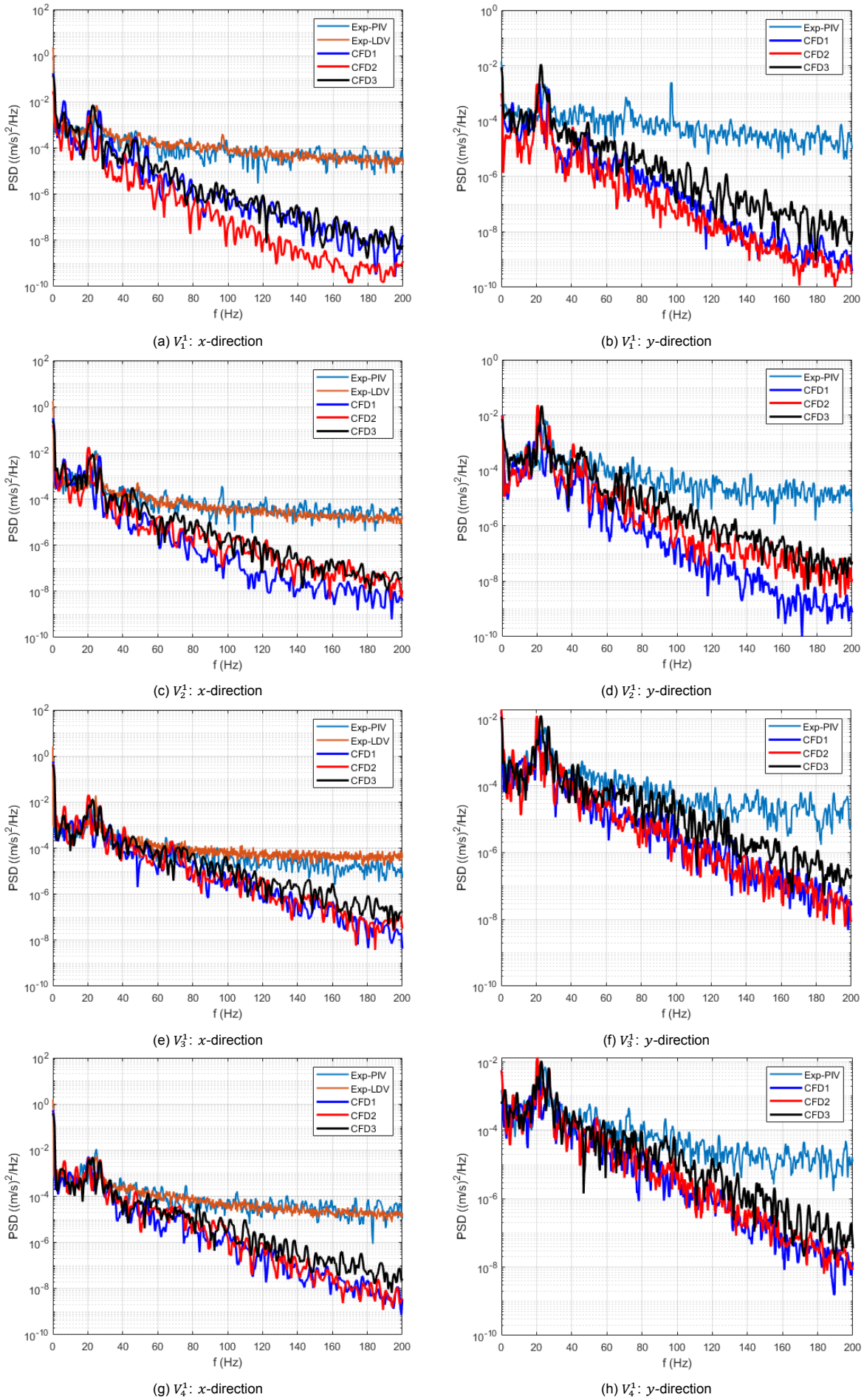
Figure 5.9: Velocity Spectra Plots: V_i^1, ($i = 1, 2, 3$)

(a) V_1^2: x-direction

(b) V_1^2: y-direction

(c) V_2^2: x-direction

(d) V_2^2: y-direction

(e) V_3^2: x-direction

(f) V_3^2: y-direction

(g) V_4^2: x-direction

(h) V_4^2: y-direction
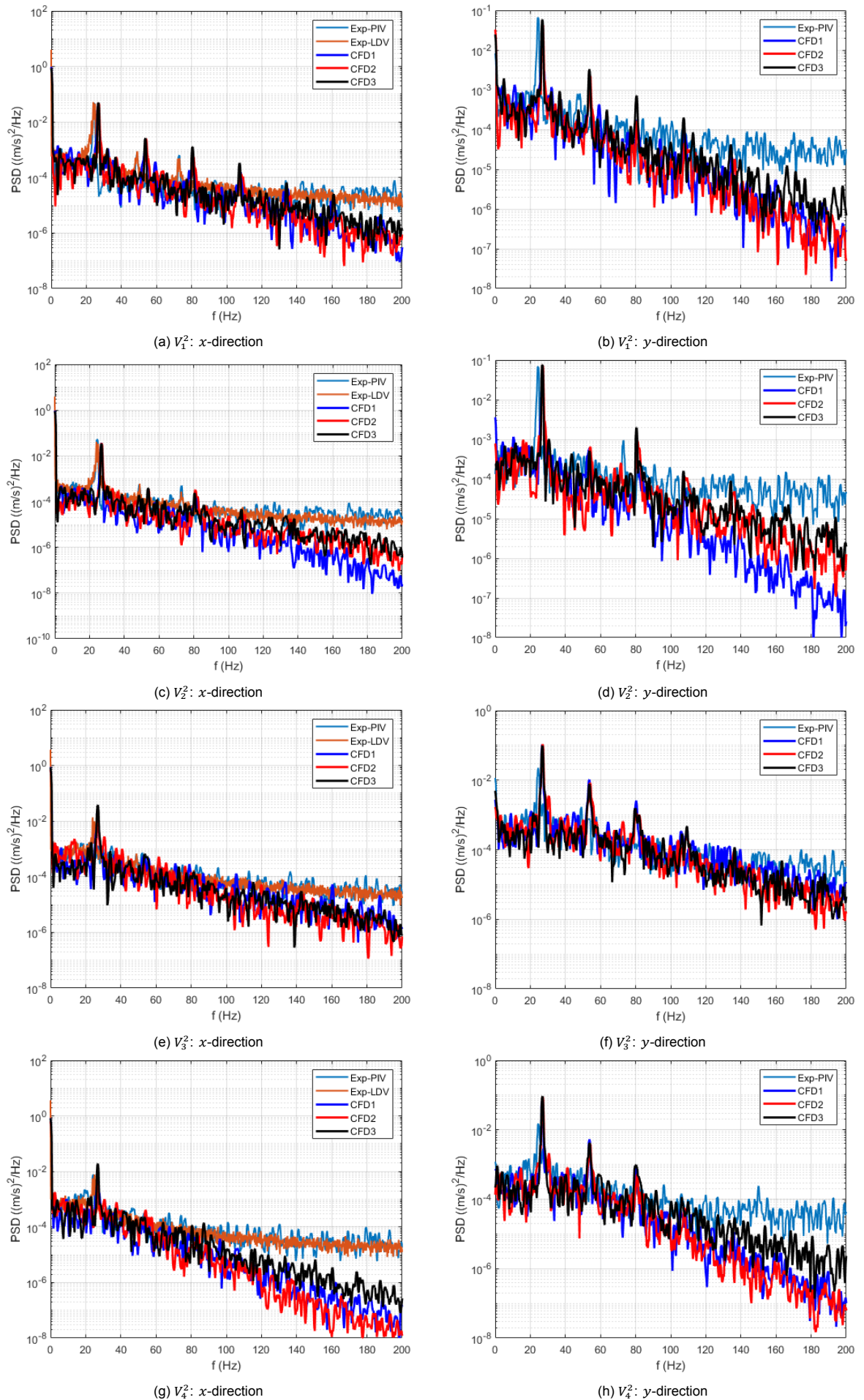
Figure 5.10: Velocity Spectra Plots: V_i^2, $(i = 1, 2, 3)$

(a) V_1^3: x-direction

(b) V_1^3: y-direction

(c) V_2^3: x-direction

(d) V_2^3: y-direction

(e) V_3^3: x-direction

(f) V_3^3: y-direction

(g) V_4^3: x-direction

(h) V_4^3: y-direction
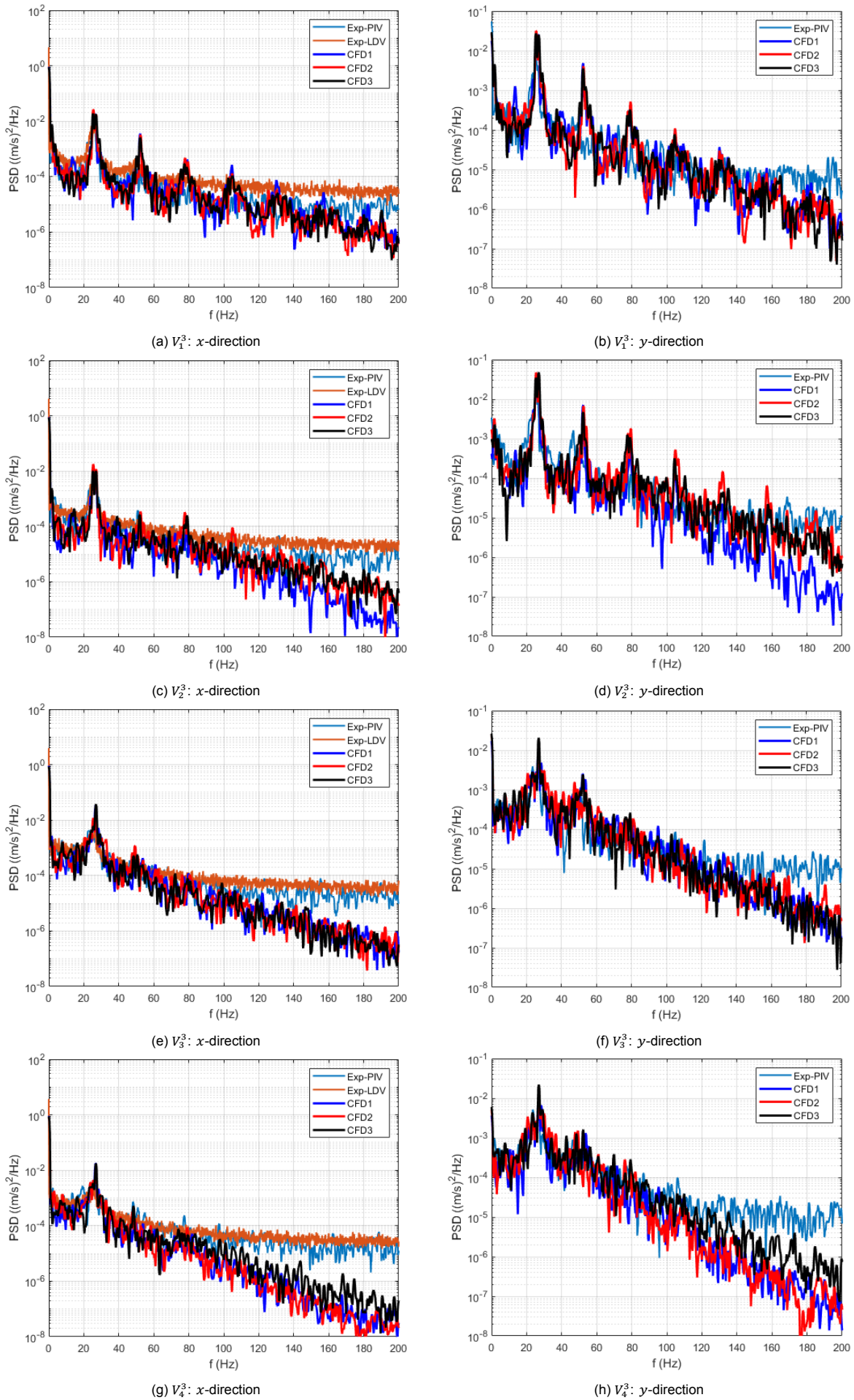
Figure 5.11: Velocity Spectra Plots: V_i^3, ($i = 1, 2, 3$)

A general observation from the trends is that the peaks are more distinct 10 mm behind the cylinders (V_1^i and V_3^i) rather than 20 mm behind the cylinders (V_2^i and V_4^i). Another observation is that the peaks are more distinct for V_1^i as compared to V_3^i. These observations are linked to the turbulent dissipation as the vortical structures travel downstream as well as the fact that with respect to Cylinder2, there exists a source of turbulence (Cylinder1) upstream which interacts with the cylinder and its generated wake to redistribute peak energies to smaller scales where they eventually get dissipated as it travels downstream. This is hinted by the vorticity plots (overlayed with the CFD meshes) created at plane Z_2 as shown in Figure 5.12.
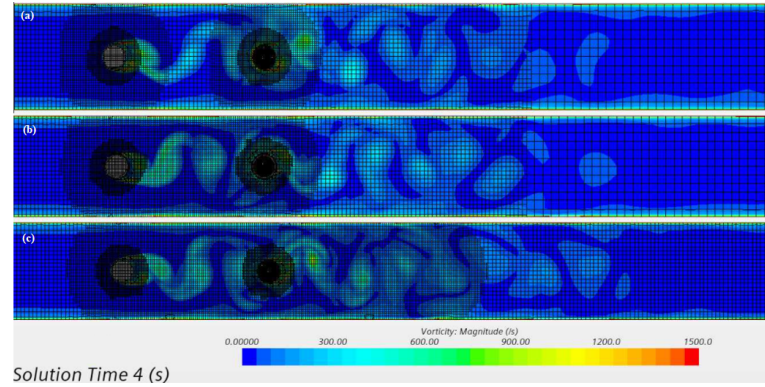
Figure 5.12: Vorticity Plots for (a) CFD1, (b) CFD2 and (c) CFD3 Test Cases

The above plot shows that the vortical structures are more well defined in the wake for the CFD3 mesh, which is expected given the longer Refine1 and Refine2 regions. The vortical structures appear to diffuse as they pass from a fine to coarse region as the vorticity is recomputed with new (and less accurate) approximations to the derivatives of the velocity for the coarse region. However, this is tolerable as it occurs more than $10D$ downstream of Cylinder2 where the strength of the wake is small.

Another observation is the mismatch in predictions of the vortex shedding frequency by the CFD results and the experimental results. It is also observed that the vortex shedding frequency captured by the experiment as well as the CFD results vary along the length of the cylinders. In particular, the prediction by V_1^i and V_3^i were found to be the same as V_2^i and V_4^i respectively. The experimental as well as CFD predictions for f_s are tabulated in Table 5.2 for V_1^i and V_3^i. It is observed that the CFD results slightly overpredict the vortex shedding frequency at planes Z_2 and Z_3 while it underpredicts at plane Z_1.

Table 5.2: Vortex Shedding Frequency Predictions by the Experiment and CFD Test Cases

	f_s at V_1^1 (Hz)			f_s at V_1^2 (Hz)			f_s at V_1^3 (Hz)		
---	Exp.	CFD1	CFD2	CFD3	Exp.	CFD1	CFD2	CFD3	Exp.	CFD1	CFD2	CFD3
x	25.1	20.5	20.5	23.0	24.3	26.7	27.0	27.0	25.1	25.3	25.3	25.3
y	24.7	21.4	20.4	22.5	24.3	26.7	27.0	27.0	25.1	25.3	25.3	25.3
	f_s at V_3^1 (Hz)			f_s at V_3^2 (Hz)			f_s at V_3^3 (Hz)		
	Exp.	CFD1	CFD2	CFD3	Exp.	CFD1	CFD2	CFD3	Exp.	CFD1	CFD2	CFD3
x	24.6	20.5	20.5	22.5	24.7	26.7	27.0	27.0	26.6	26.7	27.0	27.0
y	24.9	21.4	20.4	22.5	24.5	26.7	27.0	27.0	26.8	26.7	27.0	27.0

Near identical predictions are seen for all CFD test cases at plane Z_2 for both V_1^2 and V_3^2 which is about 10.2% higher than the experimental results. Near identical predictions are also seen for plane Z_3 with a good match with the experimental results with only about 0.8% and 1.1% error for V_1^3 and V_3^3 respectively. A clear difference between the CFD predictions is seen at plane Z_1. The results are underpredicted with the least error offered by the CFD3 test case.

Considering all the qualitative and quantitative results discussed so far, the choice is made to use the CFD3 mesh for the FSI study. The next item for discussion is the fine tuning of the structural model.

5.2.2. CSM Study

As mentioned earlier, the cylinders in the experiment are slightly longer with the extra length running into the channel wall where they are constrained by a tightening nut. The schematic of the same is shown in Figure 5.13. Furthermore, the brass accelerometer mountings were mentioned to be 12 mm in length including the solder which is lesser in density compared to brass. This and the fact that there is no accelerometer equipment (which has its own mass) in the numerical setup calls for fine tuning the structural model.
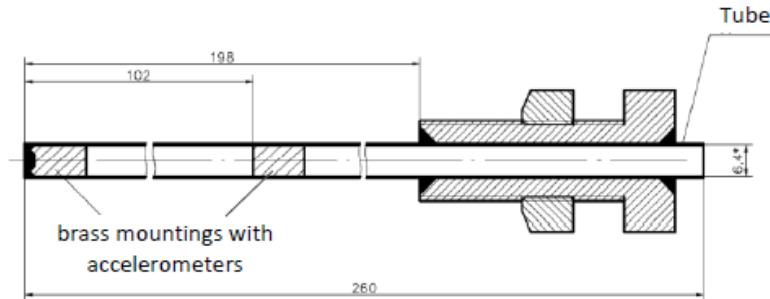
Figure 5.13: Schematic of the Cylinder used in the Experiment

In the current numerical setup, the brass mountings, the solder and the accelerometer mass is to be represented by the brass bobs alone. The fine tuning is thus aimed by modifying the bob lengths. Testing is carried out both in vacuum and in water. The results of interest are the natural frequencies in vacuum and water and the added damping for the test in water. No additional damping is made use of for these tests.

The tests are carried out as follows: For both the tests in vacuum and in water, a numerical gravity of $5g$ is applied to the cantilevered cylinders in the y-direction which would result in tip displacements comparable in magnitude to the FSI test. When the cylinders come to the position of maximum tip displacement, the gravity is switched off and free oscillations of the cylinders are captured. To calculate the natural frequencies, the time interval between successive oscillations is used. As for the damping in water, the following expression is used:

$$\zeta = \frac{1}{\sqrt{1 + \left(\frac{2\pi}{\delta}\right)^2}} \tag{5.4}$$

where δ is the logarithmic decrement of the structural response (tip displacement) in water.

In STAR-CCM+, the 'Solid Stress' solver is selected along with a 2nd order Newmark implicit integration scheme (Newmark parameter, γ=0.5). A time step satisfying the 100 sampling point rule is selected based on the natural frequency of Cylinder1 in air (107 Hz) for the vacuum tests (Δt=0.09 ms) and based on the natural frequency of Cylinder1 in water (98 Hz) for the water tests (Δt=0.1 ms). For the test in water, the fluid domain consists of still water in the channel which is obtained by setting the inlet velocity to 0 m/s. For the fluid, the 'Implicit Unsteady' SIMPLE scheme 'Segregated Flow' solver is selected with a 2nd order upwind convection scheme. The pressure and velocity equations are given UR factors of 0.2 and 0.6 respectively. For the FSI coupling, a UR factor of 0.5 is used.

Before moving on to the tests with different bob lengths, two additional tests are carried out. Earlier, it was asserted that the infinitesimal strain approximation is expected to work well for the FSI study given the low amplitude oscillations of the structure. The first additional test thus verifies this assertion by carrying out a vibration test of Cylinder1 in vacuum using the 'Nonlinear Geometry' and 'Linear Geometry' models in STAR-CCM+. For the vibration tests in water, the Reynolds number is expected to be less than 200 making it possible to use the cheaper 'Laminar Flow' model rather than a URANS turbulence model. The second additional test thus compares the results of the vibration study of the cylinders in water using the 'Laminar Flow' model and the 'K-Omega SST: QCR' turbulence model. For both the additional tests, the bobs have a length of 12 mm.

Obtained Results

The time series of the tip displacement of Cylinder1 for the first additional vacuum test comparing the 'Linear Geometry' and 'Nonlinear Geometry' models are shown in Figure 5.14. The time history for the primary motion of interest in the y-direction reveals overlapping responses for the two models as can be seen in Figure 5.14a. Both models predict exactly the same natural frequency of 104.27 Hz which translates to an error of 2.55%. Improvements in prediction are expected with change in bob lengths. The difference in the models comes in the prediction of the time history of the motion in the z-direction. The 'Linear Geometry' model predicts zero displacements with round-off errors of the order of machine precision while the 'Nonlinear Geometry' model correctly predicts non-zero displacements at double frequency. However, the z-displacement is observed to be 3 orders of magnitude lower than the y-displacement as is also expected for the experimental FSI test. The z-direction acceleration is also not measured for the experimental FSI test. Based on this fact and the obtained results, the computationally cheaper 'Linear Geometry' model is made use of herewith for all following tests.

(a) Y-displacement Time History   (b) Z-displacement Time History
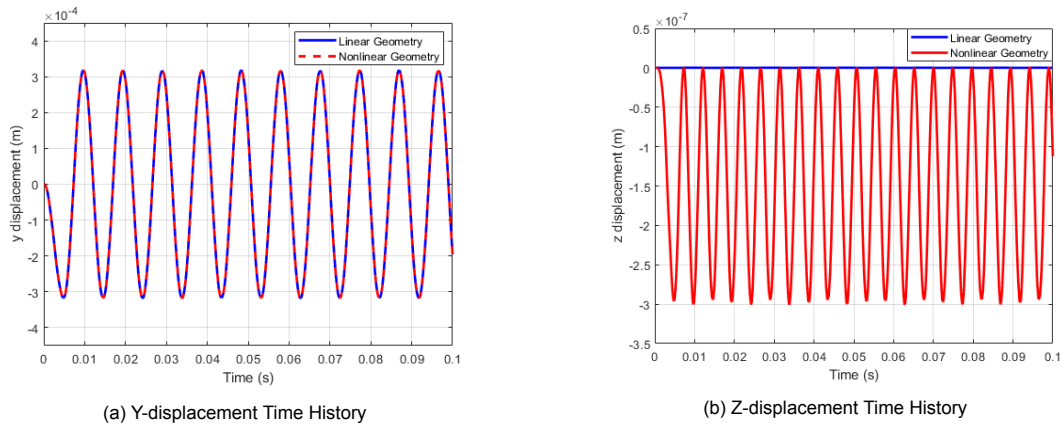
Figure 5.14: Time History Plots for the Tip Displacement of Cylinder1 in Vacuum

With the chosen 'Linear Geometry' model, the second additional test in water is carried out to compare the 'Laminar Flow' model and 'K-Omega SST: QCR' model. The time series of the tip displacements of both cylinders are shown in Figure 5.15. Both solutions show near overlapping results with the same prediction of natural frequency for Cylinder1 and Cylinder2 as 90.09 Hz and 84.03 Hz which translates to errors of 8.07% and 6.63% respectively. There is, however, a small difference in prediction of the damping ratio (ζ). For Cylinder1, the 'Laminar Flow' and 'K-Omega SST: QCR' models predict a damping ratio of 0.00564 and 0.00555 respectively, while for Cylinder2, the corresponding predictions are 0.00438 and 0.00441 respectively which are all considerably lower than the damping ratio of 0.008 in the experimental FSI test. This is later remedied after conducting the vibration study for the different bob lengths. Thus, given the near matching predictions with only minor differences in the damping, the 'Laminar Flow' model is made use of for the vibration tests in water for different bob lengths.

(a) Cylinder1   (b) Cylinder2
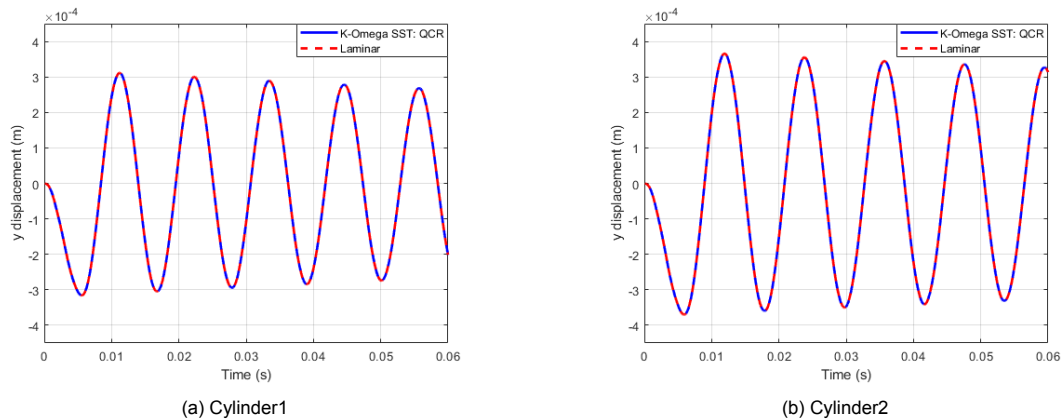
Figure 5.15: Y-displacement Time History Plots for the Tip Displacement of Cylinder1 and Cylinder2 in Water

With the preliminary tests complete, the focus is brought to the vibration tests in vacuum and in water for cylinders housing bobs of different lengths. As hinted for the results with a bob length of 12 mm, in order to improve the structural response, the bob length has to be reduced. The tests are carried out for bob lengths 12 mm, 11 mm, 10.5 mm and 10 mm. The predictions for the natural frequency of the cylinders in vacuum are tabulated in Table 5.3. Based on the tests in vacuum, a bob length of 11 mm appears to be the best choice with relative errors in natural frequency at 0.047% and 0.041% for Cylinder1 and Cylinder2 respectively.

Table 5.3: Results for Vibration Tests in Vacuum

Bob Length (mm)	Natural Frequency (Hz)	
	Cylinder1	Cylinder2
12.0	104.28	96.06
11.0	106.95	98.04
10.5	107.82	99.50
10.0	108.69	100.33
Exp. Soln.	107.00	98.00

The vibration tests are also conducted in water using the 'Laminar Flow' model. The results for the natural frequencies and the damping ratio are tabulated in Table 5.4 based on the time series shown in Figure 5.16. Based on these results, a bob length of 10 mm appears to be the best choice with regard to the natural frequency with relative errors of 1.4% and 0.1% for Cylinder1 and Cylinder2 respectively.

Table 5.4: Results for Vibration Tests in Water

Bob Length (mm)	Natural Frequency (Hz)		Damping Ratio	
	Cylinder1	Cylinder2	Cylinder1	Cylinder2
12.0	90.09	84.33	0.0056	0.0041
11.0	94.34	88.49	0.0064	0.0048
10.5	95.69	88.88	0.0065	0.0048
10.0	96.62	90.09	0.0065	0.0049
Exp. Soln.	98.00	90.00	0.0080	0.0080

(a) Cylinder1   (b) Cylinder2
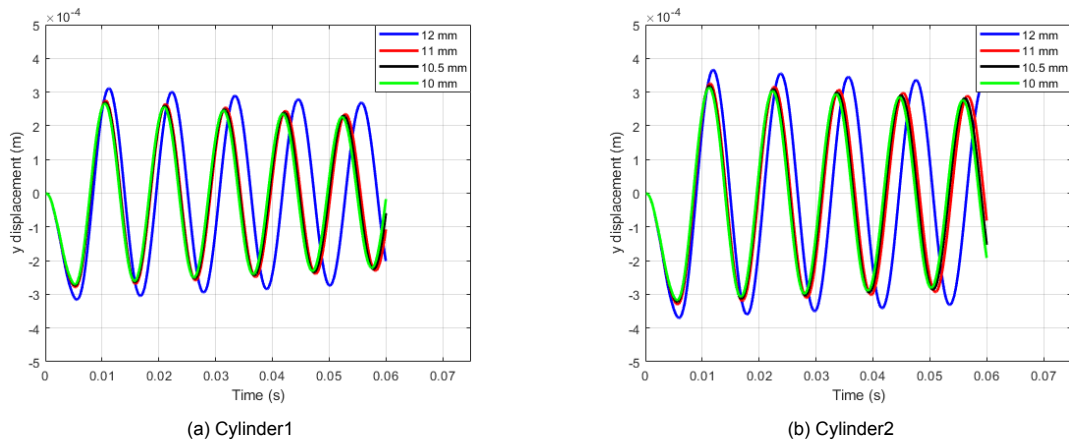
Figure 5.16: Y-displacement Time History Plots for the Tip Displacement of Cylinder1 and Cylinder2 in Water with Different Bob Lengths

The mismatch in the optimal bob length arises mainly from the overestimation of the added mass in the vibration tests in water. To calculate the added mass, STAR-CCM+ uses the volume of displaced fluid per unit area. This parameter is left to be auto-calculated rather than feeding a manual input. To accommodate such an overestimation even for the FSI test that follows this section, the final choice is made to go ahead with a bob length of 10 mm. For this selection of bob length, the mass ratio of the structures come out to m^*=2.097 and 2.350 for Cylinder1 and Cylinder2 respectively.

The last item for the FSI setup is the mismatch in structural damping. There appears to be a significant gap in the prediction of the damping ratio in the above vibration test in water even for the optimal bob length of 10 mm. This is remedied by adding structural damping via the aforementioned 'Rayleigh Damping' model. The difference between the damping calculated here and the expected value is used for calculating the stiffness constant as per Equation 3.31. With this, all relevant parameters for the FSI study are finalized and the results obtained for the same are discussed in the following section.

5.3. FSI Study

With the selected CFD3 mesh and the fine tuned structural model, the FSI test is attempted for the peak resonance case of 0.74 m/s inflow using the shortlisted turbulence models. To keep the FSI coupling stable during the start up of the simulation, a cosine ramping of the inflow velocity is given for 1 s (1.347 FP) as per Equation 5.2. A total simulation time of 7 s (9.428 FP) is provided. From the CFD study, it was observed that the numerical prediction of the vortex shedding frequency came out to be 27 Hz. To adhere to the 100 sampling point thumb rule, a time step of 0.4 ms is used during the cosine ramping and is reduced to 0.36 ms for the remainder of the simulation. Using the back-windowing approach on the created spectra plots, it was found that transient results lasted roughly a flow pass after the end of the cosine ramping period. Thus, only the results from 1.75 s to 7 s, or the last 7.071 FP, are used for creating the spectra. Before presenting the main results, the issue of inflow turbulence is addressed.

5.3.1. Inflow Turbulence

As mentioned in subsection 5.2.1, when using an inflow turbulence intensity of 2%, it was observed that the turbulent kinetic energy was quickly dissipated well before it made it to the cylinders. The choice of 2% came from the mean and RMS fluctuation velocity profiles of the streamwise component 140 mm ahead of Cylinder1. Based on the experimental data shown in Figure 5.17, a turbulence intensity of 4.95% was predicted by the PIV measurements while a value of 1.71% was predicted by LDV. Trusting the value predicted by LDV, the aim is to obtain good agreements with the LDV results at this location. To do so, the ratio of turbulent kinetic energy at the inlet to that at this location was estimated from the CFD study. Assuming similar dissipation for the FSI study for all 3 tested turbulence models and the following relation between turbulent kinetic energy and turbulence intensity, a value of 5% was selected for the inlet:

$$k = \frac{3}{2}(U_x I)^2 \tag{5.5}$$

where k is the turbulent kinetic energy, U_x is the flow velocity at the location of interest and I is the turbulence intensity at the location of interest. Based on this choice of turbulence intensity, the results so obtained by the turbulence models are also plotted in Figure 5.17. For the mean velocity shown in Figure 5.17a, the simulation results are near overlapping with good agreement (within 5%) with the PIV profile for a large part of the profile away from the walls. The PIV measurements near the walls possibly suffer from laser reflections. The simulation results match well with those of LDV near the walls.

(a) Mean Velocity   (b) RMS Velocity Fluctuation
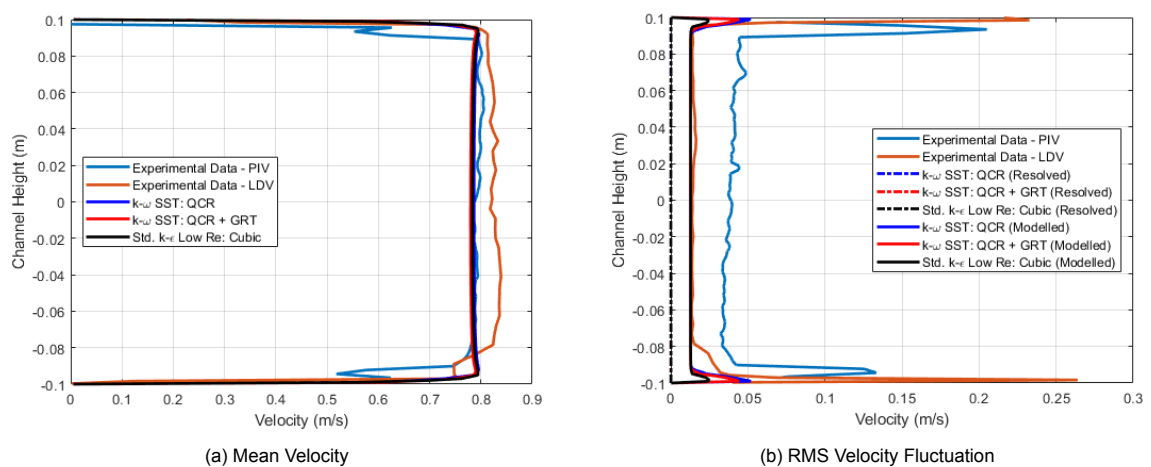
Figure 5.17: Mean and RMS Fluctuation Streamwise Velocity Profiles at a Vertical Section 140 mm ahead of Cylinder1

For the RMS fluctuations shown in Figure 5.17b, the simulation results are presented as a quantity resolved by the mesh which captures actual velocity fluctuations and as a quantity modelled through the turbulent kinetic energy as per Equation 5.5. Since there are no real turbulent structures introduced at the inlet and the distance from Cylinder1 is rather large, the resolved fluctuations are quite small, ranging from 1.2E-5 m/s at the channel center to 1E-4 m/s in the boundary layer of the channel walls. The modelled fluctuations, however, are of the same order of magnitude of the experimental data with a better match (within 10%) with the LDV results as intended. While the three models agree well with each other over the majority of the domain, a difference is noted at the peaks near the channel walls.

As per Figure 5.5, velocity profiles are also available at horizontal sections 50 mm and 200 mm ahead of Cylinder1. These are shown in Figure 5.18 and Figure 5.19 respectively.

(a) Mean Velocity at Plane Z_1

(b) RMS Velocity Fluctuation at Plane Z_1

(c) Mean Velocity at Plane Z_2

(d) RMS Velocity Fluctuation at Plane Z_2

(e) Mean Velocity at Plane Z_3

(f) RMS Velocity Fluctuation at Plane Z_3
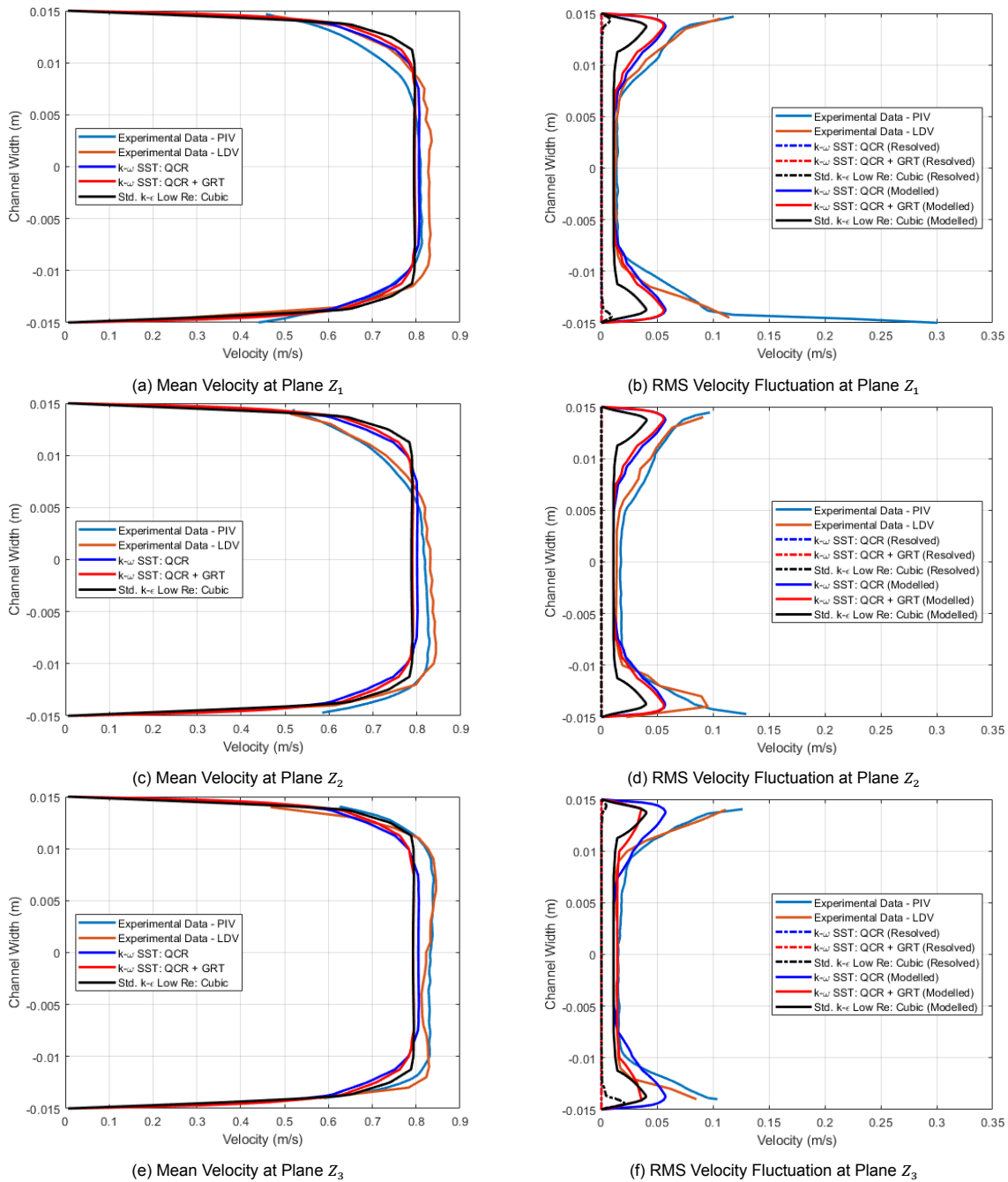
Figure 5.18: Mean and RMS Fluctuation Streamwise Velocity Profiles at a Horizontal Section 50 mm ahead of Cylinder1

(a) Mean Velocity at Plane Z_1

(b) RMS Velocity Fluctuation at Plane Z_1

(c) Mean Velocity at Plane Z_2

(d) RMS Velocity Fluctuation at Plane Z_2

(e) Mean Velocity at Plane Z_3

(f) RMS Velocity Fluctuation at Plane Z_3

(g) Mean Velocity at Plane Z_4

(h) RMS Velocity Fluctuation at Plane Z_4
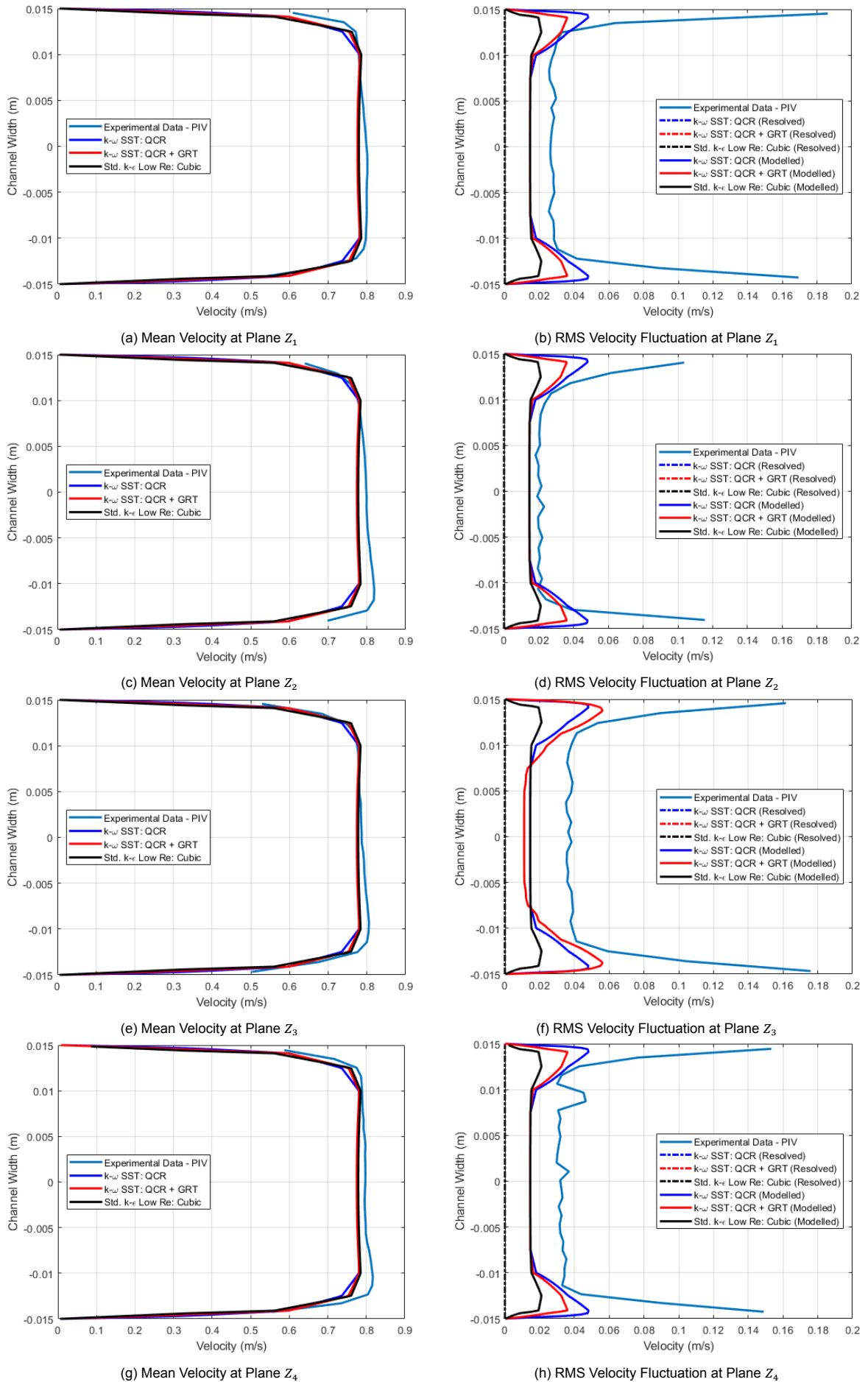
Figure 5.19: Mean and RMS Fluctuation Streamwise Velocity Profiles at Horizontal Sections 200 mm ahead of Cylinder1

Observing the mean velocity profiles of Figure 5.19 at different planes reveals near overlapping results for different turbulence models and good agreement (within 3% at the channel width center) between the simulation and the PIV results at horizontal sections 200 mm ahead of Cylinder1. This is expected given the very low influence of Cylinder1 at this distance. Although the numerical results show the same symmetric profile for all 4 planes, the PIV results show mildly varying (within 2% at the channel width center) and asymmetric profiles at different planes of measurement with the largest deviation at plane Z_2. One possible reason could be the asymmetry of the inflow turbulence at this plane. This reason stems from the corresponding asymmetry of the fluctuation profile in Figure 5.19d.

As for the RMS fluctuations, the observations for the resolved fluctuations are similar to the vertical section velocity profile with very low fluctuations detected as per expectations. The observations are also similar for the modelled fluctuations with agreement towards the center of the channel width and disagreement in the fluctuations of the channel wall boundary layer. These profiles also do not show significant difference (within 1% at the channel width center) across different planes. An exception, however, is observed with the curve for the K-Omega SST: QCR + GRT model at plane Z_3 which shows slight disagreement even at the center of the channel.

Coming closer to Cylinder1, at a distance of 50 mm, observing the mean profiles of Figure 5.18, the experimental results again show mildly varying (within 1% at the channel width center) and asymmetric profiles at different planes of measurement with the largest deviation at plane Z_2. The boundary layer at the channel wall also appears to have grown from what it was at a distance of 200 mm, as the velocity profile has become more parabolic in nature. The profiles for the K-Omega SST models show slightly more curvature with a more bulged channel center velocity than the K-Epsilon model. Correspondingly, for the RMS fluctuations, the modelled fluctuations also show a lesser range of agreement between the profiles of K-Omega SST models and that of the K-Epsilon model. Regardless, the overall match of the fluctuation profiles between the experimental and the modelled numerical predictions is still considered good (within 10% at the channel width center).

Based on the results discussed so far, the setting for the inlet turbulence is validated. The following section reveals the primary results of this study which are the pressure, acceleration and velocity spectra followed by the secondary results which include the vorticity plots and the velocity profiles aft of the cylinders.

5.3.2. Obtained Results

The primary results of interest for the FSI study are the velocity, acceleration and pressure spectra for the points as per Figure 5.4. The pressure spectra plots for the different turbulence models are shown along with the experimental results in Figure 5.20. As was done in the CFD study, to obtain clean spectra plots, linear averaging is applied with a window size of 30 and 5 for the experimental results and numerical results respectively. The experimental results show several peaks in the plots which have been discussed in subsection 5.2.1. The numerical predictions differ appreciably based on the turbulence model selected.

In general, the same peaks that were captured by the K-Omega SST: QCR model in the CFD study are also captured here with the addition of a peak corresponding to the natural frequency of Cylinder2 (f_{n2}) predicted at 88 Hz. Surprisingly, the peak corresponding to the natural frequency of Cylinder1 is not distinctly captured. As mentioned earlier, the pump frequency (f^*) has its third harmonic coinciding with the natural frequency of Cylinder1 (f_{n1}) and the fourth harmonic of the vortex shedding frequency (f_s), thereby corrupting the estimate of the spectral density at this frequency.

Although this accounts for part of the gap in expectations, the main reason is suspected to be the fact that there is a mismatch in the predicted fourth harmonic of the vortex shedding frequency and the natural frequency of Cylinder1 which is needed for resonance. The values for f_s predicted by the turbulence models are 27.04 Hz, 27.43 Hz and 27.81 Hz respectively, in the order as they appear in the plots, which translate to significant errors of 10.81%, 12.42% and 13.98% respectively.

(a) P_1

(b) P_2

(c) P_3

(d) P_4
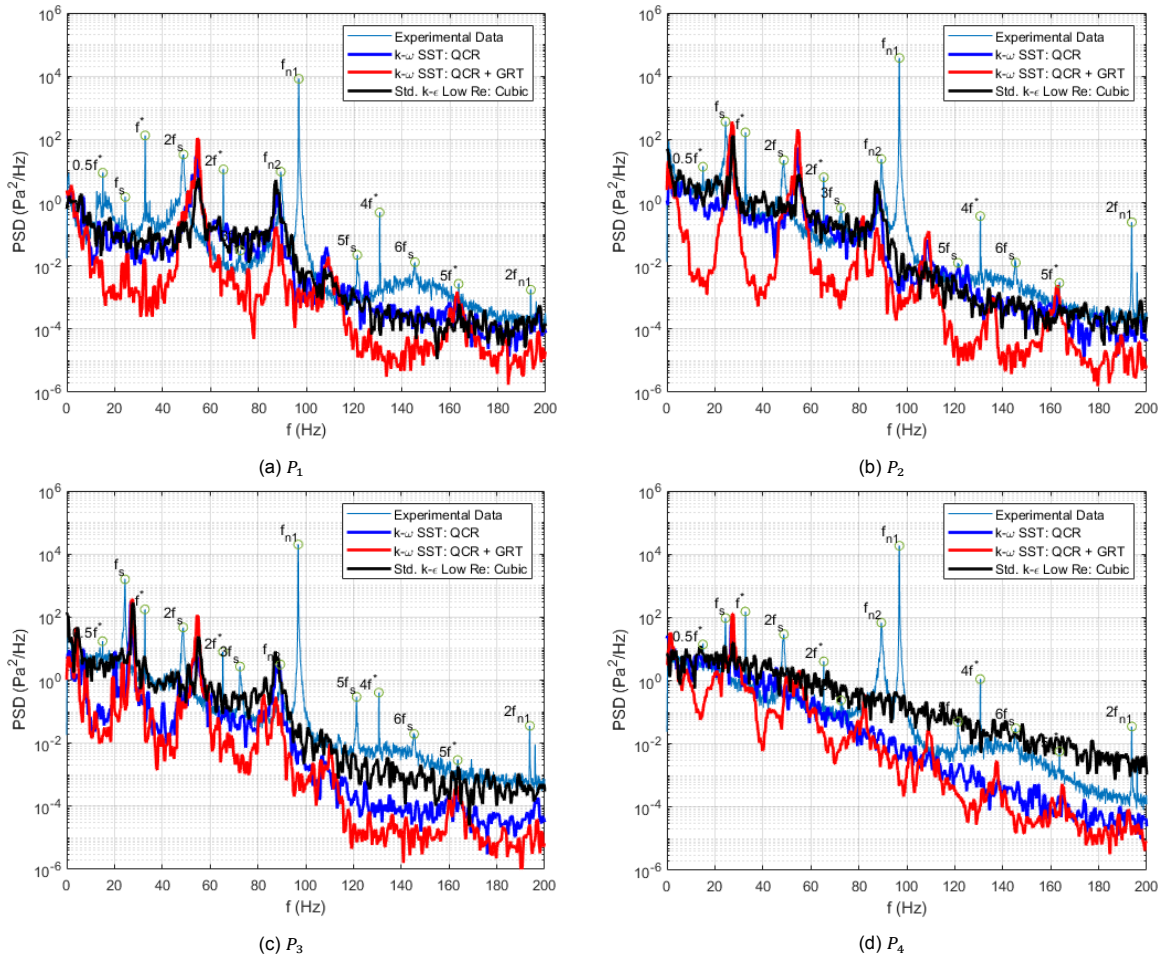
Figure 5.20: Pressure Spectra Plots

The second reason is the fact that the problem at hand is that of vibrations that are partly Vortex-Induced and partly Turbulence-Induced. Even if resonance is not captured, the presence of physical turbulence upstream of Cylinder1 would have caused a peak similar in magnitude to that of Cylinder2 which faces turbulence generated by Cylinder1. The fact that this is absent in the numerical simulation has led to a prediction of spectral density at f_{n1} at the level of the background spectra of frequencies.

Coming to the turbulence models, it is observed that the spectral densities at the peaks are similar for the two K-Omega SST models. However, it is observed that the background spectra for the other frequencies are severely underpredicted for the K-Omega SST: QCR + GRT model although it helps identifying the peaks easily. As for the Standard K-Epsilon Low Re: Cubic model, the spectra obtained for P_1 and P_2 matches closely with the K-Omega SST: QCR model. For P_3 and P_4, however, the spectra predicted by the Standard K-Epsilon Low Re: Cubic model has a higher spectral density background spectra which makes it a better fit for P_3 in the higher frequency range while it leads to an overprediction for P_4. In fact for P_4, no expected peak is clearly distinct from the background spectra for this model. This implies that by the time the turbulence generated at the cylinders arrives at the location of P_4 which is 50 mm aft of Cylinder2, the vortical structures have broken down to structures of several time scales and thereby frequencies with similar contributions of spectral density that appear in the above plot.

The acceleration spectra of the cylinders obtained from the experiment and numerical simulations are shown in Figure 5.21. The experimental results for Cylinder1 and Cylinder2 reveal distinct peaks at the vortex shedding frequency (f_s) and its multiples as well as the natural frequencies f_{n1} and f_{n2} in both streamwise (x) and cross flow (y) directions. The numerical results show distinct peaks corresponding to the even harmonics of f_s in the x-direction and the odd harmonics of f_s in the y-direction. The numerical results also show peaks for f_{n1} and f_{n2} in both directions.

(a) Cylinder1: x-direction

(b) Cylinder1: y-direction

(c) Cylinder2: x-direction

(d) Cylinder2: y-direction
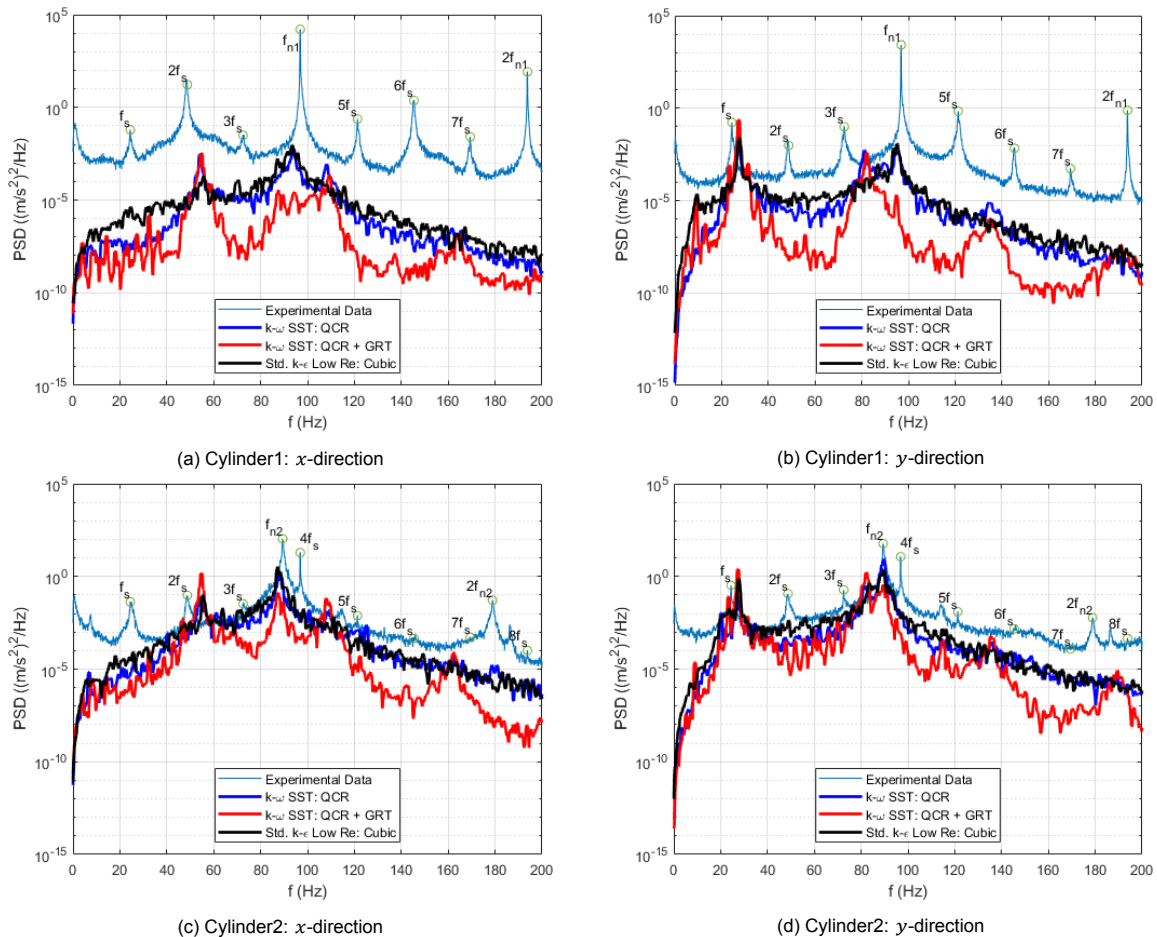
Figure 5.21: Acceleration Spectra Plots for the Cylinders

Overall, for the spectra of Cylinder1, the numerical results are severely underpredicted especially at f_{n1} which is expected to have a high value owing to resonance. As was reasoned with the pressure plots, the mismatch in peak spectral density of f_{n1} is suspected to be due to the mismatch in the fourth harmonic of f_s and f_{n1} while the background spectra mismatch is owed to the absence of physical turbulence upstream of Cylinder1. For Cylinder2, on the other hand, the obtained results match well in terms of the spectral density at the peaks, especially f_{n2}, as well as the background spectra. This is owing to Cylinder2 being in an off-resonant condition and due to the presence of turbulence generated by Cylinder1.

Coming to the individual turbulence models, the K-Omega SST: QCR + GRT model agrees well with its K-Omega SST: QCR counterpart in terms of the peaks but underpredicts the background spectra as was earlier seen in the pressure spectra plots. This could be attributed to less breakdown of vortical structures and thereby a more 2D vortex shedding behaviour. This assertion will be addressed later when discussing the vorticity plots. The other two models provide similar spectra with the Standard K-Epsilon Low Re: Cubic model offering a slightly higher background spectra in comparison.

The predictions of the vortex shedding frequency by the turbulence models are confirmed to be the same values quoted from the pressure spectra plots. The natural frequency of Cylinder1 is predicted to be 96 Hz from the y-direction spectra while it is predicted to be 95 Hz in the x-direction which translates to errors of 2.04% and 3.06% respectively. Similarly, the natural frequency of Cylinder2 is predicted to be 90 Hz from the y-direction spectra while it is predicted to be 89 Hz in the x-direction which translates to errors of 0.12% and 1.14% respectively. Further improvements can be made in the prediction of f_{n1} at the cost of f_{n2} by reducing the lengths of the bobs further. Another way would be to reduce the lengths of the bobs in Cylinder1 alone which would result in non-identical structures for the cylinders. These suggested modifications, however, are not made in the current study.

(a) V_1^1: x-direction

(b) V_1^1: y-direction

(c) V_2^1: x-direction

(d) V_2^1: y-direction

(e) V_3^1: x-direction

(f) V_3^1: y-direction

(g) V_4^1: x-direction

(h) V_4^1: y-direction
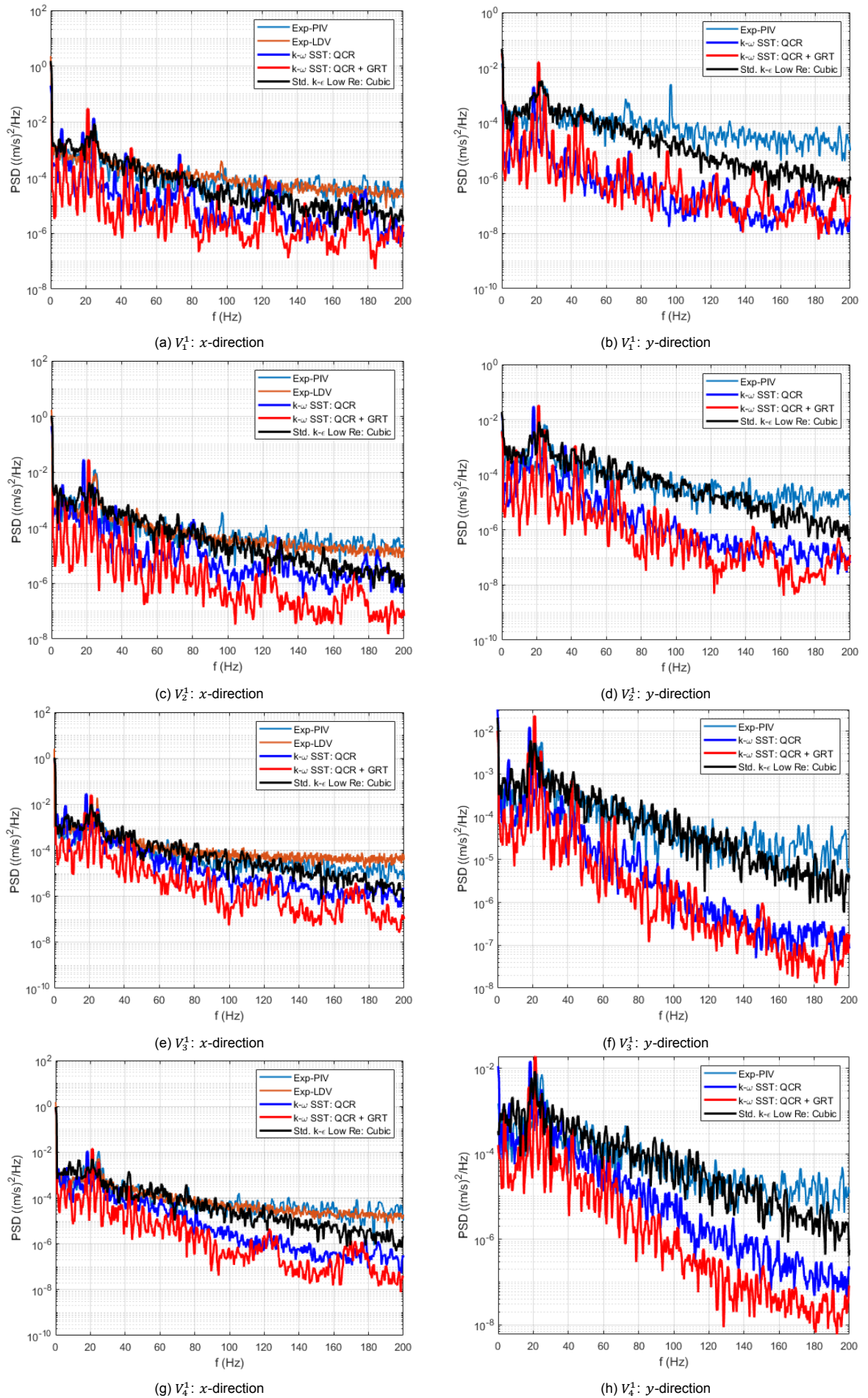
Figure 5.22: Velocity Spectra Plots: V_i^1, ($i = 1, 2, 3$)

(a) V_1^2: x-direction

(b) V_1^2: y-direction

(c) V_2^2: x-direction

(d) V_2^2: y-direction

(e) V_3^2: x-direction

(f) V_3^2: y-direction

(g) V_4^2: x-direction

(h) V_4^2: y-direction
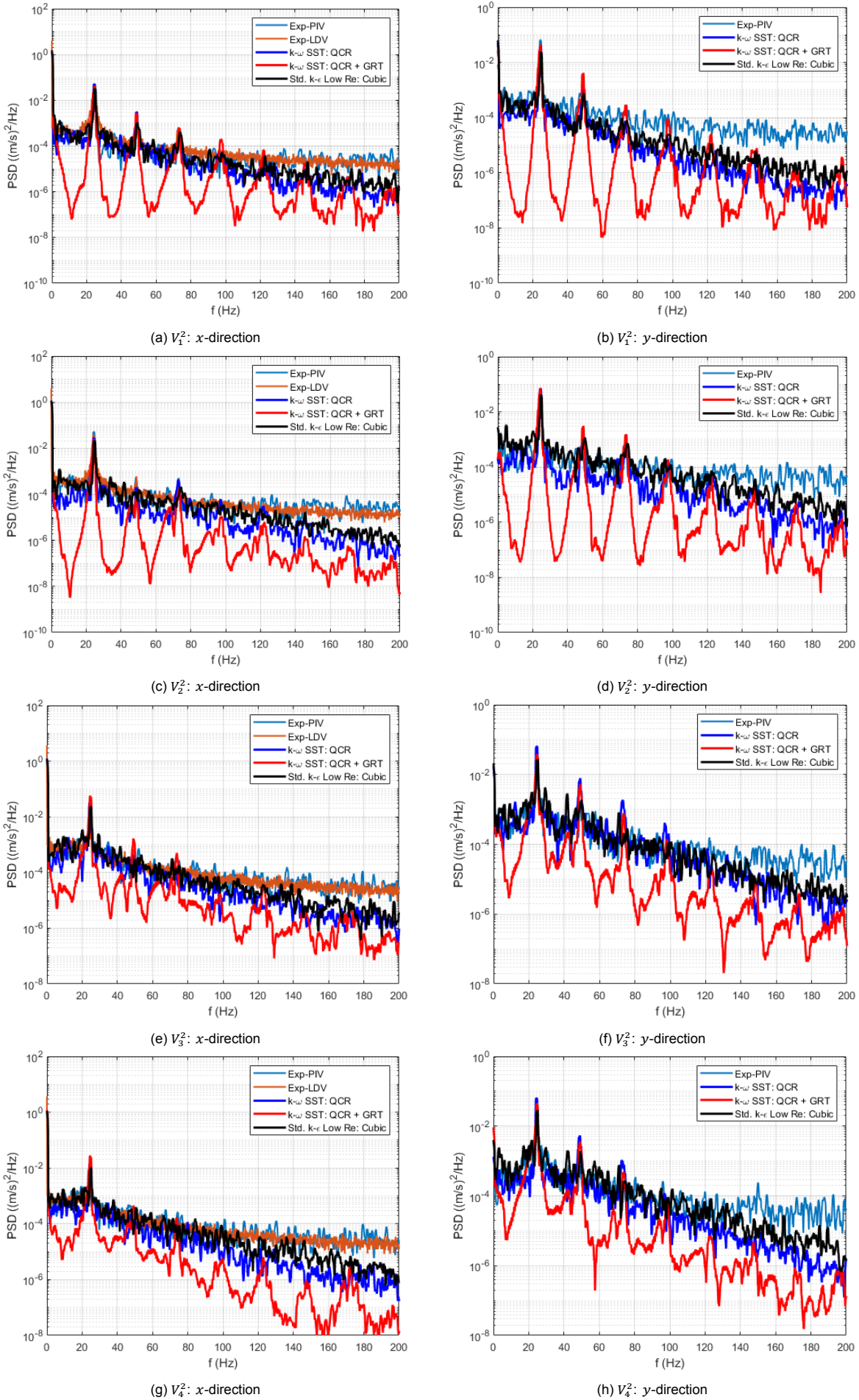
Figure 5.23: Velocity Spectra Plots: V_i^2, ($i = 1, 2, 3$)

(a) V_1^3: x-direction

(b) V_1^3: y-direction

(c) V_2^3: x-direction

(d) V_2^3: y-direction

(e) V_3^3: x-direction

(f) V_3^3: y-direction

(g) V_4^3: x-direction

(h) V_4^3: y-direction
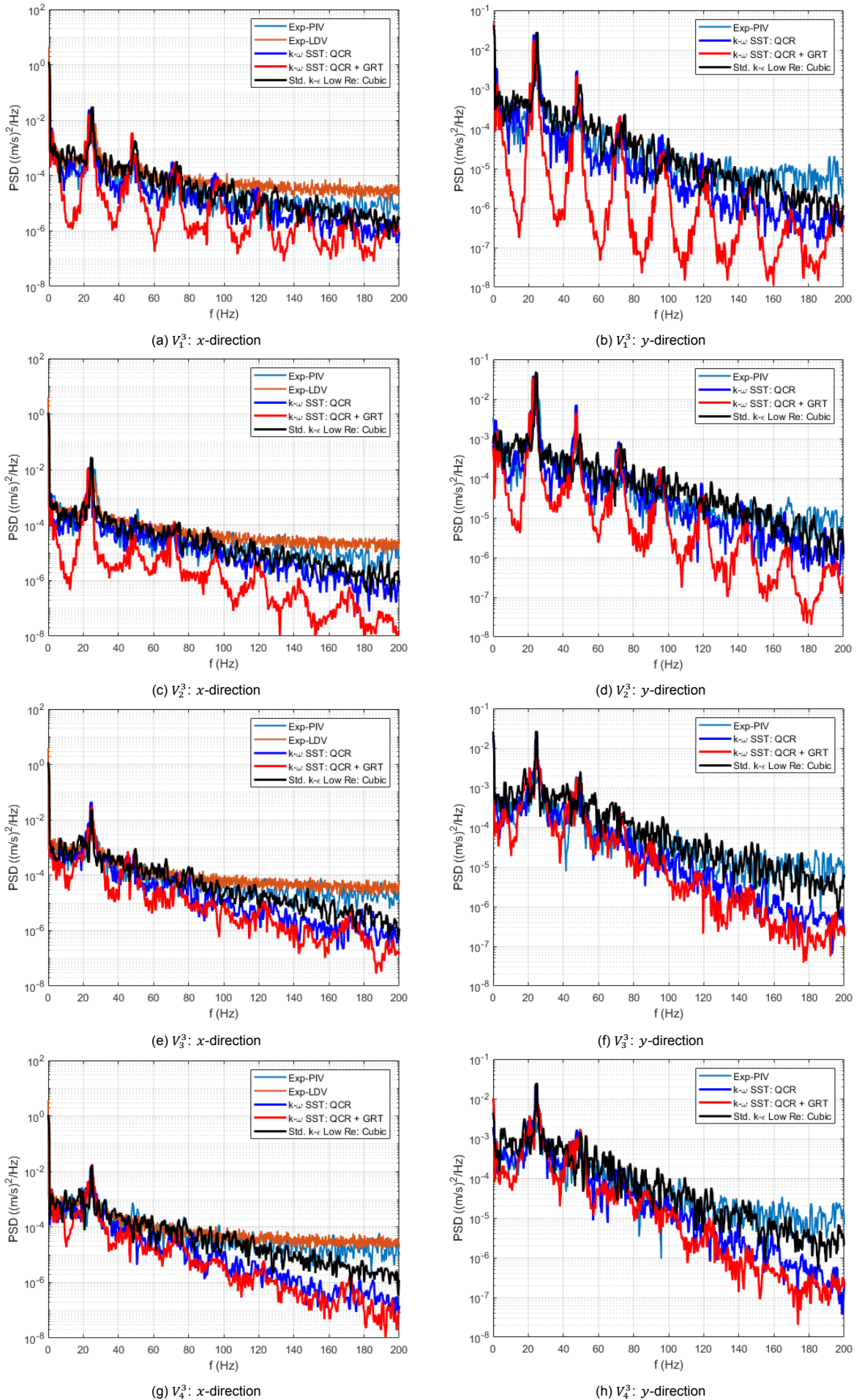
Figure 5.24: Velocity Spectra Plots: V_i^3, ($i = 1, 2, 3$)

The velocity spectra plots for different turbulence models are shown along with the experimental results in Figure 5.22 through Figure 5.24. To obtain clean spectra plots, linear averaging is applied with a window size of 30, 5 and 3 for the LDV and PIV experimental results and numerical results respectively. Key observations about the experimental results have already been discussed in subsection 5.2.1. Similar trends are observed for the numerical results with the spectra towards higher frequencies showing underpredicted results. It was earlier reasoned in subsection 5.2.1 that to improve upon the prediction in the high frequency range, a smaller time step, mesh size and a higher fidelity method may be required as a means to resolve small scale turbulence better. However, for the current choice of parameters, the Standard K-Epsilon Low Re: Cubic model shows the best agreement in the high frequency range at all locations, especially at plane Z_1 which is a critical zone given the influence of the turbulence generated at the free end of the cylinder in the 2 mm gap between the channel wall.

Another observation is the mismatch in predictions of the vortex shedding frequency by the numerical results and the experimental results. It is also observed that the vortex shedding frequency captured by the experiment as well as the numerical results vary along the length of the cylinders. In particular, the prediction by V_1^i and V_3^i were found to be the same as V_2^i and V_4^i respectively. The experimental as well as numerical predictions for f_s are tabulated in Table 5.5 for V_1^i and V_3^i. In Table 5.5, shorthands of QCR, QCRT and CKE are used for K-Omega SST: QCR, K-Omega SST: QCR + GRT and Standard K-Epsilon Low Re: Cubic models respectively.

Table 5.5: Vortex Shedding Frequency Predictions by the Experiment and FSI Test Cases

	f_s at V_1^1 (Hz)				f_s at V_1^2 (Hz)				f_s at V_1^3 (Hz)			
	Exp.	QCR	QCRT	CKE	Exp.	QCR	QCRT	CKE	Exp.	QCR	QCRT	CKE
x	25.1	24.5	24.5	24.7	24.3	24.4	24.4	24.5	25.1	23.8	23.8	25.0
y	24.7	24.3	24.7	24.7	24.3	24.4	24.4	24.5	25.1	23.8	23.8	25.0

	f_s at V_3^1 (Hz)				f_s at V_3^2 (Hz)				f_s at V_3^3 (Hz)			
	Exp.	QCR	QCRT	CKE	Exp.	QCR	QCRT	CKE	Exp.	QCR	QCRT	CKE
x	24.6	21.4	21.4	23.5	24.7	24.3	24.5	24.5	26.6	24.7	25.0	25.0
y	24.9	21.3	21.1	23.1	24.5	24.3	24.5	24.5	26.8	24.7	25.0	25.0

The numerical results are in close agreement with the experimental results. The largest difference between the predictions of the turbulence models are observed at plane Z_1 with the least error offered by the Standard K-Epsilon Low Re: Cubic model. The tabulated numerical results, although encouraging, go against the expectation of observing an overestimation of f_s as was observed in the pressure and acceleration plots. One possible reason is the error in picking the peak as caused by the applied linear averaging process to make a cleaner spectra plot. Using the averaging process does make the signal less noisy but it also flattens out the tips of the peaks. Thus, the "peaks" actually span as wide as 1.5 Hz for some curves inducing significant error in picking out the true frequency.

As was brought up earlier when discussing the spectra prediction for the high frequency range, it was asserted that the accuracy is linked to better resolving small scale turbulent structures. Thus the expectation is to have a well captured turbulent wake for the Standard K-Epsilon Low Re: Cubic model as well as the K-Omega SST: QCR model with perhaps a near 2D vortex shedding for the K-Omega SST: QCR + GRT model. The expectation is checked against the vorticity plots created at the end of the simulation as shown in Figure 5.25 and Figure 5.26 (shorthand for turbulence models is same as Table 5.5).

As can be observed from Figure 5.25, the expectation is met perfectly with respect to the type of wake captured by the turbulence models. The Standard K-Epsilon Low Re: Cubic model and the K-Omega SST: QCR model predict 3D vortex tubes being shed from Cylinder1 with these regular structures starting to break down into smaller ones as they travel towards Cylinder2. As they interact with Cylinder2 and its generated wake, the regular structures are nearly lost as per the K-Omega SST: QCR model and completely lost as per the Standard K-Epsilon Low Re: Cubic model. The K-Omega SST: QCR+ GRT model, on the other hand, predicts near regular structures even aft of Cylinder2.
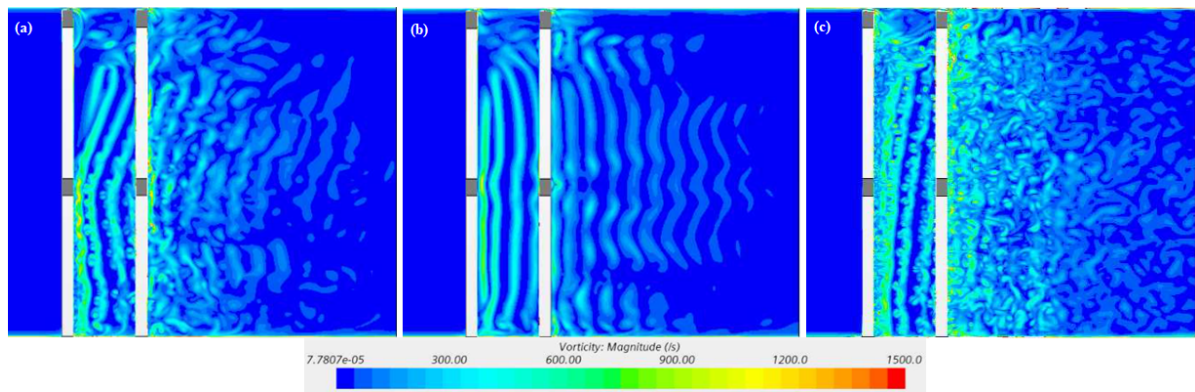
Figure 5.25: Vertical Section Vorticity Plots for (a) QCR (b) QCRT and (c) CKE
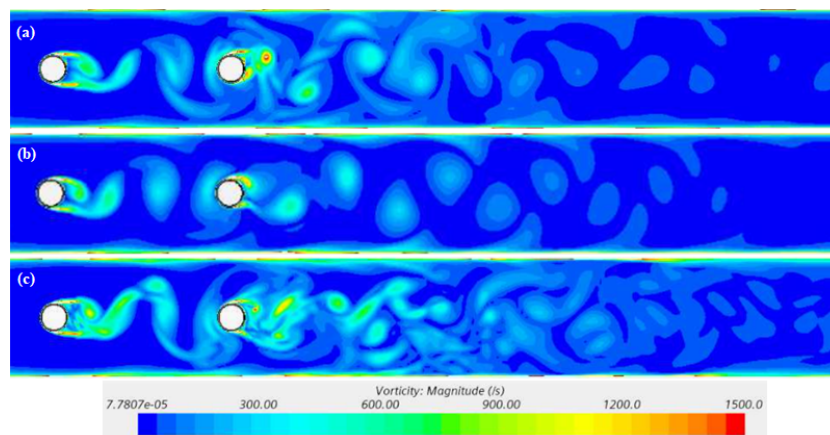
Figure 5.26: Horizontal Section Vorticity Plots for (a) QCR (b) QCRT and (c) CKE at Plane Z_2

It is also to be noted that part of the wake aft Cylinder2 appears to be subject to numerical dissipation as the vortical structures pass over from Refine2 to Refine1 refinement regions of the mesh about $10D$ aft of Cylinder2. This can be observed as a drop in the strength of vorticity as it passes over the interface of the refinement regions and is more clearly noticed in Figure 5.25c. This is linked to the recalculation of the vorticity vector as was reasoned earlier in subsection 5.2.1. This adversely affects the results but is expected to be at a low degree given the location of this issue. Improvements in the results can be expected for having a longer Refine2 refinement region but is not carried out in the current study.

The last set of results are the mean and RMS fluctuation velocity profiles at horizontal sections 10 mm and 20 mm behind each of the cylinders which are shown in Figure 5.27 through Figure 5.29. The mean velocity profiles show a low velocity in the center of the channel width and a higher velocity away from the channel center and channel walls. This makes sense as the cylinder obstructs the flow at the center of the channel width with the fluid squeezing through the remaining width of the channel at a higher than inlet velocity as a consequence of the continuity equation. For all planes, the velocity profile tends to flatten out as it gets away from the cylinders. This is owed to the internal viscous forces between fluid layers of different velocity as they try to reorient the profile back to the shape that existed ahead of the cylinders. Finally, differences are also noted in the profiles for different planes at a given location. This is owed to the fact that the problem is 3D with the cylinders having a finite length, the presence of channel walls and the 2 mm gap between the cylinder tips and the channel wall.

All simulation results also show the same trend in profiles as the experimental results at all locations and planes with the exception of the K-Omega SST: QCR profile 20 mm behind Cylinder1 at plane Z_1 (see Figure 5.27b) and the Standard K-Epsilon Low Re: Cubic profile 10 mm behind Cylinder1 at plane Z_2 (see Figure 5.28a) as they predict a larger dip in mean velocity at the center of the channel width.

(a) Mean Velocity 10 mm behind Cylinder1

(b) RMS Velocity Fluctuation 10 mm behind Cylinder1

(c) Mean Velocity 20 mm behind Cylinder1

(d) RMS Velocity Fluctuation 20 mm behind Cylinder1

(e) Mean Velocity 10 mm behind Cylinder2

(f) RMS Velocity Fluctuation 10 mm behind Cylinder2

(g) Mean Velocity 20 mm behind Cylinder2

(h) RMS Velocity Fluctuation 20 mm behind Cylinder2
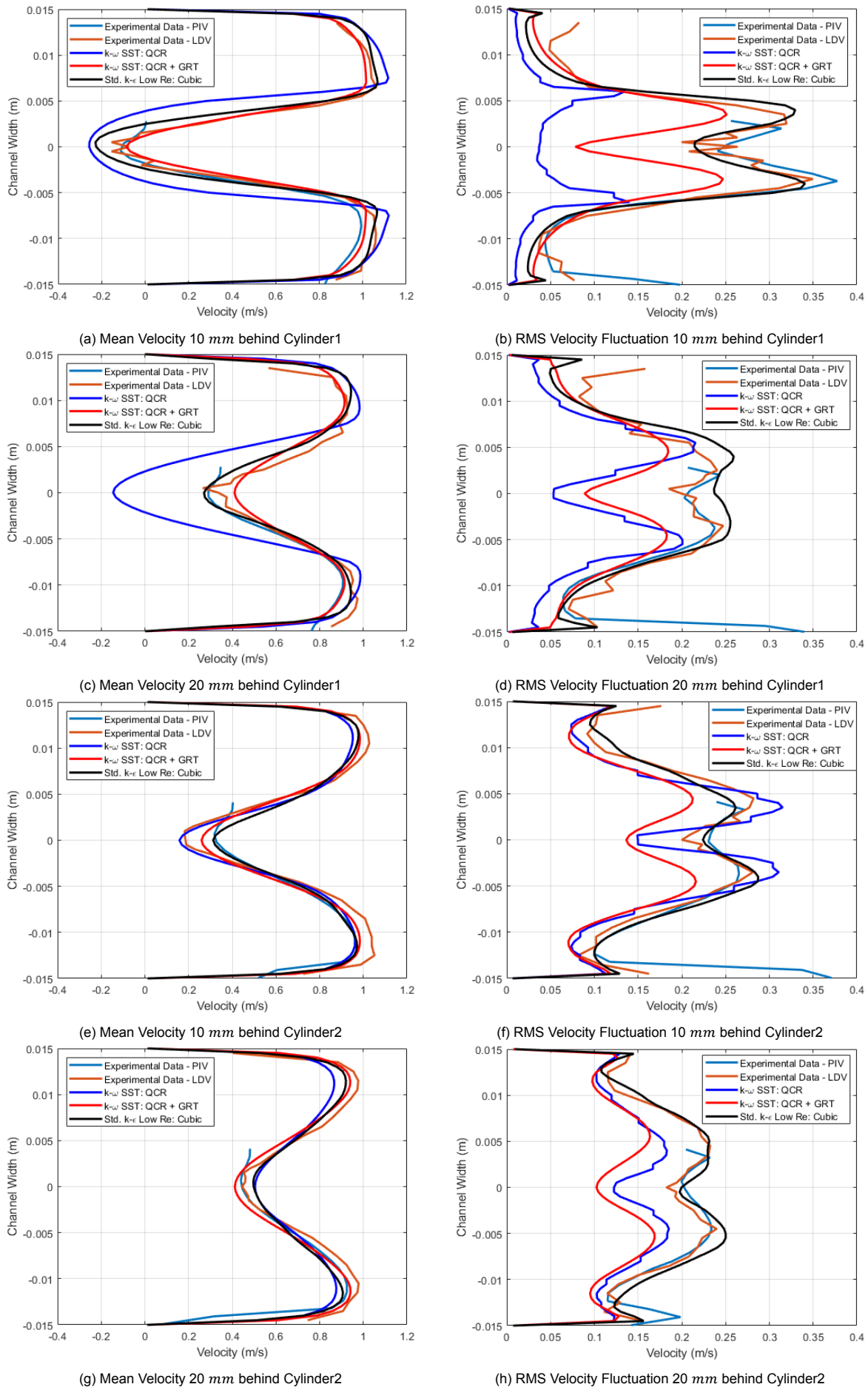
Figure 5.27: Mean and RMS Fluctuation Streamwise Velocity Profiles at Horizontal Sections in Plane Z_1

(a) Mean Velocity 10 mm behind Cylinder1

(b) RMS Velocity Fluctuation 10 mm behind Cylinder1

(c) Mean Velocity 20 mm behind Cylinder1

(d) RMS Velocity Fluctuation 20 mm behind Cylinder1

(e) Mean Velocity 10 mm behind Cylinder2

(f) RMS Velocity Fluctuation 10 mm behind Cylinder2

(g) Mean Velocity 20 mm behind Cylinder2

(h) RMS Velocity Fluctuation 20 mm behind Cylinder2
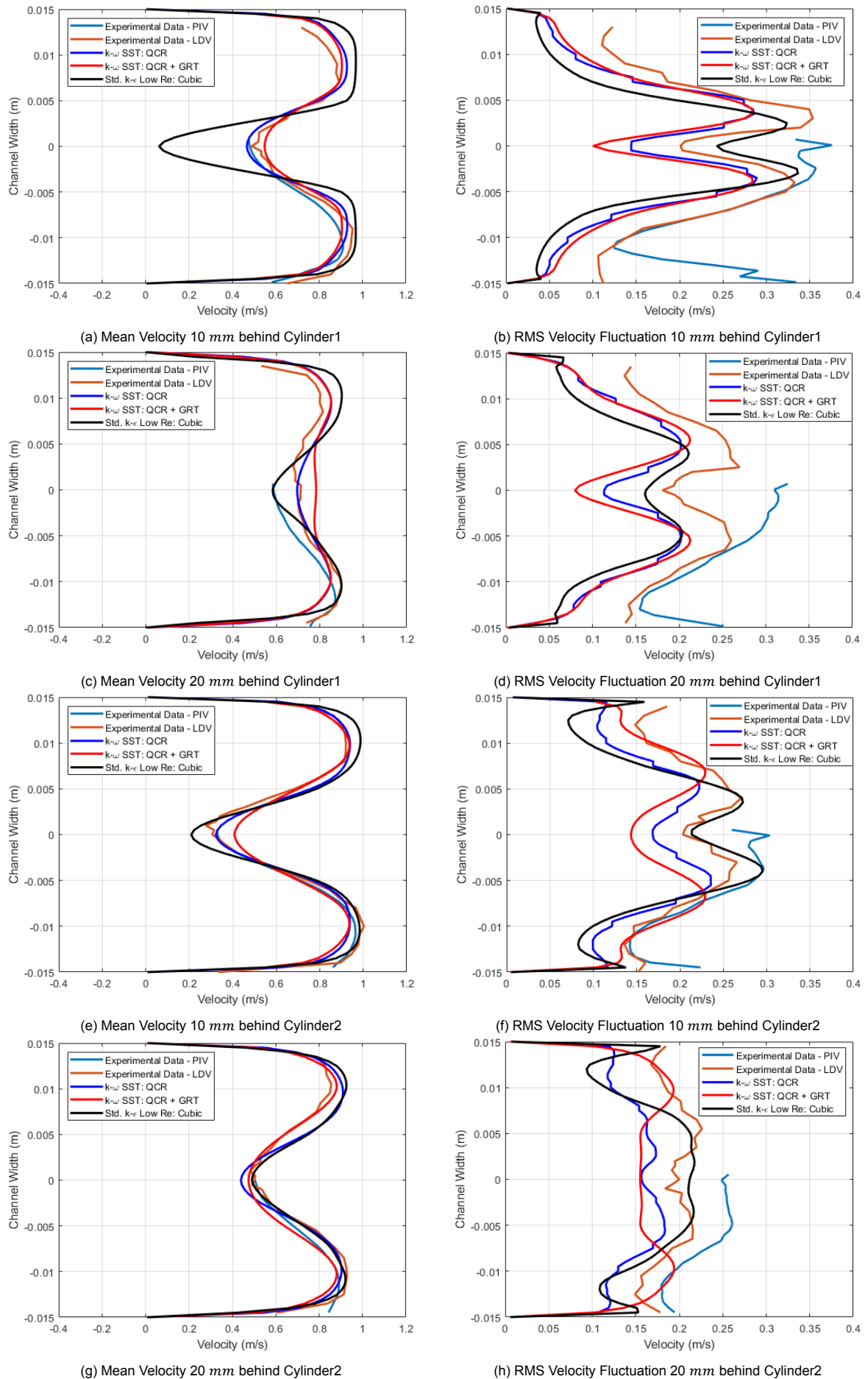
Figure 5.28: Mean and RMS Fluctuation Streamwise Velocity Profiles at Horizontal Sections in Plane Z_2

(a) Mean Velocity 10 mm behind Cylinder1

(b) RMS Velocity Fluctuation 10 mm behind Cylinder1

(c) Mean Velocity 20 mm behind Cylinder1

(d) RMS Velocity Fluctuation 20 mm behind Cylinder1

(e) Mean Velocity 10 mm behind Cylinder2

(f) RMS Velocity Fluctuation 10 mm behind Cylinder2

(g) Mean Velocity 20 mm behind Cylinder2

(h) RMS Velocity Fluctuation 20 mm behind Cylinder2
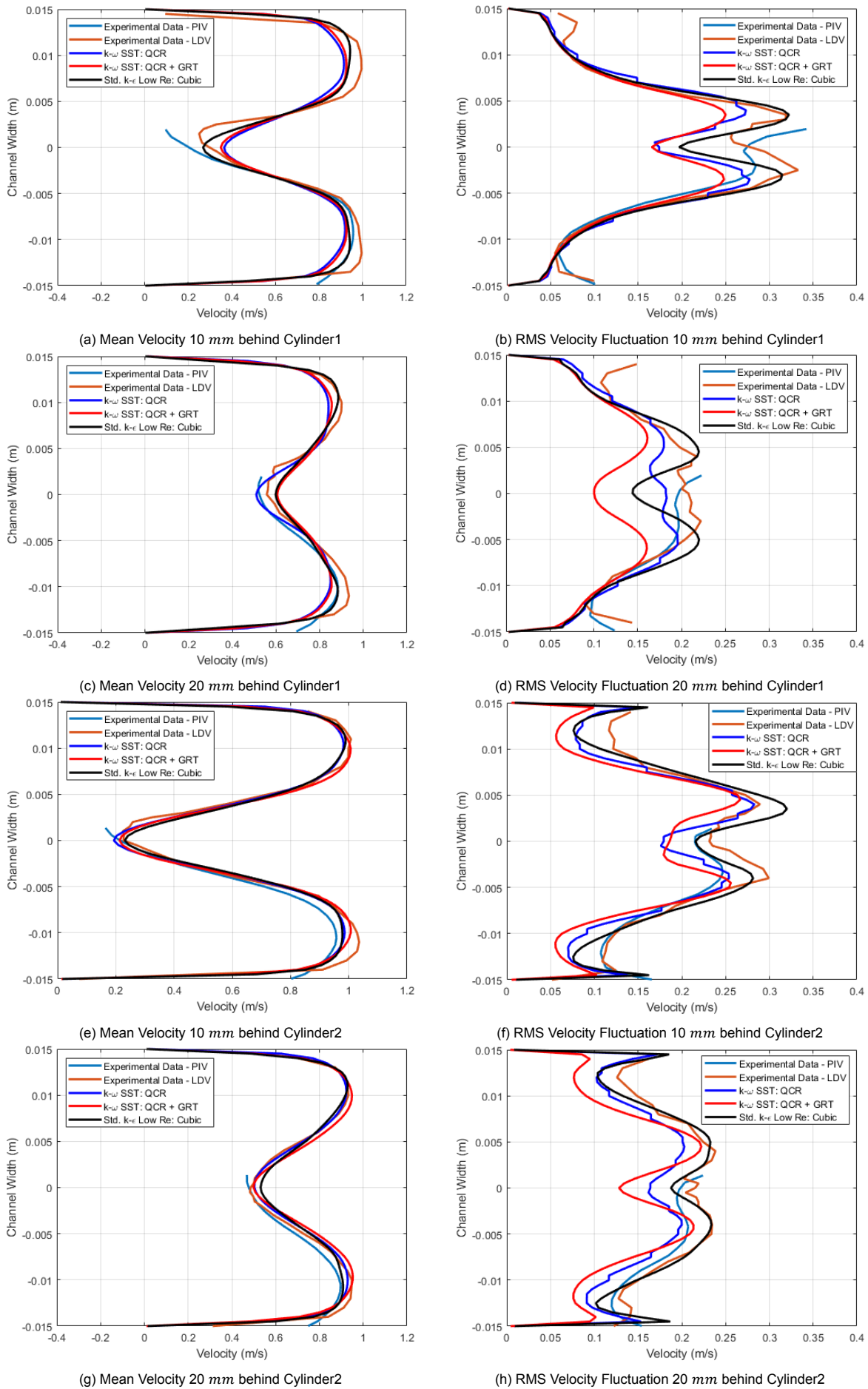
Figure 5.29: Mean and RMS Fluctuation Streamwise Velocity Profiles at Horizontal Sections in Plane Z_3

Unlike for the mean velocity profile plots, the PIV and LDV experimental results are not as well in agreement with each other for the fluctuation plots. This is especially true for planes Z_2 and Z_3. The LDV results are selected for asserting the trends and for comparison against the simulation results.

The fluctuation profiles reveal significant resolved fluctuations near the center of the channel width with the fluctuations gradually decreasing towards the channel walls and it slightly increasing again in the near vicinity of the channel walls. These fluctuations in velocity are owed to the vorticity in the flow. The center of the channel width is subject to the turbulent wake of the cylinders while in the near vicinity of the wall, there exists the boundary layer which, in this case, is also interacting with the wake of the cylinders. In particular, there are two peaks observed at an offset from the center of the channel width which is a consequence of the geometry of the vortex shedding process from the cylinder at this flow rate. The vortices shed from the top half and bottom half of the cylinders do not appear exactly in the center but at an offset which can be observed from Figure 5.26. The peak fluctuations near the center of the channel width also appear to reduce with distance away from the cylinders. This is owed to the dissipation of vorticity and thereby a decrease in the strength of vorticity as it travels downstream from the cylinders. As the strength of the wake reduces, so do the fluctuations.

The numerical results also show profile shapes similar to the experimental results with significant differences in the exact trends of the profiles. Unlike the mean profiles, the fluctuation profiles are visibly asymmetric which is not expected for this symmetric problem. Perhaps, with a longer simulation time, the solution gets more symmetric as a larger number of fluctuation cycles will be included in the calculations. Withstanding this slight asymmetry, the Standard K-Epsilon Low Re: Cubic model is observed to provide the best fit with the experimental results at all locations and planes.

Considering all qualitative and quantitative results, the Standard K-Epsilon Low Re: Cubic model is selected for the blind phase of the study on account of better modelling the wake of the cylinders which leads to more accurate spectra plots and velocity profile plots, especially the fluctuation profiles.

The current study has revealed certain shortcomings of the URANS scheme for predicting VIV, or as was reasoned in this case, a combination of VIV and TIV. While this scheme works well for off-resonant systems (in this case Cylinder2), it doesn't work well to capture resonance particularly for FSI problems that have resonance of the structural natural frequency with higher harmonics of the vortex shedding frequency (in this case Cylinder1). This is owing to the error of the URANS scheme in predicting the vortex shedding frequency which gets amplified for higher harmonics leading to a mismatch in predicting resonance. As a consequence, one would only capture resonance in the current study at a lower flow rate where the corresponding overpredicted vortex shedding frequency would be lower. Even so, that would only solve half the problem as the TIV part of the spectra would still require actual turbulent fluctuations in velocity and pressure present from the inlet and that is something that the current scheme cannot provide as is.

The above hypothesis of cause can be tested with the blind phase of the study. If the above reasoning is true, similar behaviour is expected from the blind phase solution where:

- The peaks in the spectra for the natural frequency of Cylinder1 are not well identified on account of an off-resonant condition when facing a flow that is predicted to cause resonance as per the experiment.
- This is to be accompanied with an overprediction of vortex shedding frequency and low background spectra level for Cylinder1.
- The results for Cylinder2 should be well in agreement with the experimental results given that it is confirmed to be in an off-resonant condition and that it faces actual turbulence generated by Cylinder1.
- All spectra plots will show underpredicted values in the high frequency range.

With the above expectations, the blind phase study is carried out for both off-resonant and resonant flow conditions. The associated experimental setup and the numerical results are discussed in the following chapter.

5.4. Conclusion

In this chapter, the OECD Benchmark was introduced with the open phase study. The experimental setup, including the associated measurement systems and the open phase test parameters, was briefly discussed. The primary intention with the current study was to select one out of the three shortlisted turbulence models that will be used for the blind phase study of this benchmark.

To achieve this agenda, numerical simulations are to be set up. Two challenges were identified: Selecting a fluid mesh that fits in the current timeframe and resource budget of the current study and fine tuning the structural model to the required natural frequencies in air and water. To deal with the first problem, different meshes were proposed with different sizes of refinement regions and were tested in a pure CFD study using a single (K-Omega SST: QCR) turbulence model against the FSI experimental results to select the best performing mesh. The 'CFD3' mesh with 7.05M cells was selected which had the longest Refine2 region consisting of elements of size $0.089D$ in the wake of the cylinders. To fine tune the structural model, CSM vibration studies were carried out in vacuum and water for structures with different bob lengths. A bob length of 10 mm was finalized for the FSI study.

With the selected fluid mesh, structural model and associated settings, the FSI study was carried out with the shortlisted turbulence models. Before getting into the results, the modelled inflow turbulence condition was tested by plotting the streamwise velocity mean and RMS fluctuation profiles at sections 140 mm, 200 mm and 50 mm ahead of Cylinder1. For comparing with the experimental fluctuation profiles, resolved and modelled turbulence profiles were used from the numerical simulations. Based on the plots, the selected inlet turbulence settings were considered validated.

Considering the spectra plots for pressure and acceleration, resonance was not able to be predicted for Cylinder1 by any of the URANS turbulence models. The key reason for the same is suspected to be the overprediction of the vortex shedding frequency (f_s) by 11%-14% (depending on the turbulence model) which led to a mismatch in the fourth harmonic of f_s and the natural frequency of Cylinder1 (f_{n1}). It was also noted that for the experiment, due to the presence of a non-ideal pump, the spectral density in the fluid pressure spectra at f_{n1} was possibly overestimated due to it coinciding with the third harmonic of the pumping frequency. The prediction by the URANS scheme for the acceleration spectra for Cylinder2 was much better than Cylinder1 although the error in spectral density at the natural frequency of Cylinder2 (f_{n2}) was still significant with the closest prediction giving an error of 85.11% for the K-Omega SST: QCR model.

Coming to the individual turbulence models, it was found that the K-Omega SST: QCR + GRT model had the least fit with the velocity spectra results on account of predicting a poor background spectra. This was followed by a better fit by the K-Omega SST: QCR model and the best fit provided by the Standard K-Epsilon Low Re: Cubic model. The differences in results were reasoned to stem from the type of wake predicted and was confirmed with the vorticity plots that revealed the best fitting model to predict a really turbulent wake with small scale structures. The last set of results were the streamwise velocity mean and RMS fluctuation profiles 10 mm and 20 mm behind the cylinders. While the mean velocity profiles were nearly the same for all turbulence models, the Standard K-Epsilon Low Re: Cubic model predicted the qualitatively best fitting profiles for the fluctuations. Based on all the results, this model is selected for the blind phase study.

Based on the shortcomings of the URANS scheme observed in the current study, in particular the overprediction of f_s and the absence of physical turbulence at the inlet, expectations are listed for the blind phase study which if met bring weight to the above reasonings of failure and thereby a scope for improvements in this scheme. The blind phase study is formally introduced and discussed in the following chapter.

6

OECD Benchmark: Blind Phase

With the best suited turbulence model (Standard K-Epsilon Low Re: Cubic) selected and the expectations for the results established, the blind phase of the OECD benchmark is formally introduced and tackled. The experimental results of this phase of the benchmark were disclosed to the participants much after all the obtained results were handed in. The current study is mainly used to confirm the expectations drafted at the end of the previous chapter. Given that in this phase, both off-resonant and resonant inflow rates will be tested, this is also a platform to further test the URANS framework and discuss the difference in responses for the two inflow rates.

The experimental setup and parameters of interest are given in section 6.1. In particular, the two cylinders house brass accelerometer mountings of different density and length which affect the natural frequency of the structure. This is investigated for fine tuning in a pure structural analysis and is discussed as part of the numerical setup in section 6.2. Once the setup parameters and the meshes are selected, the finalized turbulence model is put the test against the FSI problem in section 6.3.

6.1. Experimental Setup

The experimental setup again consists of two in-line cantilevered cylinders subjected to cross flow in a rectangular channel test section as per the earlier setup shown in Figure 5.1a. The same test facility located at the JSC "Afrikantov OKBM" in Russia is made use of. As was done for the open phase, only the channel and its contents are set up for the simulation based on the dimensions prescribed in the CAD drawings made available to the participants of the benchmark. The CAD model so created using STAR-CCM+ is akin to that earlier shown in Figure 5.1b.

The experimental study made use of hollow stainless steel cylinders of diameter D=10 mm, wall thickness 1 mm and length 198 mm placed 45 mm apart with the first cylinder placed at a distance of 350 mm from the inlet. For the experiment, each cylinder had different singular brass accelerometer mounting of diameter 8 mm and lengths 14 mm and 29 mm, respectively, soldered internally at the tip of the cylinder (the length does not include the solder deposit). These brass bobs for the two cylinders were also slightly different in density leading to different natural frequencies of the structures in air and water. The material properties of the structure are provided in Table 6.1. The working fluid was water at 19° C and was tested for flow rates of 16 m^3/h (off-resonance, Re=7210.96) and 35 m^3/h (peak resonance, Re=15773.96) through the aforementioned channel that houses the cylinders. The reference static pressure was 1 kgf/cm^2. In the current study, both cases are simulated and presented here.

As with the open phase, the natural frequency and structural damping of the cylinders in the channel were analyzed by measuring the vibrations under the impact excitations of the channel and producing a Frequency Response Function (FRF) plot. Based on the test of the channel without water, the natural frequencies of the cylinders were found to be $f_{n1,air} = 183.9\ Hz$ and $f_{n2,air} = 168.8\ Hz$ respectively. Based on a similar test of the channel with water, the natural frequencies of the cylinders were found to be $f_{n1,water} = 164.9\ Hz$ and $f_{n2,water} = 153.0\ Hz$ respectively.

91

Table 6.1: Structural Properties

Structure	Material	Density, ρ_s (kg/m^3)	Young's Modulus, E (GPa)	Poisson's Ratio, ν
Hollow Cylinders 1 & 2	Stainless Steel	7850	200	0.30
Bob for Cylinder1	Brass	8700	200	0.33
Bob for Cylinder2	Brass	7500	200	0.33

The FRF plot created based on the experimental results provided for the test of the channel with water is provided in Figure 6.1.
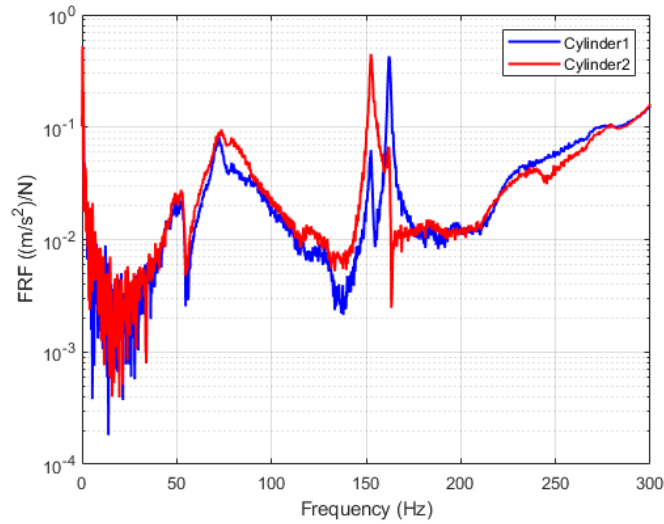
Figure 6.1: FRF Curves for the Two Cylinders under Impact Excitation of the Channel with Water

Using the above plot, the damping ratio (ζ) or its related parameters like the loss factor (η) and quality factor (Q) is found using the 'half-power' or '3 dB' rule. These damping parameters are calculated using

$$\frac{\Delta f}{f} = \eta = \frac{1}{Q} = 2\zeta\sqrt{1 - \zeta^2} \approx 2\zeta \tag{6.1}$$

where Δf is the width of the FRF curve 3 dB below the peak at frequency f. The loss factor for both cylinders vibrating in water comes out to be $\eta = 0.007$. The approximation $\zeta = 0.5\eta$ is accurate within 1.25E-3% for $\eta \in [0, 0.01]$ and is thus made use of giving $\zeta = 0.0035$. This value is later used in conjunction with the value from the numerical structural tests to provide structural damping for the FSI tests using the 'Rayleigh Damping' model available in STAR-CCM+. For the cylinders, the Rayleigh damping is restricted to stiffness proportional damping with the corresponding constant calculated as per Equation 3.31 with $\omega = 2\pi f_{n,water}$.

6.1.1. Measurement Systems

The same equipment used for the open phase is also used for the blind phase. This includes the static pressure probes, thermocouples and electromagnetic flow meter for measuring the static pressure, temperature and flow rate. To study the hydrodynamics of the flow, systems based on PIV (pulsed lasers) were used. As the tracer particles, 10 μm polyamide particles were used. To study the vibrational response of the structure, accelerometers are mounted at the top of the cylinders in two mutually perpendicular directions. Measurements of vibrations, pressure pulsations, as well as velocity pulsations were carried out synchronously. The operability of the accelerometers and pressure pulsation sensors was provided by duplication of measurements using a laser vibrometer and hydrophones, respectively. The synchronization of vibration measurements using accelerometers and a laser vibrometer were carried out by an external trigger. Further specifications of these systems have been provided in section 5.1.

6.1.2. Blind Phase Test Parameters

As with the open phase, the participants of the benchmark are free to perform one-way or two-way method of FSI calculations as well as pure CFD calculations. In the current study, the two-way coupled FSI calculations are performed for both the off-resonance and peak resonance cases.

During testing, dynamic parameters were measured correspondingly by different systems. The experimental data were registered as a function of time. The following measurements were performed:

- $v(t)$ – time oscillation of velocity pulsations
- $p(t)$ – time oscillation of pressure pulsations on the channel wall
- $a(t)$ – time oscillation of cylinders' vibration acceleration

Figure 6.2 shows the locations of the measurement points. The same coordinate system for the open phase is used here as well. As with the open phase, the accelerometer readings of a_3^{xyz} and a_4^{xyz} (see Figure 6.2b) are not made use of. The PSD (spectrum) of velocity and pressure pulsations, vibration accelerations are later calculated based on the time series.

(a) Locations of Velocity Pulsations Measurements in the ith Plane

(b) Locations of Cylinders' Vibration Acceleration Measurement

(c) Locations of Pressure Pulsations Measurements
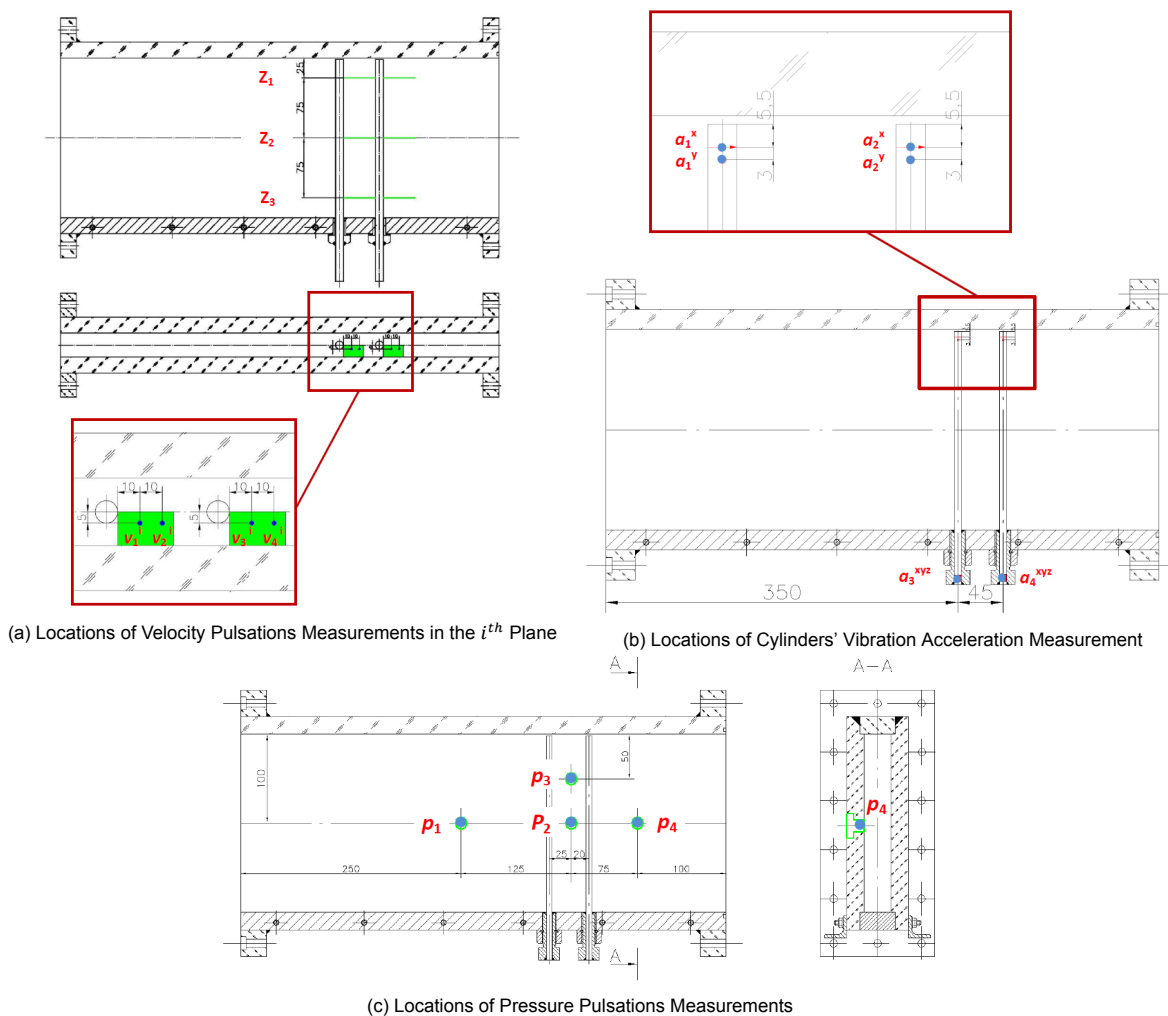
Figure 6.2: Location of Measurement Points for Different Parameters

Besides measurements at the above locations, horizontal velocity profile measurements were made 10 mm and 20 mm behind the cylinders as shown in Figure 6.3b. Furthermore, to aid in selecting inlet flow conditions, additional velocity profile measurements are made. These measurements are performed in the following sections and are shown in Figure 6.3:

- Average and Root Mean Squared (RMS) profile in the vertical plane of longitudinal velocity $V_x(z)$ in front of the 1st cylinder at a distance of 140 mm
- Average and RMS profile in four horizontal planes (40, 80, 120 and 160 mm) of longitudinal velocity $V_x(y)$ in front of the 1st cylinder at a distance of 200 mm
- Average and RMS profile in three horizontal planes (25, 100 and 175 mm) of longitudinal velocity $V_x(y)$ in front of the 1st cylinder at a distance of 50 mm

(a) Vertical Plane

(b) Horizontal Planes
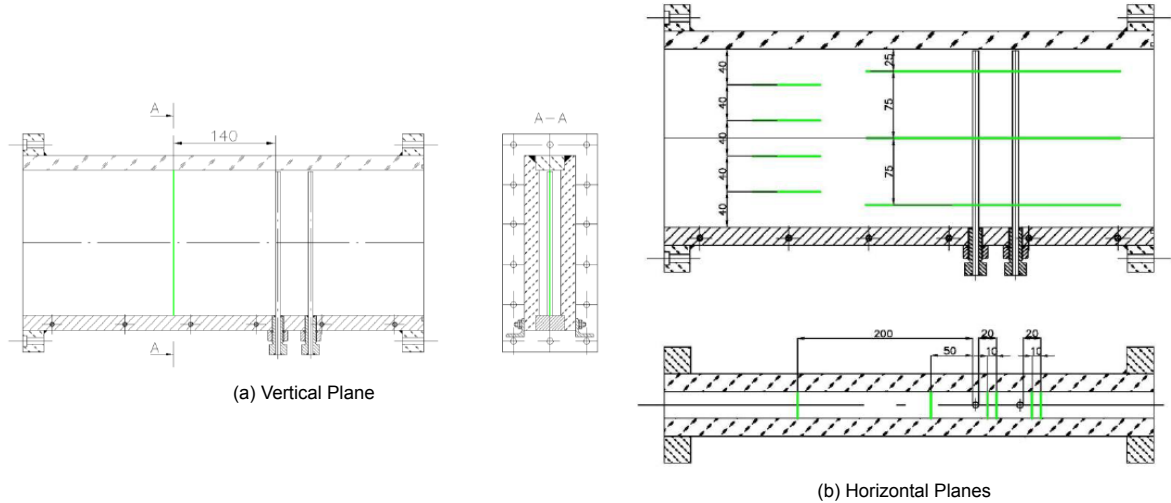
Figure 6.3: Locations of Velocity Profiles Measurement in the Vertical and Horizontal Planes

6.2. Numerical Setup

Based on the CAD drawings for the test section (and its contents) of the experimental setup, the simulation domain is set up in STAR-CCM+. The problem is set up in STAR-CCM+ as follows: For the incompressible fluid, the 'Implicit Unsteady' SIMPLE scheme 'Segregated Flow' solver is selected with a 2nd order upwind convection scheme. The pressure and velocity equations are given UR factors of 0.2 and 0.6 respectively. The four channel walls and the exposed cylinder surfaces are prescribed a no-slip boundary condition. A constant static pressure of 0 Pa is prescribed for the outlet. For the inlet, a time-varying uniform velocity is prescribed for (numerical stability of) the current FSI study as given by the equation:

$$u(0, y, z, t) = \begin{cases} u(0, y, z)\frac{1-\cos\left(\frac{\pi}{T}t\right)}{2}, & \text{if } t < T \\ u(0, y, z), & \text{otherwise} \end{cases}$$

$$u(0, y, z) = \begin{cases} 0.74\, m/s, & \text{Off-Resonance} \\ 1.62\, m/s, & \text{Resonance} \end{cases} \tag{6.2}$$

$$T = \begin{cases} 0.75\, s\, (1.01\, FP), & \text{Off-Resonance} \\ 0.7\, s\, (2.06\, FP), & \text{Resonance} \end{cases}$$

For the solid, the 'Solid Stress' solver is selected along with a 2nd order Newmark implicit integration scheme (Newmark parameter, γ=0.5). At this point, a choice is to be made between the infinitesimal strain and finite strain approximation. The expected displacements in both streamwise (x) and cross flow (y) directions are less than 0.5 mm which, relative to the 198 mm length of the cylinders, is less than 0.25% of the cylinder length. From the validation work as well as the experience from the open phase study, the infinitesimal strain approximation given by the 'Linear Geometry' model is selected. For the boundary condition, the annular surfaces at the bottom of the cylinders are grounded while the outer wetted surfaces are declared as an FSI interface. Internally, the brass bobs are fixed in their relative positions using the 'bonded' boundary condition between the bob curved surface and the cylinder inner curved surface. For the FSI coupling, a UR factor of 0.5 is prescribed.

The fluid mesh is created using the 'Automatic Mesh' functionality of STAR-CCM+. For the fluid, a structured hexahedral mesh is created with three volume refinements. Approaching the cylinder from the inlet by crossing each refinement region reduces the target base size (bs) of 3 mm by half sequentially. To ensure good transition between the refinement regions, a growth rate of 1.1 is selected. Given a budget of 128 allocated cores, 1 month of physical time for this phase of the current study and past experience with the open phase simulations, a maximum allowable number of fluid elements is again capped at 8M. The mesh is akin in placements of refinement regions as the mesh used for the open phase FSI study with care taken to ensure a Y^+ value of 1 on all walls as per the resonant inflow velocity. The mesh so created has 7.78M elements whose sectional views are shown below in Figure 6.4a.

(a) Fluid Mesh
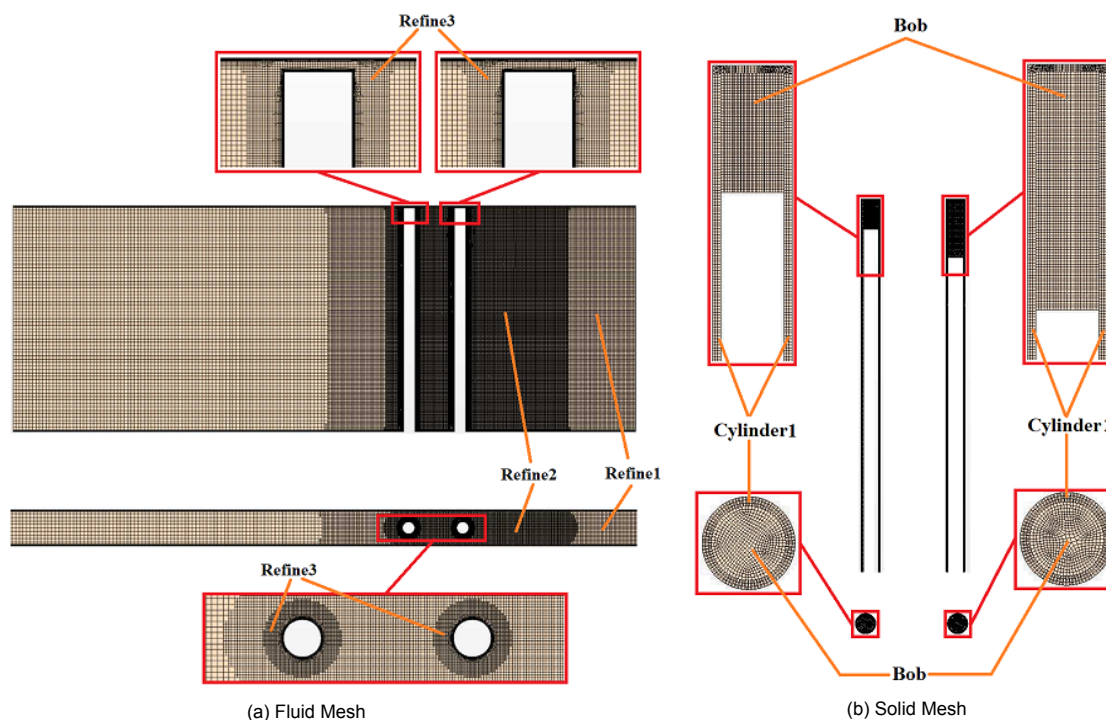
(b) Solid Mesh

Figure 6.4: Sectional Views of the Fluid and Solid Mesh

For the solid, unstructured meshes are set up for the cylinders and their internal bobs. The solid mesh for the cylinders is also created using the 'Automatic Mesh' functionality of STAR-CCM+. The 'Thin Mesher' and 'Tetrahedral Mesher' are selected with 3 thin layers, the 'Quad Dominant' meshing method and a target bs of 0.375 mm which leads to a mesh with 276205 elements for each of the cylinders. For the bobs, the 'Directed Mesh' functionality is used which creates a given number of layers of the same planar or 'Patch Mesh'. For the 'Patch Mesh', the 'Automatic Mesh' functionality is selected along with the 'Quadrilateral Mesher'. The mesh is given 40 layers for the bob in Cylinder1, 80 layers for the bob in Cylinder2 and a target bs of 0.37 mm which leads to element counts of 20992 and 43824 respectively. Sectional views of the solid mesh are shown in Figure 6.4b. For low computational effort, linear finite elements are employed by disabling the 'Mid-side Vertex' option.

For the experimental study, it was mentioned that the brass bobs were 14 mm and 29 mm in length excluding the solder. Furthermore, the cylinders had additional length that ran into the wall of the channel which was then fixed by a tightening nut arrangement. This and the fact that the mass due to the soldering process and the accelerometer itself is unaccounted for, there is a need to fine tune the structural model to have the same natural frequency as the experiment. This is done by altering the length of the bobs and is discussed further in the following subsection.

6.2.1. CSM Study

As mentioned earlier, the cylinders in the experiment are slightly longer with the extra length running into the channel wall where they are constrained by a tightening nut. The schematic of the same is shown in Figure 6.5. Furthermore, the brass accelerometer mountings were mentioned to be 14 mm and 29 mm in length excluding the solder. This and the fact that there is no accelerometer equipment (which has its own mass) in the numerical setup calls for fine tuning the structural model.
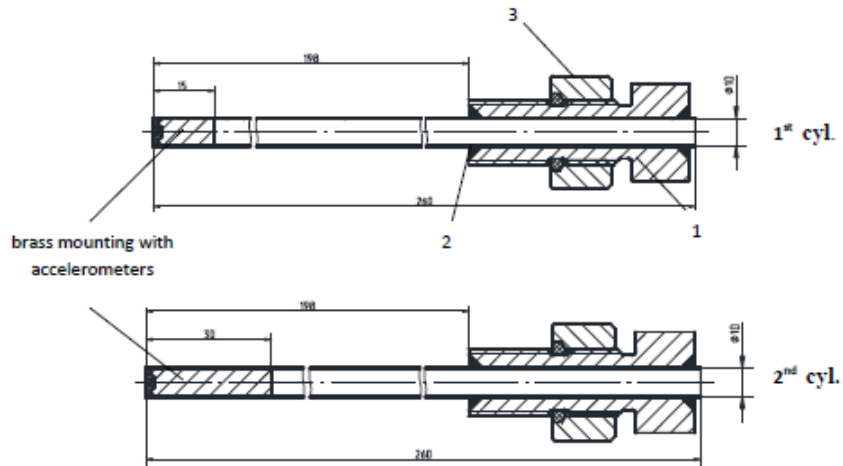
Figure 6.5: Schematic of the Cylinders used in the Experiment

In the current numerical setup, the brass mountings, the solder and the accelerometer mass is to be represented by the brass bobs alone. The fine tuning is thus aimed by modifying the bob lengths. Testing is carried out in both in vacuum and in water. The results of interest are the natural frequencies in vacuum and water and the added damping for the test in water. No additional damping is made use of for these tests.

The tests are carried out as follows: For the both the tests in vacuum and in water, a numerical gravity of 10g is applied to the cantilevered cylinders in the y-direction which would result in tip displacements comparable in magnitude to the FSI test. When the cylinders come to the position of maximum tip displacement, the gravity is switched off and free oscillations of the cylinders are captured. To calculate the natural frequencies, the time interval between successive oscillations are used. As for the damping in water, the same expression introduced in the open phase is used:

$$\zeta = \frac{1}{\sqrt{1 + \left(\frac{2\pi}{\delta}\right)^2}} \tag{6.3}$$

where δ is the logarithmic decrement of the structural response (tip displacement) in water.

In STAR-CCM+, the 'Solid Stress' solver is selected along with a 2nd order Newmark implicit integration scheme (Newmark parameter, γ=0.5). The infinitesimal strain approximation given by the 'Linear Geometry' model is also selected. A time step satisfying the 100 sampling point rule is selected based on the natural frequency of Cylinder1 in air (183.9 Hz) for the tests in vacuum and water (Δt=0.05 ms). For the test in water, the fluid domain consists of still water in the channel which is obtained by setting the inlet velocity to 0 m/s. For the fluid, the 'Implicit Unsteady' SIMPLE scheme 'Segregated Flow' solver is selected with a 2nd order upwind convection scheme and the 'Laminar Flow' model. The pressure and velocity equations are given UR factors of 0.2 and 0.6 respectively. For the FSI coupling, a UR factor of 0.5 is used.

Obtained Results

The current bob lengths of 14 mm and 29 mm do not account for the mass of the solder and the accelerometer itself. The vacuum and water tests are conducted for these bob lengths as well as slightly increased bob lengths of 15 mm and 30 mm respectively. The predictions for the natural frequency of the cylinders in vacuum are tabulated in Table 6.2. Based on the tests in vacuum, a bob length pair of 15 mm and 30 mm appears to be the best choice with relative errors in natural frequency at 0.699% and 0.018% for Cylinder1 and Cylinder2 respectively.

Table 6.2: Results for Vibration Tests in Vacuum

Pairs of Bob	Natural Frequency (Hz)	
Lengths (mm)	Cylinder1	Cylinder2
14.0, 29.0	186.34	169.97
15.0, 30.0	185.19	168.77
Exp. Soln.	183.90	168.80

The vibration tests are also conducted in water using the 'Laminar Flow' model. The results for the natural frequencies and the damping ratio are tabulated in Table 6.3 based on the time series shown in Figure 6.6. Based on these results as well, a bob length pair of 15 mm and 30 mm appears to be the best choice with regard to the natural frequency with relative errors of 0.236% and 0.941% for Cylinder1 and Cylinder2 respectively.

Table 6.3: Results for Vibration Tests in Water

Pairs of Bob	Natural Frequency (Hz)		Damping Ratio	
Lengths (mm)	Cylinder1	Cylinder2	Cylinder1	Cylinder2
14.0, 29.0	166.67	155.04	0.0023	0.0012
15.0, 30.0	165.29	154.44	0.0031	0.0012
Exp. Soln.	164.90	153.00	0.0035	0.0035

(a) Cylinder1
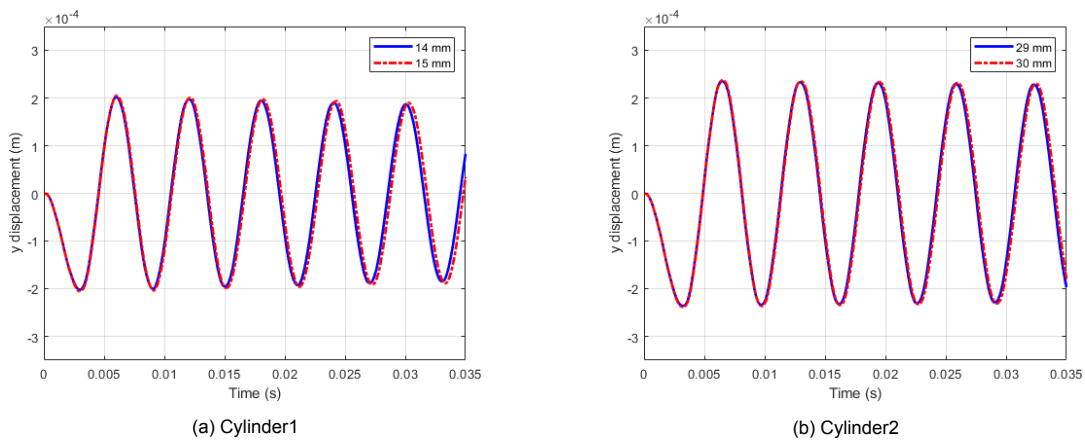
(b) Cylinder2

Figure 6.6: Y-displacement Time History Plots for the Tip Displacement of Cylinder1 and Cylinder2 in Water with Different Bob Lengths

Based on these results, the bob length pair of 15 mm and 30 mm is used for the FSI study which results in a mass ratio of m^*=3.278 and 3.584 for Cylinder1 and Cylinder2 respectively. The last item for the FSI setup is the mismatch in structural damping. There appears to be a significant gap in the prediction of the damping ratio in the above vibration test in water even for the optimal bob length pair especially for Cylinder2. This is remedied by adding structural damping via the aforementioned 'Rayleigh Damping' model. The difference between the damping calculated here and the expected value is used for calculating the stiffness constant as per Equation 3.31. With this, all relevant parameters for the FSI study are finalized and the results obtained for the same are discussed in the following section.

6.3. FSI Study

With the selected mesh and the fine tuned structural model, the FSI test is attempted for the off-resonance case of $0.74\ m/s$ inflow and the peak resonance case of $1.62\ m/s$ inflow using the shortlisted Standard K-Epsilon Low Re: Cubic turbulence model. To keep the FSI coupling stable during the start up of the simulation, a cosine ramping of the inflow velocity is given for $0.75\ s$ $(1.01\ FP)$ for the off-resonance case and for $0.7\ s$ $(2.06\ FP)$ for the peak resonance case as per Equation 6.2. A total simulation time of $11.3855\ s$ $(15.334\ FP)$ is provided for the off-resonance case while $5.5\ s$ $(16.204\ FP)$ is provided for the peak resonance case.

Since the experimental vortex shedding frequency (f_s) is unknown for the blind phase, Strouhal estimates of the same are made as per Equation 2.2 using an assumed $St = 0.21$. These lead to expected vortex shedding frequencies of $15.6\ Hz$ and $34.0\ Hz$ for the off-resonance case and peak-resonance case respectively. To adhere to the 100 sampling point thumb rule, a time step size of $0.75\ ms$ is used during the cosine ramping and is reduced to $0.5\ ms$ for the remainder of the simulation for the off-resonance case while corresponding values of $0.35\ ms$ and $0.24\ ms$ are used for the peak resonance case. Using the back-windowing approach on the created spectra plots, it was found that transient results lasted $2\ FP$ after the end of the cosine ramping period. Thus results corresponding to the last 14 FP for both cases are used for creating the spectra. Before presenting the main results, the selection of the inflow turbulence setting is addressed.

6.3.1. Inflow Turbulence

As was done for the open phase study, a choice for the turbulence intensity at the inlet is to be made. Based on the experimental data shown in Figure 6.7, a turbulence intensity of 2.21% and 2.12% were predicted by the PIV measurements for the off-resonance ('OR') case and the peak resonance ('R') case respectively. Assuming the same amount of decay of turbulent kinetic energy with distance as for the open phase and using Equation 5.5, a value of about 6% should suffice for the inlet turbulence intensity. However, rather than satisfying this parameter at a distance of $140\ mm$ ahead of Cylinder1, as was done for the open phase, it is intended here to give a sufficiently high inlet turbulence intensity such that the final value at the location of Cylinder1 matches the experimental conditions. In this regard, a value of 10% is chosen for the inlet turbulence intensity.

Based on this choice of turbulence intensity, the numerical results ('Sim') are also plotted in Figure 6.7. For the mean velocity shown in Figure 6.7a, the simulation results show underpredicted velocities at the center of the domain with better agreement close to the channel walls. The relative errors of underprediction of the mean velocity is found to be 4.19% and 3.63% at the center of the channel width for the off-resonance and the peak resonance cases respectively. For the same flow rate, this implies that the predicted boundary layer thickness at this location is much thinner than it should be as is confirmed by the early flattening out of the velocity profile.

(a) Mean Velocity

(b) RMS Velocity Fluctuation
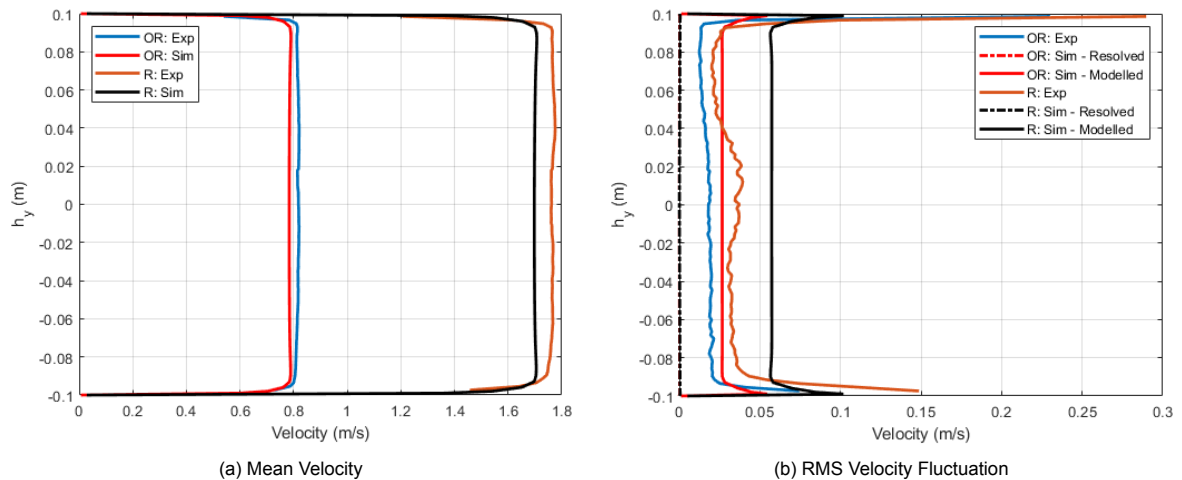
Figure 6.7: Mean and RMS Fluctuation Streamwise Velocity Profiles at a Vertical Section $140\ mm$ ahead of Cylinder1

For the RMS fluctuations shown in Figure 6.7b, the simulation results are presented as a quantity re-solved by the mesh and as one modelled through the turbulent kinetic energy as was done for the open phase study. Due to the absence of actual turbulent structures, the resolved fluctuations are small be-ing of the order of 1E-4 m/s at the channel center to 1E-3 m/s close to the channel wall. The modelled fluctuations, however, are of the same order of magnitude as the experimental data and are observed to be overpredicted at the channel center by 46.83% and 53.62% respectively for the off-resonance and the peak resonance cases. This is expected as a higher turbulence intensity was set for the inlet than estimated. It is expected that the modelled fluctuation results would be in much better agreement with those 50 mm ahead of Cylinder1 on account of the dissipation of turbulent kinetic energy.

As per Figure 6.3, velocity profiles are also available at horizontal sections 50 mm and 200 mm ahead of Cylinder1. These are shown in Figure 6.8 and Figure 6.9 respectively.

(a) Mean Velocity at Plane Z_1

(b) RMS Velocity Fluctuation at Plane Z_1

(c) Mean Velocity at Plane Z_2

(d) RMS Velocity Fluctuation at Plane Z_2

(e) Mean Velocity at Plane Z_3

(f) RMS Velocity Fluctuation at Plane Z_3
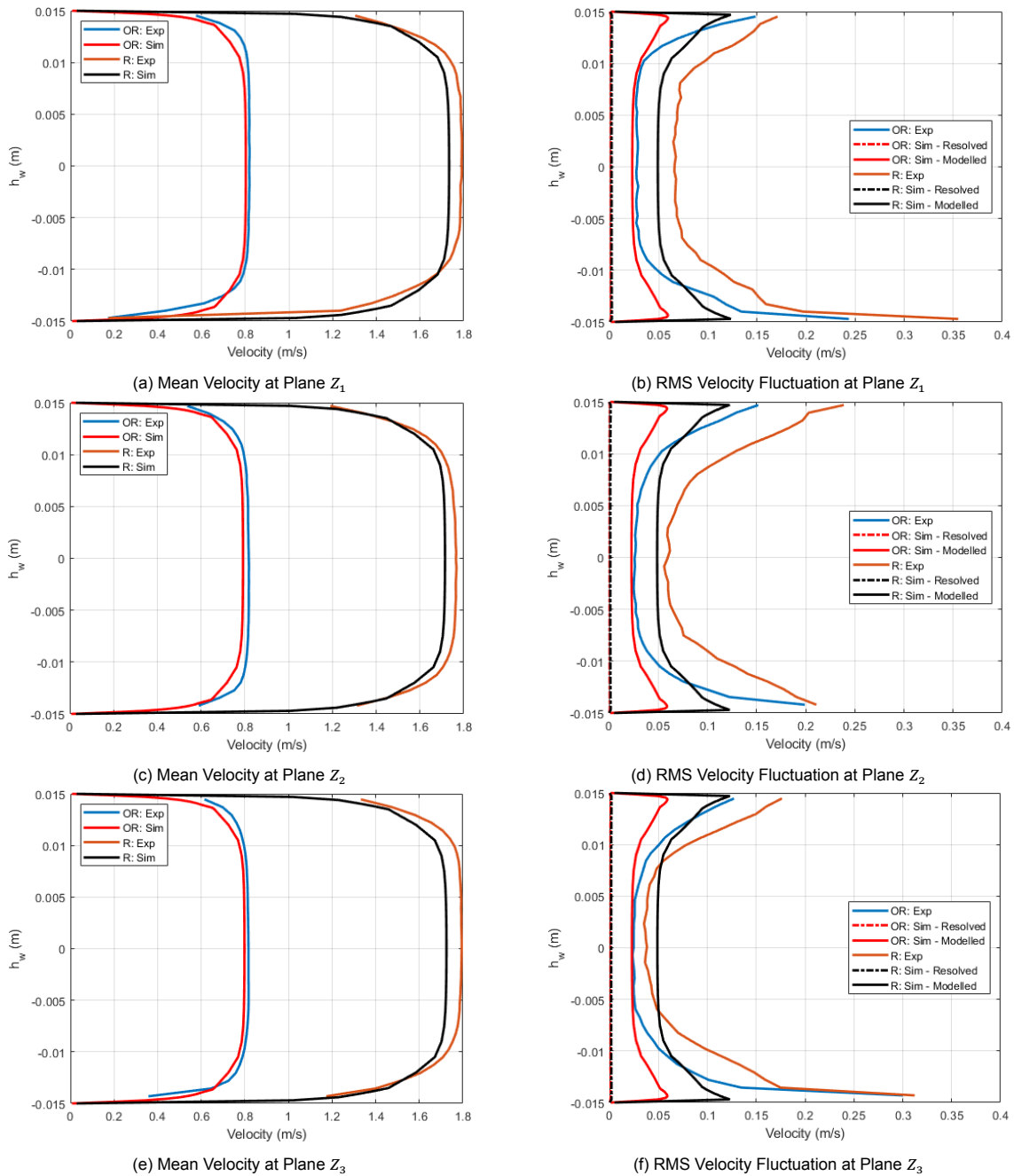
Figure 6.8: Mean and RMS Fluctuation Streamwise Velocity Profiles at a Horizontal Section 50 mm ahead of Cylinder1

(a) Mean Velocity at Plane Z_1

(b) RMS Velocity Fluctuation at Plane Z_1

(c) Mean Velocity at Plane Z_2

(d) RMS Velocity Fluctuation at Plane Z_2

(e) Mean Velocity at Plane Z_3

(f) RMS Velocity Fluctuation at Plane Z_3

(g) Mean Velocity at Plane Z_4

(h) RMS Velocity Fluctuation at Plane Z_4
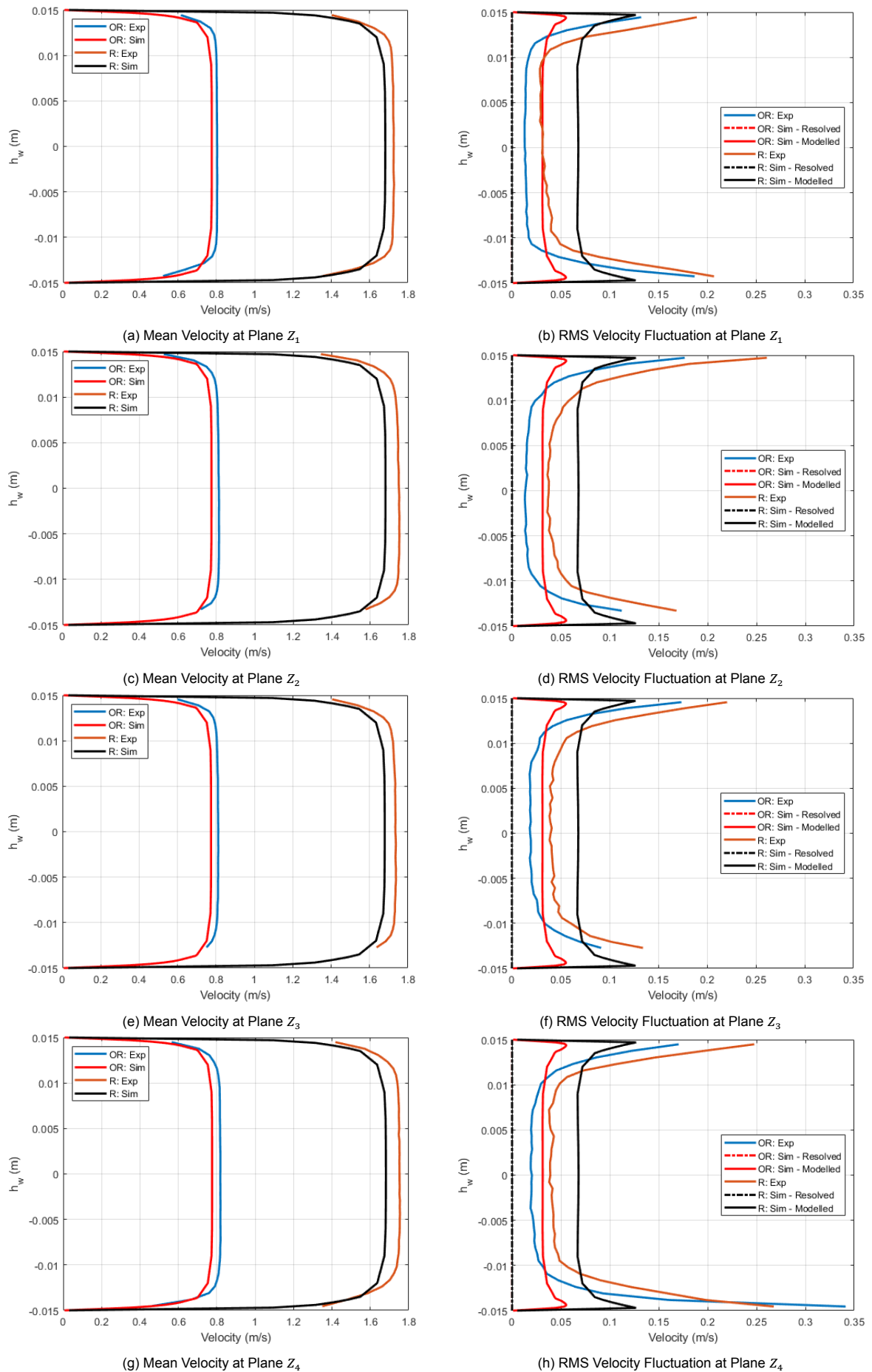
Figure 6.9: Mean and RMS Fluctuation Streamwise Velocity Profiles at Horizontal Sections 200 mm ahead of Cylinder1

The mean velocity profiles of Figure 6.9 at different planes 200 mm ahead of Cylinder1 reveal slightly underpredicted channel center velocities by the simulation as was seen for Figure 6.7 with average relative errors of 2.13% and 3.42% over the 4 planes for the off-resonance and peak resonance cases respectively. The numerical and experimental results show symmetric profiles with slight variations across different planes of measurement. This variation across planes is minimal (within 1% at the channel width center) owing to the large distance from Cylinder1.

For the RMS fluctuations of Figure 6.9, the observations for the resolved fluctuations are similar to the vertical section velocity profile with very low fluctuations detected as per expectations. The observations are also similar for the modelled fluctuations with overpredictions towards the center of the channel width as well as disagreement in the fluctuations of the channel wall boundary layer. The average relative errors of the modelled fluctuations at the center of the channel width are 91.38% and 84.99% for the off-resonance and peak resonance cases respectively. Unlike the simulation curves, the experimental curves also show slight asymmetry and significant variation (within 20% at the channel width center) across the planes of measurement.

Coming closer to Cylinder1, at a distance of 50 mm, observing the mean profiles of Figure 6.8, the experimental results show asymmetric profiles that vary slightly (within 1% at the channel width center) across different planes of measurement with the largest visible deviation at plane Z_2. The boundary layer at the channel wall also appears to have grown from what it was at a distance of 200 mm, as the velocity profile has become more parabolic in nature. The simulation results are still underpredicted at the center of the channel width with average relative errors of 2.48% and 3.31% for the off-resonance and peak resonance cases respectively which is comparable to the errors observed 140 mm and 200 mm ahead of Cylinder1.

For the RMS fluctuations of Figure 6.8, however, there is better agreement between the modelled fluctuations and experimental results especially for the off-resonance case. Unlike the results at 140 mm and 200 mm ahead of Cylinder1, however, the modelled fluctuations are underpredicted at the center of the channel width for the off-resonance case and for planes Z_1 and Z_2 for the peak resonance case. The average relative errors at the center of the channel width are 11.83% and 10.16% for the off-resonance and peak resonance cases respectively. Comparing the errors to those at 140 mm and 200 mm ahead of Cylinder1, it appears that the errors go down as Cylinder1 is approached. This implies that the dissipation of turbulent kinetic energy by the Standard K-Epsilon Low Re: Cubic model is much larger than that in the experiment. The experimental curves are observed to be asymmetric and significantly varying (within 30% at the channel width center) across the planes of measurement.

Based on the results discussed so far, the setting for the inlet turbulence is considered acceptable. The following section shows the pressure, acceleration and velocity spectra followed by the the vorticity plots and the velocity profiles aft of the cylinders.

6.3.2. Obtained Results

The primary results of interest for the FSI study are the velocity, acceleration and pressure spectra for the points as per Figure 6.2. The pressure spectra plots for the the off-resonance ('OR') case and the peak resonance ('R') case are shown along with the experimental results in Figure 6.10. To obtain clean spectra plots, linear averaging is applied with a window size of 30, 15 and 10 for the experimental results and numerical results for the OR and R cases respectively. The experimental results show several peaks that correspond to multiples of the vortex shedding frequency ($f_s = 21.81\ Hz$ [OR], $39.89\ Hz$ [R]) and the natural frequency of Cylinder1 ($f_{n1} = 160.4\ Hz$) and Cylinder2 ($f_{n2} = 152.4\ Hz$). The other distinct peaks in the experimental results are suspected to be linked with the pump frequency.

As the flow rate is increased, the PSD levels increase for both the experimental and numerical results. However, the numerical results show overpredicted background spectra levels by an order of magnitude. This was also observed to a lesser extent for the prediction of P_4 in the open phase FSI test (see Figure 5.20d). The reasoning given in the open phase about the cause being the redistribution of peak spectral densities to higher frequencies with the breakdown of turbulence to smaller scales does not seem as plausible here.

(a) P_1

(b) P_2

(c) P_3

(d) P_4
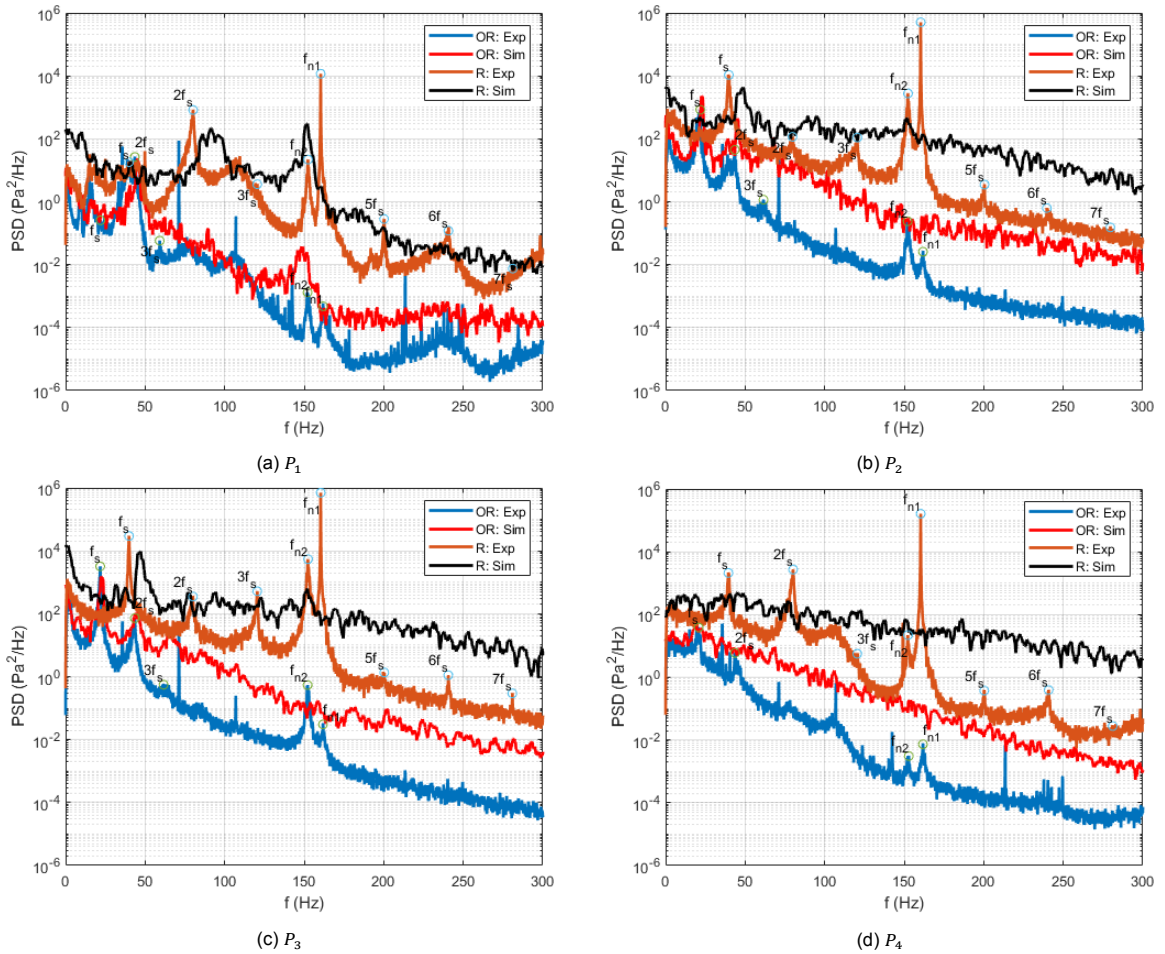
Figure 6.10: Pressure Spectra Plots

For the natural frequency of the cylinders, only that of Cylinder2 is distinct as was the case in the open phase FSI study. The absence of actual turbulence from the inlet in the simulation for both flow rates is suspected to be the reason why Cylinder1 is not excited for the off-resonance case. For the peak resonance case, this reason along with the fact that the vortex shedding frequency is overpredicted, is suspected to have caused an even larger gap between the experimental and numerical results. The vortex shedding frequencies predicted here are 22.93 Hz and 48.76 Hz which translates to relative errors of 5.13% and 22.24% for the off-resonance and peak resonance cases respectively.

Not all harmonics of f_s are distinct for the numerical solution. For P_1, only the first even harmonic is distinct while for P_2 and P_3, only the first harmonic is distinct for the peak resonance case while the first three harmonics are distinct for the off-resonance case. For P_4, no harmonic of the vortex shedding frequency is captured for either of the two cases. These observations are in line with those for the open phase FSI study where it was reasoned to imply an easier propagation of the frequency pertinent to the streamwise direction (even harmonics) than it is for the cross flow (odd harmonics) and that the first harmonic is more easily captured immediately downstream of the source (the cylinders) rather than upstream.

The acceleration spectra of the cylinders obtained from the experiment and numerical simulations are shown in Figure 6.11. The same linear averaging is applied here as the pressure spectra plots. The experimental results for Cylinder1 and Cylinder2 reveal distinct peaks at the vortex shedding frequency (f_s) and its multiples as well as the natural frequencies f_{n1} and f_{n2} in both streamwise (x) and cross flow (y) directions. The numerical results show distinct peaks corresponding to the even harmonics of f_s in the x-direction and the odd harmonics of f_s in the y-direction. The numerical results also show peaks for f_{n1} and f_{n2} in both directions.

(a) Cylinder1: x-direction

(b) Cylinder1: y-direction

(c) Cylinder2: x-direction

(d) Cylinder2: y-direction
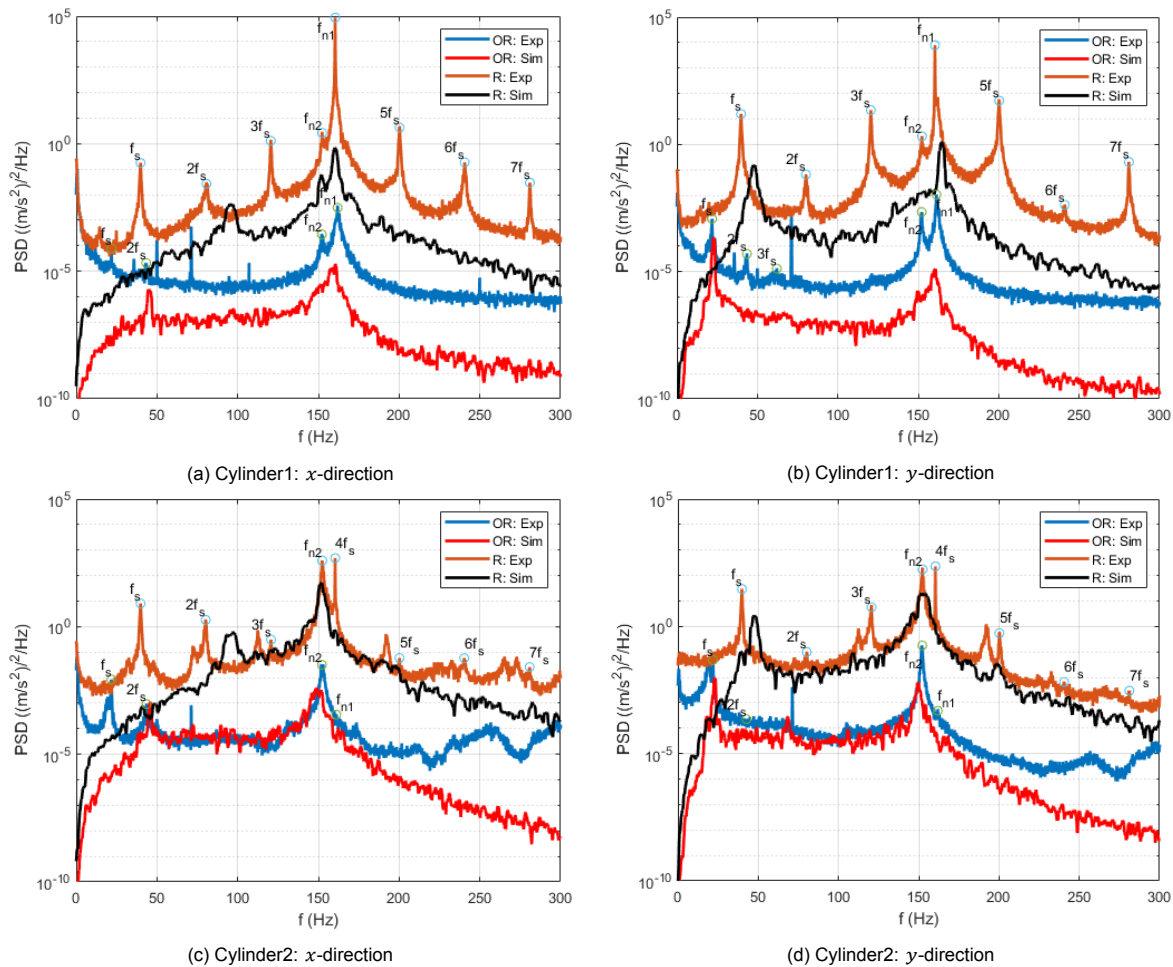
Figure 6.11: Acceleration Spectra Plots for the Cylinders

For the spectra of Cylinder1, the numerical results are underpredicted for both the off-resonance and peak resonance conditions. At f_{n1}, the error is of 2 orders of magnitude in the x-direction while it is of 3 orders of magnitude in the y-direction for the off-resonance case. The error is even more severe for the peak resonance case with corresponding errors of 5 orders of magnitude in the x-direction and 4 orders of magnitude in the y-direction. For the peak resonance case, the mismatch of the fourth harmonic of f_s with f_{n1} is suspected to be the main reason as was stated while reasoning the open phase FSI results. Even so, the other reason was reasoned to be the absence of inlet turbulence that could explain the gap in the results of the off-resonance case and that of the background spectra of the peak resonance case.

For Cylinder2, the match in the background spectra is much better for both the cases with underpredictions in the higher frequency range. The match is much better for Cylinder2 owing to the presence of actual turbulence generated from Cylinder1. As was reasoned for the open phase FSI study, having better predictions in the high frequency range requires a smaller time step, grid size and even a higher fidelity method such as LES instead of URANS. Even though the background spectra overlaps with the experimental curve in the low frequency range, the peak spectral density at f_{n2} is still underpredicted. At f_{n2}, the error is of 1 order of magnitude in the x-direction while it is of 2 orders of magnitude in the y-direction for the off-resonance case. The error is about the same for the peak resonance case with corresponding errors of 1 order of magnitude in the x- and y-direction. The error is comparatively less compared to Cylinder1 on account of the fact that Cylinder2 is always in an off-resonance condition for both cases.

The predictions of the numerical vortex shedding frequency are confirmed to be the same values quoted from the pressure spectra plots. The natural frequency of Cylinder1 is predicted to be 164.6 Hz from the y-direction spectra while it is predicted to be 160.5 Hz in the x-direction which translates to errors of 2.61% and 6.23E-2% respectively. Similarly, the natural frequency of Cylinder2 is predicted to be 151.4 Hz from the y-direction spectra while it is predicted to be 152.1 Hz in the x-direction which translates to errors of 0.66% and 0.20% respectively. The fine tuned structural model is thus confirmed to give the correct value for the natural frequency of the cylinders. Improving the prediction of the same warrants for the further modification of the pairs of bob lengths which is not carried out in this study.

The velocity spectra plots for the two cases are shown along with the experimental results (available only in the x-direction) in Figure 6.12 through Figure 6.14. To obtain clean spectra plots, the same linear averaging is applied as the pressure and acceleration spectra plots. These spectra, in principle, captures the turbulence present in the flow from the inlet (relevant for all planes) as well as that generated at the channel walls (relevant for planes Z_1 and Z_3), the cylinder curved surface (relevant for all planes) and the 2 mm gap at the free end of the cylinder (relevant for plane Z_1). The experimental results show peaks for the vortex shedding frequency and its harmonics. Not all peaks are distinct, however, with some expected peaks being at the same level as the background spectra.

Similar trends are observed for the numerical results with the spectra towards higher frequencies showing underpredicted results. It appears that the underprediction of the background spectra begins earlier for the off-resonance case (at 105 Hz on average) than it does for the peak resonance case (at 220 Hz on average). However, looking at these numbers as multiples of the vortex shedding frequency for the corresponding case reveals that the match in the background spectra is till about the fifth harmonic of the vortex shedding frequency. As reasoned earlier for the acceleration spectra as well as the corresponding plots for the open phase FSI study, a higher fidelity method along with smaller mesh size and time step is warranted for seeing improvements in the prediction as the small scale turbulence gets resolved better.

As was observed for the acceleration and pressure spectra plots, the vortex shedding frequency is overpredicted for both the off-resonance and peak resonance cases. Comparing the spectral density at the vortex shedding frequency shows predictions of the same order of magnitude as the experimental results at all planes for the off-resonance case and plane Z_3 for the peak resonance case while there is an order of magnitude difference for planes Z_1 and Z_2 for the peak resonance case. It is also observed that the vortex shedding frequency captured by the experiment as well as the numerical results vary slightly along the length of the cylinders. In particular, the prediction by V_1^i and V_3^i were found to be the same as V_2^i and V_4^i respectively. The experimental as well as numerical predictions for f_s are tabulated in Table 6.4 for V_1^i and V_3^i with corresponding (x-direction) relative errors tabulated in Table 6.5.

Table 6.4: Vortex Shedding Frequency Predictions by the Experiment and the Simulation

O	f_s at V_1^1 (Hz)		f_s at V_1^2 (Hz)		f_s at V_1^3 (Hz)		f_s at V_3^1 (Hz)		f_s at V_3^2 (Hz)		f_s at V_3^3 (Hz)	
R	Exp.	Sim.	Exp.	Sim.	Exp.	Sim.	Exp.	Sim.	Exp.	Sim.	Exp.	Sim.
x	21.5	21.2	21.5	22.6	19.0	22.1	21.3	20.6	21.6	22.8	19.7	22.3
y	-	21.7	-	22.6	-	22.0	-	21.4	-	22.7	-	22.2
R	f_s at V_1^1 (Hz)		f_s at V_1^2 (Hz)		f_s at V_1^3 (Hz)		f_s at V_3^1 (Hz)		f_s at V_3^2 (Hz)		f_s at V_3^3 (Hz)	
	Exp.	Sim.	Exp.	Sim.	Exp.	Sim.	Exp.	Sim.	Exp.	Sim.	Exp.	Sim.
x	39.9	46.4	40.0	47.1	40.7	44.7	40.1	42.7	40.0	44.4	40.0	44.2
y	-	46.4	-	47.1	-	44.7	-	45.1	-	47.3	-	44.4

Table 6.5: Relative Errors in Predicting the Vortex Shedding Frequency by the Simulation

Test Case	V_1^1 (%)	V_1^2 (%)	V_1^3 (%)	V_3^1 (%)	V_3^2 (%)	V_3^3 (%)
OR	1.395	5.116	16.316	3.286	5.556	13.197
R	16.291	17.750	9.828	6.484	11.000	10.500

(a) V_1^1: x-direction

(b) V_1^1: y-direction

(c) V_2^1: x-direction

(d) V_2^1: y-direction

(e) V_3^1: x-direction

(f) V_3^1: y-direction

(g) V_4^1: x-direction
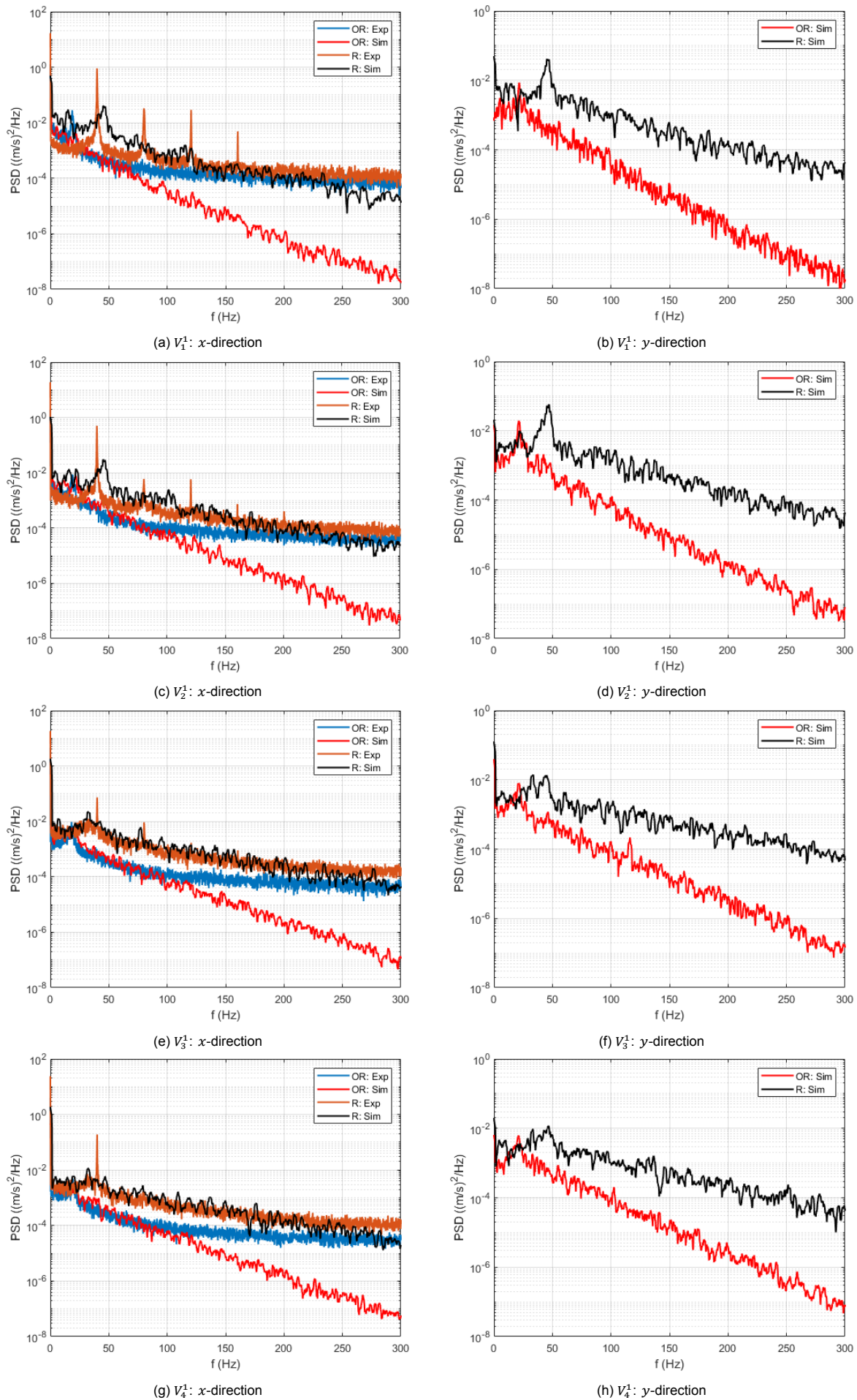
(h) V_4^1: y-direction

Figure 6.12: Velocity Spectra Plots: V_i^1, $(i = 1, 2, 3)$
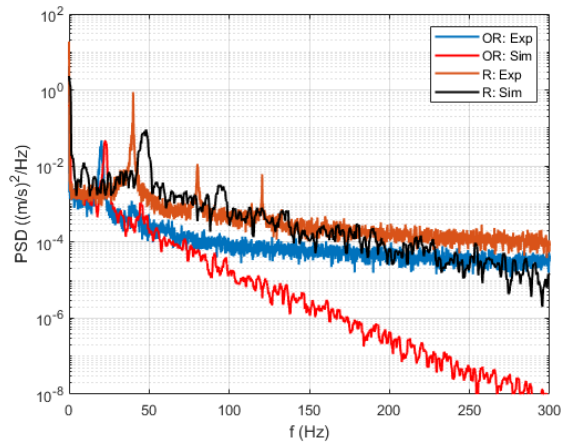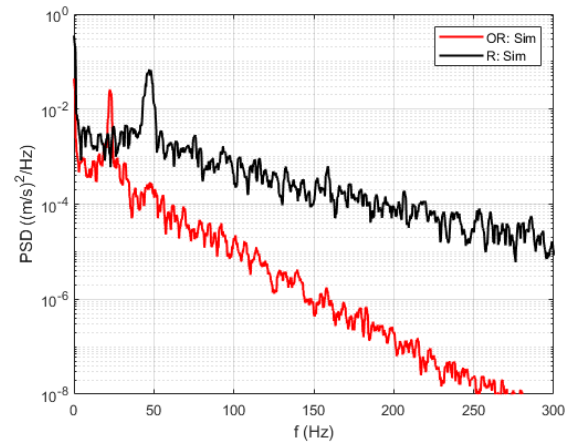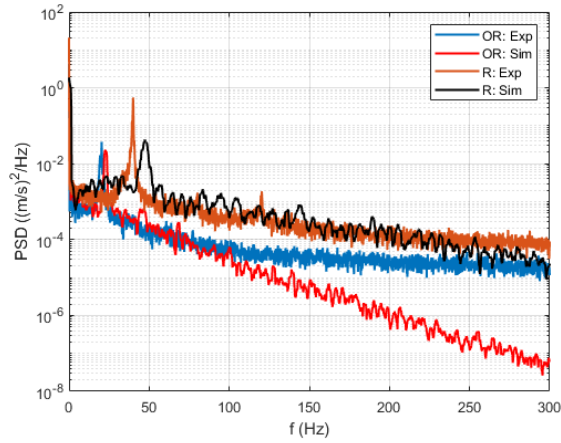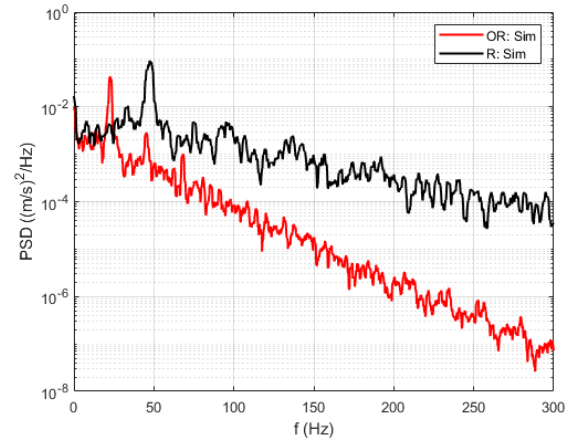
(a) V_1^2: x-direction

(b) V_1^2: y-direction

(c) V_2^2: x-direction
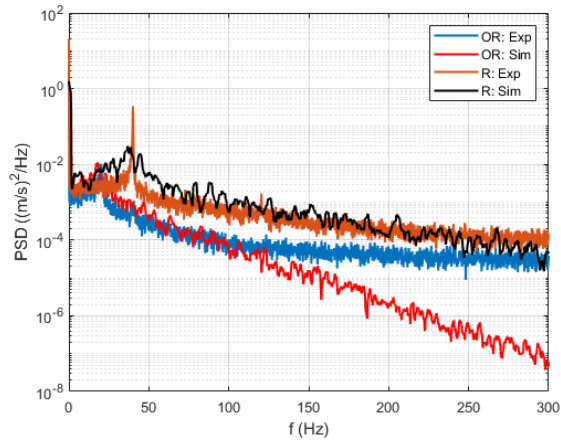
(d) V_2^2: y-direction
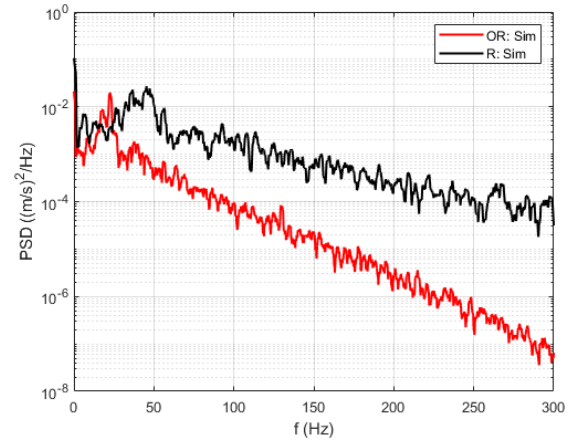
(e) V_3^2: x-direction
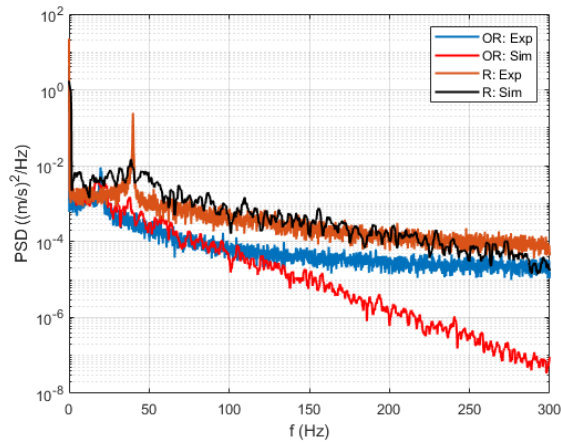
(f) V_3^2: y-direction

(g) V_4^2: x-direction
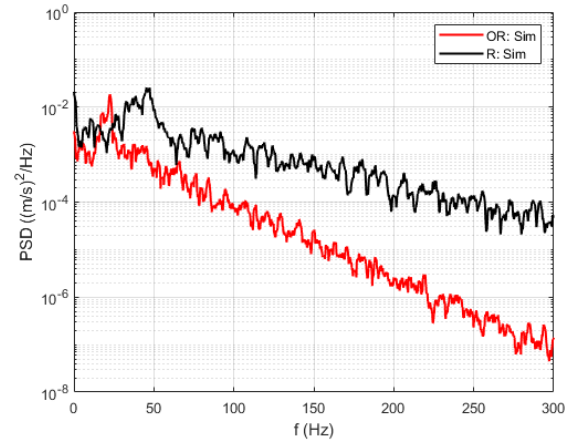
(h) V_4^2: y-direction

Figure 6.13: Velocity Spectra Plots: V_i^2, ($i = 1, 2, 3$)

(a) V_1^3: x-direction

(b) V_1^3: y-direction

(c) V_2^3: x-direction

(d) V_2^3: y-direction

(e) V_3^3: x-direction

(f) V_3^3: y-direction

(g) V_4^3: x-direction

(h) V_4^3: y-direction
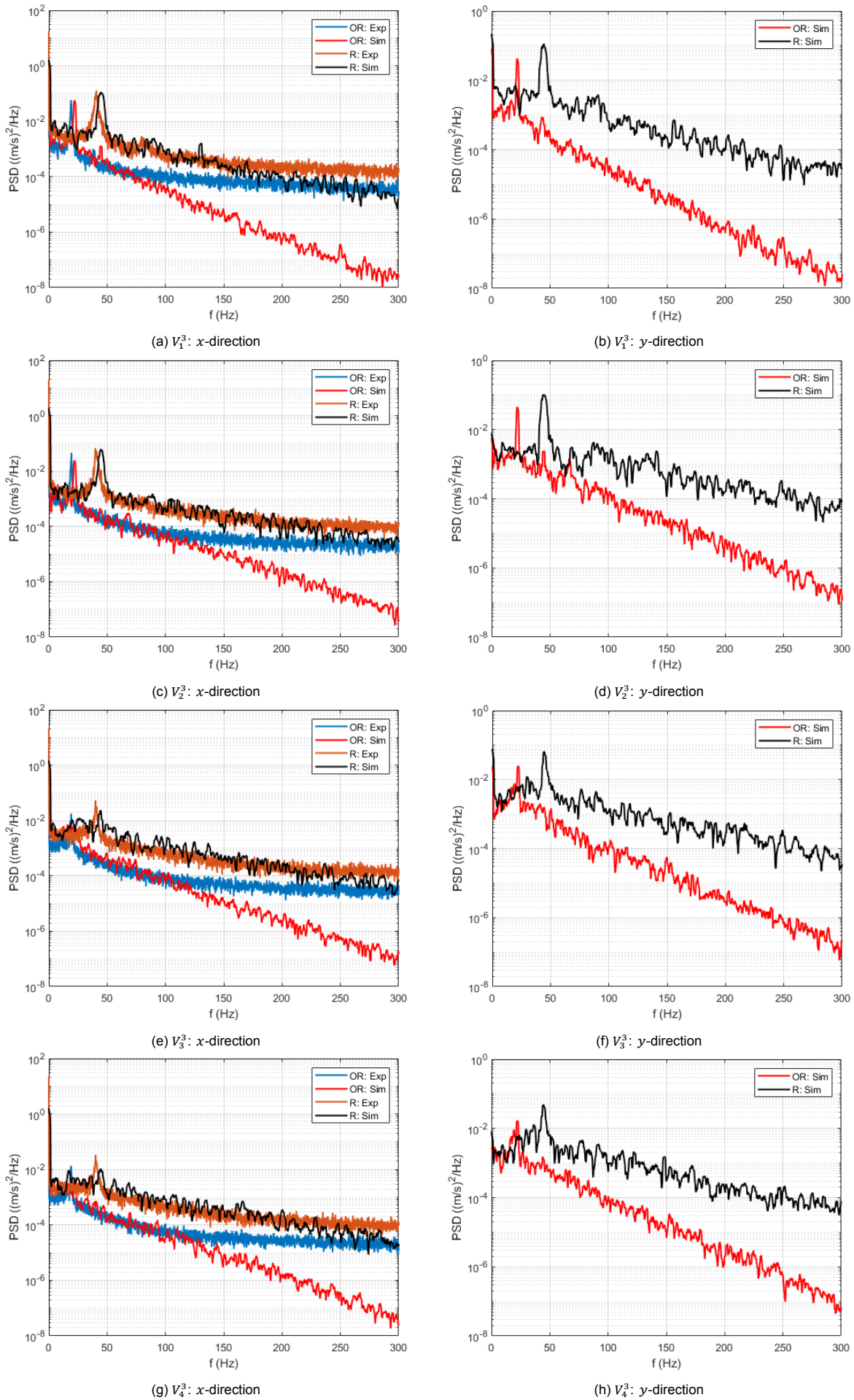
Figure 6.14: Velocity Spectra Plots: V_i^3, ($i = 1, 2, 3$)

The experimental results show the same value for the vortex shedding frequency at all locations for the peak resonance case. For the off-resonance case, the results are similar for plane Z_1 and Z_2 while there is a drop in the value at plane Z_3. The numerical results, on the other hand, predict a higher value at plane Z_2 compared to planes Z_1 and Z_3 at all locations. From Table 6.5, the largest errors are observed to be at plane Z_3 for the off-resonance case and at plane Z_2 for peak resonance case. In general, the errors are found to be higher for the peak resonance case than the off-resonance case.

Although experimental results are not available for the y-direction, the simulation results are tabulated in Table 6.4. The prediction of f_s is observed to be the same as that obtained from the x-direction velocity spectra for all locations except V_3^1 for both cases and at V_3^2 for the peak resonance case where the y-direction prediction is higher than that of the x-direction. It is to be noted that all the values quoted from the simulation have an uncertainty of about $\pm 1.5\ Hz$ in selecting the vortex shedding frequency owing to the flattening of the peak tips by the linear averaging process as was mentioned in the open phase FSI study. Withstanding this, the expectation drafted from the open phase study of overpredicting f_s for the peak resonance case is considered to be met.

A final observation from the velocity spectra trends is that the peaks are more distinct 10 mm behind the cylinders (V_1^i and V_3^i) rather than 20 mm behind the cylinders (V_2^i and V_4^i) with peaks being more distinct for V_1^i as compared to V_3^i. As was reasoned in the open phase CFD and FSI study, this is linked to the dissipation of vortical structures as they travel downstream and the presence of a source of turbulence (Cylinder1) upstream of Cylinder2. This is hinted by the vorticity plots shown in Figure 6.15 and Figure 6.16.

As was also observed from the open phase FSI study, 3D vortex tubes are shed from Cylinder1 with these regular structures breaking down into smaller ones as they travel towards Cylinder2. As they interact with Cylinder2 and its generated wake, the regular structures are completely lost for both the off-resonance and peak resonance cases. The turbulent structures are observed to have higher strength for the peak resonance case than the off-resonance case. This is expected since vorticity ($\vec{\omega} = \nabla \times \vec{U}$) scales with direction-derivatives of velocity which increase with increasing flow rate aft of the cylinders.
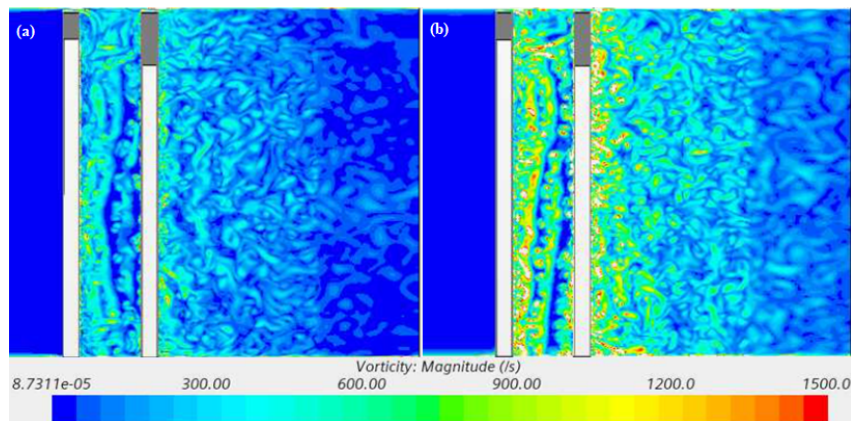
Figure 6.15: Vertical Section Vorticity Plots for (a) OR and (b) R Test Cases
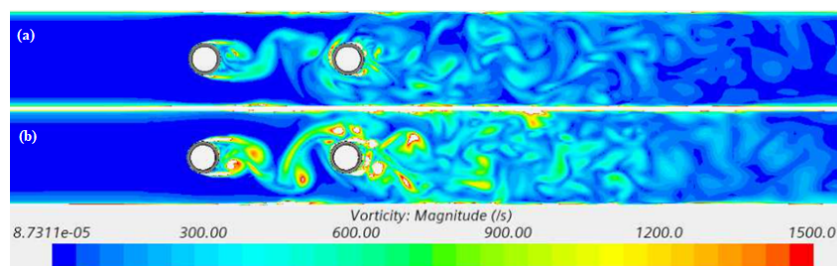
Figure 6.16: Horizontal Section Vorticity Plots for (a) OR and (b) R Test Cases at Plane Z_2

To confirm the similarity of the wake of the two cases, the vorticity is non-dimensionalized by the vortex shedding frequency which incorporates the influence of the flow rate via the Strouhal number. The non-dimensional vorticity plots so created are shown in Figure 6.17 and Figure 6.18. The near similar non-dimensional strength of the wake thus confirms the similarity of the wake for the off-resonance and peak resonance cases.
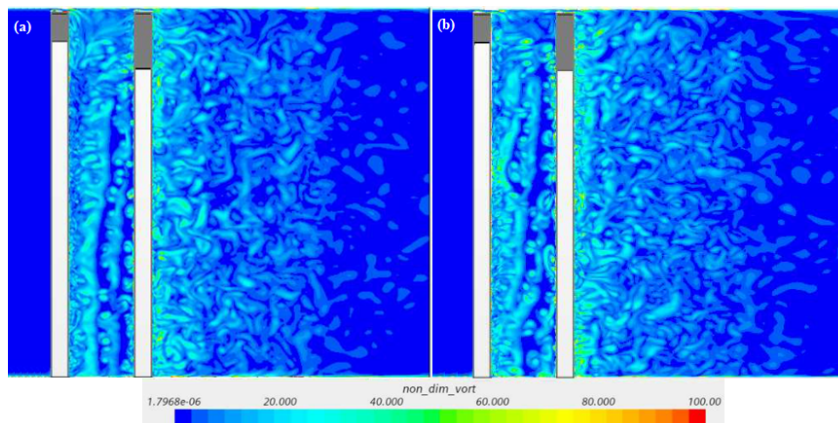
Figure 6.17: Vertical Section Non-dimensional Vorticity Plots for (a) OR and (b) R Test Cases
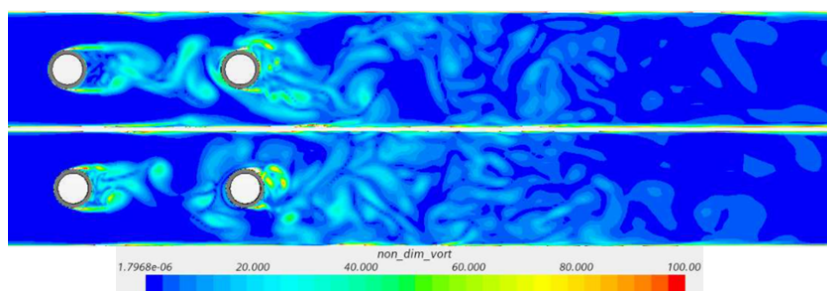
Figure 6.18: Horizontal Section Non-dimensional Vorticity Plots for (a) OR and (b) R Test Cases at Plane Z_2

The last set of results are the mean and RMS fluctuation velocity profiles at horizontal sections 10 mm and 20 mm behind each of the cylinders which are shown in Figure 6.19 through Figure 6.21. The explanation for the shape of these plots has already been discussed for the open phase FSI study. The PIV and LDV curves for the mean and RMS fluctuation velocity profiles are observed to agree with each other at all planes and locations of measurement.

The mean velocity profiles predicted for the off-resonance case qualitatively appears to match the experimental results well with the largest deviation observed for the profile 10 mm behind Cylinder1 at plane Z_2 (see Figure 6.20a) as a larger dip in mean velocity at the center of the channel width is predicted. On the other hand, the profiles for the peak resonance case have more deviations from the experimental profiles. In general, it is observed that the agreement between the numerical prediction and experimental results improves as the distance from the source of turbulence (cylinders) is increased. This observation holds for both the off-resonance and peak resonance cases.

The observations for the RMS fluctuation profiles are observed to be similar to those of the mean profiles with a better match for the off-resonance case predictions than the peak resonance case predictions with the corresponding experimental curves. The other observation of improving results with increasing distance from the cylinders seems to hold for the off-resonance case but not so for all solutions of the peak resonance case (see Figure 6.20b and Figure 6.20d for example).

(a) Mean Velocity 10 mm behind Cylinder1

(b) RMS Velocity Fluctuation 10 mm behind Cylinder1

(c) Mean Velocity 20 mm behind Cylinder1

(d) RMS Velocity Fluctuation 20 mm behind Cylinder1

(e) Mean Velocity 10 mm behind Cylinder2

(f) RMS Velocity Fluctuation 10 mm behind Cylinder2

(g) Mean Velocity 20 mm behind Cylinder2

(h) RMS Velocity Fluctuation 20 mm behind Cylinder2
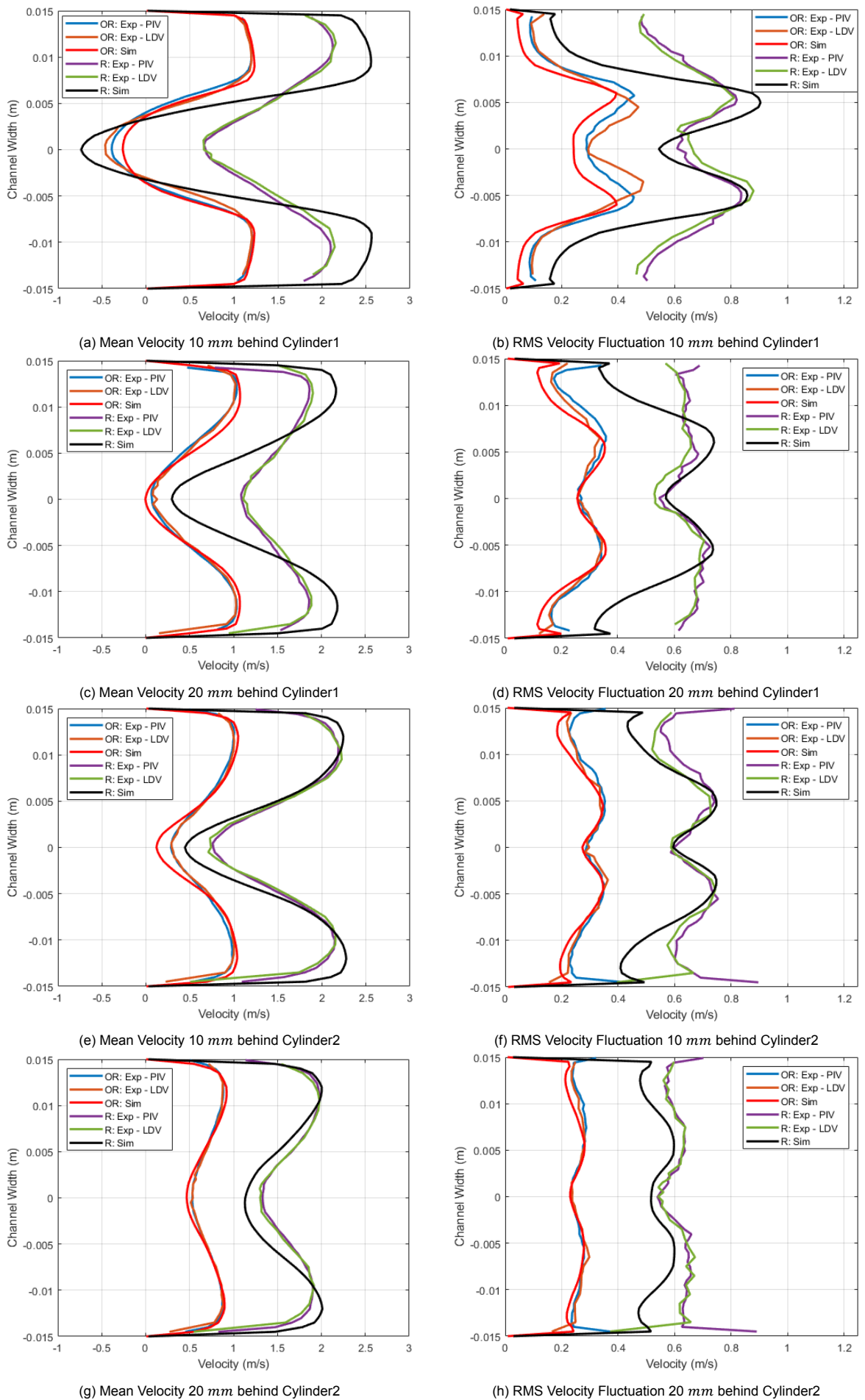
Figure 6.19: Mean and RMS Fluctuation Streamwise Velocity Profiles at Horizontal Sections in Plane Z_1

(a) Mean Velocity 10 mm behind Cylinder1

(b) RMS Velocity Fluctuation 10 mm behind Cylinder1

(c) Mean Velocity 20 mm behind Cylinder1

(d) RMS Velocity Fluctuation 20 mm behind Cylinder1

(e) Mean Velocity 10 mm behind Cylinder2

(f) RMS Velocity Fluctuation 10 mm behind Cylinder2

(g) Mean Velocity 20 mm behind Cylinder2

(h) RMS Velocity Fluctuation 20 mm behind Cylinder2
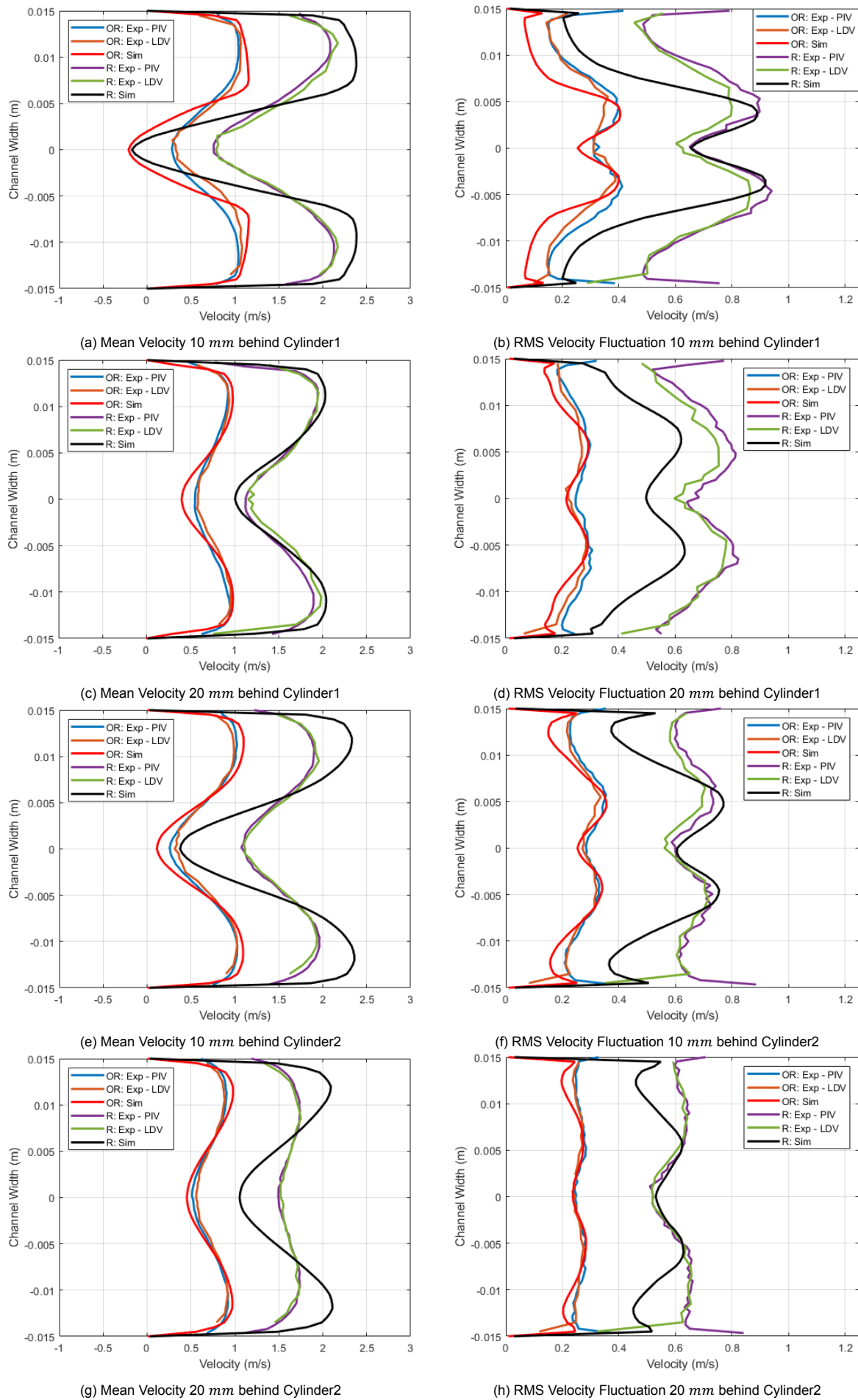
Figure 6.20: Mean and RMS Fluctuation Streamwise Velocity Profiles at Horizontal Sections in Plane Z_2
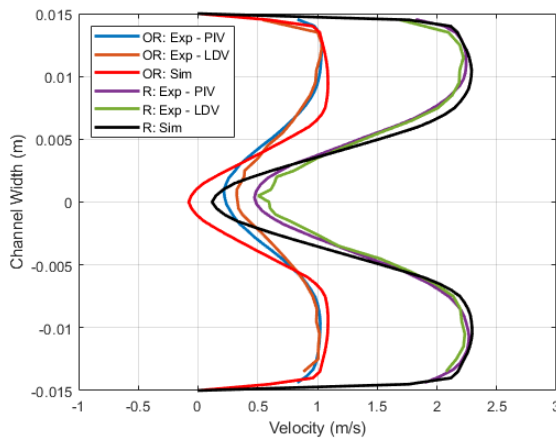
(a) Mean Velocity 10 mm behind Cylinder1
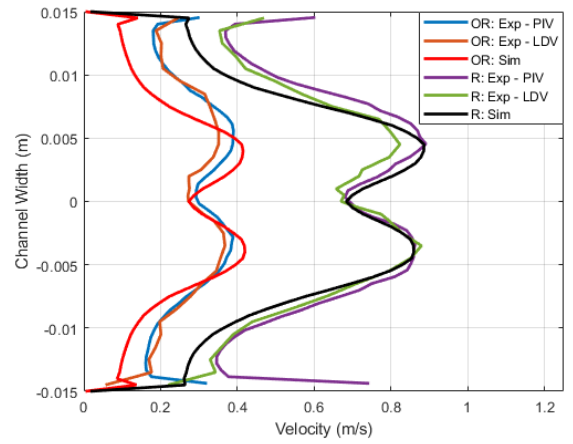
(b) RMS Velocity Fluctuation 10 mm behind Cylinder1
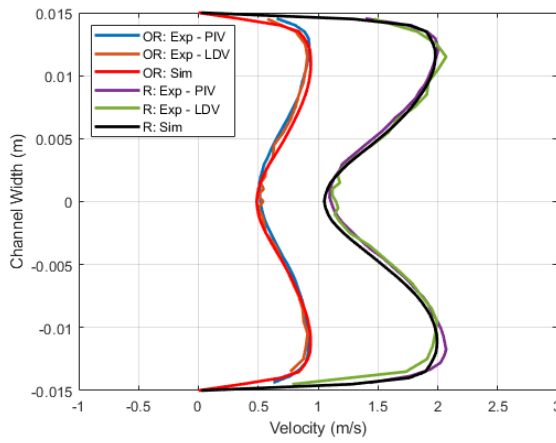
(c) Mean Velocity 20 mm behind Cylinder1
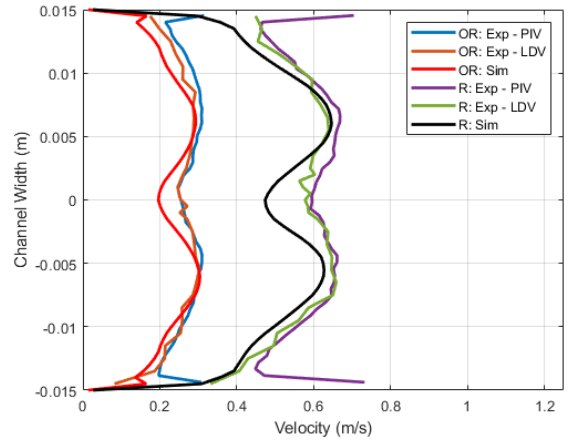
(d) RMS Velocity Fluctuation 20 mm behind Cylinder1
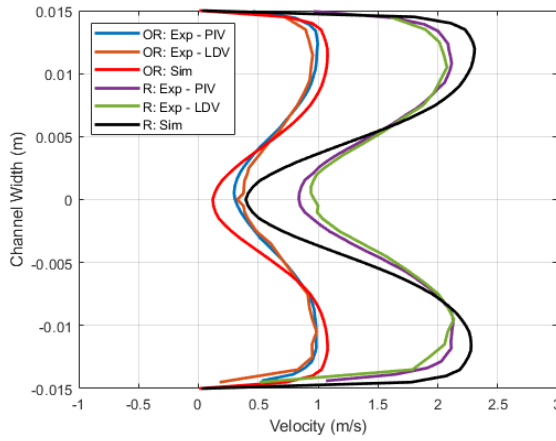
(e) Mean Velocity 10 mm behind Cylinder2
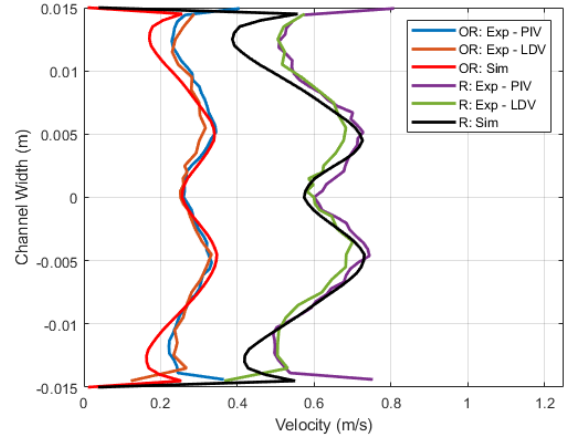
(f) RMS Velocity Fluctuation 10 mm behind Cylinder2
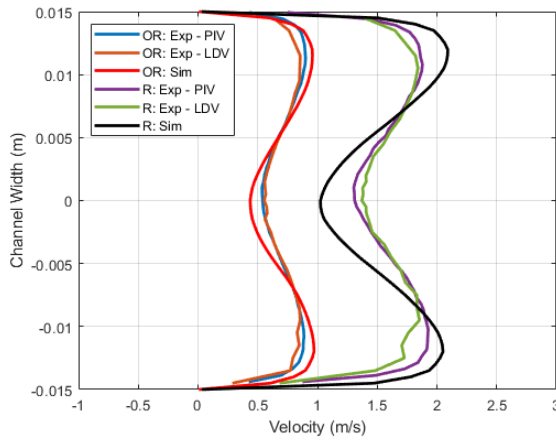
(g) Mean Velocity 20 mm behind Cylinder2
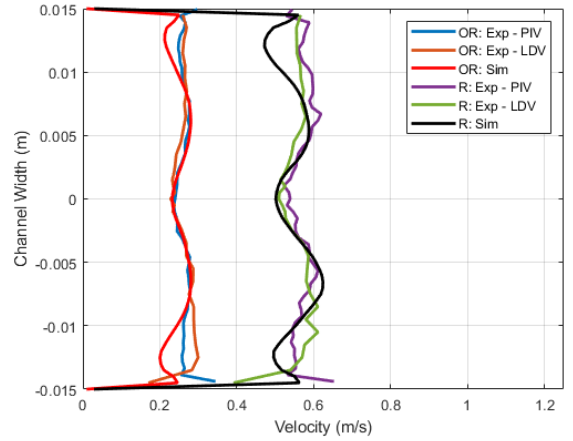
(h) RMS Velocity Fluctuation 20 mm behind Cylinder2

Figure 6.21: Mean and RMS Fluctuation Streamwise Velocity Profiles at Horizontal Sections in Plane Z_3

The current study attests to the shortcomings of the URANS scheme for predicting VIV, or as was reasoned earlier, a combination of VIV and TIV. The expectations drafted from the open phase FSI study have all been met from the blind phase results. The current scheme showed underpredicted spectra results for Cylinder1 in both the off-resonance and peak resonance cases. This was accompanied with an overprediction of the vortex shedding frequency. The results were better for Cylinder2 spectra plots, although the peak at its natural frequency was still underpredicted as was the spectral density for the higher frequency range.

With the observations of the current study corroborating those of the open phase study, the following gaps for the URANS scheme in predicting a combination of VIV and TIV still stand:

- Prediction of the vortex shedding frequency: For systems that suffer from the lock-in effect between the structural natural frequency and higher harmonics of the vortex shedding frequency, accurate prediction of the vortex shedding frequency appears to be an important criteria.

- Inflow turbulence: For systems that suffer from significant TIV contributions, it appears important to incorporate actual or modelled fluctuations of velocity and pressure (in essence turbulence) to capture accurate background spectra levels.

- Predicting high frequency range spectra: To capture the high frequency range correctly, it is requisite to capture the small scale turbulence in the flow.

The above gaps still serve as a hypothesis for the cause of the difference between the experimental and numerical FSI results for the open and blind phase. Additional tests are to be conducted to confirm this hypothesis. These future tests are recommended along with key conclusions from the current thesis work in the following chapter.

6.4. Conclusion

In this chapter, the blind phase study of the OECD Benchmark was introduced. The experimental setup, including the associated measurement systems and the blind phase test parameters, was briefly discussed. The primary intention with the current study was to confirm the expectations made from the open phase study using the shortlisted Standard K-Epsilon Low Re: Cubic turbulence model of the URANS scheme.

To schieve this agenda, numerical simulations were set up for two flow rates corresponding to the off-resonance case and the peak resonance case with respect to Cylinder1. This included fine tuning the structural model to the required natural frequencies in air and water. To do so, CSM vibration studies were carried out in vacuum and water for structures with different pairs of bob lengths. A bob length pair of 15 mm and 30 mm was finalized for the FSI study. For the FSI test, a fluid mesh similar in topology to the 'CFD3' mesh from the open phase study was set up with 7.78M cells consisting of elements of size 0.075D in the wake of the cylinders. This selection was constrained by the timeframe and resource budget of the current study.

With the selected numerical set up, the FSI study was carried out with the aforementioned shortlisted turbulence model. Before getting into the results, the modelled inflow turbulence condition was tested by plotting the streamwise velocity mean and RMS fluctuation profiles at sections 140 mm, 200 mm and 50 mm ahead of Cylinder1. For comparing with the experimental fluctuation profiles, resolved and modelled turbulence profiles were used from the numerical simulations. The chosen turbulence model showed quicker dissipation of the inlet turbulent kinetic energy as the flow moved downstream approaching the cylinders. The chosen turbulence model is also suspected to predict a smaller channel wall boundary layer height which was accompanied by a lower than expected velocity (within 5% for both flow rates) away from the channel walls as pointed out from the mean velocity profiles. All results considered, the selected overestimated inflow turbulence setting was considered satisfactory.

Considering the spectra plots for pressure, the background spectra for both flow rates were observed to be overpredicted. The reason for the same is unclear at this point.

Considering the spectra plots for acceleration, resonance was not able to be predicted for Cylinder1 as expected from the open phase study. The key reason for the same is again suspected to be the overprediction of the vortex shedding frequency (f_s) by 22.24% which led to a mismatch in the fourth harmonic of f_s and the natural frequency of Cylinder1 (f_{n1}). The results for Cylinder1 for the off-resonance case were also underpredicted. The contribution of TIV that was not captured here is suspected to be the primary reason. The match in the spectra results was much better for Cylinder2 on the other hand for both flow rates. However, the spectral density at the natural frequency of Cylinder2 (f_{n2}) was still underpredicted by an order of magnitude. An underprediction was also observed for the background spectra in the higher frequency range as was expected from the open phase study.

Coming to the velocity spectra results, the overprediction of the vortex shedding frequency was reconfirmed. Furthermore, the variation of this parameter across different measurement planes was also noted with largest error being 16.3% for the off-resonance case and 17.8% for the peak resonance case. The error in predicting the spectral density at the vortex shedding frequency was also noted to be significant (of an order of magnitude) for the peak resonance case at planes Z_1 and Z_2. The differences in results were reasoned to stem from the type of wake predicted. The vorticity plots revealed a strength difference between the off-resonance and peak resonance case. This effect was confirmed to be due to the inflow velocity magnitude by showing similar non-dimensional strengths of the wake.

The last set of results were the streamwise velocity mean and RMS fluctuation profiles 10 mm and 20 mm behind the cylinders. In general, the predicted profiles for the off-resonance case had a better qualitative fit with the experimental results than the peak resonance case with its corresponding experimental results. The mean profile curves showed improvements in prediction with increasing distance from the cylinders for both flow rates. This was also observed for the RMS fluctuation profiles although only for the off-resonance case.

Based on the shortcomings of the URANS scheme observed in the current study and the open phase, 3 reasons of gap between the current URANS results and the experimental results are formally drafted as a base for future testing. The following chapter brings forward the key conclusions of the thesis work and provides recommendations for further study.

7

Conclusions

This thesis work was set to tackle the Vortex-Induced Vibration (VIV) problem of in-line cantilevered cylinders subjected to cross flow as was proposed in the form of a benchmark by the Organization for Economic Co-operation and Development (OECD). To carry out this FSI study, one may have chosen a higher fidelity method for the CFD side such as Direct Numerical Simulations (DNS) or Large Eddy Simulations (LES) but for the current timeframe and available resources for the project, the computationally cheaper Unsteady Reynolds-Averaged Navier-Stokes (URANS) framework was selected. In doing so, the following objective was laid out for the thesis work:

> *"To test the efficacy of URANS models in the prediction of VIV by selecting the best suited URANS model (and associated settings) for the OECD benchmark and establishing the gap between this model and the available experimental data".*

To work towards this objective, a 3-phase plan of action was set up for using the commercial code *Simcenter STAR-CCM+ (v2020.3.1)*. Before carrying out this plan, an extensive literature review was conducted on VIV and the under-the-hood working of the STAR-CCM+ solvers and turbulence models. From the review, key parameters influencing VIV was realized. These included the Reynolds number, the Strouhal number and the mass-damping of the system. For a multi-cylinder configuration such as the one in the OECD benchmark, the influence of the pitch spacing between cylinders on the wake and thereby corresponding VIV was realized. From the review of the STAR-CCM+ turbulence model implementations, the formulations of the constitutive relationship options for the Reynolds stress tensor are realized. These options help in modelling the anisotropy of turbulence better, especially the quadratic (QCR) and cubic options.

The first phase of the current study dealt with the validation of the flow and structural solvers as a standalone as well as fully coupled calculations against the flexible beam FSI benchmark of Turek & Hron[26]. The test cases CFD3, CSM2 and FSI3, in particular, are carried out. From the CFD3 test case, a rule of thumb for selecting a time step size was established. The rule was to select time step size that places 100 sampling points over a fundamental cycle of interest. From the CSM2 test case, the importance of choosing the appropriate approximation for the strain is realized. The rule of thumb asserted was to apply the infinitesimal strain approximation for predicting dominant displacements that are within 10% of the length of the structure perpendicular to the displacement. Although this approximation compromised predictions of the displacement in the other direction which was predicted accurately by the finite approximation. It is to be noted, however, that the finite strain approximation is more expensive to employ. Finally, the FSI3 test case confirmed the working of the Gauss-Seidel coupling implementation of STAR-CCM+. An interesting observation was the presence of "beatings" in the force time history plots but not in the displacement time history plots. This was reasoned to be due the added mass calculations.

The second phase of the study dealt with testing 7 proposed URANS eddy viscosity turbulence model implementations available in STAR-CCM+ against the cross flow VIV study of Khalak & Williamson[27] in a 2D set up. Although the norm for such separated flows is to go for the K-Omega SST model, as a special consideration from the recent work of Liparoti[104], the testing list also includes the low Reynolds number variation of the K-Epsilon model with a cubic constitutive relationship. The amplitude and frequency responses showed the possibility of URANS capturing the 3-branch VIV response. However, shortcomings were noted in the form of a shorter lock-in regime with an earlier and shorter peak response. Judging all the results based on the performance in the initial and upper branch, the K-Omega SST: QCR, K-Omega SST: QCR + GRT and Standard K-Epsilon Low Re: Cubic models were shortlisted for the next phase of the study.

The third and final phase of the study involved the the OECD benchmark. This benchmark came in 2 phases: the open phase where experimental results were available from the beginning and the blind phase where the experimental results were only released after all participants handed in their work.

The open phase of the study was used to select the most appropriate turbulence model for the blind phase. Key observations for the open phase were 1) The overprediction of the vortex shedding frequency, 2) Severely underpredicted spectral density at the natural frequency of Cylinder1 where resonance is expected as well as low background spectra levels, 3) Better fit for the Cylinder2 spectra and 4) Underprediction for all spectra plots in the higher frequency range. Based on these observations, it was hypothesised that a major cause for the difference in numerical and experimental predictions of Cylinder1 is a combined effect of the mismatch in the fourth harmonic of vortex shedding frequency and its natural frequency as well as the absence of actual turbulence (in terms of velocity and pressure fluctuations) from the inlet. To improve upon the prediction of the higher frequency range of the spectra, a higher fidelity method accompanied with a smaller grid and time step size is suggested. From the results obtained in this phase of the study, the Standard K-Epsilon Low Re: Cubic model is finalized and similar observations are drafted as expectations for the blind phase.

The blind phase results matched all the expectations set out from the open phase study. Additionally, the off-resonance results corroborated the aforementioned cause with underpredicted results for Cylinder1 and better fitting results for Cylinder2. In doing so, the research objective is satisfied in terms of selecting the best model for the current application (Standard K-Epsilon Low Re: Cubic) as well as identifying gaps in the capability of URANS in capturing VIV or as was reasoned for the OECD benchmark, a combination of TIV and VIV where the lock-in effect is dependent on a higher harmonic of the vortex shedding frequency. These are in short:

1. Predicting the vortex shedding frequency accurately.
2. Providing actual inflow turbulence.
3. Predicting high frequency range spectra accurately.

7.1. Recommendations for Future Work

With the current gaps identified, the pathway for future work can be set in different directions. These are provided below:

1. In the open and blind phase of the OECD benchmark, the infinitesimal strain approximation was used which neglected the displacements of the cylinders in the direction along the length of the cylinders. Such a displacement, although deemed insignificant compared to the other displacements, does in fact affect the wake of the cylinders especially from the free end. The simulations can be reconducted with the finite strain approximation to quantify the significance of this displacement in the obtained results.

2. It was hypothesised that the missed lock-in of Cylinder1 was partly due to the mismatch in the fourth harmonic of the vortex shedding frequency and its natural frequency. To confirm and quantify this reason, it is suggested to either increase the natural frequency (by virtue of the bob length, for instance) or decrease the flow velocity such that the desired lock-in effect occurs. The gap between the spectral density at the new peak and the experimental results will help validate the hypothesis.

3. The second part of the hypothesis involved obtaining the TIV contribution as turbulence from the inlet. While URANS as is cannot provide actual fluctuations in pressure and velocity to partly excite Cylinder1, there do exist models that can provide artificial fluctuations to a flow. One such example is the Pressure Fluctuation Model (PFM) that was proposed in the works of Kottapalli[24] and Sharma[25] which were developed for pure TIV faced by fuel rods in axial flows. This model could be modified to flood in fluctuations for the cross flow OECD benchmark problem. By incorporating such artificial fluctuations, the second part of the hypothesis may be considered validated if the background spectra is noticed to match with the experimental results.

4. Another path of testing is to choose higher fidelity methods instead of URANS. These could be LES or hybrid models such as DES. Another recently developed hybrid model is the Scale Resolving Hybrid (SRH) model given by Duffal et. al.[105] which is also available in STAR-CCM+ from v2020 onwards. Preliminary tests at NRG show promising results with improved accuracy at a slightly higher computational cost. Using LES or its hybrid models are particularly expected to improve the high frequency range prediction of all spectra plots. Another expectation is to also perhaps show improved vortex shedding frequency predictions as the wake is better resolved. Using LES, in particular, also allows for providing actual turbulence from the inlet which could also be tested to validate the second part of the hypothesis. However, it is to be beared in mind that this venture would be computationally expensive to carry out.

References

[1] IPCC. (2018). *Global warming of 1.5° C*. IPCC, ISBN 978-92-9169-151-7, Switzerland.

[2] BP. (2019). *BP Energy Outlook 2019*

[3] IAEA. (2018). *Energy, Electricity and Nuclear Power Estimates for the Period up to 2050*. IAEA Reference Data Series No. 1/38, Vienna, Austria.

[4] IEA. (2018). *World Energy Outlook 2018*. Paris, France.

[5] MIT. (2018). *The Future of Nuclear Energy in a Carbon-Constrained World*. MIT, Boston, USA.

[6] OECD. (2019). *The Costs of Decarbonisation: System Costs with High Shares of Nuclear and Renewables*. OECD-NEA No. 7299, Paris, France.

[7] WNI. (2018). *World Nuclear Industry Status Report*. Mycle Schneider Consulting, Paris, London.

[8] Podest, M. (1984). *Plant Performance: Reducing Downtime*. IAEA Bulletin, 26(3).

[9] Païdoussis, M. P. (2006). *Real-life experiences with flow-induced vibration*. Journal of Fluids and Structures, 22(6-7), 741-755. doi:10.1016/j.jfluidstructs.2006.04.002

[10] Luk, K. H. (1993). *Pressurized-water reactor internals aging degradation study*. Technical Report, Oak Ridge National Laboratory.

[11] Weaver, D. S., Ziada, S., Au-Yang, M. K., Chen, S. S., Païdoussis, M. P., & Pettigrew, M. J. (2000). *Flow-Induced Vibrations in Power and Process Plant Components—Progress and Prospects*. Journal of Pressure Vessel Technology, 122(3), 339. doi:10.1115/1.556190

[12] The IEE (2005). *Nuclear Reactor Types. An Environment & Energy FactFile provided by the IEE*. The Institution of Electrical Engineers, London, UK. ISBN 0852965818

[13] IAEA PRIS. (2020) *Operational & long-term shutdown reactors*. Retrieved July 12, 2021 from https://pris.iaea.org/PRIS/WorldStatistics/OperationalReactorsByType.aspx

[14] IAEA PRIS. (2020) *Under Construction Reactors*. Retrieved July 12, 2021 from https://pris.iaea.org/PRIS/WorldStatistics/UnderConstructionReactorsByType.aspx

[15] Tijsseling, A. S. (2002). *Fluid-structure interaction in liquid-filled pipe systems : sources, solutions and unsolved problems*. IWDE report 02-05. Technische Universiteit Eindhoven.

[16] Trunov, N. B., Lukasevich, B. I., Veselov, D. O., & Dragunov, Y. G. (2008). *Steam generators – horizontal or vertical (which type should be used in nuclear power plants with VVER?)*. Atomic Energy, 105(3), 165–174. doi:10.1007/s10512-008-9090-1

[17] Bonavigo, L., & De Salve, M. (2011). *Issues for Nuclear Power Plants Steam Generators*. In Steam Generator Systems: Operational Reliability and Efficiency (ed. V. Uchanin), Rijeka InTech. 371–392.

[18] Pettigrew, M. J., Taylor, C. E., Fisher, N. J., Yetisir, M., & Smith, B. A. W. (1998). *Flow-induced vibration: recent findings and open questions*. Nuclear Engineering and Design, 185(2-3), 249–276. doi:10.1016/s0029-5493(98)00238-6

[19] S. Kaneko, T. Nakamura, F. Inada, M. Kato & N. W. Mureithi. (2014). *Flow-Induced Vibrations. Classifications and lessons from practical experiences*. Academic Press.

[20] Naudascher, E., & Rockwell, D. (1994). *Flow-Induced Vibrations: An Engineering Guide*. Rotterdam, Netherlands: Balkema, ISBN 9054101318.

[21] Weaver, D. S. (1976). *On flow induced vibrations in hydraulic structures and their alleviation*. Canadian Journal of Civil Engineering, 3(1), 126–137. doi:10.1139/l76-013

[22] Blevins, R. D. (1990). *Flow-Induced Vibration*. New York: Van Norstrand Reinhold.

[23] OECD/NEA (2014). *Best Practice Guidelines for the use of CFD in Nuclear Reactor Safety Applications - revision*. OECD/NEA Report NEA/CSNI/R(2014)11.

[24] Kottapalli, S. (2016). *Numerical Prediction of Flow Induced Vibrations in Nuclear Reactors through Pressure Fluctuation Modeling*. Master Thesis, Delft University of Technology, The Netherlands.

[25] Sharma, S. (2018). *Numerical Study of Turbulence Induced Vibrations Using Synthetic Fluctuation Field Modeling in Nuclear Reactor Applications*. Master Thesis, Delft University of Technology, The Netherlands.

[26] Turek, S., & Hron, J. (2006). *Proposal for Numerical Benchmarking of Fluid-Structure Interaction between an Elastic Object and Laminar Incompressible Flow*. Fluid-Structure Interaction, 371–385. doi:10.1007/3-540-34596-5_15

[27] Khalak, A., & Williamson, C. H. K. (1996). *Dynamics of a hydroelastic cylinder with low mass and damping*. Journal of Fluids and Structures, 10(5), 455–472. doi:10.1006/jfls.1996.0031

[28] Païdoussis, M. P. (1980). *Flow-induced Vibration in Nuclear Reactors and Heat Exchangers: Practical Experiences and State of Knowledge*. In Practical Experiences with Flow Induced Vibrations, eds. E. Naudascher, & D. Rockwell, Springer, Berlin, pp. 1–81.

[29] Lugt, H.J. (1983). *Vortex Flow in Nature and Technology*. Wiley, New York.

[30] Bingham, R. (2007). *On the crest of a wake.* Nature, 445(7129), 721–722. doi:10.1038/445721a

[31] Perry, A. E., Chong, M. S., & Lim, T. T. (1982). *The vortex-shedding process behind two-dimensional bluff bodies*. Journal of Fluid Mechanics, 116(-1), 77. doi:10.1017/s0022112082000378

[32] Williamson, C. H. K., & Roshko, A. (1988). *Vortex formation in the wake of an oscillating cylinder*. Journal of Fluids and Structures, 2(4), 355–381. doi:10.1016/s0889-9746(88)90058-8

[33] Zdravkovich, M. M. (1985). *Flow induced oscillations of two interfering circular cylinders*. Journal of Sound and Vibration, 101(4), 511–521. doi:10.1016/s0022-460x(85)80068-7

[34] Anderson, J. D. (2011). *Fundamentals of Aerodynamics*. 5th ed., New York, N.Y.: McGraw-Hill.

[35] Lienhard, J. H. (1966). *Synopsis of Lift, Drag and Vortex Frequency Data for Rigid Circular Cylinders*. Washington State University, College of Engineering, Research Division Bulletin 300.

[36] Panton, R. L. (1984). *Incompressible Flow*. New York, N.Y.: Wiley-Interscience.

[37] Zdravkovich, M. (1997). *Flow Around Circular Cylinders. Fundamentals, vol. 1*. New York, N.Y.: Oxford University Press.

[38] Barnett, K. M., & Cermack, J. E. (1974). *Turbulence induced changes in vortex shedding from a circular cylinder*. Technical Report No. 26, Engineering Research Center, College of Engineering, Colorado State University.

[39] Achenbach, E., & Heinecke, E. (1981). *On vortex shedding from smooth and rough cylinders in the range of Reynolds numbers* 6×10^3 *to* 5×10^6. Journal of Fluid Mechanics, 109(-1), 239. doi:10.1017/s002211208100102x

[40] Sarpkaya, T. (1995). Hydrodynamic Damping, Flow-Induced Oscillations, and Biharmonic Response. Journal of Offshore Mechanics and Arctic Engineering, 117(4), 232. doi:10.1115/1.2827228

[41] Griffin, O. M., & Ramberg, S. E. (1976). *Vortex shedding from a cylinder vibrating in line with an incident uniform flow*. Journal of Fluid Mechanics, 75(02), 257. doi:10.1017/s0022112076000207

[42] Ongoren, A., & Rockwell, D. (1988). *Flow structure from an oscillating cylinder Part 2. Mode competition in the near wake*. Journal of Fluid Mechanics, 191(-1), 225. doi:10.1017/s0022112088001570

[43] Zdero, R., Turan, Ö., & Havard, D. G. (1995). *Toward understanding galloping: Near-wake study of oscillating smooth and stranded circular cylinders in forced motion*. Experimental Thermal and Fluid Science, 10(1), 28–43. doi:10.1016/0894-1777(94)00033-5

[44] Bishop, R. E. D., & Hassan, A. Y. (1964). *The Lift and Drag Forces on a Circular Cylinder Oscillating in a Flowing Fluid*. Proceedings of the Royal Society A: Mathematical, Physical and Engineering Sciences, 277(1368), 51–75. doi:10.1098/rspa.1964.0005

[45] Feng, C. C. (1968). *The measurement of vortex-induced effects in flow past stationary and oscillating circular and D-section cylinders*. Master's thesis, University of British Columbia, Vancouver, BC, Canada.

[46] Brika, D., & Laneville, A. (1993). *Vortex-induced vibrations of a long flexible circular cylinder*. Journal of Fluid Mechanics, 250(-1), 481. doi:10.1017/s0022112093001533

[47] Brika, D., & Laneville, A. (1995). *An Experimental Study of the Aeolian Vibrations of a Flexible Circular Cylinder at Different Incidences*. Journal of Fluids and Structures, 9(4), 371–391. doi:10.1006/jfls.1995.1021

[48] Khalak, A., & Williamson, C. H. K. (1997) . *Investigation of relative effects of mass and damping in vortex-induced vibration of a circular cylinder*. Journal of Wind Engineering and Industrial Aerodynamics, 69-71, 341–350. doi:10.1016/s0167-6105(97)00167-0

[49] Williamson, C. H. K., & Govardhan, R. (2004). *Vortex-Induced Vibrations*. Annual Review of Fluid Mechanics, 36(1), 413–455. doi:10.1146/annurev.fluid.36.050802.122128

[50] Sumer, B. M., & Fredsøe, J. (1997). *Hydrodynamics around Cylindrical Structures*. Singapore: World Scientific

[51] Zdravkovich, M. M. (1982). *Modification of Vortex Shedding in the Synchronization Range*. Journal of Fluids Engineering, 104(4), 513. doi:10.1115/1.3241895

[52] Govardhan, R., & Williamson, C. H. K. (2000). *Modes of vortex formation and frequency response of a freely vibrating cylinder*. Journal of Fluid Mechanics, 420, 85–130. doi:10.1017/s0022112000001233

[53] Lighthill, J. (1979). *Waves and hydrodynamic loading*. In Proceedings 2nd International Conference Behaviour of Off-Shore Structures, 1, 140. BHRA Fluid Engineering, Cranfield, Bedford, England.

[54] Lighthill, J. (1986). *Fundamentals concerning wave loading on offshore structures*. Journal of Fluid Mechanics, 173(-1), 667. doi:10.1017/s0022112086001313

[55] Khalak, A., & Williamson, C. H. (1999). *Motions, Forces and Mode Transitions in Vortex-Induced Vibrations at low Mass-Damping*. Journal of Fluids and Structures, 13(7-8), 813–851. doi:10.1006/jfls.1999.0236

[56] Vickery, B. J., & Watkins, R. D. (1964). *Flow-Induced Vibrations of Cylindrical Structures*. Hydraulics and Fluid Mechanics, 213–241. doi:10.1016/b978-0-08-010291-7.50018-5

[57] Scruton C. (1965). *On the wind-excited oscillations of towers, stacks and masts*. In Proceedings Symposium Wind Effects on Buildings & Structures, 16, 798–836. London: HMSO

[58] Skop, R. A., & Griffin, O. M. (1973). *An Heuristic Model for Determining Flow-Induced Vibration of Offshore Structure*. Offshore Technology Conference. doi:10.4043/1843-ms

[59] Skop R. A. (1974). *On modelling vortex-excited oscillations*. NRL Memorandum Report 2927

[60] Griffin, O. M. (1980). *Vortex-Excited Cross-Flow Vibrations of a Single Cylindrical Tube*. Journal of Pressure Vessel Technology, 102(2), 158. doi:10.1115/1.3263315

[61] Sarpkaya, T. (1978). Fluid forces on oscillating cylinders. American Society of Civil Engineers, Waterway, Port, Coastal and Ocean Division, 104, 275-290.

[62] Sarpkaya, T. (1979). *Vortex-Induced Oscillations: A Selective Review*. Journal of Applied Mechanics, 46(2), 241. doi:10.1115/1.3424537

[63] Sarpkaya, T. (1993). *Offshore Hydrodynamics*. Journal of Offshore Mechanics and Arctic Engineering, 115(1), 2. doi:10.1115/1.2920085

[64] Griffin, O. M., & Ramberg, S. E. (1982). *Some Recent Studies of Vortex Shedding With Application to Marine Tubulars and Risers*. Journal of Energy Resources Technology, 104(1), 2. doi:10.1115/1.3230377

[65] Skop, R. A., & Balasubramanian, S. (1997). *A new twist on an old model for vortex-excited vibrations*. Journal of Fluids and Structures, 11(4), 395–412. doi:10.1006/jfls.1997.0085

[66] Païdoussis, M. P. (1983). *A review of flow-induced vibrations in reactors and reactor components*. Nuclear Engineering and Design, 74(1), 31–60. doi:10.1016/0029-5493(83)90138-3

[67] Weaver, D. S., & Fitzpatrick, J. A. (1988). *A review of cross-flow induced vibrations in heat exchanger tube arrays*. Journal of Fluids and Structures, 2(1), 73–93. doi:10.1016/s0889-9746(88)90137-5

[68] Weaver, D. S., Fitzpatrick, J. A., & El Kashlan, M. (1987). *Strouhal Numbers for Heat Exchanger Tube Arrays in Cross Flow*. Journal of Pressure Vessel Technology, 109(2), 219. doi:10.1115/1.3264899

[69] Fitzpatrick, J. A., Donaldson, I. S., & McKnight, W. (1988). *Strouhal numbers for flows in deep tube array models*. Journal of Fluids and Structures, 2(2), 145–160. doi:10.1016/s0889-9746(88)80016-1

[70] Abd-Rabbo, A., & Weaver, D. S. (1986). *A flow visualization study of flow development in a staggered tube array*. Journal of Sound and Vibration, 106(2), 241–256. doi:10.1016/0022-460x(86)90316-0

[71] Ziada, S., & Oengören, A. (1992). *Vorticity shedding and acoustic resonance in an in-line tube bundle part I: Vorticity shedding*. Journal of Fluids and Structures, 6(3), 271–292. doi:10.1016/0889-9746(92)90010-z

[72] Ziada, S., & Oengören, A. (1993). *Vortex Shedding in an In-line Tube Bundle with Large Tube Spacings*. Journal of Fluids and Structures, 7(6), 661–687. doi:10.1006/jfls.1993.1039

[73] Polak, D. R., & Weaver, D. S. (1995). *Vortex Shedding in Normal Triangular Tube Arrays*. Journal of Fluids and Structures, 9(1), 1–17. doi:10.1006/jfls.1995.1001

[74] Ziada, S. (2006). *Vorticity shedding and acoustic resonance in tube bundles*. Journal of the Brazilian Society of Mechanical Sciences and Engineering, 28(2), 186–189. doi:10.1590/s1678-58782006000200008

[75] Zdravkovich, M. M. (1977). *REVIEW—Review of Flow Interference Between Two Circular Cylinders in Various Arrangements*. Journal of Fluids Engineering, 99(4), 618. doi:10.1115/1.3448871

[76] King, R., & Johns, D. J. (1976). *Wake interaction experiments with two flexible circular cylinders in flowing water*. Journal of Sound and Vibration, 45(2), 259–283. doi:10.1016/0022-460x(76)90601-5

[77] Chen, S. S. (1985). *Flow-Induced Vibration of Circular Cylindrical Structures*. United States. doi:10.2172/6331788

[78] Jendrzejczyk, J. A., Chen, S. S., & Wambsganss, M. W. (1979). *Dynamic responses of a pair of circular tubes subjected to liquid cross flow*. Journal of Sound and Vibration, 67(2), 263–273. doi:10.1016/0022-460x(79)90489-9

[79] Boman, R. (2010). *Développement d'un formalisme Arbitraire Lagrangien Eulérien tridimensionnel en dynamique implicite. Application aux opérations de mise à forme, Université de Liège*. Ph.D. Dissertation, University of Liège, Belgium. Available at http://bictel.ulg.ac.be/ETDdb/collection/available/ULgetd-05172010-091736/

[80] Gatzhammer, B. (2014). *Efficient and flexible partitioned simulation of fluid-structure interactions*. ISBN 978-3-8439-1990-6, Ph.D. Dissertation, TU Munich, Germany.

[81] Zienkiewicz, O. C. & Taylor, R. L. (2006). *The Finite Element Method for Solid and Structural Mechanics*. 6th edition, Elsevier Butterworth-Heinemann, Oxford, ISBN 9781493302895.

[82] Siemens (2020). *Simcenter STAR-CCM+ Documentation, Version 2020.3*. Available at https://docs.sw.siemens.com/en-US/product/226870983/doc/PL20200805113346338.starccmp_userguide_pdf/pdf/

[83] IAPWS (2007). *Revised Release on the IAPWS Industrial Formulation 1997 for the Thermodynamic Properties of Water and Steam*, International Association for the Properties of Water and Steam Secretariat, Lucerne, Switzerland. (available at www.iapws.org).

[84] Lien, F. S., Chen, W. L., & Leschziner, M. A. (1996). *Low-Reynolds-Number Eddy-Viscosity Modelling Based on Non-Linear Stress-Strain/Vorticity Relations*. Engineering Turbulence Modelling and Experiments, 91–100. doi:10.1016/b978-0-444-82463-9.50015-0

[85] Yap, C. (1987). *Turbulent heat and momentum transfer in recirculating and impinging flows*. Ph.D. Dissertation, Faculty of Technology, University of Manchester, U.K.

[86] Menter, F. R. (1994). *Two-equation eddy-viscosity turbulence models for engineering applications*. AIAA Journal, 32(8), 1598–1605. doi:10.2514/3.12149

[87] Durbin, P. A. (1996). *On the k-3 stagnation point anomaly*. International Journal of Heat and Fluid Flow, 17(1), 89–90. doi:10.1016/0142-727x(95)00073-y

[88] Arolla, S. K., & Durbin, P. A. (2013). *Modeling rotation and curvature effects within scalar eddy viscosity model framework*. International Journal of Heat and Fluid Flow, 39, 78–89. doi:10.1016/j.ijheatfluidflow.2012.11.006

[89] Spalart, P. R. (1999). *Strategies for turbulence modelling and simulations*. Engineering Turbulence Modelling and Experiments 4, 3–17. doi:10.1016/b978-008043328-8/50001-1

[90] Durbin, P. A. (2017). *Perspectives on the Phenomenology and Modeling of Boundary Layer Transition*. Flow, Turbulence and Combustion, 99(1), 1–23. doi:10.1007/s10494-017-9819-9

[91] Langtry, R. B. (2006). *A correlation-based transition model using local variables for unstructured parallelized CFD codes*. Ph.D. Dissertation, University of Stuttgart, Germany. doi:10.18419/opus-1705

[92] Menter, F. R., Langtry, R. B., Likki, S. R., Suzen, Y. B., Huang, P. G., & Völker, S. (2006). *A Correlation-Based Transition Model Using Local Variables—Part I: Model Formulation*. Journal of Turbomachinery, 128(3), 413. doi:10.1115/1.2184352

[93] Lee, S., Wolberg, G., & Shin, S. Y. (1997). *Scattered data interpolation with multilevel B-splines*. IEEE Transactions on Visualization and Computer Graphics, 3(3), 228–244. doi:10.1109/2945.620490

[94] Degroote, J., Bathe, K.-J., & Vierendeels, J. (2009). *Performance of a new partitioned procedure versus a monolithic procedure in fluid–structure interaction*. Computers & Structures, 87(11-12), 793–801. doi:10.1016/j.compstruc.2008.11.013

[95] Küttler, U., & Wall, W. A. (2008). *Fixed-point fluid–structure interaction solvers with dynamic relaxation*. Computational Mechanics, 43(1), 61–72. doi:10.1007/s00466-008-0255-5

[96] Degroote, J., Haelterman, R., Annerel, S., Bruggeman, P., & Vierendeels, J. (2010). *Performance of partitioned procedures in fluid–structure interaction*. Computers & Structures, 88(7-8), 446–457. doi:10.1016/j.compstruc.2009.12.006

[97] Tian, F. B., Dai, H., Luo, H., Doyle, J. F., & Rousseau, B. (2014). *Fluid–structure interaction involving large deformations: 3D simulations and applications to biological systems*. Journal of Computational Physics, 258, 451–469. doi:10.1016/j.jcp.2013.10.047

[98] Giannelis, N. F., & Vio, G. A. (2015). *Computational Benchmark of Commercial Fluid-Structure Interaction Software for Aeroelastic Applications*. In Proceedings of the 16th International Forum on Aeroelasticity and Structural Dynamics, St. Petersburg, Russia.

[99] De Santis, D., & Shams, A. (2019). *An advanced numerical framework for the simulation of flow induced vibration for nuclear applications*. Annals of Nuclear Energy, 130, 218–231. doi:10.1016/j.anucene.2019.02.049

[100] Cole, R. E., & Neu, W. L. (2019). *Validation of a commercial fluid-structure interaction solver with applications to air cushion vehicle flexible seals*. Ocean Engineering, 189, 106287. doi:10.1016/j.oceaneng.2019.106287

[101] Siemens (2020). *STAR-CCM+ Verification Suite 15.06.007*. Available at https://support.sw.siemens.com/en-US/product/226870983/download/PL20200805113346338

[102] Guilmineau, E., & Queutey, P. (2004). *Numerical simulation of vortex-induced vibration of a circular cylinder with low mass-damping in a turbulent flow*. Journal of Fluids and Structures, 19(4), 449–466. doi:10.1016/j.jfluidstructs.2004.02.004

[103] Dobrucali, E. & O. Kinaci (2017). *URANS-Based Prediction of Vortex Induced Vibrations of Circular Cylinders*. Journal of Applied Fluid Mechanics 10(3), 957-970. doi:10.18869/acadpub.jafm.73.238.27339

[104] Liparoti, S. (2020). *Simulation of cross-flow around bluff-bodies using URANS methods: paving the way for Fluid-Structure Interaction analyses*. Master Thesis, URN etd-10302020-102840, University of Pisa, Italy.

[105] Duffal, V., de Laage de Meux, B., & Manceau, R. (2019). *Development and Validation of a Hybrid RANS-LES Approach Based on Temporal Filtering*. Proceedings of the ASME-JSME-KSME 2019 8th Joint Fluids Engineering Conference. Volume 2: Computational Fluid Dynamics. San Francisco, California, USA. July 28-August 1, 2019.